Application of Laser-Interfaced Mass Spectrometry to Biological and Pharmaceutical Molecules

Rosaria Cercola

PhD

University of York

Chemistry

September 2019

Ai miei genitori,
zia Marina ed
Alessandro

Abstract

This thesis demonstrates the use of laser photodissociation spectroscopy to explore the photochemistry of molecular and cluster ions isolated in a commercially adapted mass spectrometer.

Chapter 3 describes gas-phase photodissociation experiments on adenosine nucleotides with phosphate chains of varying lengths with single and double negative charges. Direct comparison between the photochemistry of this series of compounds shows that the adenine $\pi \rightarrow \pi^*$ transition is relatively unaffected by the charge state. In addition, the experiments show that photostability is enhanced as the number of phosphate groups increases.

Near-threshold excitation of $I^- \cdot A$ and $H_2PO_3^- \cdot A$ is investigated in Chapter 4 to explore whether it leads to electron transfer from the anion to the adenine. It is shown that the adenine dipole-bound excited state is prepared from excitation of $I^- \cdot A$. In contrast, electron detachment in $H_2PO_3^- \cdot A$ occurs from the neutral nucleobase and not from the anion. We identify $H_2PO_3^- \cdot A$ as an example of an anion-molecule cluster where photodetachment initiates intra-molecular hydrogen atom transfer.

In Chapter 5, photodissociation spectroscopy is applied to protonated TryptoCORM ($[MnL(CO)_3(CH_3CN)] \cdot H^+$ and $[MnL(CO)_3] \cdot H^+$ L=deprotonated tryptophan), a metal carbonyl that was proven effective against bacteria such as *E. Coli*. Photofragmentation yield spectra reveal the wavelength-dependence of the photofragmentation pathways. This analysis provides insight on the CO release of TryptoCORM across the visible spectral range, with $[MnL(CO)_3(CH_3CN)] \cdot H^+$ and $[MnL(CO)_3] \cdot H^+$ releasing three CO molecules as the predominant fragmentation pathway below 400 nm.

Finally, Chapter 6 presents photodissociation spectroscopy on a series of metal carbonyl complexes, $[Ru(\eta^5-C_5H_5)CO(PPh_3)_2]^+$, $[Ru(\eta^5-C_5H_5)(dppe)CO]^+$ and $[Mn(CO)_4Br_2]^-$ and compares the results to solution-phase photolysis. For $[Ru(\eta^5-C_5H_5)CO(PPh_3)_2]^+$ and $[Ru(\eta^5-C_5H_5)(dppe)CO]^+$, the solution-phase photolysis products closely match those for gas-phase photolysis. For $[Mn(CO)_4Br_2]^-$, our results highlight the benefit of studying metastable species in the gas phase. Finally, we discuss the utility of LIMS as a tool for aiding rational design of photopharmaceuticals.

List of Contents

List of Abbreviations

AC	Alternating current
AMP	Adenosine monophosphate
ADP	Adenosine diphosphate
ATP	Adenosine triphosphate
BBO	β-barium borate
cAMP	Cyclic adenosine monophosphate
cADP	Cyclic adenosine diphosphate
CASSCF	Complete active space self-consistent field
CI	Conical intersection
CID	Collision induced dissociation
CIVS	Cryogenic ion vibrational spectroscopy
CLIO	Centre laser infrarouge d'orsay
CRM	Charge residue model
CORM	CO-releasing molecule
dAMP	Deoxy adenosine monophosphate
DC	Direct current
DCM	Dichloromethane
DFT	Density functional theory
Dppe	1,2-Bis(diphenylphosphino)ethane
ED	Electron detachment
ECP	Effective core potential
EM-CCD	Electron Multiplying charge-coupled device
EPR	Electron paramagnetic resonance
ESI	Electrospray ionisation
ETD	Electron-transfer dissociation
FELIX	Free electron lasers for infrared experiments
FTMS	Fourier transform mass spectrometry

HCD	Higher-energy collision induced dissociation
HOMO	Highest occupied molecular orbital
HWHM	Half width at half maximum
IC	Internal conversion
ICR	ion cyclotron resonance
IEM	Ion evaporation model
IMS	Ion-mobility mass spectrometry
IR	Infrared
IRM	Ion routing multipole
IRMPD	Infrared multiphoton dissociation
IVR	Intramolecular vibrational redistribution
LED	Light emitting diode
LIMS	Laser-interfaced mass spectrometry
LIT	Linear ion trap
LUMO	Lowest unoccupied molecular orbital
MCA	Multiply charged anion
MLCT	Metal-to-ligand charge transfer
MRCI	Multireference configuration interaction
MRM	Multiple reaction monitoring
MS	Mass spectrometry
OPA	Optical parameter amplifier
OPO	Optical parameter oscillator
PD	Photodissociation
PF	Photofragmentation
QIT	Quadrupole ion trap
RCB	Repulsive Coulomb barrier
REMPI	Resonance-enhanced multiphoton ionisation
RF	Radio frequency

RRKM	Rice–Ramsperger–Kassel–Marcus
SDD	Stuttgart/Dresden
SHB	Spectral hole burning
TDDFT	Time-dependent density functional theory
TFA	Trifluoroacetic acid
TKER	Total kinetic energy release
TNI	Transient negative ions
TOF	Time-of-flight
TRIR	Time-resolved infrared spectroscopy
TRMPI	Time resolved multiphoton ionization
TRPEI	Time-resolved photoelectron imaging
TRPES	Time-resolved photoelectron spectroscopy
UV	Ultraviolet
UVPD	Ultraviolet photodissociation
VDE	Vertical detachment energies
Vis	Visible
YAG	Yttrium aluminium garnet

List of Tables

experimental spectrum. Only the main transitions and the HOMO-LUMO are shown.

List of Figures

List of Schemes

Acknowledgements

This PhD has been the most intense journey of my life, and I would not have made it to the end if it was not for the people with whom I have shared it and to whom my most sincere acknowledgement is going.

First and foremost, I need to thank my supervisor, Dr Caroline Dessent, for letting me on this path; for her guidance and support all throughout; for encouraging my personal growth; and, most of all, for pushing me and convincing me that I could do it, even on my own. From her, I learned how to be a better scientist and a better person.

I always say that Karl Heaton has been the first friend that I made here. I feel extremely grateful for his human presence from the beginning of my PhD, but also for his role as my supervisor at the mass spectrometry service. Furthermore, I need to express my gratitude to Karl and the Chemistry Department for my PhD studentship.

I would like to thank Prof. Etienne Garand and his group at the University of Wisconsin-Madison for hosting me to conduct the cryogenic ion experiments and for making me feel at home. I also need to thank deeply the Wild Foundation for the funding that helped me get there.

My gratitude goes to Prof. Ian Fairlamb, Dr. Jason Lynam and Prof. Robin Perutz for the stimulating scientific discussions over the CORMs. I would like to thank Lewis Hall, Benjamin Aucott and the other members of the Fairlamb and Lynam groups for the synthesis of the CORMs and all the help and the interesting discussions.

Sincere thanks go to the departmental staff, Leonie, Cristina, Sharon, Rachel and Alice for the guidance, the advice and all the support. Thanks also to Chris Rhodes

for all the help on the development of the on-line photolysis cell, and Ed Bergström for all the times I needed some help with the amaZon or the Orbitrap.

I would like to thank Edward for his help and precious friendship throughout this journey and Mathew for understanding every time I needed a hug. I had great fun with you two, and I will always remember the three of us aligning the laser while fighting over the YouTube control.

Kelechi, you are an incredible human being, and, during our bizarre relationship, you thought me so much. You care about everyone and see the best in everyone. I will always always try to be the person that you see, the best version of myself.

Natalie, I always joke saying that you are a kid, but actually, you are a proper adult, so much more than I will always be. Thank you for helping me every time I had an "adult" issue, like job hunting, organising things and proofreading, but most of all, thank you for always being there.

Jake, you always know what to say and what to do to make me mad (ahahah). Jokes aside, thank you for all the support during this tough year. Furthermore, you helped me gaining new perspective and enlarging my horizons, and I feel really lucky for this time, however short.

Further thanks go to everyone that has joined our group during the years: it has always been stimulating, and fun and I have been very fortunate.

I would also like to thank the "office": Michi, Pete, Barbara, Soul, Fiona and everyone that has shared with me that room (often at very improbable times). You really helped me through many difficult times and contributed to my mental sanity.

Throughout this journey, I have met some fantastic people, and I feel so incredibly lucky to have been blessed enough to be able to call you my friends: Chiara, Marco, Manuela and Martina, this thesis is a bit yours as well. You have been caring and supporting and you often gave me the push I needed to get here. You have no idea how much I love you and how much I will miss you.

Chiara, you took care of me as a sister when I most needed help (mi hai raccolta con il cucchiaino proprio). I always looked forward to the drinks and the meals we shared during my second year and they are one of the reasons I am still here.

Marco, with you everything is beautiful and funny but is also deep and profound. I love how we can go from sharing our life experiences to being stupid together in 5 minutes. Thank you for always being there.

Manuela you have been an incredible companion during this last year. Living with you has been one of the best things I could have done, no matter how old and challenging (scarrupata) that house was. Thank you for everything and for taking care of me, especially these past two weeks.

Martina! How can I tell you how much I have loved stopping by at your office or how much I hoped you would appear at the mass spec window? I am so grateful for joining that gym! Thank you so much for being here with me.

I would also like to thank Silvia, Michela and Zac for being there, however far, every time I needed a friendly voice, or any help.

Thanks also to Anna Claudia for all the fun we had while studying Arabic.

I would like to express my immense gratitude to Gabriella, Lello and Andrea for the constant presence during these four years. I know that we were far, and I was often busy, but knowing that you were there, supporting me and cheering for me has always been on the back of my mind, as part of my safety net.

A special thanks to my aunt Marina. You will always be my role model. It is thanks to you and your immense strength, that I have always known I could do and be everything I wanted and that I could always overcome any obstacles.

I heartily thank my parents, Maria and Genny, for being my support, constantly and unconditionally. Everything I have done so far and everywhere I am and will be is primarily your merit. Thank you for pushing me but also for understanding every time I needed some space, time, or encouragement when things were difficult. I know that it has been really painful and that you did not choose the thousands of kilometres that separated us, but I know you have chosen my happiness, always, and for this I thank you with all my heart. (la pizza mi dovevate insegnare a fare!)

Finally, my deepest thanks go to Alessandro, for being my best friend, my motivation, and my support. This PhD is also yours for the constant inspiration, encouragement and cheer, especially every time I wanted to give up. You have been my rock, you have given me the strength to keep going, the imagination to see the end and the willpower to get here. I do not know where we are going next, but I know that, as long as we are together, I can do it all. Thank you so much for letting me in your life.

Author's Declaration

I declare that the research presented in this thesis is my own and is original. This thesis has not previously been submitted for award at this or any other institution. All sources are acknowledged as References.

Chapter 3 has been published:

"*Photoexcitation of Adenosine 5'-Triphosphate Anions in Vacuo: Probing the Influence of Charge State on the UV Photophysics of Adenine*"

R. Cercola, E. Matthews and C.E.H. Dessent, *J. Phys. Chem. B*, 2017, **121**, 5553. https://doi.org/10.1021/acs.jpcb.7b03435

Chapter 4 has been published:

"*Near-threshold electron transfer in anion-nucleobase clusters: does the identity of the anion matter?*"

R. Cercola, E. Matthews and C.E.H. Dessent, *Molecular Physics*, 2019, **117**, 3001. https://doi.org/10.1080/00268976.2019.1596327

Part of the data in Chapter 3 was acquired by Edward Matthews, however all the data analysis and the interpretation were carried out by the candidate. Part of the data presented in Chapter 6 was acquired alongside Lorna Olijnyk, during her Master project. Synthesis of the molecules in Chapter 5 and 6 was done by the members of Lynam and Fairlamb groups.

Chapter 1

Introduction to Gas-Phase Photodissociation Spectroscopy of Biological and Pharmaceutical Ions

1.1. Why Conduct Spectroscopy in the Gas-Phase?

The investigation of matter via its interaction with light is key to understanding molecular properties such as geometric and electronic structures, and reaction mechanisms. [1] According to the scope of the investigation, matter can be interrogated while in different phases. The choice of the state to investigate is associated with the information that is needed. Solid- and solution-phases are related to many everyday environments, and therefore, they can seem the most obvious ones to study. However, the gas-phase offers an arena where intrinsic properties can be studied in more detail. [2] For example, certain molecular properties can vary in solution according to the identity of the solvent, such as the well-known bathochromic or hypsochromic shifts of UV-Vis spectroscopy. [3] Aggregation, ion association and micelle formation can also perturb molecular properties to varying extents depending on the specific experimental condition, leading to problems for interpreting condensed-phase experimental results. [3-5]

Computational chemistry is a powerful tool for calculating some molecular-level properties, such as binding energies or intrinsic spectra, but it is essential that those calculations are benchmarked against experimental data. Gas-phase spectroscopy is a great tool for measuring fundamental properties such as electronic structure, geometry and photochemistry, and produces experimental data that can be directly compared with computational results, providing excellent benchmarking of different theoretical methods. [2]

1.2 Gas-Phase Spectroscopy

1.2.1 Photodissociation Spectroscopy

Since the first experiments performed by Brauman and Smyth in 1969, [6] when they measured the photodetachment energies of hydroxide anions with an ion cyclotron resonance (ICR) spectrometer, photodissociation (PD) spectroscopy has become a standard tool to explore electronic absorption spectra, [7] photofragmentation mechanisms, [8] and excited-state dynamics of gaseous ions. [9] Technological advances have allowed the application of the technique to species of widely different molecular dimensions: from diatomic molecules to aggregates, clusters and proteins. [6] [10] [11]

Lasers are commonly chosen as the light source for gas-phase studies due to characteristics such as monochromatic light, collimation and power. [12] In the gas-phase, if the decay to the ground state is a non-radiative process, the absorption of a resonant UV-Vis photon can lead to dissociation of the parent ion. This situation is quite distinct from solution-phase excited-state dynamics where non-radiative decay prepares a hot ground-state molecule that can transfer the excess thermal energy to the solvent *via* vibrational relaxation. [12]

In a UVPD experiment, gas-phase species (ions or ionic clusters) are investigated in mass spectrometers that can be exploited to produce, select, isolate, and interrogate the ionic species upon irradiation. [13]

When spectroscopy is performed in a mass spectrometer, the number of molecular species that typically interacts with a laser pulse is in the order of 10^3-10^6: The small ensemble size means that differences between the initial and transmitted laser beam are not measurable. Photodissociation spectroscopy employs ion detection as an alternative method to acquire absorption spectra to compensate for the immeasurable

beam depletion: Mass spectra are collected and compared at each wavelength, and the extinction coefficient is approximated by the number of species that are depleted upon light irradiation. By scanning the wavelengths, an absorption spectrum can be compiled.

The use of the mass spectrometer adds another dimension to the absorption action spectra, the recognition of any photofragments. Hence, dissociative intramolecular reaction pathways are mapped as a function of wavelength. Two main mechanisms can be identified: ionic fragmentation (1.1) and, for the anions, electron detachment (1.2).

$$AB^{+(-)} + h\nu \rightarrow A^{+(-)} + B \qquad\qquad (1.1)$$

$$M^{n-} + h\nu \rightarrow M^{(n-1)-} + e^{-} \qquad\qquad (1.2)$$

1.2.2 Laser-Interfaced Mass Spectrometry

Two different instrumental approaches can be considered as having been used to perform photodissociation spectroscopy, with experiments either being performed in custom-built instruments, [14] [15] or *via* the adaptation of commercial mass spectrometers. [16-18] Both experimental approaches present advantages and disadvantages. The advantages of modifying commercial mass spectrometers to be interfaced with lasers and perform action spectroscopy are numerous. These instruments are easy to use, reliable over long timescales and robust. Technical assistance can be readily obtained when necessary. Moreover, these instruments require very little weekly maintenance and often do not need expert instrumentalists to run an experiment. However, the compactness of the instruments can make it challenging to modify and adapt them to certain desired experiments. In contrast, custom-built instruments can be perfectly tailored to the desired experiment but are often challenging to build, use and maintain.

As the experimental work in this thesis has been conducted in a commercial mass spectrometer, the rest of this section focuses on such experiments. More information on custom-built PD experiments can be found in Ref. [19].

For the earliest photodissociation experiments in a commercial mass spectrometer, different layouts were explored. In 1983, Bowers and co-workers interfaced a VG Instruments ZAB-2F (chemical ionisation) with an argon ion laser (Coherent Innova 20) and dye laser (Coherent Model 599) to obtain the photodissociation spectrum of $(NO)_2^+$ radical over the range 488-660 nm. [20] In 1984, Freiser and co-workers used Fourier-transform ICR mass spectrometers (Nicolet FTMS-1000) to study photodissociation processes and bond energies of organometallic compounds. [21] In this experiment, the ions were created *via* laser desorption, and the ICR cell was modified by replacing the transmitter plates with 80% transmittance screens. Once isolated, the ions were irradiated with light from a 2.5-kW mercury-xenon arc lamp.

Different modifications of Nicolet FTMS-1000 and 2000 were implemented in different laboratories where lasers were used for experiments including infrared multiphoton dissociation (IRMPD) (10.6 μm CO_2 laser) [22] and UVPD (193 nm ArF excimer laser) [23] in single-wavelength experiments. The power of the laser and the irradiation time were varied to control the degree of fragmentation. Within five years, Williams and co-workers were using photofragmentation to fragment heavy peptides. [24]

Numerous experiments interfacing IR lasers with commercial mass spectrometers have been implemented with IRMPD on modified Bruker FT-ICR, having become a powerful tool for structural analysis. Some of these experiments are now performed at free-electron laser facilities such as the Centre Laser Infrarouge d'Orsay, CLIO (7 T FT- ICR Apex Qe) [25]. IRMPD spectroscopy is also implemented on ion traps at

CLIO and at the Free Electron Lasers for Infrared eXperiments, FELIX (Bruker amaZon Speed ETD, Bruker Esquire 3000+) [26] [27]. To provide some illustration, IRMPD was used by Maitre et al. at CLIO to characterise the structures of the organometallic complexes involved in the reduction of Pd(II) to Pd(0) within [(phosphabarrelene)Pd(allyl)Cl] with K_2CO_3/PhB(OH)$_2$. They determined the η^3 coordination of the allyl and κ^1 of the CO_3^- to the Pd(II). [28] Using a similar experimental configuration, Oomens and co-workers have studied the deprotonation sites of small peptides interacting with metal ions and the influence of microsolvation on their interaction. [29] [30] Further examples of IRMPD experiments in modified commercial mass spectrometers can be found in Refs. [31] and [32].

UVPD spectroscopy within commercial mass spectrometers is far less common, and there are only a few such instruments worldwide. Weinkauf and co-workers were one of the first to use commercial ion trap mass spectrometers for UV photodissociation analysis. [33] In this first configuration, a frequency-doubled excimer-pumped dye laser was interfaced with a modified Esquire 3000 (Bruker, Daltonik) and used to explore the S_0-S_1 transition of tryptophan in the gas-phase. [33] The basic approach of performing UV excitation in a mass spectrometer has more recently been extended in several different experiments.

Ion-mobility mass spectrometry (IMS) separates ions based on their mobility in a carrier buffer gas. Following custom-built IMS-UVPD experiments implemented by the Rizzo, Jarrold and Bowers groups, [34-36] Dugourd coupled the IMS drifting tube to a Bruker quadrupole time-of-flight (Maxis Impact, Bruker Daltonik) that is used as a detector after IMS separation. The laser beam was introduced in the instrument collinearly to the ion path. [37] Very recently, they used this instrument to photoactivate the isomerisation of a ruthenium complex ([Ru(bpy)$_2$(DMSO)$_2$], bpy=2,2'-Bipyridine) and detected it *via* IMS. [38]

An Esquire 3000+ (Bruker Daltonics) was modified in Jockush's group to record gas-phase absorption and laser-induced fluorescence of trapped ions. [39] In this configuration, a third hole was drilled in the ring electrode, to collect any fluorescence produced upon photoexcitation that was then directed onto a spectrograph, thus dispersing the fluorescence onto an EM-CCD camera. Using this instrument, it was possible to apply fluorescence (Förster) resonance energy transfer to a gas-phase mass-selected protein. [40]

Time-resolved fragmentation action spectroscopy has been implemented recently by Riehn and co-workers, on a modified commercial mass spectrometer (amaZon Speed, Bruker Daltonics), integrated with a femtosecond laser. [41-43] The experiment has been used to probe the photofragmentation dynamics of organometallic complexes such as $[(^{t}bbpy)_2Ru(tpphz)Pt(Cl)_2]^{2+}$ and $[(^{t}bbpy)_2Ru(tpphz)Pd(Cl)_2]^{2+}$ ($^{t}bbpy=4,4'$-di-tert-butyl-2,2'-bipyridine and tpphz=tetrapyrido[3,2-a:2'3'-c:3'',2'-h:2''',3'''-j]phenazine). [41] They found that 440 nm excitation resulted in photodecay mechanisms and time constants that were largely similar to those obtained in solution.

1.3 Nucleobase Photophysics and Gas-Phase Properties

The survival of DNA nucleobases to UV radiation under early earth conditions, and the evolutionary choice to make them the life's building blocks, is thought to be directly linked to their photostability. [44] The canonical nucleobases (Scheme 1.1) have short excited-state lifetimes and decay to the electronic ground-state in a few picoseconds upon UV excitation. [45] This mechanism preserves the base itself from fragmentation, which is crucial for complementary recognition in double-helix assembly. [46] [47]
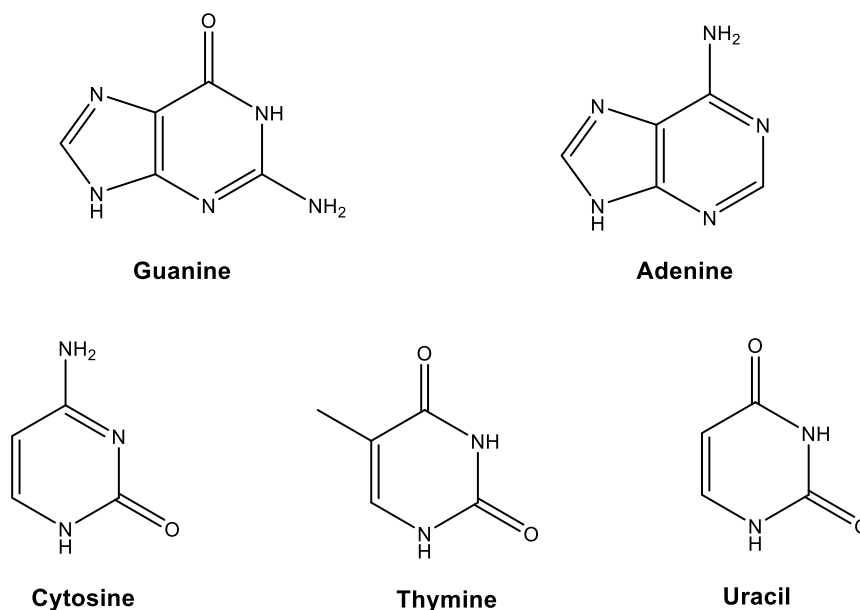
Scheme 1.1 Canonical DNA and RNA nucleobases.

Nevertheless, UV radiation is still linked to DNA damage and photocarcinogenesis. [48] [49] The nucleobase pairs, the sugar-ring and phosphate scaffold that constitute the DNA structure, make it necessary a bottom-up approach in the study of its photodynamics. The main historic challenge for gas-phase studies of biological molecules and ions was their volatilisation since they generally have low vapour pressures and tend to decompose with heat. [2] This hampered progress in this field and led to initial studies being conducted on small biomolecular units such as nucleobases.

1.3.1 Gas-Phase Spectroscopy of Neutral Nucleobases

The first well-resolved gas-phase spectra of neutral nucleobases were obtained via resonance-enhanced multiphoton ionisation (REMPI) spectroscopy by Nir et al., using laser desorption to produce a molecular beam that was jet-cooled by supersonic expansion. The molecular beam was overlapped with a laser beam for photoexcitation, and a time-of-flight mass spectrometer was used to detect photoionisation. [50-52] Nucleobase tautomers were frequently present in the spectra but could be disentangled *via* IR-UV and UV-UV spectral hole burning (SHB)

techniques. [53] Nir et al. reported hole-burning spectra from the 9H and 7H-Keto forms of guanine after blocking the Keto-Enol tautomerism using 1-methylguanine (Scheme 1.2). [54]

9H-Keto   9H-Enol

7H-Keto   7H-Enol
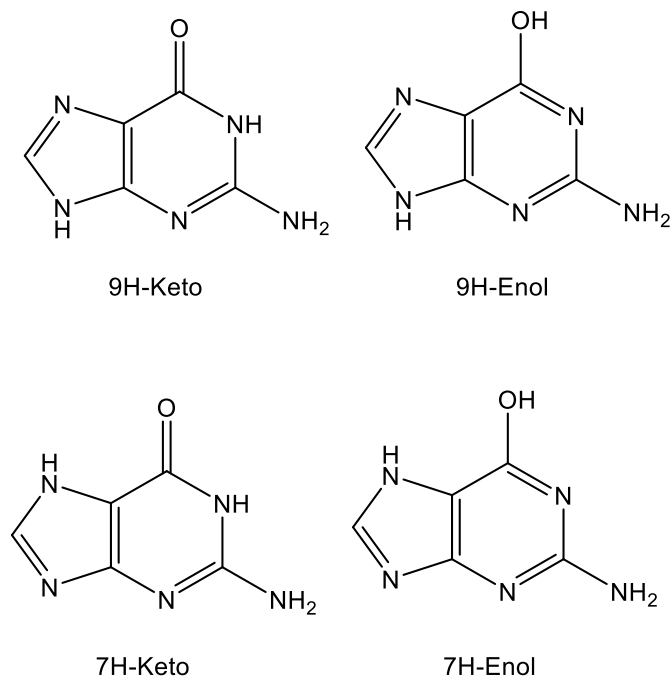
Scheme 1.2 Keto-Enol forms of 9H and 7H isomers of guanine.

The first dynamics experiments on nucleobases were performed by Fischer and co-workers using two-colour picosecond time-resolved photoionisation (TRMPI). [55] In this study, the lifetime of the canonical adenine $\pi\pi^*$ excited state produced *via* 277 nm excitation was found to be 9 ps. The dominant decay channel was proposed to be intersystem crossing to the T_1 state. This mechanism was later confirmed by femtosecond time-resolved photoelectron spectroscopy (TRPES), performed by Stolow and co-workers in 2004. [56] [57]

Further excitation of the $\pi\pi^*$ state at 250 and 267 nm proved that higher vibronic levels have much shorter lifetimes (< 50 fs), due to vibronic coupling between $\pi\pi^*$ and $n\pi^*$ states which then relaxe to S_0 in 750 fs *via* internal conversion. A $\pi\sigma^*$ state, which is dissociative along the N9-H coordinate, was proposed to be the dominant relaxation channel from the bright $\pi\pi^*$ state accessed by excitation at 267 nm. [56]

[57] [58] At 250 nm, the molecule was proposed to access numerous pathways leading to the nπ* state. [58]

A further mechanism was proposed by Broo, [59] involving a distortion of the C2 carbon in the six-membered ring of the adenine (ring puckering), and leading the system to evolve towards a conical intersection between the ππ* state and the ground state. [60]
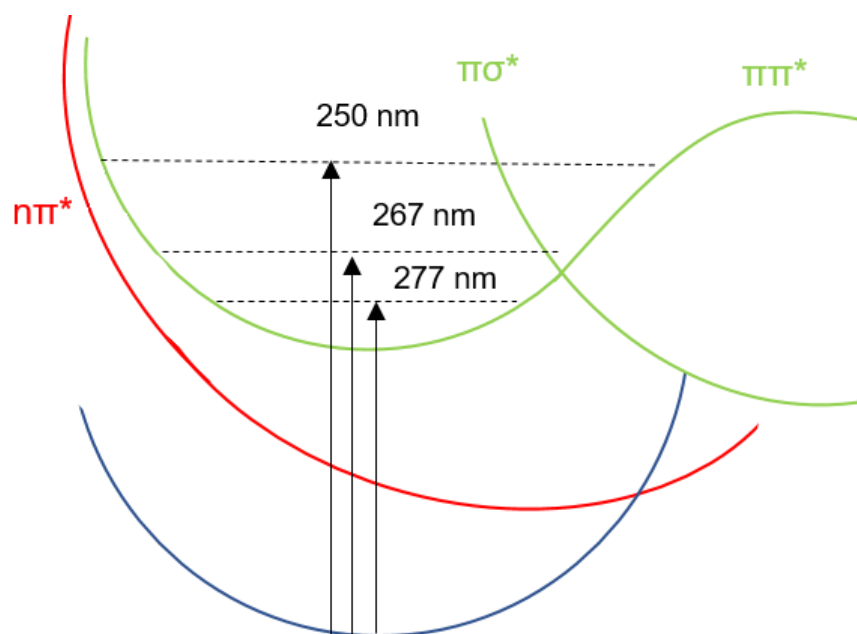
Figure 1.1 Simplified scheme of the electronic relaxation dynamics of adenine as described in Ref. [58]. The triplet state accessed upon 277 nm excitation is not shown

In 2010, Ullrich and co-workers performed a TRPES experiment at six excitation wavelengths between 265 and 200 nm, that confirmed the previous results and provided some further information on the wavelength dependence and the excited states lifetimes. [61] At wavelengths higher than 240 nm, the primary relaxation mechanism resulted to be ππ* → nπ* → S_0 with the first step being shorter than 100 fs. The lifetime of nπ* changes with the absorption wavelength (1032 to 700 fs), becoming shorter with higher photon energy. Only at lower wavelengths (< 240 nm), a channel with faster relaxation time is accessible and consistent with the ππ* → πσ* → S_0 pathway. [58]

Ashfold and co-workers reported total kinetic energy release (TKER) spectra of the H (Rydberg) atom produced upon UVPD of jet-cooled adenine molecules. [62] The experiment was performed at different wavelengths in the UVC adenine absorption band, to assess the role of the $\pi\sigma^*$ orbital in the decay process to the ground state. They observed $\pi\sigma^*$-induced N9-H dissociation only at wavelengths lower than 233 nm, contradicting the results obtained previously by Stolow and co-workers in Ref. [56]. Hassan et al. performed computational calculation *via* CASSCF and MRCI on adenine radiationless decay pathways. [63] They observed an energy difference of 0.1 eV between the first conical intersection of the $\pi\pi^* \rightarrow \pi\sigma^* \rightarrow S_0$ and $\pi\pi^* \rightarrow n\pi^* \rightarrow S_0$ mechanisms (i.e. $\pi\pi^* \rightarrow \pi\sigma^*$ lies 0.1 eV above $\pi\pi^* \rightarrow n\pi^*$). [63] While debate is still open on the role of the $\pi\sigma^*$ state, the role of ring-puckering on the pyrimidine ring in the ultrafast decay mechanisms is well-acknowledged , being characteristic of most of the conical intersections. [64] [65]

1.3.2 From Nucleobases to Nucleotides

Photodynamics of nucleobases in nucleotides and oligonucleotides are studied to investigate how their photostability evolves in going from nucleobases to DNA. Electrospray ionisation (ESI) of deprotonated nucleotides coupled with time-resolved photoelectron imaging (TRPEI) is an elegant method to investigate the gas-phase properties of neutral nucleobases in the presence of the sugar ring and the phosphate chain. This method was implemented by Verlet and co-workers in 2014 to investigate deprotonated 2′-deoxy-adenosine-5′-monophosphate (dAMP⁻, Scheme 1.3) and its di- and trinucleotides. [66] Upon excitation at 266 nm, the direct $\pi\pi^* \rightarrow S_0$ mechanism is active and is faster than 400 fs, in the three species. A comparison with solution-phase transient-absorption spectra performed by Stuhldreier et al. suggests that the charge and the environment do not affect the dynamics of the base in the gas phase, and the phosphate group can be seen as a spectator to the photodecay. [67]
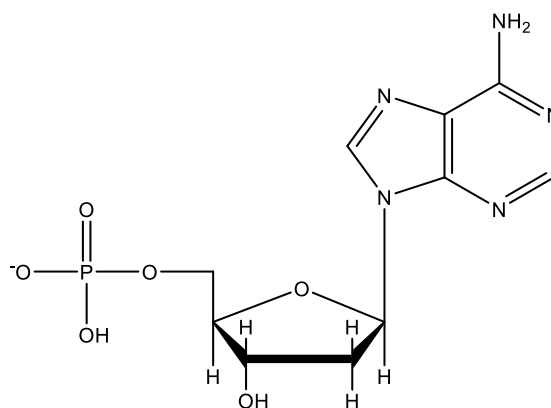
Scheme 1.3 Structure of 2′-deoxy-adenosine-5′-monophosphate.

1.3.3 Slow Electrons and DNA Damage

Although more photostable than other UV-absorbing molecules, UV light is still accepted to cause some direct photodamage to DNA. However, the primary mechanism of radiation-induced DNA damage involves slow secondary electrons that attach to the nucleobase and initiate single- and double-strand DNA breaks. [68] These electrons produce transient negative ions (TNI, metastable species described as [I$\cdots$N]$^{*-}$) upon attachment to the nucleobases that can subsequently decay in a dissociative manner (1.3). [68] [69] Dissociation or electron detachment can be accessed within a few femtoseconds. [70]

To observe and further understand TNIs, Neumark and co-workers have investigated gas-phase I$^-$·nucleobase clusters *via* TRPES. [71-73] In the near-threshold region, the iodide excess electron is photoejected and captured by the nucleobase. The experiments focus on the role of the nucleobase dipole-bound anion in the electron capture process and the cluster's subsequent dynamics. In a dipole-bound state, the electron is loosely bound to the neutral molecule dipole moment. In these states, the electron is in a very diffuse orbital, akin to a Rydberg state of a neutral molecule, only weakly interacting with the core of the molecule. For the dipole-bound state to be stable, the molecular dipole moment has to be higher than 2 D. [74] Dipole-bound states have been shown in a number of TRPES experiments to act as "doorway" to

valence-bound states, [69] [75] corresponding to the anionic state where the electron is held in the valence orbital, π* in the case of nucleobases.

The decay of these TNIs can result in electron photodetachment, in cluster photodissociation and photofragmentation as shown in the following set of equations:

$$I^-\cdot N + h\nu \quad \rightarrow [I\cdots N]^{*-} \quad \rightarrow I\cdot N\ + e^- \quad\quad (1.3a)$$

$$\rightarrow I + N^- \quad \rightarrow I + N\ + e^- \quad\quad (1.3b)$$

$$\rightarrow I^- + N \quad\quad (1.3c)$$

$$\rightarrow HI + [N\text{-}H]^- \quad\quad (1.3d)$$
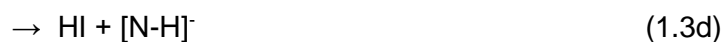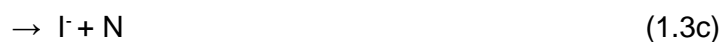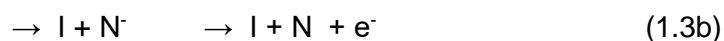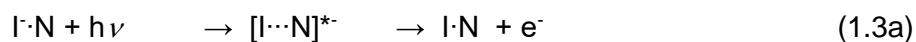
Neumark and co-workers studied electron attachment to adenine by investigating the iodide adenine cluster, $I^-\cdot A$. [72] In their photoelectron spectra, they found the presence of two adenine isomers, A9 and A3 (Scheme 1.4). For $I^-\cdot A9$ TRPEI showed the formation of a dipole-bound anion in the near-threshold region, undergoing monoexponential autodetachment decay (1.3a). The transition between dipole-bound and valence-bound anions was precluded due to the valence anion of A9 being metastable. In contrast, $I^-\cdot A3$ revealed both dipole-bound and valence-bound anions below the electron vertical detachment energy and an efficient transition (3-11 ps) between the two was observed. [72] Current experiments in Neumark's group are focused on microsolvation of these clusters to investigate the number of water molecules that is necessary to stabilise the valence-bound anion and suppress the dipole-bound state. [73]

Adenine 9H   Adenine 3H
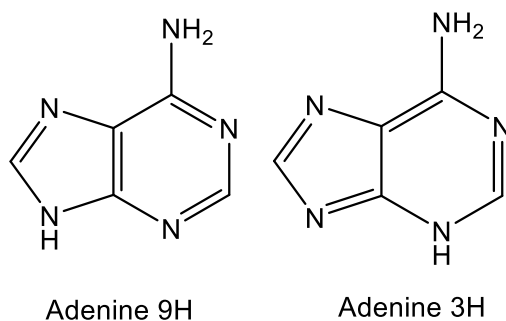
Scheme 1.4 Structures of A9 and A3 isomers of adenine.

1.4 Metal Carbonyls and CO-Releasing Molecules

Carbon monoxide is a common ligand in organometallic chemistry. [76] Transition metal carbonyls can undergo reactions such as nucleophilic attack to the carbonyl, electrophilic attack to the oxygen, migratory insertions, and ligand substitution. [76] [77] They are widely explored for their reactivity, [76-79] their catalytic properties, [80-83] for medical applications, [84] [85] as CO-releasing molecules, [86] or for bioanalytical purposes, such as for carbonyl metal immunoassay. [76]

When bonding with the metal, CO behaves as a σ donor (with the lone pair on the carbon) and a π acceptor (from the metal d orbitals), thus stabilising metals in low oxidation states. [76] (Figure 1.2)
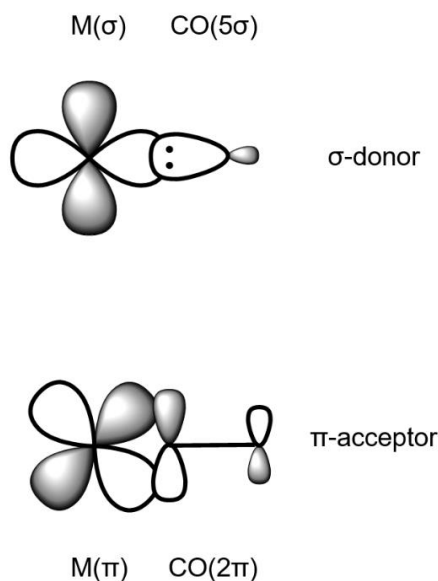
Figure 1.2 Interaction of CO molecular orbitals with the metal d orbitals.

Metal carbonyls are relatively straightforward to study because of the characteristic strong CO-stretching band that is observed in a largely empty region of the IR spectrum. [76] Carbonyl-containing complexes are often very stable compared to other coordination compounds and have an 18-electron configuration. [87] For the 18-e carbonyls, ligand substitution is a slow reaction. Indeed, the rate-limiting step is the CO dissociation, which is slow compared to dissociation of other ligands. [76] These reactions can be photolytically activated, in the spectral region where the complex absorbs. In general, CO-photodissociation occurs mainly *via* a 'prompt' mechanism on an femtosecond time-scale. [88] However, in the presence of ancillary ligands, long-lived 'equilibrated excited states' can be formed as in the case of *fac*-ReCl(CO)$_3$(bpy) (**4**, Scheme 1.5). [89]
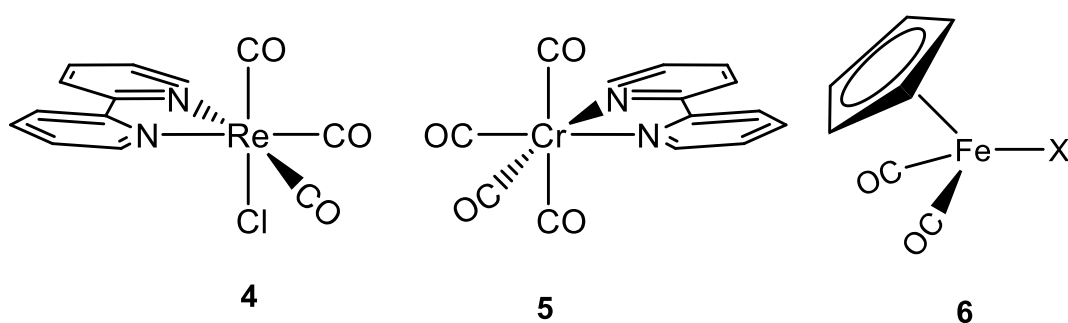
Scheme 1.5 Some metal carbonyls structures that are mentioned in the text.

Initial studies on photofragmentation of metal carbonyls were performed in low-temperature matrices coupled to IR spectroscopy. [90] [91] In these experiments, stabilisation of short-lived transient species by the matrix allowed the investigation of their structures. [92] In a series of papers, Turner and co-workers characterised M(CO)$_5$ (M = Cr, Mo, W) complexes photoproduced from their respective hexacarbonyls, finding that the complexes adopted C$_{4v}$ symmetries. [93-95]

To understand the mechanism and the photodynamics of M-CO photodissociation required expensive computational calculations [96-98] and time-resolved experiments [99-102] that were initially conducted on model homoleptic metal carbonyls such as

$Cr(CO)_6$. In these gas phase experiments, one-photon ultrafast excitation was followed by time-resolved detection based on mass spectrometry, and it was concluded that upon prompt photodissociation of the first CO, other CO ligands could be thermally ejected, down to the bare metal. [101]

Renewed interest in the dissociation mechanism was prompted by a computational reassessment of the ligand-field orbital energy compared to the $\pi^*(CO)$, suggesting that the previously adopted interpretation was incorrect. [103] [104] The ligand-field excited states were found to be at much higher energy than was thought previously. In the accepted mechanism, photoexcitation of metal carbonyls initially prepares excited states in which the electron density is transferred from the metal to the carbonyl ligands in a metal-to-ligand charge transfer (MLCT). However, the MLCT acquires CO-dissociative character *via* mixing with the ligand-field excited state, which is caused by a Jahn-Teller distortion (a few fs after excitation). [101]

Substituted metal carbonyls can undergo competitive dissociation pathways with wavelength-dependent quantum yields. Moreover, type of metal, oxidation state and ancillary ligands are known to shift the absorption wavelength. [88] An example is $Cr(CO)_4(bpy)$ (Scheme 1.5, **5**). Time-resolved infrared spectroscopy (TRIR) and time-resolved absorption experiments conducted in solution phase by Vlček and co-workers showed that, upon excitation at 500 nm, the initially populated $^1MLCT(bpy)$ excited state can undergo ultrafast CO substitution (Eq. 1.4) or slower non-dissociative decay through a ^3MLCT "trapping" state (Eq. 1.5). [105] [106] At 400 nm, a $^1MLCT(CO)$ is also populated, together with the MLCT(bpy).

$$Cr(CO)_4(bpy) + h\nu + Sol \rightarrow\ ^1MLCT \rightarrow Cr(CO)_3(Sol)(bpy) + CO \qquad (1.4)$$

$$Cr(CO)_4(bpy) + h\nu + Sol \rightarrow\ ^1MLCT \rightarrow\ ^3MLCT \rightarrow Cr(CO)_4(bpy) \qquad (1.5)$$
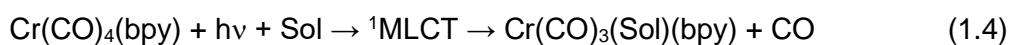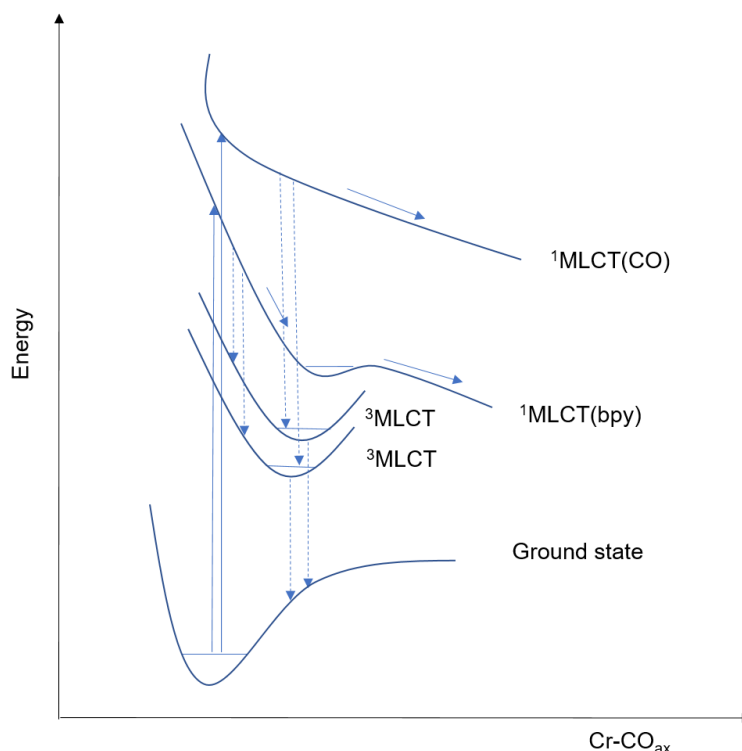
Figure 1.3 Schematic of key excited states involved in the photochemistry of $Cr(CO)_4(bpy)$ from Ref. [106]

Both $^1MLCT(bpy)$ and $^1MLCT(CO)$ states relax according to Eqs. (1.4) and (1.5), but the quantum yield for photosubstitution (1.4) increases going to lower wavelengths suggesting that a lower barrier to the Cr-CO photodissociation is encountered when $^1MLCT(CO)$ is populated (Figure 1.3).

The investigation of substituted metal carbonyls UV photoexcitation and their photodecay mechanisms is generally performed in solution phase. [105-109] Gas-phase experiments are limited to time-resolved studies at discrete wavelengths. [110]

1.4.1 Gas-Phase Fragmentation of Metal Carbonyls

Among the first gas-phase studies on metal carbonyl, Freedman et al. studied, in 1978, di-nuclear metal carbonyls ($M_2(CO)_{10}$ M=Mn, Re) in a molecular beam crossed with a ~ 300 nm laser beam. Neutral, hot fragments were then ionised and analysed via a time-of-flight (TOF) spectrometer. [111] They concluded that $M(CO)_5^+$ was

photoproduced at this wavelength with cleavage of the M-M bond (1.6). The photofragments' angular distribution was analysed as a function of polarisation, demonstrating that dissociation proceeded from an excited state complex on the picosecond timescale. Further studies on these systems showed that CO could be photoejected upon excitation at different wavelengths (1.7). [112] [113]

$$M_2(CO)_{10} + h\nu \rightarrow 2M(CO)_5 \qquad\qquad (1.6)$$

$$M_2(CO)_{10} + h\nu \rightarrow M_2(CO)_9 + CO \qquad\qquad (1.7)$$

The gas-phase photophysics of substituted metal carbonyls has not been explored at a wide spectral range in the UV-Vis region yet. However, one-colour time-resolved experiments were performed on species such as $CpFe(CO)_2X$ ($Cp=C_5H_5$; X=Cl, Br, I) to determine the role of the halogen ligands on the photodissociation of $CpFe(CO)_2X$ (Scheme 1.5, **6**). The clusters were excited by a 400 nm pump followed by an 800 nm probe, and the photofragments were ionised and investigated by TOF mass spectrometry. [114] The mechanism proposed by the authors is a sequential ligand loss from the initial CO, to the chloride that is lost last with a timescale that is influenced by the halide. A more complicated and concerted mechanism is observed for the heavy halogens.

Thermal fragmentation *via* ESI mass spectrometry has also been performed on derivatised homoleptic [115] and substituted metal carbonyls and metal carbonyl clusters by varying the ESI cone voltage. [116-118] The fragmentation mass spectra that are produced can be directly correlated to the stability of the metal-ligand bond. [115] As an example, Basu and co-workers studied $M(CO)_6$ (M= Cr, Fe, Mo, and W) *via* energy-dependent ESI mass spectrometry. These neutral species were derivatised to $[M(CO)_5(COOMe)]^-$ via methoxylation before ESI. For Cr, the fragmentation spectra at different cone voltages showed sequential loss of CO up to

[Cr(OMe)]$^-$ produced via methoxide migration. For the other metals, a second pathway was identified following hydride ion migration that led to the formation of [M(CO)H]$^-$ for the iron and [MH]$^-$ for tungsten and molybdenum.

The series of substituted metal carbonyl clusters [Ir$_4$(CO)$_{11}$(PR$_3$)+OMe]$^-$ revealed the competitive loss of CO and phosphine, however [Ru$_6$C(CO)$_{16}$(PPh$_3$)+OMe]$^-$ showed initial loss of the phosphine followed by sequential loss of CO ligands. [116]

1.4.2 Metal Carbonyl Photo-CORMs

Although CO is known for its toxicity, [119] it is produced endogenously during haem metabolism. [120] Since this process was discovered in 1949, interest in its biological role has grown, and it is now recognised as a signalling molecule. [121] It has also been proved to have anti-bacterial, anti-proliferative, anti-apoptotic and cardiovascular effects. [122-126] Much effort is going into the development of CO-delivering systems for pharmaceutical use, [86] with metal carbonyls being widely explored as CO-releasing systems. [86] [127] In this context, they are called CO-releasing molecules (CO-RMs) [127] and can be triggered *via* different mechanisms such as thermal activation, enzymatic reaction [128] and photoexcitation. [129]

[Ru(CO)$_3$Cl$_2$]$_2$, also known as CORM-2 (**7**, Scheme 1.6), was shown to be the first thermal CORM with a therapeutic effect, in 2002 by Motterlini and co-workers. [127] However, the complex was not water-soluble, and most of the characterisation was done in DMSO, that was proved to play a significant role in the CO dissociation mechanism (solvent-triggered CO-release). Water solubility was implemented with CORM-3 (**8**, Scheme 1.6), with glycine as a chelating ligand. [125] [130] The use of amino acids as co-ligand has the advantage that a biological moiety can be metabolised by the organism upon dissociation. CORM-3 was confirmed to have numerous medical applications in animal models, such as the treatment of sepsis

[131] and *Pseudomonas aeruginosa* infections. [132] However, it was shown that it was sensitive to pH-dependent equilibria in water, [133] and that it formed protein-CORM complexes with different types of plasma proteins. [134] [135] Other thermal CORMs have been synthesised with biological ligands, carrying a galactose derivative [136] or a vitamin B_{12} unit as ligands. [137] The use of ancillary ligands that are known to have medicinal properties can convert the CORMs into a multi-action mode pharmaceutical. An example was developed in Fairlamb's group, where pyrones, known anticancer drugs, [138] [139] were incorporated as ancillary ligands. [140] [141] However, thermal or solvent-triggered release mechanisms can incur some disadvantages such as low selectivity that could be detrimental for medical purposes.
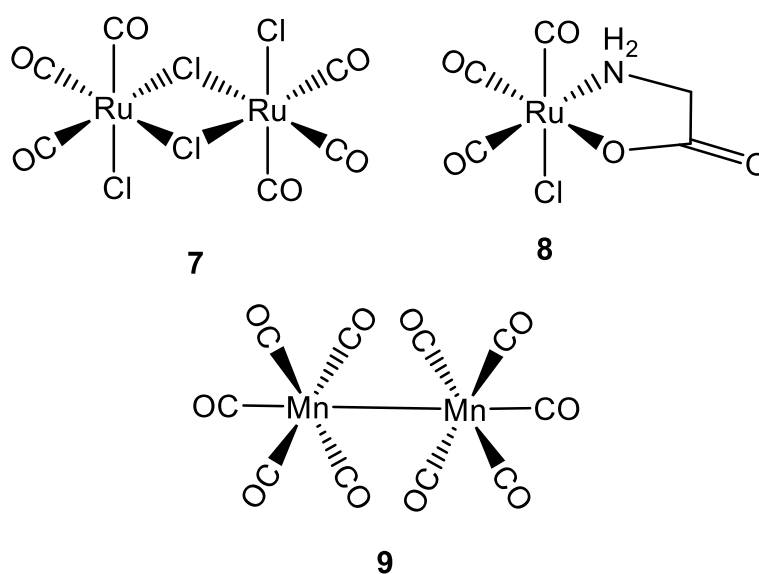
Scheme 1.6 Structure of CORMs described in Ref. [125] and [127].

Photo-CORMs are stable in the dark, both in aqueous solution and in biological systems, and release CO upon photoexcitation. The first Photo-CORM with biological activity was $Mn_2(CO)_{10}$, (Scheme 1.6, **9**). [127] This complex releases CO after excitation in the UV. [111] However, absorption in the visible or near IR is more suitable from a therapeutic point of view, since these wavelengths penetrate tissue

better [142] and are less hazardous than UV light. [143] To shift the CO photodissociation to higher wavelengths, a good strategy is the use of ancillary ligands with low-energy π^* orbitals. [144] Mascharak and co-workers have used tripoidal Mn(I) complexes with highly-conjugated chelating ligands, moving the MLCT to the visible region. They also investigated the use of σ-donating ligands, resulting in a λ_{max} of 535 nm for [Mn(qmtpm)(CO)$_3$Br] (qmtpm= 2-quinoline-N-(2'-methylthiophenyl)methyleneimine, [**10,** Scheme 1.7]), and 586 nm for *fac*-[Mn(azpy)(CO)$_3$Br] (azpy=2-(phenylazo)pyridine, [**11,** Scheme 1.7]). In the latter complex, the azo-nitrogen is in *trans* position relative to a CO: the back-bonding competition between them increases the velocity of CO release. [144] Detecting CO released by a PhotoCORM is particularly helpful to understand the releasing mechanism and hence rationalise the design of new Photo-CORMs.
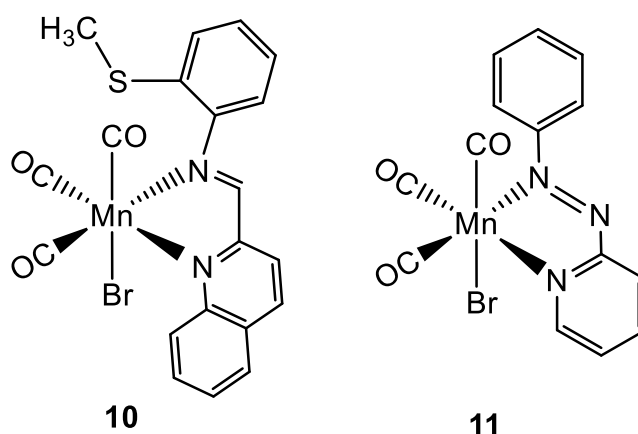
Scheme 1.7 Structures of visible-absorbing Photo-CORMs from Ref. [144].

The most common method of CO detection from CORMs is the myoglobin CO-release assay that exploits the change in the myoglobin absorption spectrum upon CO coordination, with a band appearing at 540 nm. [137] The myoglobin assay is primarily used to study the Photo-CORMs CO-releasing activity and to test their stability in other conditions, such as in the dark. During a typical assay, a solution with µM concentration of the Photo-CORM is irradiated to initiate CO release, and the absorbance is monitored over time. The method is quantitative and relies on the

capture of all of the CO released. A paraffin oil layer placed on top of the solution blocks any CO escape. [145] However, visible absorbing Photo-CORMs may absorb as well at 540 nm, making quantitative measurements less straightforward. [145] Moreover, myoglobin assays must be performed in anaerobic conditions to remove the O_2 bound to myoglobin.

The characterisation of the degradation products can be performed *via* different techniques such as TRIR, [146] EPR, [147] or mass spectrometry. [148] However, the need for more specific techniques that can determine the CO-release quantum yield and elucidate the photodissociation mechanisms has been frequently expressed in literature. [149] [150]

In this dissertation, we propose the use of gas-phase photodissociation spectroscopy to investigate the CO release and photofragments production from Photo-CORMs. In particular, we perform PD for a wide wavelength range and explore the energy dependence of photodecay products.

1.5 Thesis Outlook

This thesis is focused on the use of laser-interfaced mass spectrometry (LIMS) to investigate the photochemistry of gaseous molecular ions, aggregates, and organometallic complexes. In these experiments, an Nd:YAG pumped OPO (optical parametric oscillator) laser, ranging from 580 to 220 nm, is coupled to an electrospray ion-trap mass spectrometer. Ions are accumulated in the instrument's ion trap and interact with the laser beam, producing photofragmentation mass spectra that are acquired at each wavelength.

Chapter 2 describes in detail the experimental protocol and design used for PD and thermal dissociation experiments. The computational methods that were used alongside the experiments are also described.

The subsequent part of the thesis can be divided into two distinct sections:

Chapters 3 and 4 describe LIMS experiments that have been applied to probe the effect of an excess negative charge on the stability and photophysics of nucleobases. In particular, we investigated the role of the phosphate chain length and the negative charges in adenosine nucleotides and discussed them in Chapter 3. Chapter 4 describes UVPD experiments on $I^-·A$ and $H_2PO_3^-·A$ clusters and how the anion influences the electron detachment in the near-threshold region.

Chapters 5 and 6 show the use of LIMS to measure the spectroscopy and photochemistry of CORMs and, more generally, metal carbonyls. In particular, Chapter 5 describes gas-phase thermal and photodissociation of an Mn(I) Photo-CORM (TryptoCORM), [148] [151] while Chapter 6 describes the application of LIMS to explore the photochemistry of three metal carbonyls, two half-sandwich Ru(II) complexes and a thermal Mn(I) CORM (EBOR-CORM-1). [152] In this dissertation, we are mainly concerned with metal carbonyls that are photoactivated to release CO for medical purposes. Although we will be focusing on them, UVPD can be applied to all metal carbonyls to understand their gas-phase photodynamics.

Chapter 2

Experimental and Theoretical Methods

2.1 Laser-integrated Bruker amaZon

Figure 2.1 shows a block diagram of the instrument that was used to conduct the UV-Vis photodissociation experiments presented in this thesis. A modified electrospray-ionisation quadrupole ion trap (ESI-QIT) mass spectrometer (amaZon SL, Bruker Daltonik) was coupled to a 10 Hz Nd:YAG (Surelite, Continuum) pumped OPO (Horizon I, Continuum) and exploited to perform the photodissociation experiments. More specifically, two holes were drilled into the ring electrode of the ion trap creating a route for the pulsed laser to enter and leave. After isolation in the QIT, the ions can be investigated *via* electronic excitation. Optical guides lead the laser to the mass spectrometer, where a beam shutter (SH05, Thorlabs Inc.), controlled *via* the amaZon remote interface, regulates the transmission of the laser beam into the ion trap.

A motorised flip-mount (MFF001, Thorlabs Inc.) is used to move a prism that directs the laser beam to either the trap or to a power meter (Power Detector UP19K-15S-VR, Monitor is a Gentec-EO Tuner) where the power is measured.

These units are controlled from a workstation, allowing the automation of the experiment. Further details on the mass spectrometer and the OPO laser are described in the following sections.
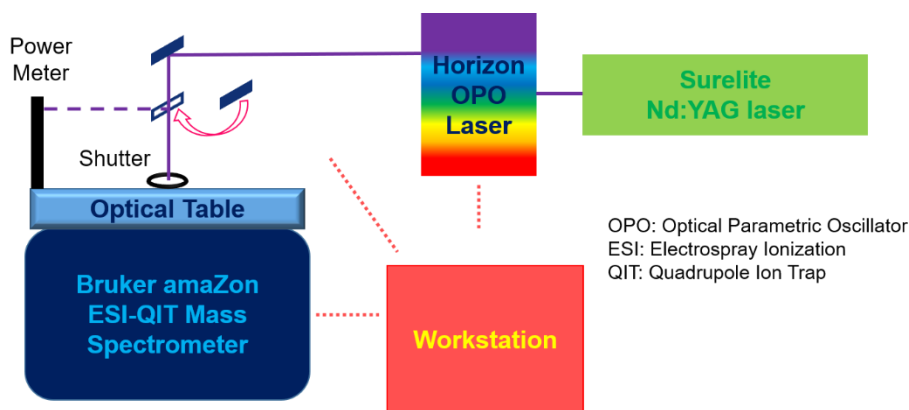
Figure 2.1 Simplified diagram of the photodepletion experimental setup.

2.1.1 Nd:YAG Pumped OPO Laser

A Q-switched neodymium-doped yttrium aluminium garnet laser (Nd:$Y_3Al_5O_{12}$, Nd:YAG, Surelite, Continuum) is used in this experiment to pump an OPO (Horizon I, Continuum). The two components are described in the next sections.

2.1.1.i Nd:YAG Pump Laser

In the Nd:YAG laser, Nd(III) is a YAG dopant, replacing *circa* 1% of the yttrium ions, and is responsible for the lasing activity of the crystal. The diagram in Figure 2.2 describes the main transitions involved. [153]
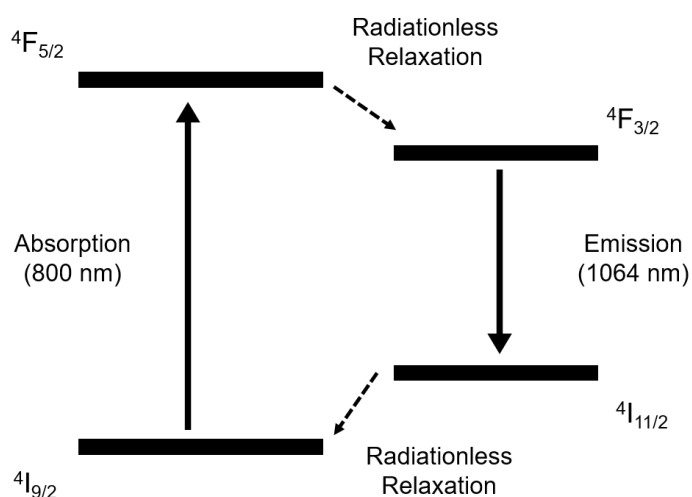
Figure 2.2 Simplified diagram of the energy levels of Nd^{3+} involved in the Nd:YAG lasing activity. [153]

Figure 2.2 shows a simplified diagram of the four-level laser where Nd^{3+} ions are in the electronic ground state ($^4I_{9/2}$). Flashlamps surround and irradiate the crystal that absorbs at 800 nm, to promote electronic excitation to a $^4F_{5/2}$ state. Fast, non-radiative decay to $^4F_{3/2}$ is followed by radiative decay to $^4I_{11/2}$ with the emission of a photon at 1064 nm. Lastly, $^4I_{11/2}$ quickly decay (non-radiatively) to the electronic ground state. The radiative decay (between $^4F_{3/2}$ and $^4I_{11/2}$) is the slowest step (τ ~230 µs) – being a forbidden transition – and thus $^4F_{3/2}$ is always more populated than $^4I_{11/2,}$ and population inversion between the two states is achieved. The emission from $^4F_{3/2}$ can be stimulated by iso-energetic photons to those of the laser cavity. [153]

The flashlamps irradiate the YAG rod with a frequency of 10 Hz; thus, population inversion and lasing are achieved with the same repetition rate. Frequency doubling is used to generate the second harmonic at 532 nm, while the third harmonic (355 nm) is obtained by mixing the fundamental and the second harmonics. Q-switching is achieved through a Pockels cell, enclosed within the laser cavity. This cell changes the polarisation of the laser beam that can only be released when the right voltage is applied. The working mechanism of the Pockels cell is shown in Figure 2.3.
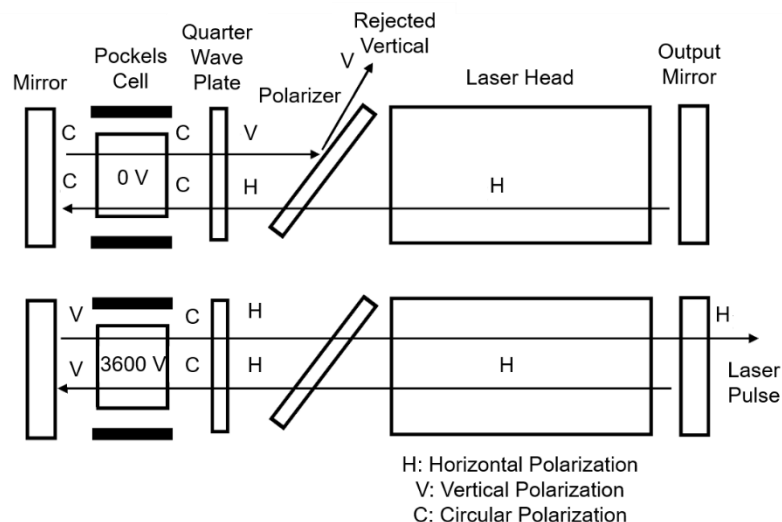
Figure 2.3 Diagram of the Q-Switch used in the Surelite Nd:YAG laser. Image adapted from the Surelite manual. [154]

2.1.1.ii Optical Parametric Oscillator

The laser beam produced from the Nd:YAG crystal is used to pump an OPO laser (Horizon I, Continuum), producing widely-tunable photons for the photodissociation experiment. Non-linear crystals in the OPO (β-barium borate crystals [BaB_2O_4, BBO]) convert the laser wave, with a given frequency ω_{pump} (fundamental, second or third harmonics), into two waves (idler and signal waves) that have to conserve the total photon energy (*E*; Eq. 2.1) and the momentum (*k*; Eq. 2.2):

$$E_{pump} = E_{idler} + E_{signal} \tag{2.1}$$

$$k_{pump} = k_{idler} + k_{signal} \tag{2.2}$$

The angle between the optical axis of the BBO crystal and the pump beam determines the frequencies of the generated waves with respect to these two conditions. By rotating the BBO crystals, wavelengths from the far UV to the near-IR can be accessed. In the PD experiments described in this thesis, the OPO is used in the UV-Vis range, (580-215 nm).
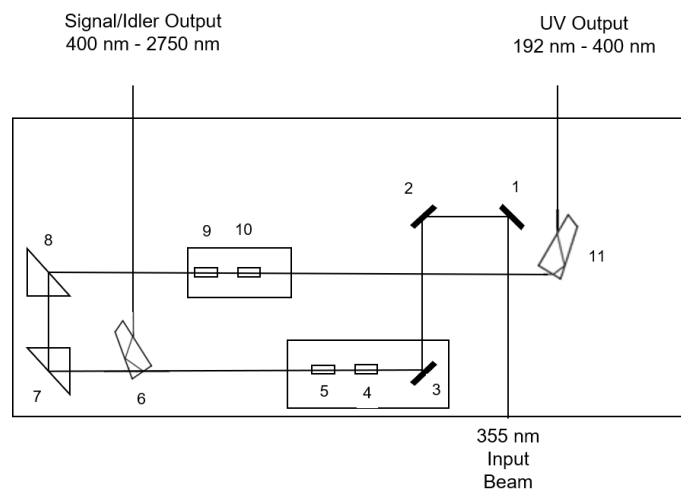
Figure 2.4 Simplified Horizon OPO optical layout. [155]

Figure 2.4 illustrates the path that the photons, generated by the Nd:YAG laser, take in the OPO laser to produce different wavelengths. To give the visible wavelengths, the third harmonic of the Nd:YAG (355 nm) laser is split by the BBO crystals 4 and 5.

A Pelin Broca prism (6) ensures the beams exit with 90° reflection. The idler and the signal are emitted from the left exit port. UV photons are obtained *via* the BBOs 9 and 10. In this case, frequency doubling and sum-frequency generation between the idler / signal and the fundamental wavelength are used. Again, a Pelin Broca prism (11) ensures the exit of the beams with 90° of reflection from the right exit port. Switching between UV and visible regions requires the adjustment of the position of three optical elements.

The OPO is controlled from the workstation using the Horizon software. The orientation of the BBO crystals – mounted on step-motors – and of the Pelin Broca prisms are adjusted from the workstation to obtain the desired wavelengths and control the alignment and the power of the laser beam. Approximately 1mJ of energy was used at each wavelength, in the UV-Vis region.

2.1.1.iii Beam Route Between the OPO and the Mass Spectrometer

The laser beam is guided into the ion trap by a set of optic crystals that are installed on an optical breadboard on top of the mass spectrometer. Figure 2.5 shows labelled pictures of the optical board on the amaZon and indicates the routes taken by both the UV and visible photons. The two beams leave the OPO from two different sides and reach the enclosed work area *via* two black tubes. Two right-angled UV fused silica prisms at the exit of the UV tube adjust the height of the beam by ~ 8 cm, making it easier to manipulate. Another right-angled prism, at the exit of the visible tube, and an adjustable prism are used to overlap the two routes and direct the visible beam onto the first prism encountered by the UV light (Figure 2.6b).
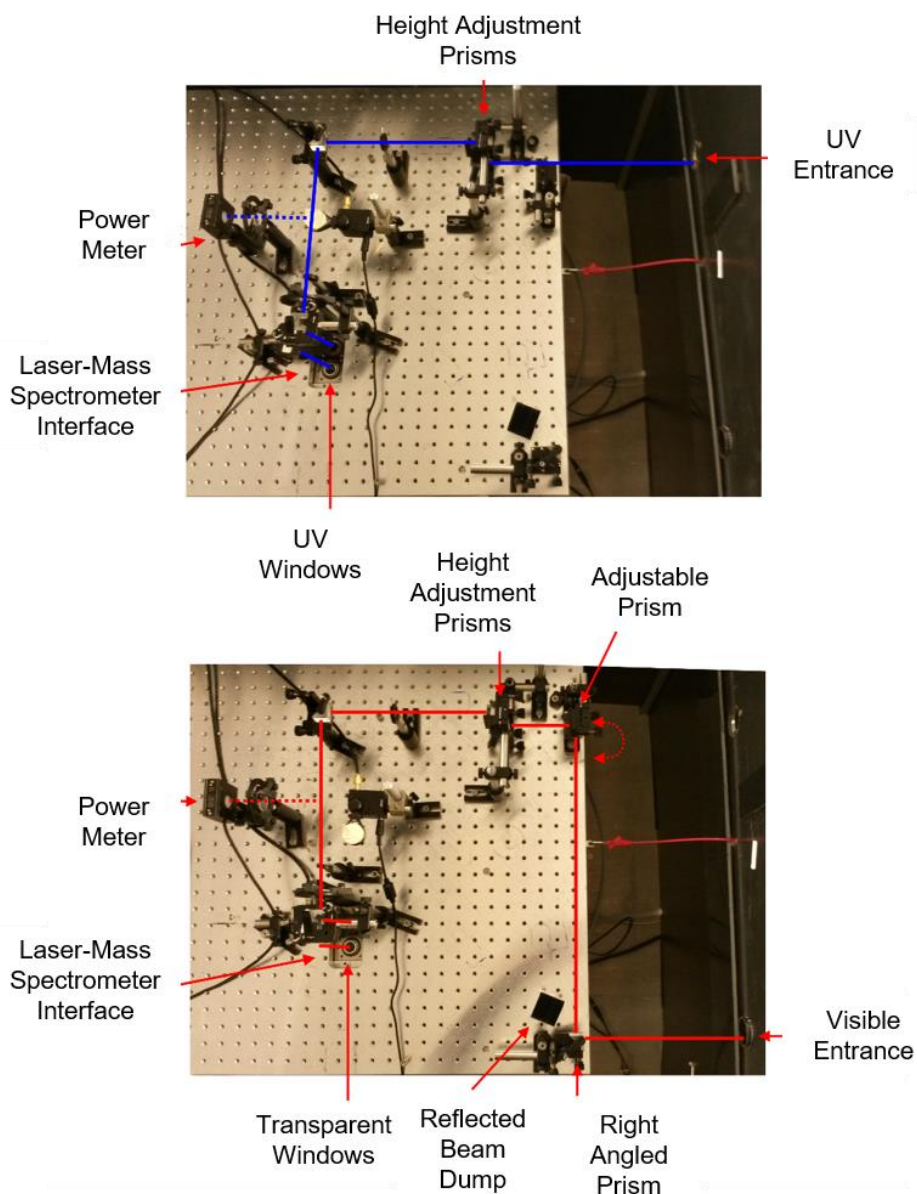
Figure 2.5 Labelled pictures of the optical bench on top of the amaZon mass spectrometer. The laser path from the OPO to the ion trap is shown in the top picture for the UV and the bottom for the visible/NIR wavelengths. Adapted from Ref. [156].

The optical pathway that photons follow from the height-adjusting prisms is shown in more detail in Figure 2.6. After passing through the iris (a), the beam encounters a right-angled prism (j) and is reflected 90° towards the mass spectrometer (e). If the adjustable prism (b) is on the laser route, the beam is directed onto a power meter (h), going through a lens (i). Otherwise, it will be directed onto a right-angled prism (d) above the ion trap (e) that guides the beam downwards. After passing through a lens

(g), the laser encounters an optomechanical shutter (f) and enters the mass spectrometer through a window. The pathway of the laser within the mass spectrometer is described in Section 2.1.2.iii.
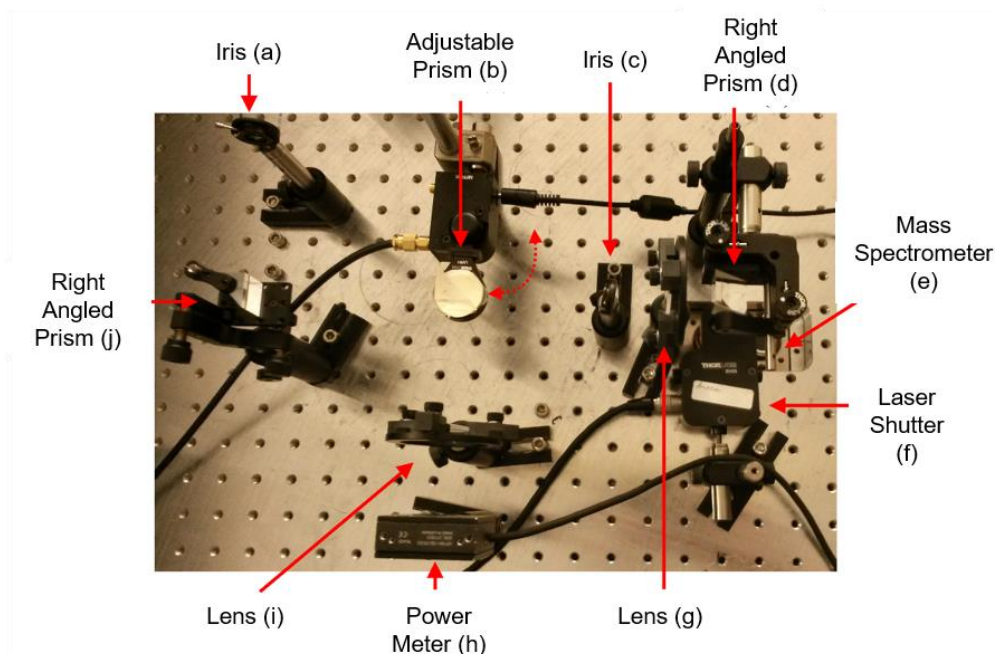
Figure 2.6 Labelled picture of the optical bench above the amaZon mass spectrometer. The picture is focused on the region containing the power measurement set up and the mass spectrometer interface.

2.1.2 Modified Bruker Amazon Mass Spectrometer

The amaZon SL is a Bruker mass spectrometer with a quadrupole ion trap (QIT) mass analyser. The ion trap is suitable for tandem mass experiments *via* collision-induced dissociation (CID) where selected molecular ions are trapped and fragmented upon collision with helium buffer gas. [157] The gas pressure within the trap is maintained at ~ 5×10^{-9} bar while the ions are accelerated by applying an excitation frequency with an amplitude that is varied from 0 to 2.5 V.

The instrument is equipped with atmospheric pressure ionisation sources. An electrospray ionisation (ESI) [158] source was used throughout this study to obtain positive and negative ions. Four vacuum stages (*via* rough pumps and turbo-pumps)

are used to maintain the pressure gradient between the source and the ion trap. Electric fields lead the ions from the ESI to the QIT.
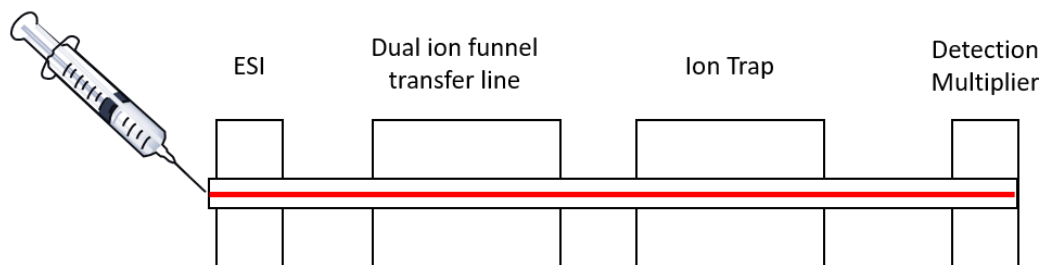
Figure 2.7 Simplified diagram of the amaZon mass spectrometer. [159]

The sample nebulization is aided by N_2 within the ESI chamber, where pre-heated drying gas (N_2) helps volatilisation and ionisation (Figure 2.8). The ions are focused to the entrance of a metal-coated glass capillary, which is also the inlet to the vacuum system. A dual-funnel configuration collects the ions and transfers them to the next vacuum stage, where two multipole ion guides and two lenses lead them into the QIT, that collects, stores, and mass-analyses the ions but also isolates and fragments them through collisions with the helium buffer gas (*i.e.* CID). In our photodepletion experiments, the ions are isolated in the trap and photofragmented using the laser. After this stage, the ions are ejected according to their *m/z* ratio and detected by a dynode-based system (Daly detector).

The amaZon mass spectrometer is controlled *via* the Bruker software (trapControl 7.2, Bruker Daltonik). 'trapControl' is used to regulate the ionization settings (e.g. ESI voltage; nebulising gas pressure; drying gas flow rate; and drying gas temperature), the ion-guide voltages (e.g. ion funnels; multipoles, and lens voltages) and the ion trap times and conditions (e.g. ion accumulation time; mass isolation; and ion fragmentation time and amplitude). Moreover, trapControl is used to record the mass spectra of the trapped ions before and upon laser excitation.

2.1.2.i Electrospray Ion Source

The ion-inlet device used within the laser-coupled mass spectrometer is a Bruker Apollo-source with an ESI spray chamber. The sample enters the spray chamber *via* the nebuliser to be electrosprayed in four steps: ion formation, nebulisation, desolvation, and ion evaporation.

The ions can be present in solution, under the right conditions (sample, solvent and buffer), or they can be formed during the other steps of electrospray. The solution enters the chamber *via* a spray needle that is kept at ground potential. The strong electrostatic field that is established between the needle and the spray shield (up to 6 kV) and the presence of a high-flow nebulising gas distorts the shape of the solution into a so-called Taylor cone (Figure 2.8). Subsequently, the repulsion between ions of the same charge splits the solution into charged droplets where the charges that are attracted to the electrostatic field are aligned onto the surface.

At this point, the counter flow of drying gas (N_2) assists the solvent evaporation, decreasing the volume of the droplets and simultaneously increases the repulsion between the charges at the surface.
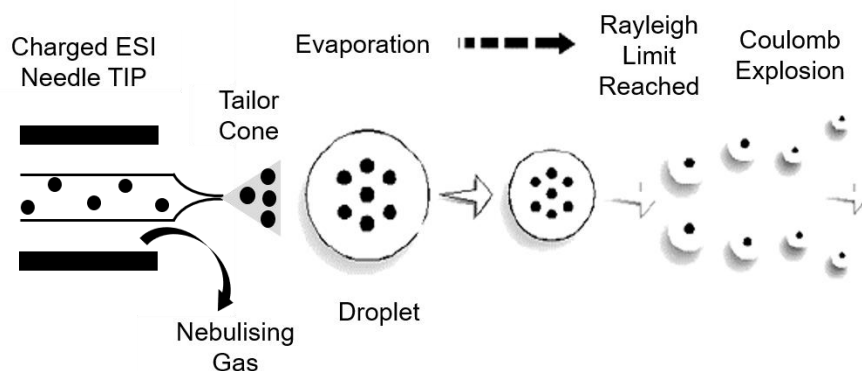
Figure 2.8 Diagram of an electrospray ionisation (ESI) source.

Two main theories can be used to explain ion formation: desolvation (charge residue model, CRM) [160] and ion evaporation (ion evaporation model, IEM). [161]

CRM proposes that the droplet explodes into daughter droplets once the Coulomb repulsion equals the surface tension (Rayleigh Stability limit). Repeating cycles of evaporation and explosions lead to the formation of sequentially smaller and denser droplets. Ion evaporation can occur when the charge density is ~ 10^8 V/cm^3. [162]

IEM suggests direct evaporation of the charged species from the droplet into the gas phase occurs when the field created by the ions at the surface is strong enough to assist field desorption of the ions. [161]

There is still uncertainty regarding which mechanism occurs, although this seems to be dependent on the solubility of the sample in the solvent and on the dimension of the charged species (i.e. small molecules may be predominantly transferred *via* IEM, while bigger globular species are mainly transferred *via* CRM). [163]

2.1.2.ii Quadrupole Ion Trap Analyzer

A Paul quadrupole ion trap (QIT) is a ~1 cm^3 3D mass analyser, where the ions can be accumulated, selected, excited (*via* CID) and then ejected according to their mass to charge ratio (*m/z*). The QIT is made by two metal electrodes (end caps, 1 and 3 Figure 2.9) and a ring electrode halfway between them (2, Figure 2.9) such that its internal surface has a nearly hyperbolic profile. The ions enter and leave the trap *via* two small holes in the centre of the end caps.
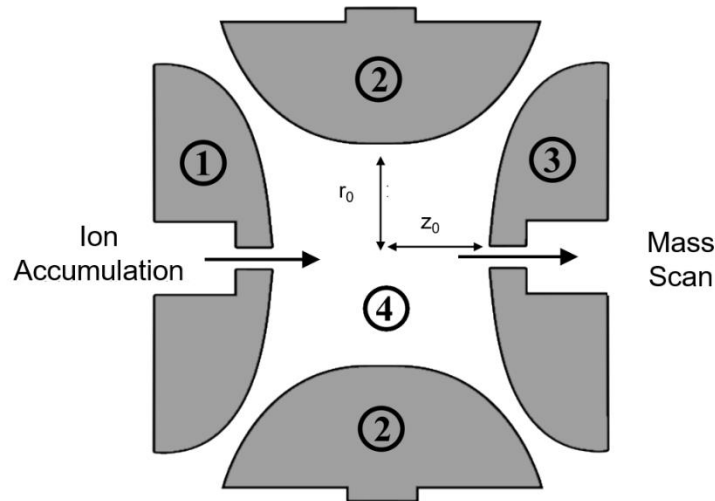
Figure 2.9 Diagram of a quadrupole ion trap (QIT) mass spectrometer. **1** is the entrance end cap; **2** the ring electrode; **3** the exit end cap; and **4** the ion cloud and buffer gas.

Once in the trap, the ions are stored in an oscillating quadrupolar electric field that is generated by a high voltage applied to the ring electrode, while the end caps are kept at ground potential. The sign of the applied voltage switches between positive and negative at a radio frequency rate. In this electric field, a charged particle is subjected to alternate acceleration towards the centre and the edges of the trap, both in the axial and the radial directions. Moreover, since the field is periodically inhomogeneous, there is a small average force that is not cancelled over time into the centre of the trap; therefore, a pseudo-potential well is formed, enabling ion storage over time. [164] Low-energy collisions with helium buffer gas, which is constantly leaked into the trap, decrease the ions' kinetic energy and accordingly increase their storage times.

The motion of the particles is described by the Mathieu equations and is expressed in terms of the Mathieu coordinates, [159] [164] a and q, that are dependent on DC (U) and AC (V) voltages, respectively:

$$a_z = -\frac{16zU}{mr_0^2\Omega^2} \tag{2.3}$$

$$q_z = \frac{8zV}{mr_0^2\Omega^2} \tag{2.4}$$

Where m and z mass and charge of the ion, Ω radial frequency of the potential applied to the ring electrode and r_0 its distance from the centre of the trap (Figure 2.9). An ion is stable when its trajectory does not exceed r_0. Eq. 2.5 and 2.6 indicate that radial and axial stability have to be maintained simultaneously:

$$a_z = - 2a_r \qquad (2.5)$$

$$q_z = - 2q_r \qquad (2.6)$$

A wide range of masses can be trapped and analysed at the same time (according to the RF, DC and m/z values) and they are described using a stability diagram. Figure 2.10 shows a 2D representation of the solution of the equations of motion expressed in terms of a_z and q_z.
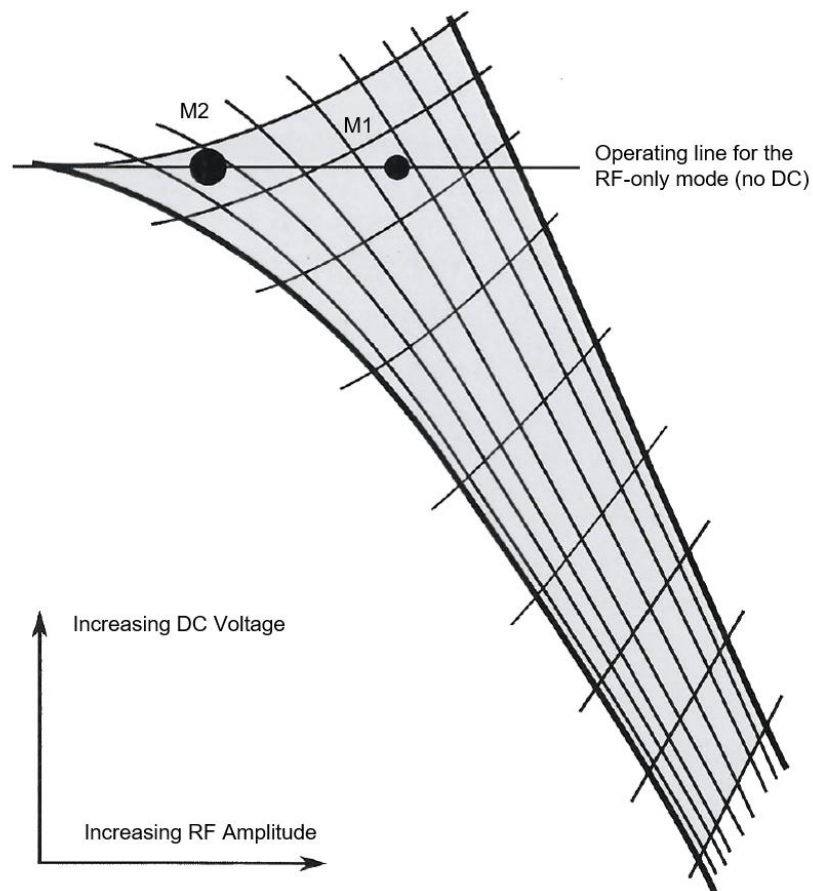
Figure 2.10 Stability diagram for ions in a quadrupole ion trap. Adapted from the amaZon manual. [159]

The ion trap works in the RF-only mode, on the $a_z = 0$ axes (Figure 2.10), thus, by scanning the RF potential, an ion with an m/z value is stabilised or destabilised and moves along the axes according to the q_z expression. In the mass-selective instability mode, RF is ramped up and when the q_z of an ion is > 0.908 it is expelled from the trap [159] and detected by the Daly detector.

The amaZon QIT applies the resonance ejection mode: the oscillating (so-called secular) frequency of the ions is excited resonantly *via* a supplemental AC potential applied to the end caps, activating the ions in the z-direction. Once the ions have gained enough kinetic energy, they are expelled from the trap. q_z is inversely proportional to m/z. Therefore, at each RF value, higher masses are on the left of smaller masses, and there is a low-mass cut-off. [159]

During an experiment, the accumulation of the ions and their analysis follow a cyclic sequence that can be controlled with the trapControl software: (a) clear trap; (b) accumulation; and (c) mass analysis.

The clear trap step empties the ion trap - between two mass acquisitions - by dropping the quadrupolar field to zero; during this time, a blocking voltage on the ion gate is applied. When this voltage is dropped, the accumulation stage starts, and the ions are let into the trap. Ions are trapped by the pseudo-potential well for a time that can be varied with trapControl to regulate the number of ions in the trap (usually between 1 and 100 ms). At the end of this stage, a voltage is applied to the ion gate, and the ions are cooled *via* their collisions with the buffer gas. Stage (c) is the last step where the ions with m/z values can be progressively ejected from the trap by scanning the RF voltage.

If the experiment requires fragmentation, the sequence becomes: (a) clear trap; (b) accumulation; (c) isolation; (d) fragmentation; and (e) mass analysis.

After the ions have been accumulated (b), they are resonantly ejected *via* an intense broadband RF field that contains all the secular frequencies except for the one corresponding to the precursor ion of interest (c). During fragmentation (d), a weak resonant RF field is used to excite the isolated ions, which collide with the helium gas in the trap. These collisions cause the dissociation of the ions. The fragments are not resonant with the acceleration RF, and thus are not further fragmented. A fragmentation mass spectrum is then produced by scanning the RF voltages on the ring electrode. The fragmentation time is set to 100 ms, to ensure the interaction with only one shot of the 10 Hz laser. Different stages of isolation and fragmentation can be performed so that a given ion can be fragmented sequentially up to ten cycles.

2.1.2.iii Modifications to the Ion Trap

The PD experiments described throughout this thesis were conducted in an amaZon SL that was modified to allow the excitation of isolated ions within the ion trap. The diagram in Figure 2.11 shows the alterations that were implemented on the instrument, along with the laser path.
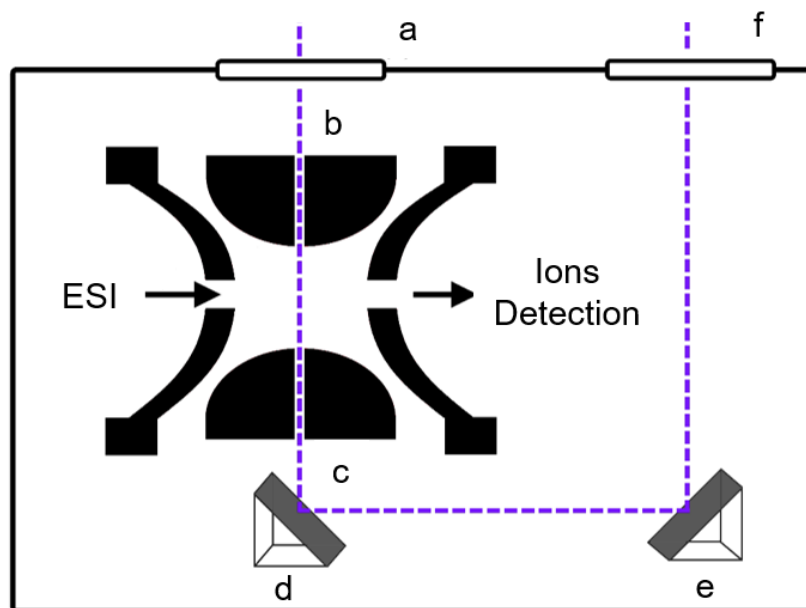
Figure 2.11 Diagram of the modifications made to the QIT mass spectrometer to allow photodissociation spectra to be recorded. a) and f) are a pair of flange mounted uncoated UV Fused silica windows; b) and c) are 2 mm holes drilled through the ring electrode of the ion trap to allow the passage of laser beam; d) and e) are a pair of aluminium mirrors.

Two UV fused silica (d = 5 mm) windows on the upper flange of the mass spectrometer, which are transparent to UV and visible light, allow the laser beam to enter and leave the high-vacuum chamber. Two holes were drilled into the upper vacuum flange of the mass spectrometer, and a KF-16 ring was fit to host the two windows and to maintain the low pressure that is necessary to run such experiments. The window through which the laser enters the trap, (a), is directly positioned above the ion trap. Additionally, two holes were drilled in the ring electrode of the QIT so that the laser can enter the trap through the top hole (b), interact with the stored ions and then leave through the second one (c). Both holes are tapered to minimise the loss of helium buffer gas and lessen any interference with the optimal operation of the trap. A 6 mm thick aluminium mirror is kept underneath the ring electrode (d), on a mirror mount, that collects the beam once it is out of the trap and reflects it onto a second aluminium mirror (e). The latter is held in place underneath the exit window (f) to reflect

the laser beam out of the vacuum chamber. This configuration assists the alignment of the laser beam through the trap.

2.1.3 Experiment Overview

The instrument that has been described so far was used for the gas-phase photodissociation experiments described in this dissertation. In this section, an overview of the data collection, processing and extraction is presented. A complete description can be found in Ref. [156]. Experimental details of specific systems (e.g. solution preparation, mass spectrometry and CID conditions) are given in the Chapters 3-7.

2.1.3.i Mass Spectrometry Methods

As described in Section 2.1.2.i, ESI was used throughout this work to introduce molecular ions and ionic clusters into the gas phase. Sample solutions, of concentrations between 10^{-4} and 10^{-6} M, were injected using a 1 cm^3 syringe connected to the ESI needle by PEEK tubing. ESI source conditions, adjusted through trapControl, ensured an intense signal and a stable flow. Similarly, the software was used to optimise the QIT conditions and the voltages leading to it.

Mass spectra of the electrosprayed solutions were collected to identify the nature of the species obtained by ESI, and species identification was verified by isotopic pattern evaluation.

Target species were then isolated (by one- or two-stage isolation) and analysed *via* CID. The CID experiment was conducted by exciting the secular frequency of the isolated ions *via* an RF voltage with an amplitude that could be changed between 0 and 2.5 V. In a typical CID experiment, RF amplitude was increased until the parent ion was completely fragmented, and the thermal fragments identified. CID spectra

were obtained by plotting the ion production percentage (Eq. 2.7) versus the % RF amplitude. [165] [166]

$$\% \text{ CID} = (\text{I}_F / \Sigma_{\text{Ion Count}})\cdot 100 \tag{2.7}$$

2.1.3.ii Photodepletion Methods and Gas-phase Absorption Spectra

Mass spectrometry is a highly sensitive technique, able to detect low ion concentrations. The small number of isolated ions (10^3 - 10^6) is not enough to read an intensity difference between the transmitted and the detected laser beams when a resonant photon is absorbed by the ion. Unlike solution-phase UV-vis spectroscopy, the depletion in the beam intensity, therefore, cannot be measured to determine an absorption spectrum. To overcome this issue, gaseous absorption cross-sections can be obtained *via* action spectroscopy, where the light absorption is approximated by measuring the variation in the intensity of the parent ion after the interaction with the laser beam. It is assumed that any photochemical reaction activated by the laser beam results in the depletion of the parent ion, either by photofragmentation or electron detachment, *i.e.* radiative relaxation is not involved. [167] [168] Photodepletion can be considered as gas-phase absorption, in the limit where fluorescence is not a significant decay channel following electronic excitation. In this case the ion would release the excess energy *via* photon emission without showing any depletion. [169]

One of the first photodissociation action experiments, published by Brauman and Smyth, [6] describes the absorption cross-section in terms of a probability for photodetachment (*P)*:

$$P = t\,f\,\int \sigma(\lambda)\rho(\lambda)\mathrm{d}\lambda \tag{2.8}$$

Where t is the time that the ion spends in the beam; σ is the cross-section for the photodetachment; f is the geometrical overlap between the ion and the light beams, and ρ is the photon flux. The integration is over the wavelength range used to irradiate the ion beam. This equation can be re-written considering the parent ion initial intensity (I_0) and its intensity after being irradiated for a time t, $I(t)$:

$$I(t) = I_0 \exp\left(-t f \int \sigma(\lambda)\rho(\lambda)\mathrm{d}\lambda\right) = I_0 \exp(-P) \tag{2.9}$$

The pulsed laser (10 Hz) used allows control over the irradiation time and wavelength of the experiment. Assuming that the overlap between the laser pulse and the ion packet is constant at every wavelength and that a single laser pulse irradiates the ions, we can write:

$$\sigma(\lambda) = \ln\left(\frac{I_0}{I}\right)\bigg/\rho(\lambda) \tag{2.10}$$

Where I is the intensity of the parent ion after photoexcitation with a laser pulse. We can assume that the profile and duration of each laser pulse are the same and can approximate the photon flux, $\rho(\lambda)$, using the average number of photons per pulse that, in turn, is assumed proportional to the average laser pulse power (p), measured for each wavelength, and the wavelength of the laser (λ). Eq 2.10 can be simplified and written as photodepletion (PD):

$$PD = \frac{\ln\left(\frac{I_0}{I}\right)}{\lambda \times p} \tag{2.11}$$

We note that these are relative and not absolute cross-sections and that are specific of this instrumental configuration.

As shown in Section 2.1.2.iii., the amaZon mass spectrometer was modified to allow the laser beam to access the QIT and interacts with the mass-isolated ions. Gas-phase absorption spectra were obtained by comparing the intensity of the parent ion before and after laser irradiation.

An optomechanical shutter that opens and closes according to an external stimulus, controls the transmission of the laser through the QIT. In the PD experiment, a Transistor-Transistor Logic signal is emitted by the amaZon mass spectrometer during the fragmentation stage of the QIT cycle (Section 2.1.2.ii) and triggers the shutter. In this phase, the ions are isolated and stored for fragmentation, but the RF amplification voltage is set to 0 such that laser photodissociation is the only cause of fragmentation. The fragmentation time used in this work was 100 ms, to ensure the interaction of an ion packet with only one laser shot from the 10 Hz Nd:YAG laser. When fragmentation is disabled, the mass spectrum of the parent ion without irradiation is collected.

To obtain a gas-phase absorption spectrum, both the *Laser ON* and *Laser OFF* mass spectra are collected and compared, according to Eq. 2.10. The data in Chapters 3 and 4 are obtained by collecting two separated mass spectra at each wavelength. The data in Chapters 5 and 6 were collected in the Multiple reaction monitoring (MRM) functionality of the amaZon mass spectrometer. [156] The MRM function on trapControl can be used to set CID on multiple (up to ten) mass-selected precursors and monitor their fragmentation. The instrument records all the fragmentation mass spectra and stores them within a chromatogram. Single chromatograms and mass spectra can then be deconvoluted from the trapControl software.

In this functionality, up to five *Laser ON* and *Laser OFF* spectra can be collected within the same scan. For each species*,* two ions are isolated with the same *m/z* value; for

one of them (the *Laser ON* acquisition)*,* the fragmentation function is turned on, and this allows the shutter to open. Each ion is measured for 60 s, and the mass spectrum is averaged over this time. The experiment that is described in Chapter 5 was conducted by studying TryptoCORM and TryptoCORM-CH$_3$CN in the same scan, isolating four ions, two for each species.

For each wavelength, data are collected and analysed using an automated routine implemented in Ref. [156] and are plotted against the wavelength (or the photon energy) so to obtain gas-phase action spectra. For each wavelength, the laser power is collected to account for the photon flux within the ion trap.

2.1.3.iii Laser Power Method

The probability of n-photon absorption is proportional to the n-photon excitation cross-section, σ(*nPA*), and the photon flux to the power of n. [170] In Eq. 2.12, the total photodepletion is written as a power series of single- and multi-photon processes.

$$\ln \frac{I_0}{I} = \sigma(1PA,\lambda) \times \rho(\lambda) + \sigma(2PA,\lambda) \times \rho(\lambda)^2 + \sigma(3PA,\lambda) \times \rho(\lambda)^3 \ldots \qquad (2.12)$$

Because the σ(nPA) is many orders of magnitude smaller than the cross-sections for one-photon transition, it needs a high light intensity to be significant. In our experiment, to exclude multiphoton effects, photodepletion is measured at different values of laser power at one or more fixed wavelengths, close to the absorption maxima. These values are chosen above and below (~ ± 5 mW) the laser power used for the PD scan (~10 mW). The logarithmic depletion of the ion signal, $\ln(I_0/I)$, is plotted against the logarithm of the laser power to be fitted to a polynomial function and compared with Eq. 2.12. [170-172] As an alternative, a good fit to a linear function can be an indication of a one-photon process. [173]

2.1.3.iv Photofragmentation Method

The setup that is used in this thesis can measure the production of all the charged fragments above 50 m/z, and this information is an invaluable spectroscopic and photochemical tool. The photofragmentation action spectrum is calculated with Eq. 2.13 from the fragment ion intensity, I_f.

$$PF = \frac{\left(\frac{I_F}{I_0}\right)}{\lambda \times p} \tag{2.13}$$

When an ion is electronically excited in the gas phase, fragmentation can happen from a dissociative excited-state surface, either accessed vertically or after relaxation *via* a conical intersection (CI). In this mechanism, the potential energy surface of said state is repulsive with respect to a bond coordinate and the time scale of the dissociation along the repulsive surface is shorter, or comparable to the lifetime of the excited state. [174] Another mechanism involves a vibronically excited electronic ground-state surface where ultrafast relaxation to a vibrationally hot state onto the electronic ground state can be followed by fragmentation. [33] The two mechanisms are illustrated in Figure 2.12.
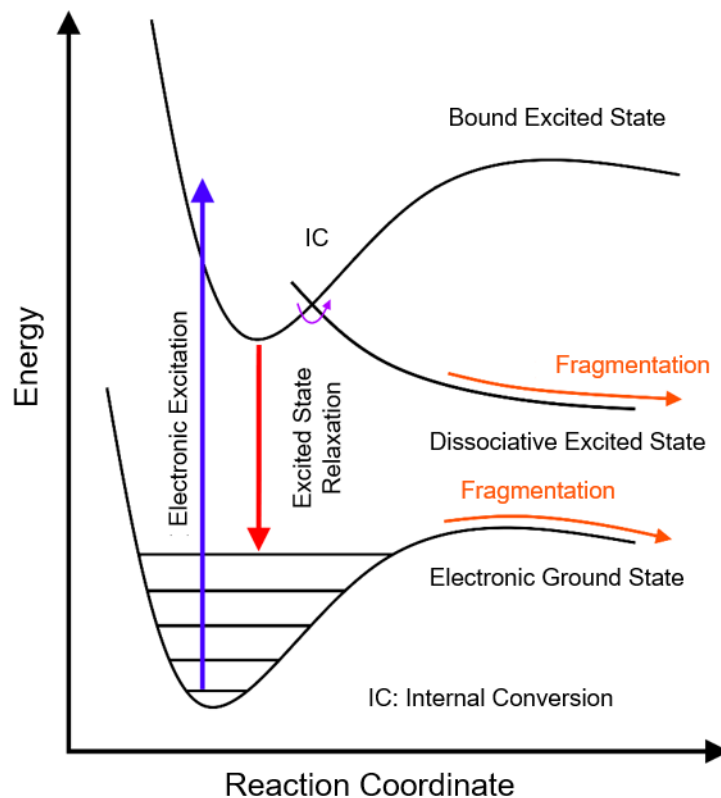
Figure 2.12 Schematic potential energy surfaces of a molecule in the gas-phase showing two possible fragmentation mechanisms (in the electronic excited and ground states), following photoexcitation.

In the solution phase, collisions with solvent molecules induce vibrational relaxation of the vibrationally hot molecule, a mechanism not accessible in the gas phase.

In Chapters 5 and 6, the photofragment ion yield was calculated at each wavelength according to Eq. (2.14)

$$\text{Ion Yield} = \frac{Int_{Frag}}{Int_{PFT}} * 100 \qquad (2.14)$$

Where Int_{PFT} is the sum of the photofragment ion intensities obtained with the laser on.

2.1.3.v Electron Detachment Yield Spectra

Electron detachment is an important process that can lead to depletion of the parent ion population in a gas-phase photodissociation experiment (Eq. 1.2). For it to take place the photon energy must be higher than the binding energy of the excess electron. For a multiply charged anion (MCA), the photon energy has to overcome the repulsive-Coulomb barrier (RCB) associated with the excess charges. [175] [176] From MCAs it is possible to measure the electron detachment directly, however, if the electron is detached by a monoanion, a neutral molecule is produced that cannot be detected by the mass spectrometer. [177]

In Chapters 3 and 4, we calculate the electron detachment (ED) yield by assuming that any depleted ions that are not detected as ionic photofragments are decaying *via* electron detachment (Eq. 2.15). This analysis assumes that both the parent ions and photofragments are detected equally in the mass spectrometer, a reasonable assumption for the systems studied here where the parent ions and fragment ions are reasonably close in m/z. To homologate our description of ED with PF, we divide it by the laser flux as well.

$$ED = [(PD_{IC} - \Sigma\, I_F\,)/I_{OFF}]/(\lambda \cdot \mathrm{p}) \tag{2.15}$$

Where

$$PD_{IC} = I_{OFF} - I_{ON} \tag{2.16}$$

We compare these results with the amount of photodepleted ions, PD*:

$$PD^* = (PD_{IC}/I_{OFF}\,)/(\lambda \cdot p) \tag{2.17}$$

2.2 Orbitrap

2.2.1. Instrument Overview

As described in Section 2.1.3.i, ground state fragmentation of the studied ions was investigated *via* CID. In addition, higher-energy collisional dissociation (HCD) was performed and compared to laser PF.

An Orbitrap Fusion Tribrid mass spectrometer (Thermo Fisher Scientific), equipped with an ESI source and available at the Centre of Excellence in Mass Spectrometry of the Chemistry Department, was employed for these experiments (Figure 2.13). The HCD fragmentation technique, as implemented on this instrument, provides tandem mass spectrometry, similar to triple quadrupole fragmentation. [178]
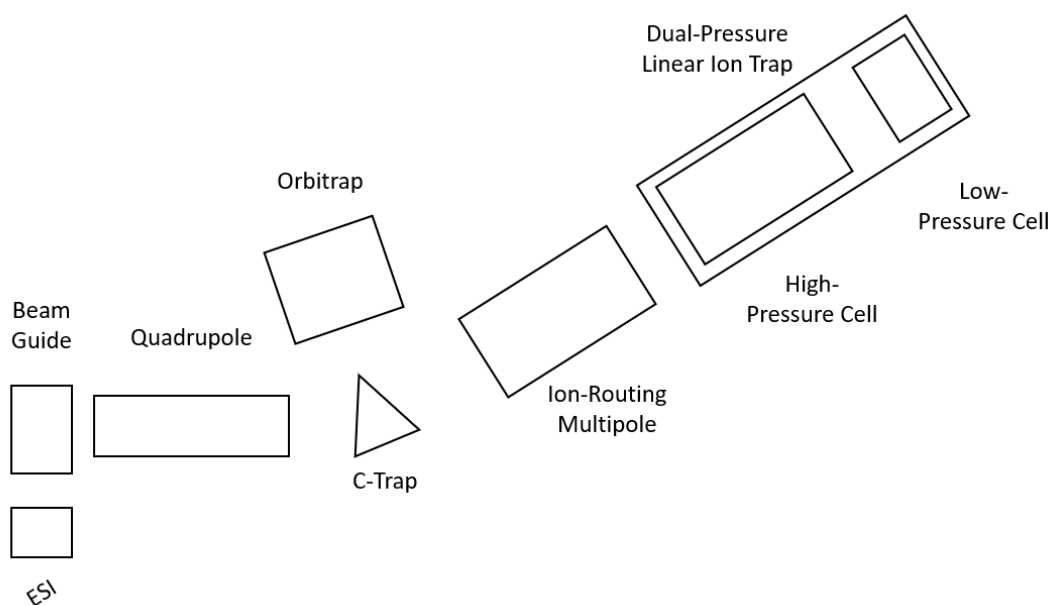
Figure 2.13 Schematic of the Orbitrap Fusion Tribrid mass spectrometer. [179]

The instrument is equipped with an ESI source, two mass filters (i.e. quadrupole or linear ion trap, LIT) and two mass analysers (i.e. LIT and Orbitrap). During the HCD mass analysis, either the quadrupole or the LIT are used for the mass selection. The ions are transferred from the curved linear trap (C-trap) to the ion routing multipole

(IRM) where they collide with nitrogen gas and produce ground-state fragments that are then sent to either the Orbitrap or the LIT for detection.

E_{CM}, the maximum amount of kinetic energy available for conversion to internal energy in a single collision, depends on the mass of the buffer gas, N, and is defined by Eq. (2.18):

$$E_{CM} = zRN / (m_p + N) \qquad (2.18)$$

Where z and m_p are the charges and the mass of the precursor ion, R is related to the instrument settings and N the mass of the collision gas. [180]

The Orbitrap Fusion Tribrid uses N_2 as the buffer gas, resulting in collisional energy that is higher than the CID energy in the amaZon ion trap (where He is the buffer gas). As standard procedure during the experiments, [181] [182] the normalised HCD collisional energy (the difference between the potential of the C-trap lenses and the ion routing multipole) is varied between 0 and 50 % (where 100 % is $\sim$ 100 V), and the intensity of the ion in percentage is calculated as for CID.

2.3 On-line Photolysis

Solution-phase photolysis was performed on the species $[Ru(\eta^5\text{-}C_5H_5)(PPh_3)_2CO]^+$, $[Ru(\eta^5\text{-}C_5H_5)(dppe)CO]^+$ and $[Mn(CO)_4Br_2]^-$ studied in Chapter 6 *via* the home-built on-line photolysis cell (Figure 2.14) that is mounted directly on top of the ESI needle.
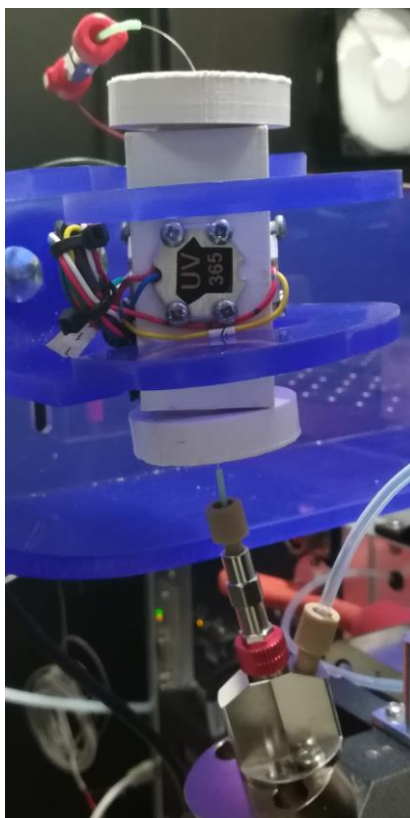
Figure 2.14 Picture of the photolysis cell on top of the electrospray needle.
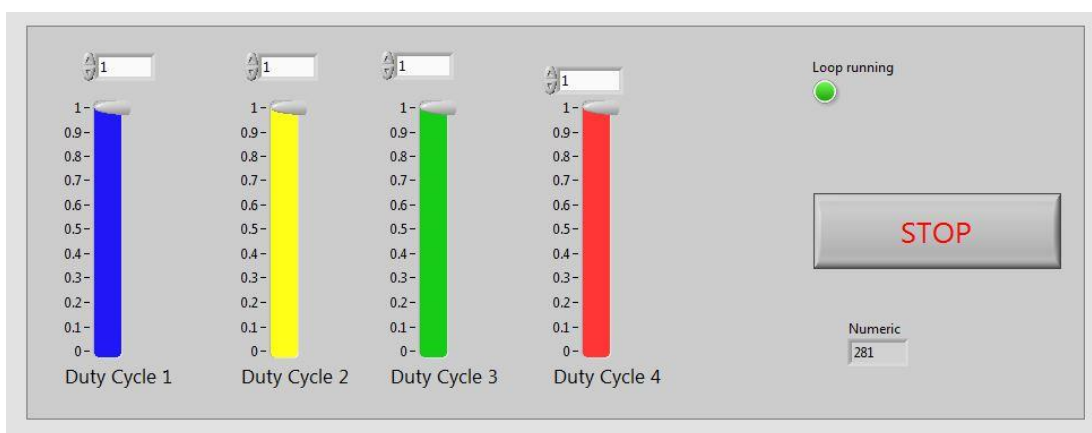
Figure 2.15 Interface of the LabVIEW software developed to be used with the photolysis cell.

The cell, in the shape of a hollow rectangular parallelepiped, was 3D printed. On each one of the four long faces, an LED of a different wavelength (365, 400, 460 and 523 nm) was mounted. The software allowed selective control of the power and brightness of each LED.

On the two short faces, end caps were added to access the inside of the cell, which was covered in foil to maximise the irradiation from the LEDs. Holes were drilled in the end caps to accommodate a UV transparent fused silica capillary tubing (100 µm ID, 375 µm OD, Molex/Polymicro Technologies, Phoenix, AZ) that was connected to the ESI needle. The capillary was also connected to the syringe pump via PEEK tubing (Figure 2.16).
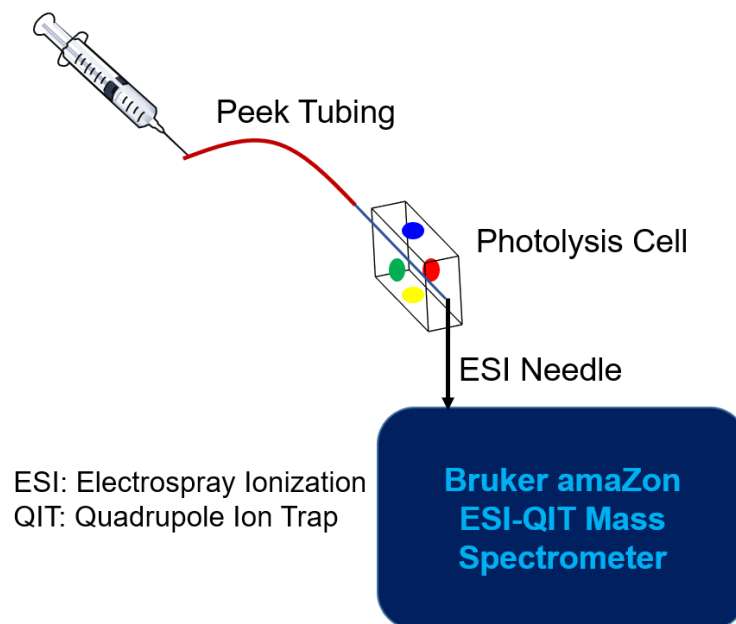
Figure 2.16 Diagram of the on-line photolysis cell.

2.4 Cryogenic Ion Vibrational Spectroscopy

Chapter 5 includes gas-phase IR spectra of TryptoCORM-CH$_3$CN measured at the University of Wisconsin-Madison in the Garand laboratory. The data were obtained *via* cryogenic ion vibrational spectroscopy (CIVS), in a homebuilt cryogenic spectrometer shown in Figure 2.17. [183]
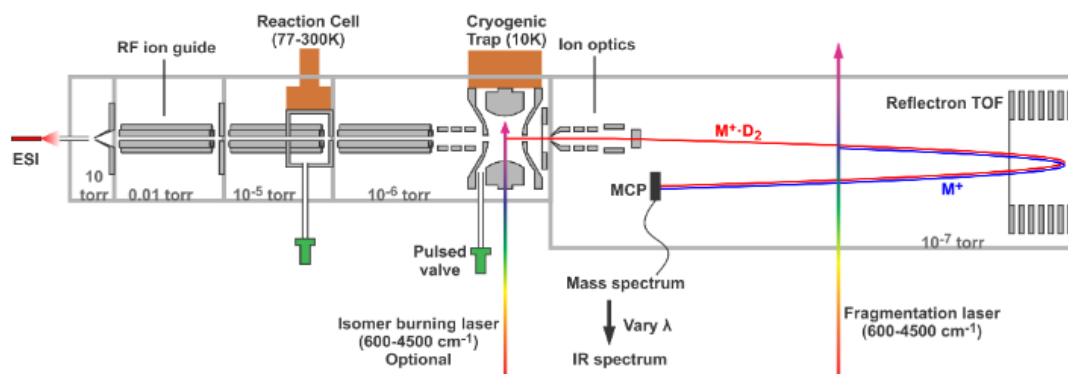
Figure 2.17 Schematic of the cryogenic ion vibrational spectrometer. The image is taken from Ref. [183].

In this experiment, electrosprayed ions were directed to a reaction cell kept at 80 K before reaching a QIT held at 10 K by a closed-cycle helium cryocooler. A ~ 1 ms burst of helium, seeded with 10 % D_2, is introduced into the trap to form weakly bound D_2–tagged adducts. $[MnL(CO)_3]\cdot H^+\cdot(D_2)$ aggregates were then ejected into the TOF mass spectrometer, mass-selected *via* a gated deflector, and intersected with the output of an Nd:YAG pumped tuneable OPO/OPA laser. The low vapour pression of D_2 allows to keep the trap at 10 K. [184] The perturbation that the system undergoes upon tagging is thought to be minimal, and the spectra only affected by small incremental shifts. [185] [186]

The loss of the D_2 tag, caused by resonant absorption of an IR photon, was monitored by measuring the intensity of the produced $[MnL(CO)_3]\cdot H^+$ as a function of photon wavelength, resulting in the IR action spectrum. The peak intensities were normalised to the most intense feature.

$$[MnL(CO)_3]\cdot H^+\cdot(D_2) + h\nu \rightarrow [MnL(CO)_3]\cdot H^+ + D_2 \qquad (2.19)$$
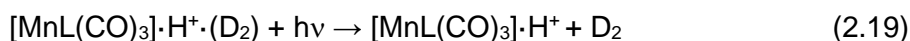
To discriminate between different possible isomers, isomer-selective CIVS was performed *via* hole burning with a second Nd:YAG pumped tuneable OPO/OPA laser

at the centre of the QIT (isomer burning laser). [187] In this method, the pump laser was fixed to a specific IR transition. All the structures absorbing at a given wavelength lost the tag before leaving the QIT and were not mass-selected by the mass-gate. The fragmentation laser (in the TOF) was then scanned, and a new IR spectrum with a dip in the burned feature (and in all the features associated with the structure) was obtained.

2.5 Computational Methods

The experimental data presented in this thesis have been supported by computational calculations, using density functional theory (DFT) and time dependent DFT (TDDFT) in Gaussian 09 (revision D.01, Gaussian Inc.). [188] Calculations were performed *via* York Advanced Research Computing Cluster (YARCC).

Methods and details of the specific calculations conducted for the different systems studied are given in the subsequent chapters. In general, DFT was used to investigate the ground-state properties: to explore different conformers and isomers and geometry of the parent ions; to find the gas-phase lowest-energy structure and to optimise it; to predict the structures of the fragments, and to calculate vertical and adiabatic electron detachment energies of anionic parent ions. Frequency calculations were performed following all geometry optimisations to ensure that the optimised structures corresponded to true energy minima. When required, solution-phase properties were calculated using an implicit solvent model. Moreover, TDDFT was used in Chapters 3 and 4 to simulate electronic excitation spectra and to predict excited states.

2.5.1 Density Functional Methods within This Thesis

Density functional theory does not accurately predict exchange and correlation energies that are approximated differently by individual functionals. In this section, details on the functionals used throughout the thesis are given.

The B3LYP functional uses the Lee-Yang-Parr (LYP) and Vosko-Wilk-Nusair (VWN) correlation functionals and the Becke's three-parameter (B3) exchange functional, which includes 20% exact (HF) exchange and is parametrised for rare gases. [189-191]

CAM-B3LYP is a hybrid exchange-correlation Coulomb-attenuating method. It combines the hybrid qualities of the B3LYP functional, and a long-range correction developed by Yanay et al. [192]

PBE0 is a so-called *ab initio* method, where no experimental parameters are included. The exchange energy is obtained with 75% Perdew, Burke and Ernzerhof (PBE) exchange functional and 25% exact exchange. Correlation is calculated with the Perdew-Wang functional. [193] [194]

M06-2X method is parametrised for non-metals and is ideal for studying main group thermochemistry. It calculates the exchange energy using 54% exact exchange and 46 using an earlier exchange functional (M05); correlation energy of the M06-2X functional is calculated using the M05 correlation functional. [195] [196]

Chapter 3

Photoexcitation of Adenosine-5'-Triphosphate Anions in Vacuo: Probing the Influence of Charge State on the UV Photophysics of Adenine

3.1 Abstract

We report the first UV laser photodissociation spectra (4.0-5.8 eV) of gas-phase deprotonated adenosine 5'-triphosphate, diphosphate and monophosphate anions. The photodepletion spectra of these anions display strong absorption bands across the region of 4.6-5.2 eV, consistent with excitation of a primarily adenine-centred π-π^* transition. The spectra appear insensitive to the charge of the species (*i.e.* the spectrum of [ATP-2H]$^{2-}$ closely resembles that of [ATP-H]$^-$), while the spectral profile is affected to a greater extent by the variation of the molecular structure, *i.e.* the [AMP-H]$^-$ and [ADP-H]$^-$ photodepletion spectra display similar profiles while the [ATP-H]$^-$ spectrum is distinctive. The photodepletion cross-section also decreases for the ATP anions compared to both the AMP and ADP anions, reflecting a high intrinsic photostability of ATP versus both AMP and ADP. A range of photofragments are produced across the 4.0-5.8 eV spectral range for all of the ATP analogues studied. These fragments are primarily associated with fragmentation on the ground-state electronic surface, indicative of a statistical decay process where ultrafast decay is followed by ergodic dissociation. However, while the photofragments observed following photoexcitation of the monoanionic species, [AMP-H]$^-$ to [ADP-H]$^-$ to [ATP-H]$^-$ are entirely consistent with statistical decay, an additional group of photofragments are observed for the dianionic species, [ADP-2H]$^{2-}$ and [ATP-2H]$^{2-}$, that we associate with electron detachment, and subsequent fragmentation of the resulting electron-detached photofragment. TDDFT calculations are presented to support the

interpretation of the experimental data and confirm that the electronic structure of the adenine moiety is relatively unperturbed by varying the overall charge.

3.2 Introduction

The ultrafast photophysical and photochemical processes that occur in DNA following UV excitation have been the subject of intense investigation, since the absorption of UV radiation can lead to biological damage, including mutations and strand breaks. [18][197] Such photodamage processes display low quantum yields, however, due to the operation of non-radiative decay mechanisms that enable nucleobases to dissipate the harmful electronic excitation into more benign thermal energy. Much effort has been expended into obtaining a molecular-level understanding of these processes, with a particular focus both experimentally and theoretically on adenine. [198-203]

Gas-phase experiments provide a useful complement to solution-phase measurements, since they can often provide more detail and allow a more straightforward comparison between experiment and theory. Instrumental developments linking electrospray ionisation with UV laser spectroscopy provided a route to extend earlier gas-phase experiments on the simple nucleobases to the more complex oligonucleotides. [66] [204-210] For example, Marcum *et al.* have used photodissociation spectroscopy to study photodamage in isolated mononucleotides, [205] and Chatterley *et al.* have used time-resolved photoelectron imaging spectroscopy to explore the ultrafast dynamics of the nucleotide and selected oligonucleotides of adenine. [66] One of the key questions raised by these studies is the extent to which the native negative charge carried by a deprotonated oligonucleotide can affect the intrinsic photophysics and photochemistry of the adenine moiety.

In this work, we present the first gas-phase UV laser photodissociation spectra of a series of deprotonated anions of adenosine 5'-triphosphate (ATP), diphosphate (ADP) and monophosphate (AMP), illustrated in Scheme 3.1.
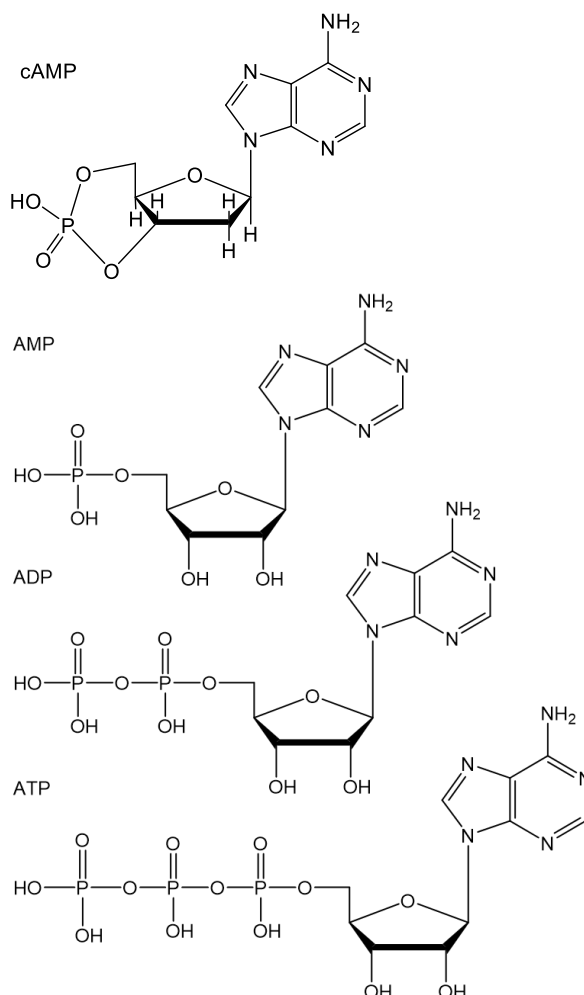
Scheme 3.1 Chemical structures of the neutral forms of cAMP, AMP, ADP and ATP.

Adenosine 5'-triphosphate plays the central role in the storage and distribution of energy in cells, and is also of key importance in signal transduction via the production of 3',5'-cyclic adenosine monophosphate (cAMP, Scheme 3.1). [211] cAMP is a cyclic form of AMP, with the phosphate group binding to the 3' and 5' carbons of the sugar ring upon dehydration. It is an important messenger used for intracellular signal transduction and activation of protein kinases.

Although ATP is an important biological molecule, our focus in this work is on using the ATP/ADP/AMP series of molecules as a facile test system to investigate the effect of changing the charge state on the UV photochemistry of the adenine nucleobase. The question of how an adjacent negative charge influences the UV photophysics of a nucleobase is also of fundamental relevance to the correct interpretation of a number of recent laser experiments on molecular clusters that include nucleobases, e.g. iodide ion-nucleobase clusters and platinum complex anion-nucleobase clusters. [8] [72] [212] [213]

Importantly, Compagnon *et al.* identified a strong bathochromic shift in the electronic excitation of tryptophan on going to the monoanionic deprotonated species. [177] This shift was attributed to the impact of an adjacent excess negative charge on the tryptophan chromophore. The experiments performed here allow us to investigate whether this is a general phenomenon or an effect specific to the tryptophan system.

3.3 Methods

ATP was purchased from Sigma Aldrich and used without purification. We anticipate that the ATP analogues will be deprotonated on the phosphate side chains. This point is discussed further in Ref. [214]. Solutions of ATP (1×10^{-5} M) in deionised water were sprayed in the amaZon ESI-QIT with nebulising gas pressure of 10.0 psi, injection rate of 250 μL/hr, drying gas flow rate of 8.0 L min^{-1}, and capillary temperature of 180 °C. The PD spectrum was acquired across the range 215-345 nm (4-5.8 eV) at ~1 mJ laser power. ADP and AMP anions were formed upon dissolution of ATP in water or electrospray of the solution. Photofragmentation experiments were run with an ion accumulation time of 100 ms and 100 ms fragmentation time. Solution-phase UV absorption spectra (aqueous solution, 3×10^{-5} M) were recorded using a Shimadzu 1800 UV spectrophotometer with a 1 cm UV cuvette, using distilled water as a baseline.

HCD was performed on the Orbitrap at a flow rate of 20 µL/min and with the following parameters: spray voltage -2453 V; sweep gas flow rate, 0; sheath gas flow rate, 35; aux gas flow rate, 10; ion transfer tube temperature, 325 °C; vaporizer temperature, 150 °C; MS^1 detector, Ion Trap; MS^1 scan range, 50–600; MS^1 maximum injection time, 100 ms; MS^1 automated gain control target, 100,000; MS^2 detector, Ion trap; MS^2 AGC target, 100,000; MS^2 maximum injection time, 100, S-lens RF level, 60 V (10 V for the dianions). The HCD collisional energy was varied between 0 and 45 % (100 % HCD energy is approximately 100 V), and the intensity of the ion in percentage was calculated.

Geometry optimization and vertical detachment energies (VDEs) were obtained *via* DFT at the M06-2X/6-311++G** level. Simulated absorption spectra were calculated at the B3LYP/6-311++G** level. Further details are given in Section 3.7.1 and 3.7.3.

3.4 Results and Discussion

3.4.1. Photodepletion Spectra

The photodepletion spectra of the [AMP-H]$^-$, [ADP-H]$^-$, [ATP-H]$^-$, [ADP-2H]$^{2-}$ and [ATP-2H]$^{2-}$ anions are displayed in Figure 3.1. (We label these species as [AXP-nH]$^{n-}$ where X = M, D, T and n = 1, 2.)
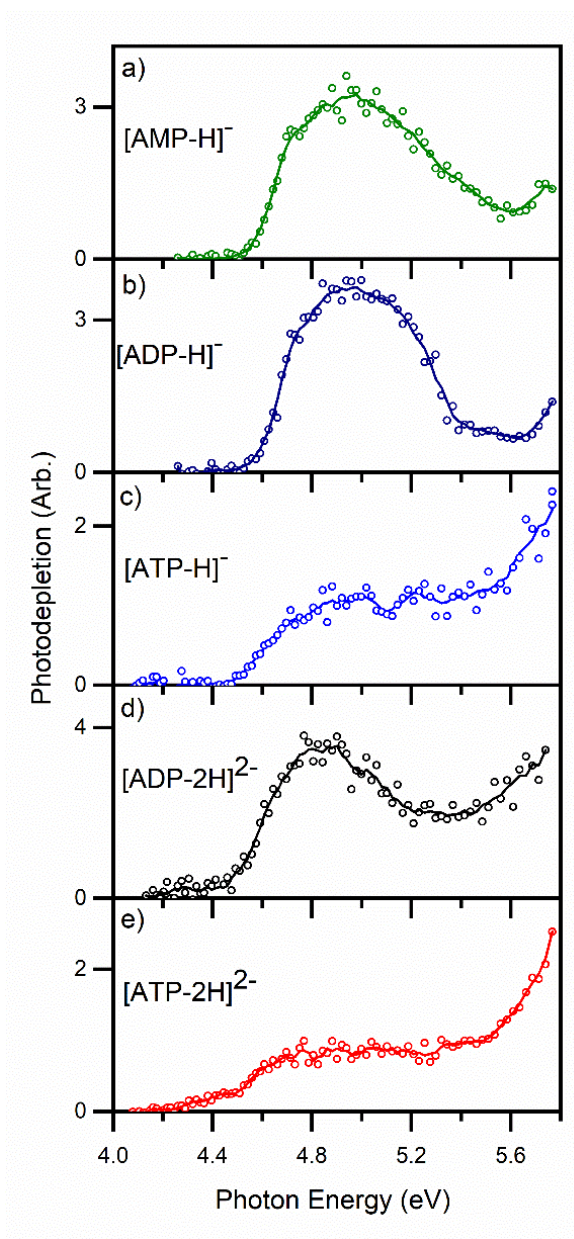
Figure 3.1 Photodepletion (absorption) spectra of a) [AMP-H]⁻, b) [ADP-H]⁻, c) [ATP-H]⁻, d) [ADP-2H]²⁻, and e) [ATP-2H]²⁻ across the range 4.07-5.77 eV. The solid lines are five-point adjacent averages of the data points.

The spectra are all similar in that they display broad absorption features between ~ 4.6-5.2 eV, with the photodepletion cross section remaining considerable (or increasing) towards the high-energy limit of the scans. We note that the photodepletion intensity of ATP is markedly smaller than the photodepletion intensities of AMP and ADP, indicating that the ATP anions are inherently more photostable than the AMP and ADP analogues. To test that the photodepletion

spectra correspond to single-photon absorption spectra, laser-power dependent photodepletion measurements (0.5 to 1.5 mJ) were conducted at 4.9 eV, close to the maximum of the broad absorption maxima bands. Figure 3.2 displays these power-dependent measurements, which are linear across this range, confirming that photoexcitation under the experimental conditions employed here (100 ms fragmentation time, 1.0 mJ pulse energy) is a one-photon process.
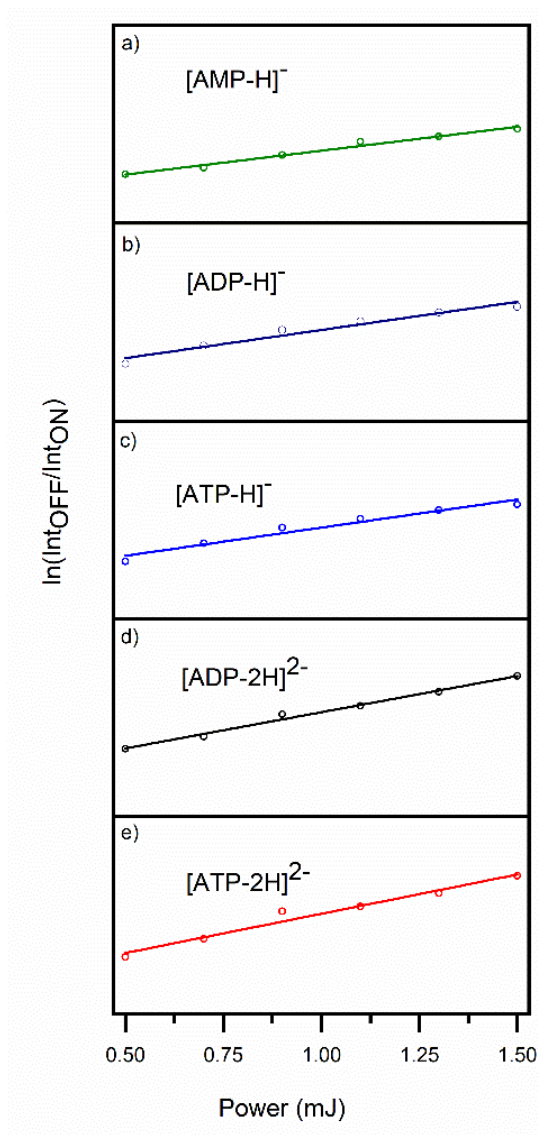
Figure 3.2 Laser power measurements for photodepletion of the a) [AMP-H]⁻, b) [ADP-H]⁻, c) [ATP-H]⁻, d) [ADP-2H]²⁻, and e) [ATP-2H]²⁻ anions, recorded at 4.9 eV.

Figure 3.3 presents the aqueous absorption spectra of solutions of ATP recorded at a range of pHs (between 1 and 12) for comparison with the gas-phase spectra.

Despite the change in pH, these solution-phase absorption spectra are remarkably similar, displaying a prominent absorption between 4.6 and 5.2 eV ($\lambda_{max} \sim$ 4.75 eV), followed by a strongly increasing absorption profile towards the high-energy limit of the scan. The $\lambda_{max} \sim$ 4.75 eV absorption band has been associated with the π-π^* transition centred on the adenine moiety, [201] [202] [215] [216] and this feature dominates the spectra irrespective of the fact that the various ATP solutions will contain mixtures of differentially deprotonated ATP, ADP and AMP species.
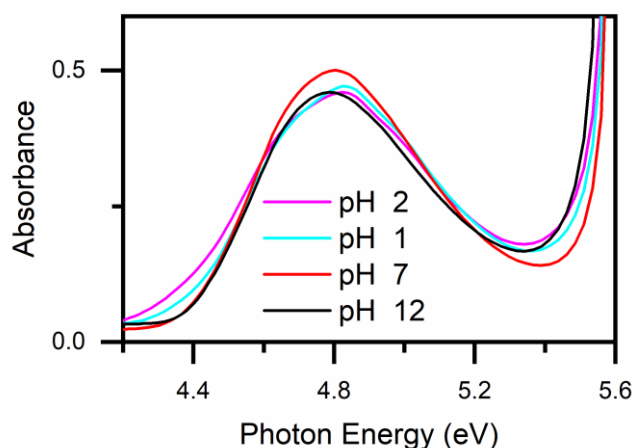
Figure 3.3 Aqueous absorption spectra of ATP (3×10^{-5} mol dm^{-3}) recorded at pH = 1, 2, 7 and 12.

Returning to the gas-phase photodepletion spectra (Figure 3.1), we therefore assign the broad absorptions observed between $\sim$ 4.6-5.2 eV as arising from the same, predominantly adenine-centred π-π^* transition that appears with $\lambda_{max} \sim$ 4.75 eV for the solution-phase ATP species. [217]

It is evident that this absorption is relatively insensitive to whether the species carries a single or a double negative charge (e.g. the [ATP-H]$^-$ spectrum closely resembles that of the [ATP-2H]$^{2-}$ spectrum). Although the photodepletion spectra of all of the [AXP-nH]$^{n-}$ anions are broadly similar, the spectra are modified by whether the adenosine species carries a mono-, di- or triphosphate tail. This is most evident for the [ATP-nH]$^{n-}$ species which have spectra that display a considerably more sharply-

increasing absorption profile at high energy compared to the ADP and AMP species. We note that the strong absorption towards the high-energy tail we observe here mirrors the spectral profile of solution-phase ATP (Figure 3.3).

It is instructive to consider where the photodepletion spectra appear with respect to the electron detachment energies of the [AXP-nH]$^{n-}$ anions. Photoelectron spectra of the dianionic species have been recorded by Schinle *et al.*,[218] but since we have no experimental electron affinities for the monoanions, we calculated electron affinities for all of the species studied here and use them as a complete set of values, where relative values should be reliable. These calculated vertical detachment energies (VDEs) are included in Table 3.1.

Table 3.1 M06-2X/6-311++G** calculated VDEs and electron detachment onset energies of the [AXP-nH]$^{n-}$ (n = 1, 2) anions.[a]

Ion	Calculated VDEs [b] eV	Electron Detachment Onset Energies[c] eV
[AMP-H]$^-$	6.04	-
[ADP-H]$^-$	6.17	-
[ATP-H]$^-$	6.24	-
[ADP-2H]$^{2-}$	3.10	5.3
[ATP-2H]$^{2-}$	4.11	6.0

[a] See Section 3.7.1 for details.
[b] Not zero-point energy corrected.
[c] Calculated VDEs combined with the experimental RCB from Ref. [214].

For the monoanions, [AXP-H]$^-$, the VDEs all lie above the high-energy limit of the scans, indicating that the electronic transitions observed in Figures 3.1a-3.1c lie well below the electron detachment continuum. The situation is slightly different for the dianionic species, [ADP-2H]$^{2-}$ and [ATP-2H]$^{2-}$, which we predict to have vertical

detachment energies of 3.10 and 4.11 eV. However, the threshold for electron detachment is only reached around ~5.3 and 6.0 eV, [218] respectively, when the repulsive Coulomb barrier (RCB) for electron detachment is exceeded. [165] [219] Therefore, the dianion photodepletion spectra also lie predominantly below the electron detachment continuum, although there is likely to be some photodetachment below these energies associated with electron tunnelling through the RCB. [165] [219]

While the overall spectral profile is similar for all of the [AXP-nH]$^{n-}$ anions, it is evident that there are differences between the spectral profiles. One prominent example of this is the way that the ATP species (Figures 3.1c and 3.1e) display a much more strongly increasing photodepletion cross-section to high-energy. To further explore the differences in the photodepletion spectra and the decay pathways that follow photoexcitation, [220] we will investigate the spectral profile for the photofragment production spectra that accompany the photodepletion spectra in Section 3.4.3.

3.4.2 Collision-Induced Dissociation

Upon photoexcitation, these molecules can undergo two main types of decay. The first mechanism requires an ultrafast internal conversion to a hot electronic ground state surface, followed by intramolecular vibrational redistribution (IVR). IVR leads to bond dissociation according to the Rice–Ramsperger–Kassel–Marcus (RRKM) theory, where the bonds with lowest activation barriers and lowest density of states are preferentially broken. [221] The second possible mechanism is a cleavage on the excited state surface, that may be related to the changes in electron density between the ground and the excited state.

Higher-energy collisional dissociation (HCD) was performed for the series of [AXP-nH]$^{n-}$ (X = M, D, T and n = 1, 2) anions to fully characterise their ground electronic-state fragmentation behaviour, a list with the m/z values of the fragments and their

species assignments is included in Table 3.2. The HCD fragmentation curves are displayed in Figure 3.4. Inspection of the fragmentation curves shows that a number of larger molecular fragments are produced only over a limited energy range, with fragmentation into smaller ionic species becoming dominant at higher collision energies. One example is provided by the [ADP-H]$^-$ anion (Figure 3.4b) which fragments with production of [cAMP-H]$^-$ only between 10-35% HCD, and also the corresponding dianion, [ADP-2H]$^{2-}$ (Figure 3.4d) which produces the [AMP-H]$^-$ fragment only between 0-28% HCD. Although there have been previous collision-induced dissociation (CID) measurements conducted on the [ATP-2H]$^{2-}$ and [ADP-2H]$^{2-}$ dianions (low-energy CID), [214] and the [AMP-H]$^-$ monoanion (higher-energy CID), [33] this is the first time that a comparable set of CID profiles have been obtained for the [AXP-nH]$^{n-}$ series.

Table 3.2 List of the m/z of the fragments obtained in this study and relative assignments.

m/z ($\pm$0.2)	Species	m/z ($\pm$0.2)	Species
79	PO$_3^-$	291	[ADP-H-A]$^-$
97	H$_2$PO$_4^-$	328	[cAMP-H]$^-$
134	[A-H]$^-$	346	[AMP-H]$^-$
159	HP$_2$O$_6^-$,	370	[ATP-2H-A]$^-$
177	H$_3$P$_2$O$_7^-$	408	[cADP]$^-$
211	[AMP-H-A]$^-$	425	[ADP-2H]$^-$
212.5	[ADP-2H]$^{2-}$	426	[ADP-H]$^-$
252.5	[ATP-2H]$^{2-}$	505	[ATP-2H]$^-$
257	H$_4$P$_3$O$_{10}^-$	506	[ATP-H]$^-$
273	[ADP-H-A-H$_2$O]$^-$		

In the previous CID measurements of the [AMP-H]$^-$ anion by Ho and Kebarle, [222] an absolute measurement of centre of mass collision energy was obtained through absolute calibration. Comparison of the current results for [AMP-H]$^-$ (Figure 3.4a) with these earlier measurements, [222] allows us to obtain an approximate calibration of the HCD fragmentation curves presented in Figure 3.4. From this comparison, it appears that the 4-6 eV energy range (i.e. the photon range employed in our laser experiments, and hence the maximum amount of energy that would be available to fragment the ground state surface anions) corresponds to the 20-38% range on the HCD fragmentation plots.
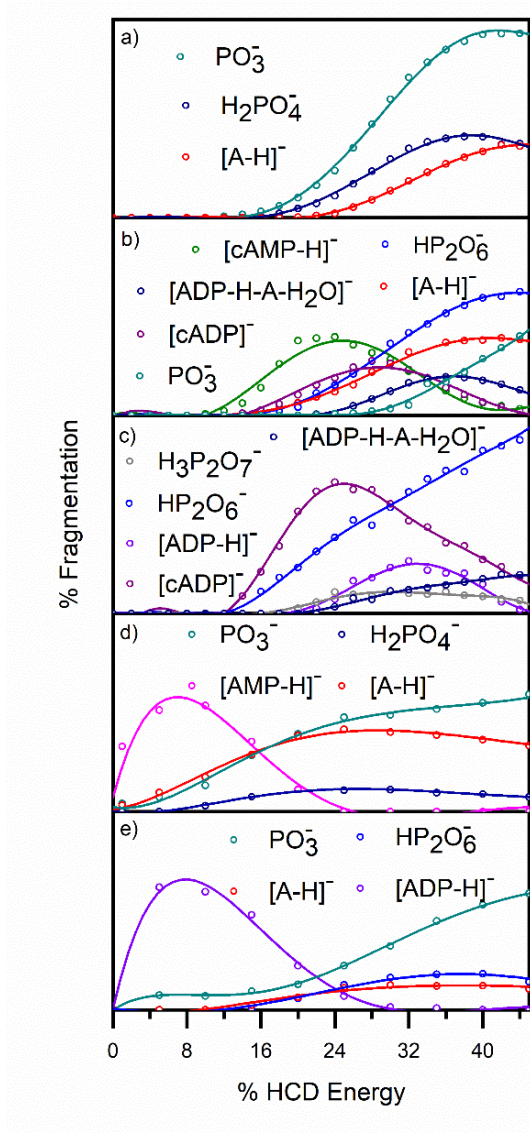
Figure 3.4 Fragment production curves for a) [AMP-H]⁻, b) [ADP-H]⁻, c) [ATP-H]⁻, d) [ADP-2H]²⁻ and e) [ATP-2H]²⁻ upon HCD between 0 and 45 % energy (100 % HCD energy is approximately 100 V).

3.4.3 Photofragmentation Mass Spectra

Figure 3.5 displays the photofragment mass spectra obtained for photoexcitation of the [AXP-nH]$^{n-}$ anions at 4.9 eV, close to the peaks of the photodepletion spectra (A list of the prominent photofragments observed is included in Table 3.3).
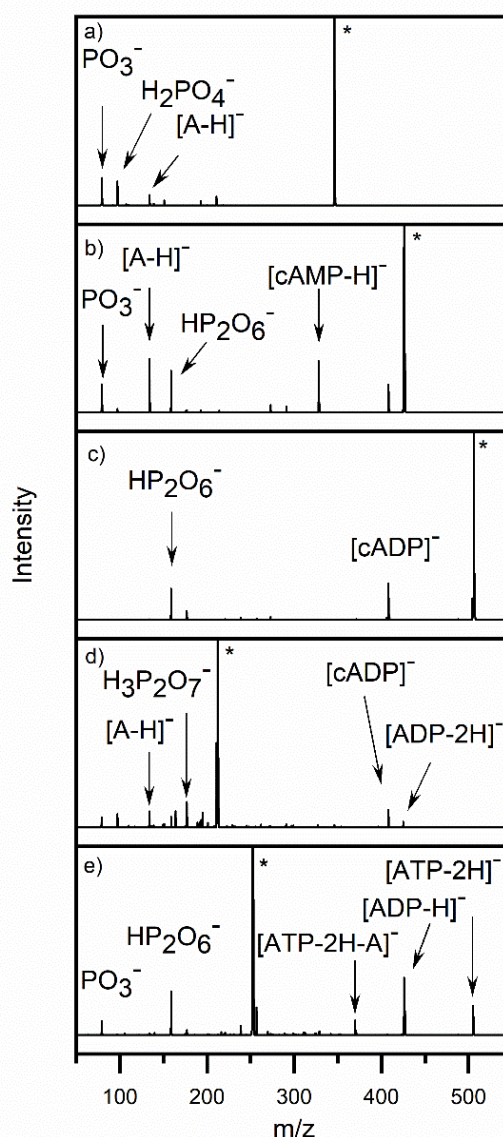
Figure 3.5 Photofragment mass spectra of a) [AMP-H]⁻, b) [ADP-H]⁻, c) [ATP-H]⁻, d) [ADP-2H]²⁻, and e) [ATP-2H]²⁻ excited at 4.9 eV. * indicates the depleted parent ion signal.

Photofragments associated with fission of the phosphate side chain are common, *e.g.* PO_3^- and $HP_2O_6^-$. For $[ATP-2H]^{2-}$ (Figure 3.5e), the PO_3^- photofragment is observed with the accompanying monoanion in photofragmentation of the dianionic species, consistent with a photoinduced ionic fragmentation process, [165] [205] [214] *e.g.*

$$[ATP-2H]^{2-} + h\nu \rightarrow PO_3^- + [ADP-H]^- \qquad (3.1)$$

Deprotonated adenine, $[A-H]^-$ is seen as a prominent photofragment for $[AMP-H]^-$, $[ADP-H]^-$, and $[ADP-2H]^{2-}$ (Figures 3.5a, 3.5b and 3.5d).

It should be noted that although we refer to this fragment as deprotonated adenine, it could equivalently be described as A^-, *i.e.* the anionic nucleobase formed upon rupture of the CN glyosidic bond. [222] The $[A-H]^-$ anion has been observed as a stable photofragment in several recent studies of clusters that include adenine. [8] Intriguingly, $[A-H]^-$ it is not observed as a significant intensity photofragment for either of the ATP anions (Figures 3.5c and 3.5e). Electron detachment is observed for both of the dianionic species (Figures 3.5d and 3.5e), *e.g.*

$$[ADP-2H]^{2-} + h\nu \rightarrow [ADP-2H]^- + e^- \qquad (3.2)$$
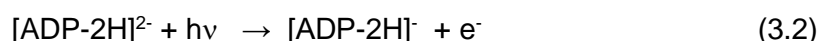
This is despite the fact that this photoexcitation energy, although greater than the adiabatic electron affinity, is still considerably below the electron detachment onsets associated with exceeding the RCB (see Section 3.4.1).

As described in Section 3.4.2, a series of HCD experiments were conducted on the $[AXP-nH]^{n-}$ anions to establish which ionic fragments are produced on the ground state surface following collisional excitation.

Table 3.3 Photofragments observed following photoexcitation at 4.9 eV and higher-energy collisional dissociation (HCD) fragments obtained at 24% collisional energy for the $[AXP\text{-}nH]^{n-}$ (n = 1,2) anions.[a]

Parent ion	Photofragments[b]	HCD fragments[c]
$[AMP\text{-}H]^-$	$PO_3^- \approx H_2PO_4^-$, $[A\text{-}H]^-$, $[AMP\text{-}H\text{-}A]^-$	PO_3^-, $H_2PO_4^-$, $[AMP\text{-}H\text{-}A]^-$, $[A\text{-}H]^-$
$[ADP\text{-}H]^-$	$[A\text{-}H]^-$, $[cAMP\text{-}H]^-$, $HP_2O_6^-$, $[cADP]^- \approx PO_3^-$, $[ADP\text{-}H\text{-}A]^-$, $[ADP\text{-}H\text{-}A\text{-}H_2O]^-$	$[cAMP\text{-}H]^-$, $[cADP]^-$, $HP_2O_6^-$, $[A\text{-}H]^-$, $[ADP\text{-}H\text{-}A\text{-}H_2O]^-$, PO_3^-, $[ADP\text{-}H\text{-}A]^-$
$[ATP\text{-}H]^-$	$HP_2O_6^- \approx [cADP]^-$, $H_3P_2O_7^-$	$[cADP]^-$, $HP_2O_6^-$, $H_3P_2O_7^-$
$[ADP\text{-}2H]^{2-}$	$H_3P_2O_7^-$, $[A\text{-}H]^- \approx [cADP]^-$, $HP_2O_6^-$, $H_2PO_4^-$, PO_3^-, $[ADP\text{-}2H]^-$, $[AMP\text{-}H]^-$	PO_3^-, $[A\text{-}H]^-$, $H_2PO_4^-$, $[AMP\text{-}H]^-$
$[ATP\text{-}2H]^{2-}$	$[ADP\text{-}H]^- \approx HP_2O_6^-$, $[ATP\text{-}2H]^-$, $H_4P_3O_{10}^-$, $[ATP\text{-}2H\text{-}A]^-$, PO_3^-, $[cAMP\text{-}H]^-$, $[A\text{-}H]^-$	PO_3^-, $[ADP\text{-}H]^-$, $HP_2O_6^-$, $[A\text{-}H]^-$, $[cAMP\text{-}H]^-$

[a] Photofragments and HCD fragments are listed in order of decreasing intensity
[b] At 4.9 eV
[c] At 24 % HCD Energy.

Table 3.3 presents a comparison of the major photofragments obtained with a photoexcitation energy of 4.9 eV, along with the anionic fragments obtained with an HCD centre-of-mass collision energy of 24%, *i.e.* a similar energy to the laser photon energy. For systems where photoexcitation is followed by rapid decay back to the ground-state surface and subsequent ergodic (statistical) dissociation, the

photofragments are expected to mirror the HCD fragments produced when an amount of energy equivalent to the photon energy is deposited in the ground-state system. [205] [204] Inspection of Table 3.3 reveals that the major 4.9 eV photofragments largely mirror the major 24% HCD fragments, consistent with a predominantly statistical decay process.

For the dianionic systems, all the fragments observed in the HCD experiment are seen as photofragments, along with a small number of additional photofragment species e.g $[cADP]^-$ from $[ADP-2H]^{2-}$ (the $[cADP]^-$ is a fragment that is common between the $[ADP-2H]^{2-}$, $[ADP-H]^-$ and $[ATP-H]^-$ anions, and is associated with loss of OH^-, H_2O and H_3PO_4, respectively). DFT calculations were conducted to investigate the structure of this cADP unit (Section 3.7.4) and predict a stable cyclic ADP structure. It appears that photofragmentation represents a slightly softer fragmentation process than HCD, since larger fragments such as $[cADP]^-$ can be seen in photofragmentation but are absent in HCD, presumably due to secondary fragmentation of primary thermal fragments that are produced with high internal energy.

We note that while similar sets of photofragments and HCD fragments are observed for all of the ATP analogues, the relative intensities (of a set of fragments produced by a single $[AXP-nH]^{n-}$ species in photofragments *versus* HCD) vary more on going to longer phosphate chain length and to higher charge (Table 3.3 and 3.4). For the dianionic systems, this observation can largely be attributed to the electron-detachment decay pathway of a multiply charged anion being accessed *via* photoexcitation in addition to adenine-centred π-π^* transitions.

The observation that all of the $[AXP-nH]^{n-}$ anions produce a group of photofragments that mirrors the CID fragments indicates that each of the $[AXP-nH]^{n-}$ anions follow

broadly similar decay pathways after photoexcitation at 4.9 eV, irrespective of the charge state or the phosphate chain length. This picture is consistent with the photodepletion spectra discussed above, and with the known photophysics of adenine (*i.e.* ultrafast decay with subsequent ergodic dissociation), [200-204] and thus again indicates that the adenine moiety is largely unaffected across the $[AXP-nH]^{n-}$ series.

Table 3.4 compares the photofragment mass spectra observed following photoexcitation at 5.6 eV with the ionic fragments produced upon HCD at 36% collision energy. The propensity for production of lower mass fragments (*e.g.* PO_3^- and $H_2PO_4^-$) can be seen to increase, as both the laser excitation energy and the collision excitation energy increase. As for the 4.9 eV photoexcitation data presented above, similar fragmentation patterns are observed for both laser excitation and collisional excitation, indicating that a largely ergodic dissociation process is also occurring at higher energy, along with the additional multiply charged anion photofragment pathways.

Table 3.4 Photofragments observed following photoexcitation at 5.6 eV and higher-energy collisional dissociation (HCD) fragments obtained at 36% collisional energy for the $[AXP-nH]^{n-}$ ($n = 1, 2$) anions.[a]

Parent ion	Photofragments[b]	HCD fragments[c]
$[AMP-H]^-$	$PO_3^- \approx H_2PO_4^-$, $[A-H]^-$	PO_3^-, $H_2PO_4^-$, $[A-H]^-$
$[ADP-H]^-$	$[A-H]^-$, $HP_2O_6^-$, $[ADP-H-A-H_2O]^-$, PO_3^-	$HP_2O_6^-$, $[A-H]^-$, $[ADP-H-A-H_2O]^-$, PO_3^-
$[ATP-H]^-$	$HP_2O_6^-$, $[cADP]^-$, $H_3P_2O_7^-$, $[ADP-H-A-H_2O]^-$	$HP_2O_6^-$, $[cADP]^-$, $[ADP-H]^-$, $[ADP-H-A-H_2O]^-$, $H_3P_2O_7^-$
$[ADP-2H]^{2-}$	$[cADP]^- \approx H_3P_2O_7^-$, $[A-H]^-$, PO_3^-, $H_2PO_4^-$ $[ADP-2H]^-$	PO_3^-, $[A-H]^-$, $H_2PO_4^-$
$[ATP-2H]^{2-}$	$HP_2O_6^-$, $H_4P_3O_{10}^-$, $[ATP-2H]^-$, $[ATP-2H-A]^-$, PO_3^-, $[ADP-H]^- \approx H_3P_2O_7^- \approx [cAMP-H]^-$	PO_3^-, $HP_2O_6^-$, $[A-H]^-$, $[cAMP-H]^-$, $[ADP-H]^-$

[a] Photofragments and HCD fragments are listed in order of decreasing intensity
[b] At 5.6 eV
[c] At 36 % HCD Energy.

3.4.4 Photofragment Action Spectra
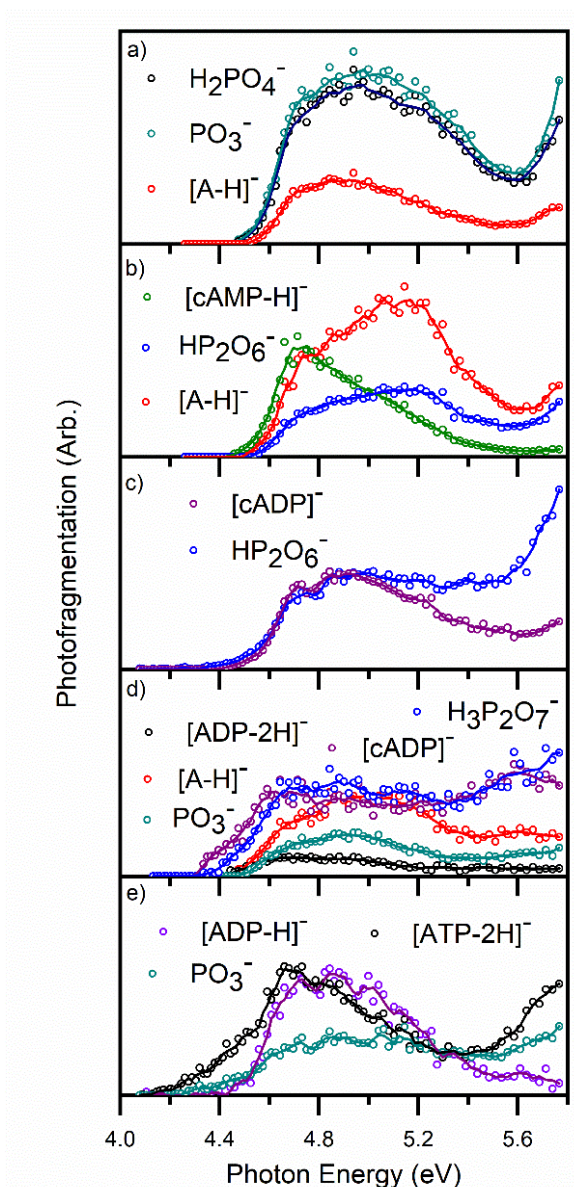
Figure 3.6 Photofragment action spectra of the major photofragments produced following photoexcitation of mass-selected a) [AMP-H]$^-$, b) [ADP-H]$^-$, c) [ATP-H]$^-$, d) [ADP-2H]$^{2-}$, and e) [ATP-2H]$^{2-}$, across the range 4.07-5.77 eV. The solid lines are five-point adjacent averages of the data points.

Figure 3.6 displays the photofragment action spectra (4.0-5.8 eV) for production of some photofragments of the [AXP-nH]$^{n-}$ anions. For the [AMP-H]$^-$ anion (Figure 3.6a), the major photofragments PO$_3^-$ and H$_2$PO$_4^-$ are produced smoothly through the main photodepletion band ($\lambda_{max} \sim 5.0$ eV), and then increase strongly in intensity towards the high-energy tail of the spectrum. The [A-H]$^-$ anion displays a similar profile,

although production of this photofragment peaks slightly lower in energy (~ 4.85 eV) and increases less strongly towards the high-energy limit. This difference in the band shapes for production of the [A-H]$^-$ photofragment compared to the PO$_3^-$ and H$_2$PO$_4^-$ pair of photofragments explains the shape of the overall photodepletion spectrum (Figure 3.1a), where a step is visible at ~4.85 eV associated with production of the [A-H]$^-$ photofragment peaking at this excitation energy.

Figure 3.6b displays the photofragment action spectra for [ADP-H]$^-$. This set of photofragment action spectra show the advantage of recording the photofragment action spectra, compared to just the photodepletion spectrum (Figure 3.1b) since they clearly reveal that two distinct fragmentation processes occur across the spectral region investigated. Production of the [cAMP-H]$^-$ photofragment peaks strongly at 4.7 eV, dropping to zero above 5.6 eV, while the [A-H]$^-$ photofragment peaks close to 5.25 eV, probably due to the [cAMP-H]$^-$ fragmenting into [A-H]$^-$ with maximum cross section around this energy.

The distinctive profile of the [cAMP-H]$^-$ photofragment between 4.7-5.6 eV closely mirrors the production of this ion at only a limited range of HCD energies (Figure 3.4b) and is strong evidence that this photofragment is produced through a statistical decay process. The HP$_2$O$_6^-$ photofragment appears to be produced concurrent with both of the [cAMP-H]$^-$ and [A-H]$^-$ photofragments.

HP$_2$O$_6^-$ and [cADP]$^-$ are observed as the major photofragments for the [ATP-H]$^-$ monoanion (Figure 3.6c). Both photofragments are produced with identical profiles across the 4.0-5.0 eV region, although the [cADP]$^-$ fragment is produced much less strongly than the HP$_2$O$_6^-$ fragment above 5.0 eV. This behaviour again mirrors the HCD results for this anion (Figure 3.4c), with production of HP$_2$O$_6^-$ increasing towards

high collision energy, while the intensity of the $[cADP]^-$ fragment tails off, again

probably due to the $[cADP]^-$ fragmenting into $HP_2O_6^-$.

Figure 3.6d displays the photofragment action spectra for the fragments produced

from the $[ADP-2H]^{2-}$ dianion. These spectra show similar profiles, although the PO_3^-

fragment and the $H_3P_2O_7^-$ both show an increasing production profile towards high

energy. The $H_3P_2O_7^-$ and $[cADP]^-$ fragments also display a similar profile, with an onset

around 4.3 eV and a maximum close to the maximum of the electron detachment

fragment $[ADP-2H]^-$. It is intriguing that the $[ATP-2H]^-$ electron detachment fragment

is produced so strongly through the 4.4-5.2 eV region in Figure 3.6e, since this energy

is considerably below the expected electron detachment threshold (Section 3.4.1). It

appears that the excited state accessed in this region is able to couple efficiently to

an electron detachment coordinate that circumvents the repulsive Coulomb barrier.

This phenomenon is not unique to the $[ATP-2H]^{2-}$ dianion, since in a recent

photoelectron spectroscopy study of $Pt(CN)_4^{2-}\cdot$nucleobase clusters, delayed electron

detachment signals were observed when the adenine cluster was irradiated at 266

nm (4.66 eV). This appeared to be due to excitation of long-lived adenine-centred

excited states that can effectively couple to the electron detachment continuum. [176]

To summarise, the $[AXP-nH]^{n-}$ anions produce a range of different photofragments

across the 4.0-5.8 eV range. In general, production of the smaller fragment ions, *e.g.*

$H_2PO_4^-$, PO_3^- and $HP_2O_6^-$, increases towards the high-energy region of the spectrum,

and the overall patterns for production of photofragments as a function of excitation

energy mirror those observed using higher-energy collisional excitation. The energy

redistribution process involved in ergodic dissociation following fast internal

conversion back to the ground state may not exactly match the energy transfer (and

subsequent energy redistribution) that occurs upon higher-energy collision induced

dissociation. However, the close relationship between photofragments and collisional

fragments observed here, strongly indicates that the $[AXP\text{-}n\text{H}]^{n-}$ anions do undergo rapid conversion back to the electronic ground state following photoexcitation, as would be expected for a system with a largely adenine-centred chromophore.

3.4.5 Time-Dependent Density Functional Theory Calculations

To gain further insight into the nature of the electronic excitations involved in photoexcitation of the $[AXP\text{-}n\text{H}]^{n-}$ anions across the 4-6 eV range, time-dependent density functional theory (TDDFT) calculations were performed. Full details of these calculations, along with the full results are presented in Section 3.7.3. The TDDFT calculations were able to accurately predict the general form of the photodepletion spectra, with each anion displaying a broad absorption between 4.4-5.6 eV, followed by an increasing absorption profile to high photon energy. In general, the main electronic transitions originated from orbitals with electron density on both the adenine and the phosphate group(s), indicating extensive orbital mixing across the molecular framework. The dominant transition in the region of the maximum (~ 5.0 eV) of the 4.4-5.6 eV absorption band was found to be associated with the expected $\pi\text{-}\pi^*$ transition on adenine. $n\text{-}\pi^*$ and $\pi\text{-}\sigma^*$ transitions are also common, particularly in the high-energy excitation regions. It is important to underline that orbital mixing is fundamental to explain excited state dissociations, as it can comport depletion of electron density in a bonding orbital. An example is a transition at 5.8 eV in $[ADP\text{-}2\text{H}]^{2-}$ where the ground state electron density includes σ contribution from the C-N glycosidic bond.

Comparing the calculated spectra and the component electronic excitations for pairs of anions with the same molecular framework but different excess negative charges (*e.g.* $[ATP\text{-}2\text{H}]^-$ *versus* $[ATP\text{-}2\text{H}]^{2-}$), indicates that there is little change in the excitation energies or extinction coefficients of the main electronic excitations with variation in excess charge. For the adenine-centred chromophoric molecules studied here, we

therefore conclude that there is no substantial bathochromic shift associated with negative charges existing in close proximity to the nucleobase. [177]

3.5 Further Discussion

Nielsen *et al.* studied the photodestruction of [AMP-H]$^-$ at 266 nm (4.66 eV), [204] and found that the excited state lifetime was 16 μs, with the major part of photofragmentation occurring by an ergodic (statistical) process. During this type of process, the molecule statistically redistributes the energy on the ground electronic surface *via* intramolecular vibrational relaxation that follows internal conversion. [174] The photofragment identities associated with excited state decay could not be identified in that experiment due to instrumental limitations. However, the set of photofragments of [AMP-H]$^-$ observed in the current study (*i.e.* PO_3^-, $H_2PO_4^-$ and [A-H]$^-$) with 4.9 eV excitation are consistent with photofragmentation occurring *via* an ergodic process since the photofragments are almost identical to the major HCD fragments observed with a similar collisional excitation energy.

The ultrafast dynamics of adenine following 4.66 eV photoexcitation was also investigated by Verlet and co-workers *via* time-resolved photoelectron imaging of the deprotonated 3'-deoxy-adenosine-5'monophosphate nucleotide, and its di- and trinucleotides. [66] [206] These experiments revealed that the dynamics of the base are relatively insensitive to the surrounding environment, and led to the conclusion that the decay mechanism primarily involves internal conversion from the initially populated $^1\pi$-π^* states to the ground states.

These results again mirror the results found in this study, across the 4.4-5.2 eV absorption band. In another related work, Weber and co-workers studied the photodissociation spectroscopy of a series of deprotonated nucleotides, including deprotonated 2'-deoxy-adenosine-5'-monophosphate. [205] Their results are again

largely consistent with a photodecay mechanism that involves rapid electronic relaxation followed by unimolecular fragmentation on the vibrationally hot ground-state surface.

The results presented herein complement these earlier results, since they demonstrate how the ATP anions appear to share much of the photophysical properties that were observed previously. Photoexcitation across the 4.0-5.8 eV region appears to largely follow the expected adenine-centred excitation followed by rapid relaxation *via* a conical intersection and subsequent ground-state statistical decay. The TDDFT calculations provide a picture of electronic excitations that contain significant adenine-centred π-π^* character, but are delocalised across the entire molecular framework, possibly facilitating statistical decay. One interesting point of note in comparing the ATP experiments conducted with the deoxy-nucleotides studied by Verlet and Weber is that the presence of two OH groups on the ribose in the ATP analogues, means that the anions are able to maintain a hydrogen-bond network across the molecular ion (see Section 3.7.1 for calculated geometric structures). Such molecular structures have recently been identified to facilitate ultrafast decay mechanisms, [202] and appear likely to be a key factor in the overall photostability of ATP.

It is interesting to consider the results of the current work in the context of the photodetachment study of the tryptophan anion conducted by Compagnon and co-workers. [177] They found *via* experiment and TDDFT calculations that the tryptophan chromophore was sensitive to the presence of the excess negative charge in the anion, resulting in substantial bathochromism of the main electronic excitations of up to 25 nm. No such dramatic shift is observed here on going from the monanionic to dianionic species, either experimentally or in the TDDFT calculations. It seems possible that this differing behaviour can be traced to the very different geometric

arrangements of the chromophores and excess charges in the tryptophan anion compared to the [AXP-nH]$^{n-}$ anions. Alternatively, it may be that the electronic excitations of the adenine chromophore studied here are particularly insensitive to environmental changes, [66] [207] including excess charge. Nonetheless, the considerable differences in bathochromism between deprotonated tryptophan and ATP are notable. Further investigation of a broader range of molecular anions where excess charge is located at a distance from a chromophore are desirable to clarify the generality of excess-charge induced electronic transition shifts.

3.6. Concluding Remarks

The photofragmentation measurements conducted on the [AXP-nH]$^{n-}$ series of anions indicate that the decay dynamics are consistent with photoexcitation of a largely adenine centred chromophore that undergoes ultrafast decay following photoexcitation. Both the photodepletion spectra and photofragmentation patterns indicate that the adenine moiety within the ATP anions appears to be unaffected by the charge state of the molecular system. This is an important result for clarifying the interpretation of recent experiments that have been conducted on anion-nucleobase clusters such as I$^-$·uracil and Pt(CN)$_4^{2-}$·adenine. [176] [212] In further work, it would be interesting to directly monitor the inferred decay dynamics by probing the production of the various photofragments *via* ultrafast spectroscopy. Time-resolved photodetachment photoelectron spectroscopy provides a facile approach to such measurements, [223] and could be readily applied to the system studied here.

3.7 Supplemental Information

3.7.1. Computational Results for the [AXP-nH]$^{n-}$ (X = M, D, T and n = 1, 2) Anions.

The [AXP-nH]$^{n-}$ (X = M, D, T and n = 1, 2) series of anions represent a challenging series of systems to study computationally due to their considerable conformational

and tautomeric flexibility. The dianions, [ADP-2H]$^{2-}$ and [ATP-2H]$^{2-}$ have however been the subject of two previous computational studies, [214] [218] and so the global minima structures identified there were used as a basis for the calculations performed here.

Density functional theory (DFT) was used to calculate vertical excitation energies (VDEs). Calculations were performed at the M06-2X/6-311++G** level as implemented in Gaussian 09, after a first, explorative, calculation at the M06-2X/6-31G* level. [188] [195] [224-226] The starting point geometry for optimising the structure of [ATP-2H]$^{2-}$ followed the structure reported by Schinle *et al.*, [218] where the αβ$_1$ tautomer (with negative charges on the α and β phosphate groups) was identified as the lowest energy tautomer. The reoptimised structure obtained using M06-2X/6-311++G** closely resembled the structure of Schinle *et al.* [218]A proton was added to the optimised M06-2X/6-311++G** [ATP-2H]$^{2-}$ structure, as a starting point for optimising the [ATP-H]$^-$ anion structure. The possible different tautomeric structures were explored, with the global minimum being found to correspond to the tautomer with the negative charge on the β phosphate group. Next. a phosphate group was removed from the M06-2X/6-311++G** optimised [ATP-2H]$^{2-}$ structure to obtain a starting point for the [ADP-2H]$^{2-}$ M06-2X/6-311++G** calculation, and then an [ADP-H]$^-$ optimised structure was obtained following the method described above to obtain the [ATP-H]$^-$ structure. For [AMP-H]$^-$, a phosphate group was again removed from the [ADP-H]$^-$ M06-2X/6-311++G** optimised structure, to obtain a starting point for the [AMP-H]$^-$ calculation. All reported structures (Figure 3.7) correspond to true minima as confirmed by frequency calculations. Vertical Detachment Energies (VDEs) were then calculated using these optimised structures.

We emphasise that, while there may be some uncertainty that the [AXP-nH]$^{n-}$ anion conformations that we have used here conform to the global minima conformers,

minor conformational changes should not have a major effect on the VDEs we have calculated.

[AMP-H]⁻   [ADP-H]⁻   [ATP-H]⁻

[ADP-2H]²⁻   [ATP-2H]²⁻
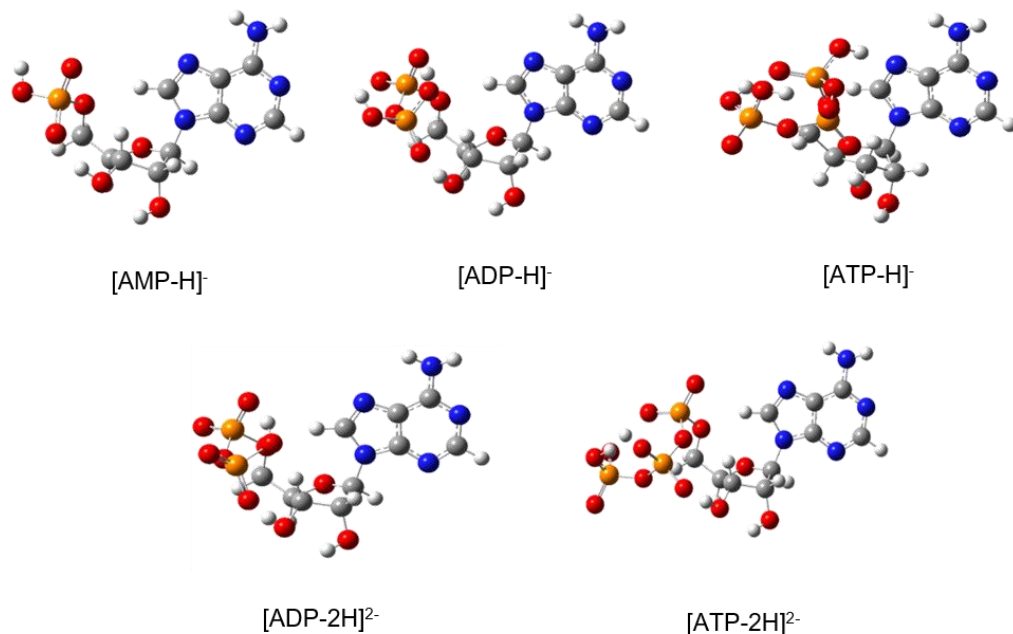
Figure 3.7 M06-2X/6-311++G** optimised structures of $[AXP-nH]^{n-}$ (X = M, D, T and n = 1, 2) used for VDEs calculations shown in Table 3.1.

Table 3.5 Deprotonated phosphates in $[AXP-nH]^{n-}$ (X = M, D, T and n = 1, 2) series of anions. The data refer to the optimised structures shown in Figure 3.7.

Ion	Phosphate carrying the charge [a]
[AMP-H]⁻	α
[ADP-H]⁻	α
[ATP-H]⁻	β
[ADP-2H]²⁻	αβ
[ATP-2H]²⁻	αβ

[a] The phosphates are indicated with Greek letters that proceed in alphabetical order as they move further from the adenosine moiety.

3.7.2. Photofragment Mass Spectra at 4.7 and 5.6 eV of the $[AXP-nH]^{n-}$ (X = M, D, T and n = 1, 2) Anions.

Figure 3.8 displays the photofragment mass spectra obtained for photoexcitation of the [AXP-nH]$^{n-}$ anions at 4.7 eV at the beginning of the main absorption band in the photodepletion spectra (Figure 3.1). The ionic photofragments observed at 4.7 eV photoexcitation are very similar to the photofragmentation mass spectra obtained at 4.9 eV, close to the top of the main absorption band (Figure 3.5).
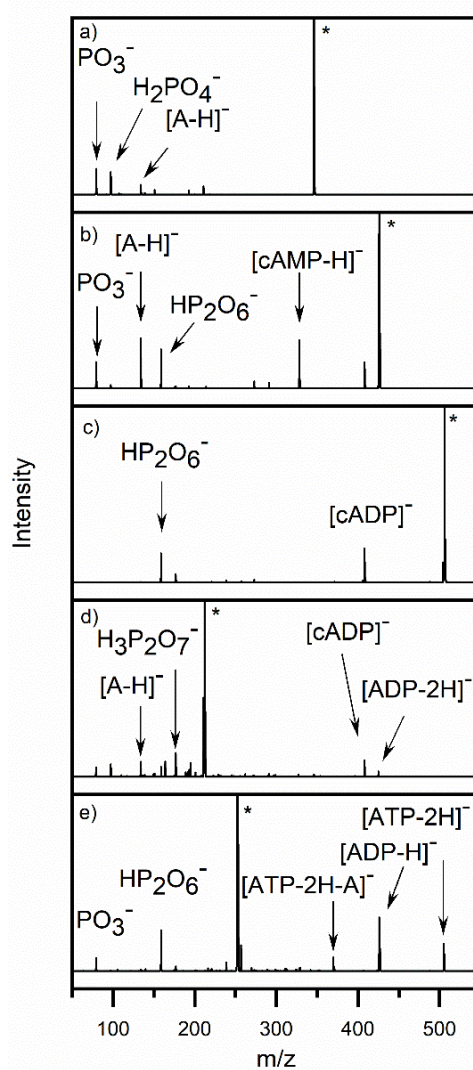
Figure 3.8 Photofragment mass spectra of a) [AMP-H]$^-$, b) [ADP-H]$^-$, c) [ATP-H]$^-$, d) [ADP-2H]$^{2-}$, and e) [ATP-2H]$^{2-}$ excited at 4.7 eV. * indicates the depleted parent ion signal.

The photofragmentation mass spectra obtained for photoexcitation of the [AXP-nH]$^{n-}$ anions at 5.6 eV are shown in Figure 3.9. These spectra illustrate formation of the electron detachment photofragments (*e.g.* [ADP-2H]$^-$ from [ADP-2H]$^{2-}$, and [ATP-2H]$^-$

from [ATP-2H]$^{2-}$) at high fragmentation energy, along with reduced production of the
larger molecular photofragments (*e.g.* [ADP-H]$^-$ from [ATP-2H]$^{2-}$).
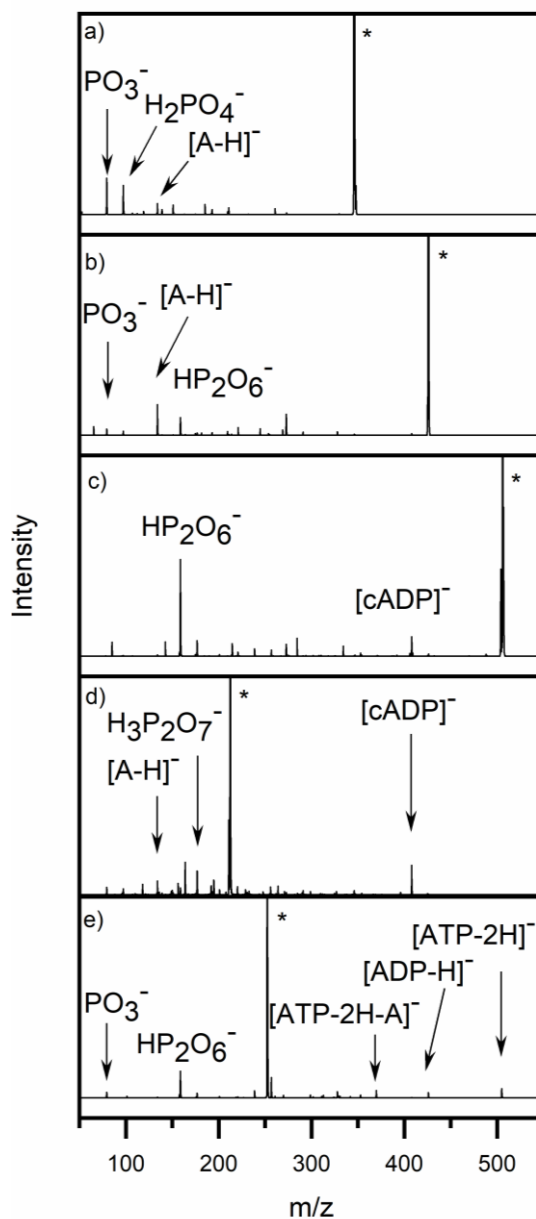
Figure 3.9 Photofragment mass spectra of a) [AMP-H]$^-$, b) [ADP-H]$^-$, c) [ATP-H]$^-$, d)
[ADP-2H]$^{2-}$, and e) [ATP-2H]$^{2-}$ excited at 5.6 eV. * indicates the depleted parent ion
signal.

3.7.3 TDDFT Excitation Spectra of [AXP-Nh]$^{n-}$ (X = M, D, T and n = 1, 2) Series of Anions.

Time-dependent density functional theory (TDDFT) was used to predict the excitation
spectra of all the five studied anions. Both M06-2X and B3LYP were explored with 6-

311++G** basis set to predict the excitation spectra of the different anionic species. In this section, we present B3LYP/6-311++G** TDDFT calculation compared to experimental results. [189] Tables 3.5,3.6,3.97,3.8 and 3.9 show the oscillator strengths for the main transitions. In the tables the nature of the orbitals involved in these transitions and the percentage contributions to the single transition (calculated from Gaussian coefficients as the double of the square multiplied by 100) are also described.

The three monoanionic species, $[AXP-nH]^{n-}$ (X = M, D, T), present four main transitions in the region between 4 and 6 eV. For these transitions, the excited state is an adenine orbital (π^* or diffused orbitals). The ground state represents the main difference between the three species. In some cases, sigma orbitals on the adenine are also predicted to contribute to the ground state.

3.7.3.i [AMP-H]⁻

Figure 3.10 shows a comparison between the PD and the calculated spectra of [AMP-H]⁻. As shown in Table 3.6, the four main transitions originate from orbitals with electron density on both adenine and phosphate group.
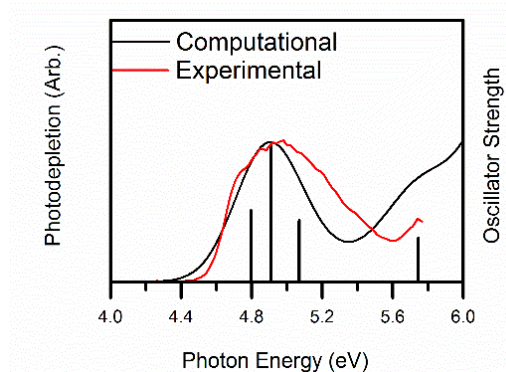
Figure 3.10 B3LYP/6-311++G** calculated excitation energies of [AMP-H]⁻. The oscillator strengths of the strongest transitions are given by the vertical bars. The full black line spectrum represents a convolution of the calculated spectrum with a Gaussian function (0.20 eV HWHM). The red line is the PD spectrum obtained as five-

point adjacent average of the data points. The calculated spectrum is redshifted by 0.1 eV to better fit the experimental spectrum.

Table 3.6 Transition energies and oscillator strengths of [AMP-H]$^-$ from TDDFT calculation with B3LYP functional. The calculated energies are redshifted of 0.1 eV to better fit the experimental spectrum. Only the main transitions (and the HOMO-LUMO) are shown.

Transition energy eV	Involved Orbitals	Nature of the transition	Oscillator strength
4.51	90→91	99 % n→π*	0.0002
4.80	89→91	54 % π→π*	0.0654
4.91	88→91	36 % π→π*	0.125
	83→91	19 % π→π* [a]	
5.07	88→93	43 % π→π*	0.0562
5.74	78→91	40 % π→π* [b]	0.0402
	86→92	23 % n→σ* [c]	

[a] Ground state electron density includes σ contribution from the 5'C-C bond.
[b] Main contribution to the ground state from adenosine moiety.
[c] Ground state electron density mainly on phosphate and sugar.
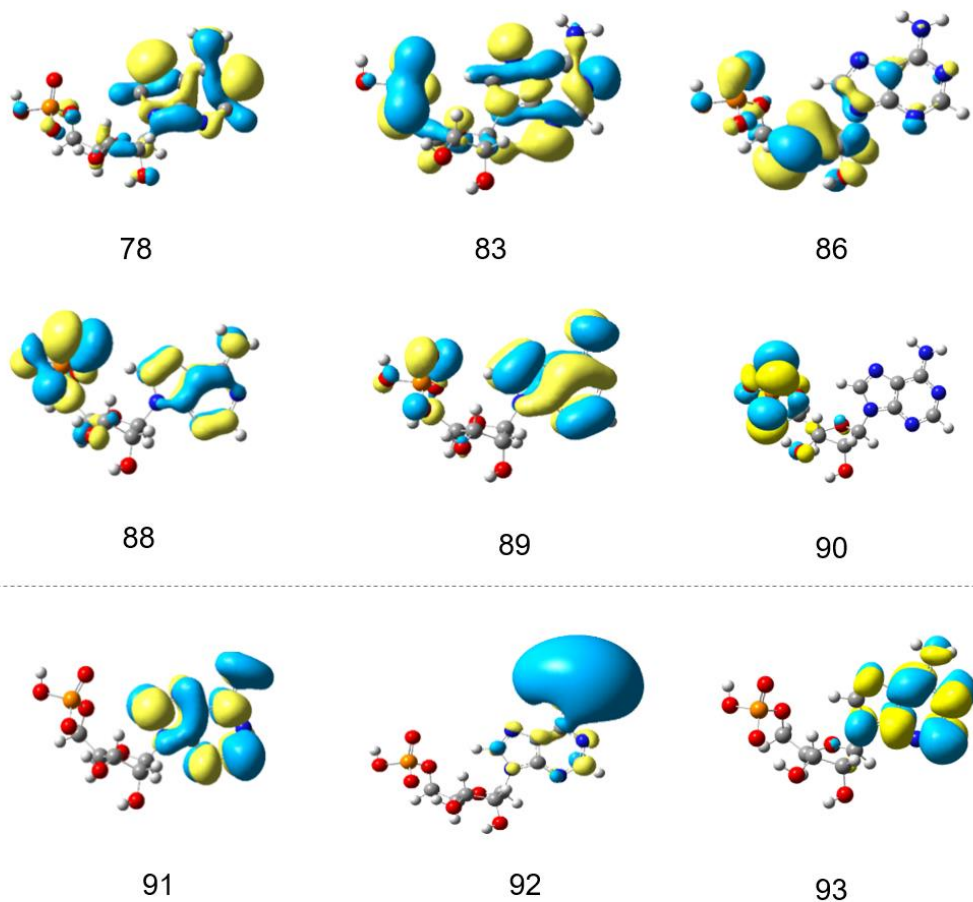
Figure 3.11 B3LYP/6-311++G** calculated MOs involved in the most intense electronic transitions of [AMP-H]⁻ between 4 eV and 6 eV, as described in Table 3.6.Separation between occupied and unoccupied orbitals is shown.

3.7.3.ii [ADP-H]⁻

Figure 3.12 shows a comparison between the PD and the calculated spectra of [ADP-H]⁻. The four most intense transitions predicted by TDDFT for [ADP-H]⁻ show ground states with electron density mainly on the adenine moiety. The nature of the orbitals on the adenine is shown in Table 3.7.
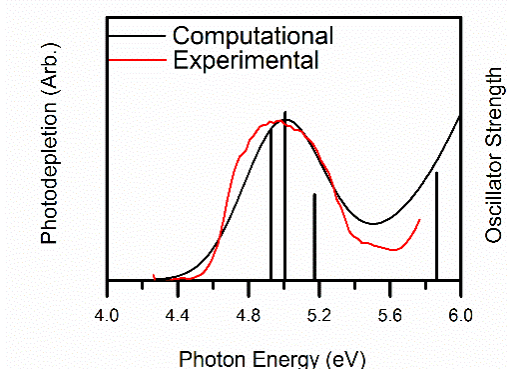
Figure 3.12 B3LYP/6-311++G** calculated excitation energies of [ADP-H]⁻. The oscillator strengths of the strongest transitions are given by the vertical bars. The full black line spectrum represents a convolution of the calculated spectrum with a Gaussian function (0.20 eV HWHM). The red line is the PD spectrum obtained as five-point adjacent average of the data points.

Table 3.7 Transition energies and oscillator strengths of [ADP-H]⁻ from TDDFT calculation with B3LYP functional. Only the main transitions are shown.

Transition energy eV	Involved Orbitals	Nature of the transition	Oscillator Strength
4.93	110→111	49 % π→π*	0.103
	110→112	26 % π→ σ*	
5.01	110→111	31 % π→π*	0.115
	110→112	30 % π→ σ*	
	106→111	24 % π→π* [a]	
5.17	110→111	57 % π→π*	0.0586
	104→111		
5.86	105→112	34 % π→ σ * [a]	0.0736
	106→112	30 % π→ σ* [a]	
	105→111	18 % π→π* [a]	

[a] Ground state electron density on the adenosine moiety.
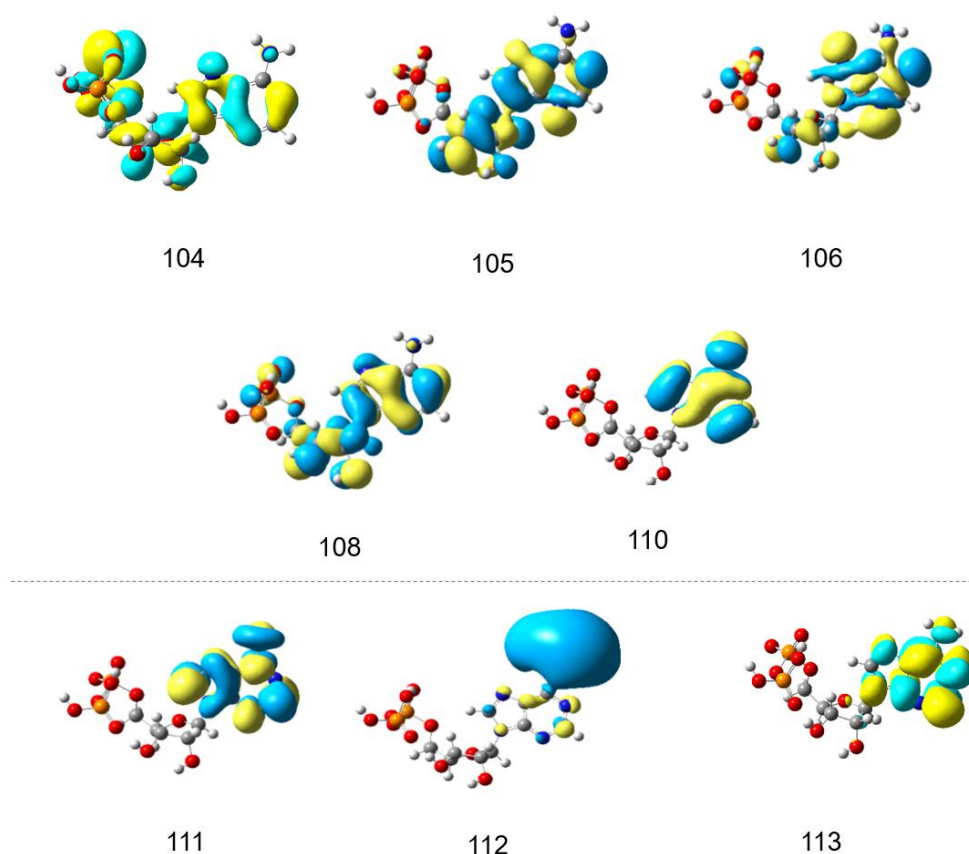
Figure 3.13 B3LYP/6-311++G** calculated MOs involved in the most intense electronic transitions of [ADP-H]⁻ between 4 eV and 6 eV, as described in Table 3.7 Separation between occupied and unoccupied orbitals is shown.

3.7.3.iii [ATP-H]⁻

Calculations on [ATP-H]⁻ are presented in Figure 3.14. The first three main transitions involve ground state orbitals on the adenine moiety. The ground state in the fourth transition has contributes from orbitals which electron density is extended to the sugar and to the phosphate chain. In Table 3.8 the nature of the adenine orbital is described.
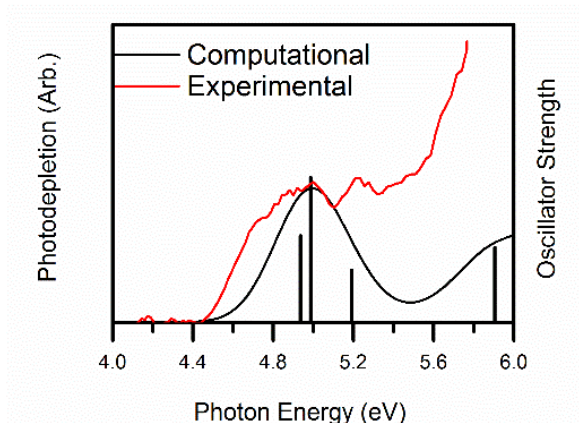
Figure 3.14 B3LYP/6-311++G** calculated excitation energies of [ATP-H]⁻. The oscillator strengths of the strongest transitions are given by the vertical bars. The full black line spectrum represents a convolution of the calculated spectrum with a Gaussian function (0.20 eV HWHM). The red line is the PD spectrum obtained as five-point adjacent average of the data points.

Table 3.8 Transition energies and oscillator strengths of [ATP-H]⁻ from TDDFT calculation with B3LYP functional. Only the main transitions are shown.

Transition energy eV	Involved Orbitals	Nature of the transition	Oscillator Strength
4.94	128→131	44 % π →π* [a]	0.0873
	130→131	34 % π→π*	
4.99	130→131	49 % π→π *	0.146
5.19	130→133	59 % π→π*	0.0525
5.91	123→131	18 % π→π* [a,b]	0.0756
	127→131	17 % n→π* [c]	
	124→131	13 % π→π* [c]	
	119→131	11 % π→π* [c]	

[a] Ground state electron density on the whole molecule.
[b] Ground state electron density includes σ contribution from the 5'C-C bond.
[c] Ground state electron density on sugar and phosphate chain.
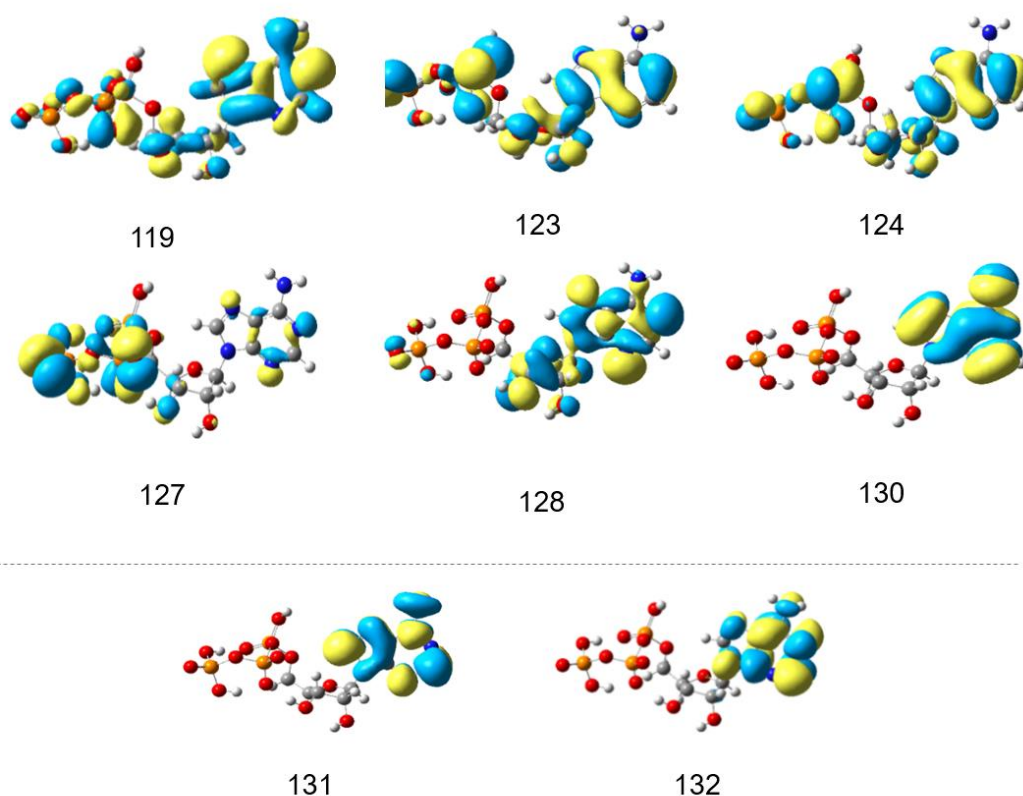
Figure 3.15 B3LYP/6-311++G** calculated MOs involved in the most intense electronic transitions of [ATP-H]$^-$ between 4 eV and 6 eV, as described in Table 3.8. Separation between occupied and unoccupied orbitals is shown.

3.7.3.iv [ADP-2H]$^{2-}$

Calculations with B3LYP show that also [ADP-2H]$^{2-}$ excitation spectra can be described with four main transitions (Figure 3.16), oscillator strength being smaller than for the monoanionic species described above (Section 3.7.3.ii). The excited state is again localised on the adenine. Charge transfer from the phosphate chain to the adenine is the main contribution to the transitions at 5.06 eV and 5.74 eV. Table 3.9 shows the transitions and the nature of the involved orbitals.
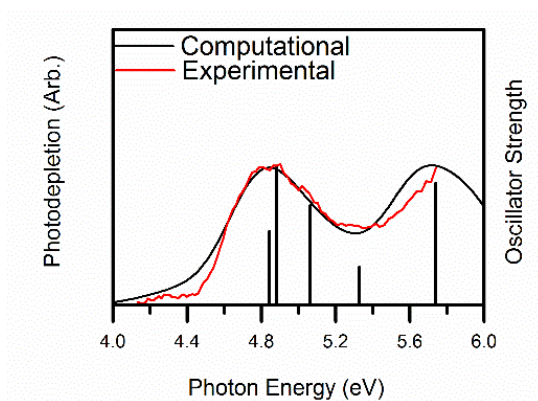
Figure 3.16 B3LYP/6-311++G** calculated excitation energies of [ADP-2H]$^{2-}$. The oscillator strengths of the strongest transitions are given by the vertical bars. The full black line spectrum represents a convolution of the calculated spectrum with a Gaussian function (0.20 eV HWHM). The red line is the PD spectrum obtained as five-point adjacent average of the data points. The calculated spectrum is redshifted by 0.1 eV to better fit the experimental spectrum.

Table 3.9 Transition energies and oscillator strengths of $[ADP-2H]^{2-}$ from TDDFT calculation with B3LYP functional. The values are redshifted of 0.1 eV to better fit the experimental spectrum. Only the main transitions and the HOMO-LUMO are shown.

Transition energy eV	Involved Orbitals	Nature of the transition	Oscillator Strength
4.44	110→111	61 % n→σ* [a]	0.0047
	105→112	n→π* [b]	
4.84	101→112	29 % π→π*	0.0399
4.88	101→112	29 % π→π* [b]	0.075
	95→112	26 % π→π* [c]	
5.06	105→114	55 % n→π* [a]	0.0542
	100→111	20 % n→σ* [a,d]	
5.74	100→114	53 % n→π* [a,d]	0.0661
	98→114	22 % n→π* [a,e]	

[a] Ground state electron density on sugar and phosphate chain.
[b] Ground state electron density on the adenosine moiety.
[c] Ground state electron density includes σ contribution from the 5'C-C bond.
[d] Ground state electron density includes σ contribution from the C-O (phosphate) bond.
[e] Ground state electron density includes σ contribution from the C-N glycosidic bond.
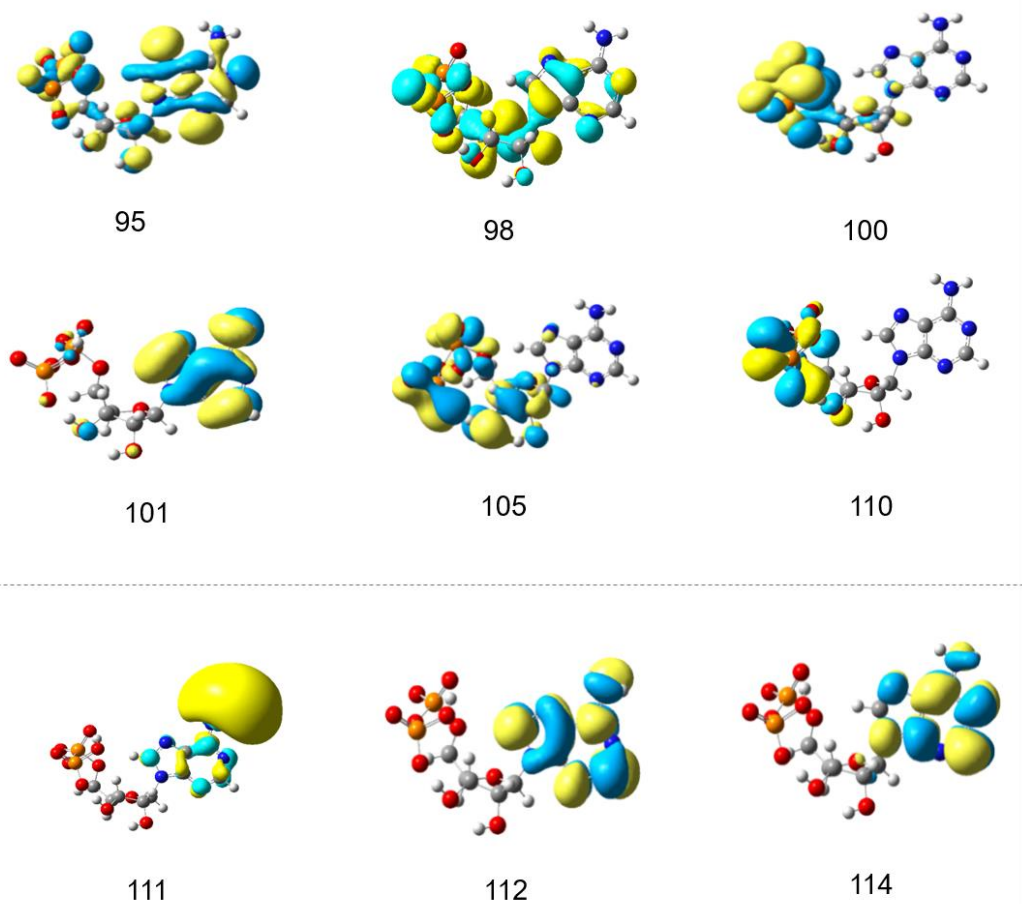
Figure 3.17 B3LYP/6-311++G** calculated MOs involved in the most intense electronic transitions of [ADP-H]$^{2-}$ between 4 eV and 6 eV, as described in Table 3.9. Separation between occupied and unoccupied orbitals is shown.

3.7.3.v [ATP-2H]$^{2-}$

Figure 3.18 shows a comparison between the PD and the calculated spectra of [ATP-H]$^{2-}$. Weaker transitions are predicted for [ATP-2H]$^{2-}$. The excited state orbitals of the transitions are once again on the adenine moiety. However, the ground states show major contributions from electron density on the sugar and the phosphate chain. Table 3.13 presents the transitions and the nature of the involved orbitals. Unless stated otherwise, the transitions originate from orbitals with electron density on the whole molecule.
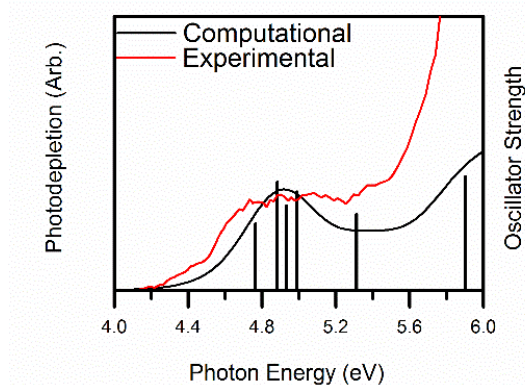
Figure 3.18 B3LYP/6-311++G** calculated excitation energies of [ATP-2H]^{2}. The oscillator strengths of the strongest transitions are given by the vertical bars. The full black line spectrum represents a convolution of the calculated spectrum with a Gaussian function (0.2 eV HWHM). The red line is the PD spectrum of [ATP-2H]$^{2-}$ obtained as five-point adjacent average of the data points. The calculated spectrum is redshifted by 0.1 eV to better fit the experimental spectrum.

Table 3.10 Transition energies and oscillator strengths of [ATP-2H]$^{2-}$ from TDDFT calculation with B3LYP functional. The values are redshifted of 0.1 eV to better fit the experimental spectrum. Only the main transitions and the HOMO-LUMO are shown.

Transition energy eV	Involved Orbitals	Nature of the transition	Oscillator Strength
3.99	130→131	78 % n→σ* [a]	0.0003
4.77	125→132	29 % π→ π*	0.0365
	126→131	19 % n→σ* [a,b]	
	125→131	17 % π→σ*	
4.88	117→132	39 % π→π* [c]	0.0594
	117→131	17 % π→ σ *	
4.93	123→131	42 % n→σ* [a]	0.0464
	123→132	18 % n→π*	
	124→131	14 % π→σ*	
4.99	123→131	15 % n→π* [a]	0.0539
	121→131	13 % n→π* [a]	
	123→131	12 % π→π *	
	124→132	8 % π→ π*	
5.31	120→131	27 % n→σ* [a]	0.0417
	121→132	23 % n→π* [a]	
5.90	114→132	45 % π→ π*	0.0623
	117→133	10 % π→σ*	

[a] Ground state orbital does not involve the adenine moiety.
[b] Ground state electron density includes σ contribution from the 5'C-C bond.
[c] Ground state orbital localised on the adenine.
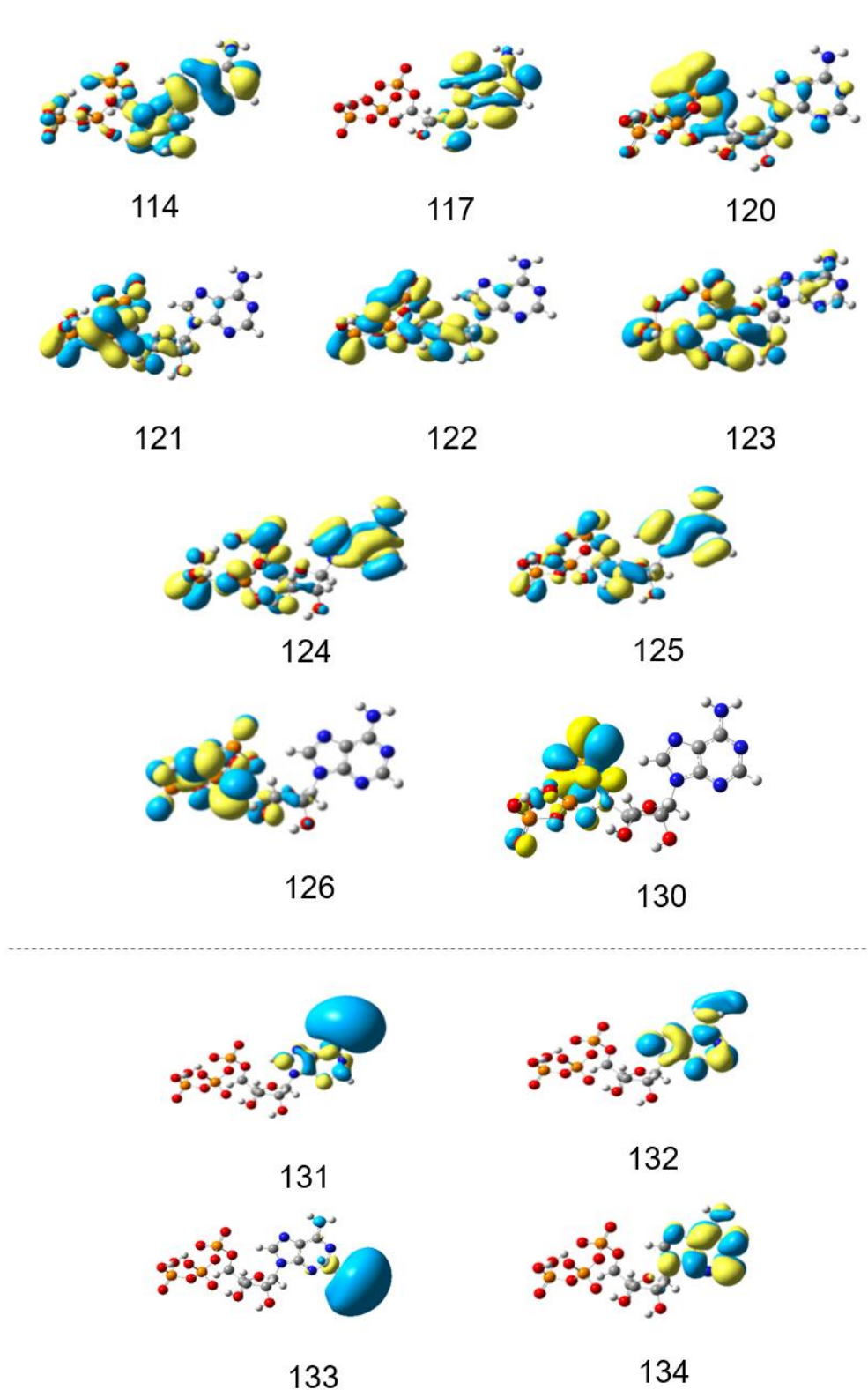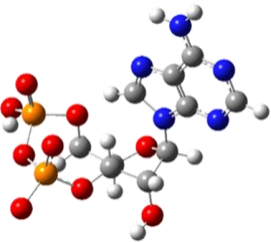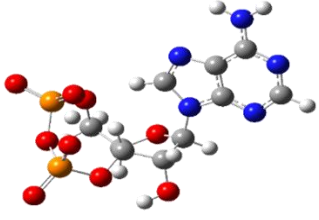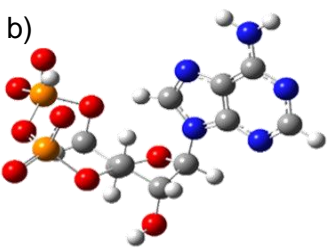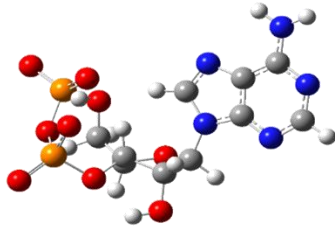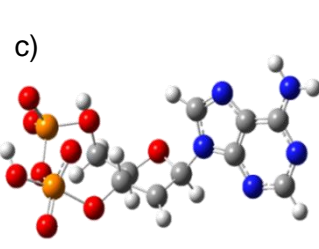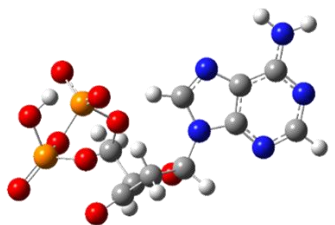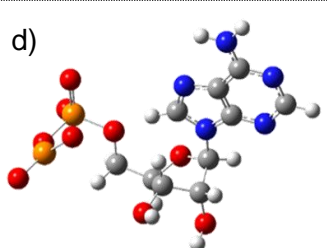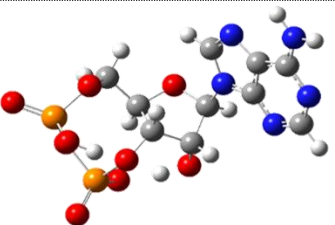
Figure 3.19 B3LYP/6-311++G** calculated MOs involved in the most intense electronic transitions of [ATP-H]$^{2-}$ between 4 eV and 6 eV, as described in Table 3.10. Separation between occupied and unoccupied orbitals is shown.

3.7.4 DFT calculations of [ADP-H-H2O]⁻ supporting the hypothesis of cyclization

Preliminary calculations *via* M06-2X/3-21G support the cyclization hypothesis of [ADP-H-H$_2$O]⁻. The calculations were done starting from the [ADP-H]⁻ lower energy structure and eliminating two hydrogens and an oxygen from different positions, forcing the cyclization in the structures a, b and c. The last structure, d, although not forced into a cycle, cyclizes. Relative energies are also presented.

Table 3.11 M06-2X/3-21G calculated structure of [ADP-H -H2O]⁻. Input structures and relative energies are also shown.

	Input structure	Output structure	Relative energy [a] kJ/mol
a)			0
b)			0
c)			52.2
d)			42.9

[a] Non zero-point energy corrected

Chapter 4

Near-Threshold Electron Transfer in Anion-Nucleobase Clusters: Does the Identity of the Anion Matter?

4.1 Abstract

Laser dissociation spectroscopy of I$^-$·adenine (I$^-$·A) and H$_2$PO$_3^-$·adenine (H$_2$PO$_3^-$·A) has been utilised for the first time to explore how the anion identity impacts on the excited states. Despite strong photodepletion, ionic photofragmentation is weak for both clusters, revealing that they decay predominantly by electron detachment. The spectra of I$^-$·A display a prominent dipole-bound excited state in the region of the detachment energy, which relaxes to produce deprotonated adenine. In contrast, near-threshold photoexcitation of H$_2$PO$_3^-$·A does not access a dipole-bound state, but instead displays photofragmentation properties associated with ultrafast decay of an adenine-localised π-π^* transition. Notably, the experimental electron detachment onset of H$_2$PO$_3^-$·A is around 4.7 eV, which is substantially lower than the expected detachment energy of an ion-dipole complex. The low value for H$_2$PO$_3^-$·A can be traced to initial ionization of the adenine followed by significant geometric rearrangement on the neutral surface. We conclude that these dynamics quench access to a dipole-bound excited state for H$_2$PO$_3^-$·A and subsequent electron transfer. H$_2$PO$_3^-$·A represents an important new example of an ionic cluster where ionization occurs from the neutral cluster component and where photodetachment initiates intra-molecular hydrogen atom transfer.

4.2 Introduction

Low-energy electron attachment to DNA is a biologically important process, which can result in single- and double-strand cleavage, and also lead to the breakdown of individual nucleobases. [18] [227-233] Such low-energy electrons are produced when

either ionising radiation or high-energy particles pass through biological matter and can hence trigger mutagenic changes. [234] [235] Due to the importance of low-energy electron-DNA interactions, a wide number of studies have been carried out to better understand the key molecular-level processes involved. Through this range of theoretical and experimental studies it has been found that both dissociative σ^* phosphate orbitals and unoccupied low-lying π^* orbitals of the nucleobases can be involved in preliminary electron capture prior to the secondary process which involves transient negative ion formation. [232] [233]

Gas-phase iodide ion-nucleobase clusters have been used in a number of recent experimental studies, to probe low-energy electron-nucleobase coupling in a highly controlled environment. [71] [212] [236-238] In such experiments, the iodide ion is photodetached to produce a 'spectator' iodine atom and a low-energy free electron with a well-defined kinetic energy that can be captured by an adjacent molecule. [239-241] The resulting dynamics of the temporary negative ion can then be monitored either *via* time-resolved photoelectron spectroscopy or photofragment action spectroscopy. [71] [212] [236-241]

We have recently investigated the role played in these experiments by the spectator iodine in a dynamical study of the iodide-uracil complex (I⁻·U). [212] Photoexcitation was found to produce I⁻ photofragments as well as deprotonated uracil, i.e. (U-H)⁻, as a minor photofragmentation channel. Electron production from decay of a transient negative ion was also observed. The production spectra for both photofragment ions displayed two peaks centred at ~ 4.0 and ~ 4.8 eV, with the lower-energy band being assigned to a dipole-bound excited state of the complex, while the higher-energy band was primarily assigned to excitation of a π-π^* transition localised on the uracil. Crucially, although excited states are quite distinctive in nature, the time-resolved photoelectron imaging (TRPEI) measurements indicated that across both bands, the

I$^-$ ion was being produced *via* internal conversion of the initially formed excited states back to the I$^-$·U electronic ground state followed by I$^-$ evaporation. [212]

In this work, we aim to further investigate the role played by the iodide ion in electron transfer excitations of these clusters, by directly comparing the laser-induced photodissociation behaviour of I$^-$·adenine (I$^-$·A) with $H_2PO_3^-$·adenine ($H_2PO_3^-$·A), *via* laser excitation across the region around and above the electron detachment threshold. The I$^-$·A cluster has been investigated by Neumark and co-workers previously *via* TRPEI, [72] although any ionic photofragments that accompany near-threshold photoexcitation were not characterised in that study. Thus, the current work is the first investigation to probe directly the I$^-$·A photofragment channels.

In the TRPEI study of I$^-$·A, [72] two adenine isomers were observed in the clusters: the biologically relevant A9 isomer and the A3 isomer. Adenine is well-known to exist in fourteen stable isomers, with the amine forms A9, A7 and A3 being lower in energy than the enamine/imine forms. [242] The A9 isomer is computed to be the lowest energy isomer in the gas phase, while the A7 isomer is stabilised in polar solvents and in polar clusters due to its large dipole moment. [242] A dipole-bound anion of the A9 tautomer has been observed *via* Rydberg electron transfer, with an associated electron affinity of +12 meV. [243] However, the dipole-bound anions of the A7 and A3 tautomers have not been observed to date, despite having larger dipole moments than A9. [244] From a number of experimental and theoretical studies, the valence bound A9 anion is thought to be adiabatically unstable. Indeed, theoretical calculations by Raczynska *et al*. suggest that only the A3 isomer forms a stable valence anion. [245] Scheme 4.1 illustrates the structures of the key A9, A7, and A3 isomers.

Adenine 9H
2.65 D

Adenine 7H
6.77 D
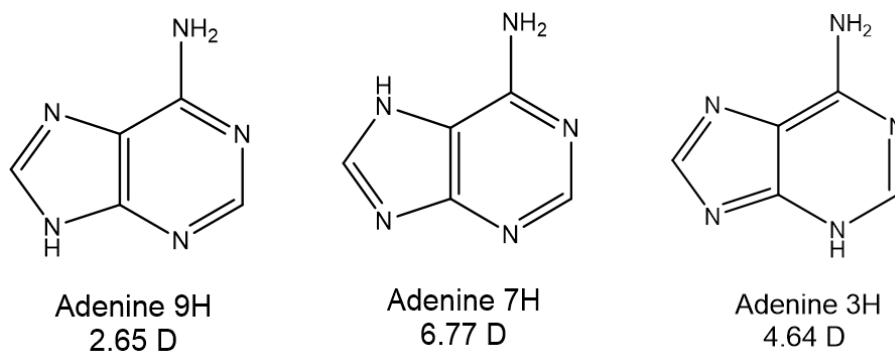
Adenine 3H
4.64 D

Scheme 4.1 Structures of the A9, A7 and A3 amine tautomers of adenine. Left: adenine amine-9H (A9), centre: adenine amine-7H (A7) and right: adenine amine-3H (A3). Calculated dipole moments of the tautomers are also shown. [242]

4.3 Methods

All chemicals were purchased from Sigma Aldrich and used without further purification. The clusters were generated by electrospraying a solution of adenine (1 × 10^{-4} mol dm^{-3}) mixed with droplets of t-butyl ammonium iodide (1 × 10^{-2} mol dm^{-3}) or with a NaH$_2$PO$_3$ solution in deionised water (1 × 10^{-4} mol dm^{-3}).

Geometry optimization and vertical detachment energies (VDEs) were obtained *via* DFT. Cluster structures of the X$^-$ ions coordinated to known adenine isomers were optimised at the B3LYP/6-311++G(2d,2p) level of theory on C, N, O, and H, and 6-311G(d,p) on I, with the iodine core electrons being described using the Stuttgart/Dresden (SDD) electron core pseudopotential. MP2 and M06-2X level calculations were performed to calculate the dipole moments and the spin densities, respectively. Cluster binding energies were calculated using the counterpoise correction method. Electronic excitations were calculated at the B3LYP/6-311++G(2d,2p) method with SDD on iodide. Further details are given in Sections 4.7.2 and 4.7.4.

4.4 Results

4.4.1 Geometric Structures of X⁻·A Clusters

| $H_2PO_3^-·A7$ | $H_2PO_3^-·A9$ |

| $I^-·A7$ | $I^-·A9$ |
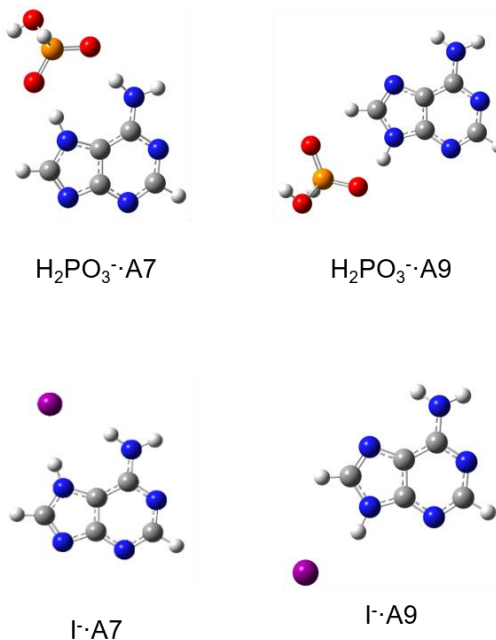
Figure 4.1 Lowest-energy calculated structures of the X⁻·A clusters. See text for details.

Figure 4.1 shows the two lowest-energy calculated structures of the X⁻·A (X⁻ = I⁻ and $H_2PO_3^-$) clusters, with Table 4.1 listing the corresponding relative energies and other properties. In the $H_2PO_3^-$·A structures, the dihydrogen phosphite anion forms a bifurcated hydrogen bond across NH and CH groups. Similar structures have been observed using IR spectroscopy for NO_3^- and HCO_3^- in their clusters with water. [246] For the I⁻·A structures, the iodide ion is again involved in two hydrogen bonds to adenine, although in the I⁻·A9 structure, one of these hydrogen bonds is close to a typical linear geometry.

In the $H_2PO_3^-$·A7 complex, the iodide ion is bound along the axis of the permanent electric dipole moment of A7. It is notable that the A7 dipole moment is higher than that of A9 so that in these dominantly ion-dipole complexes, [242] the A7 tautomer is

present in the lowest-energy cluster, with the biologically active tautomer cluster, A9, being found at relatively higher energy. The binding energies of both X^-·A7 clusters are significantly higher than those of the X^-·A9 clusters, reflecting their ion-dipole nature. From the calculated room-temperature Boltzmann population (Table 4.1), we expect the A7 isomer clusters to be dominant in our electrosprayed ions. The A9 isomer will not be visible in the experimental spectra, as it is expected to be four orders of magnitude less populated than the A7 isomer cluster.

Table 4.1 Properties of the X^-·A clusters calculated at the B3LYP/6-311++G(2d,2p) theory level, with 6-311G(d,p)/SDD for I^-.

Cluster	Relative Energy kJ mol^{-1}	Boltzmann population[a] %	Calc. VDE eV	Exp. VDE[b] eV	Binding Energy kJ mol^{-1}
I^-·A7	0.0	99.9	4.34		134
I^-·A9	20.8	2.27×10^{-2}	4.08	3.96	82.3
I^-·A3	42.1	4.21×10^{-6}	4.13	4.11	63
$H_2PO_3^-$·A7	0.0	99.9	4.66		177
$H_2PO_3^-$·A9	25.6	3.27×10^{-3}	4.92		118
$H_2PO_3^-$·A3	44.4	1.66×10^{-6}	4.90		134

[a] Room temperature.
[b] Ref. [72].

Neumark and co-workers have measured the VDE values of the I^-·A9 and I^-·A3 clusters previously, and our calculated VDEs are in good agreement with these results. [72] Although they were also working in the gas-phase, their experiment uses an electron gun-molecular beam set-up to produce clusters, an approach that does not produce the I^-·A7 isomer.

The VDE values calculated here warrant further comment. For the iodide ion clusters, the calculated VDE is in line with a value for an anionic ion-dipole complex, which transfers to a neutral complex where the iodine atom interacts only very weakly with the adenine once the electron is removed. In such systems, the VDE of the cluster is effectively blue-shifted from the electron binding energy of the bare iodide ion by the cluster ion-molecule binding energy (~1 eV). [247] [248] However, this is not the case for the $H_2PO_3^-$ cluster. We calculate that bare $H_2PO_3^-$ has a VDE of 4.73 eV, so that the calculated VDEs of the $H_2PO_3^- \cdot A$ complexes are considerably lower than would be expected if a weakly-interacting neutral cluster results once the electron is removed. Wang and Kass have previously observed similar 'reduced electron binding energy' in hydrogen-bonded anion clusters. [249]

TDDFT spectra of the lowest-energy $X^- \cdot A7$ clusters have also been calculated and are shown in Figure 4.2. As we have discussed previously, [250] such calculations are not expected to accurately predict dipole-bound excited states since tailored, diffuse functionals are necessary to accurately mimic dipole-bound orbitals. [251-253] The TDDFT calculations predict a strong transition around 4.8 eV for both $X^- \cdot A7$ clusters, which is associated with a nucleobase-localised $\pi \rightarrow \pi^*$ excitation. The two spectra differ mainly in the number and the intensity of the predicted charge-transfer transitions, which arise from the n orbital on X^-. Intriguingly, these are far more numerous for the $I^- \cdot A7$ cluster. We note that similar charge-transfer transitions have recently been calculated by Mensa-Bonsu et al. to appear in the near-threshold region of the $I^- \cdot CF_3I$ complex. [254]
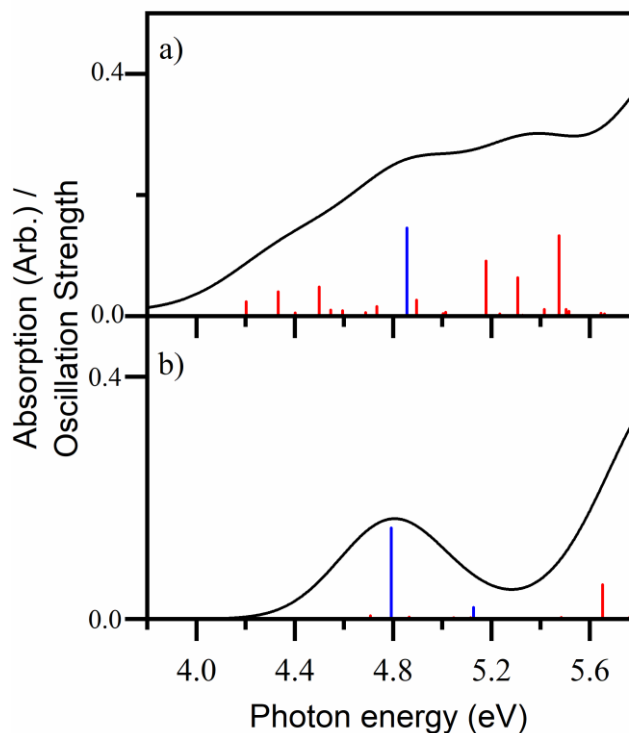
Figure 4.2 TDDFT calculated spectra (50 states) of a) I^-·A7 and b) $H_2PO_3^-$·A7. The oscillator strengths of the strongest transitions are given by the vertical bars. Blue lines are $\pi \rightarrow \pi^*$ transitions, the others are mainly $n \rightarrow \pi^*$. The full black line spectrum represents a convolution of the calculated spectrum with a Gaussian function (0.25 eV HWHM).

4.4.2 Photodepletion of the X⁻·A Clusters

Photodepletion spectra of the X⁻·A clusters across the range 3.8-5.7 eV are shown in Figure 4.3. These spectra correspond to gas-phase absorption in the limit where the excited states decay without fluorescence. [169] However, it is important to note that at energies above the VDEs, the spectra will reflect contributions from electron detachment, as well as intra-cluster electronic excitations.

Figure 4.3a displays the photodepletion spectrum for I^-·A, with a photodepletion onset at ~4.0 eV and two bands (**I** and **II**) with λ_{max} at ~ 4.4 and ~ 5.2 eV, respectively. Above band **I**, the absorption cross section is relatively flat before rising again towards the band **II** maximum, with a distinct shoulder visible below band **I** at ~ 4.2 eV. Beyond band **II**, the cross section rises sharply to high energies. Comparison of the spectral

profile of the I^-·A spectrum to those of similar clusters we have studied previously, [247] [255]suggests that the VDE of the I^-·A cluster present in our experiment is ~ 4.2 eV. Our calculated VDE for I^-·A7 is included on the spectrum shown in Fig. 4.3a.

The photodepletion spectrum of $H_2PO_3^-$·A is shown in Figure 4.3b, with an onset above ~ 4.3 eV leading up to a broad band with a maximum at 4.7 eV (labelled **I**). A shoulder is again visible below band **I** at ~ 4.4 eV. In contrast to I^-·A, the $H_2PO_3^-$·A spectrum decreases after band **I** until around 5.4 eV when it starts increasing to the high-energy spectral edge. The calculated VDE for $H_2PO_3^-$·A7 is again included on the spectrum shown in Figure 4.3b.
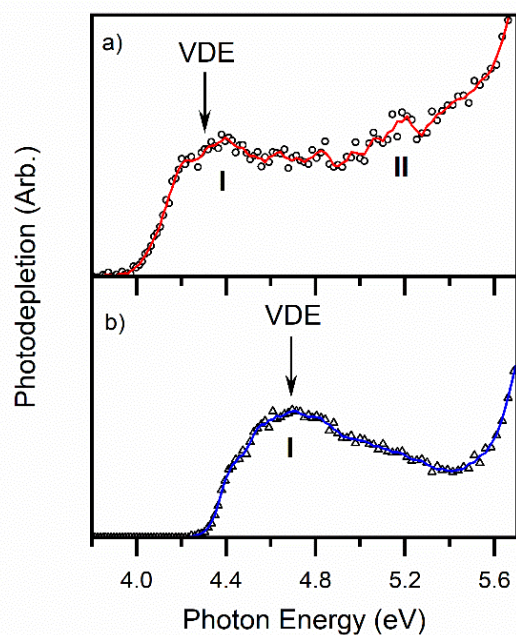
Figure 4.3 Photodepletion spectra of a) I^-·A and b) $H_2PO_3^-$·A. The lines are five-point adjacent average of the data points. Calculated VDEs for I^-·A7 and $H_2PO_3^-$·A7 are shown on the spectra. The data in a) were acquired by Edward Matthews.

4.4.3 Photofragmentation of the X^-·A Clusters

To further explore the nature of the excited states that are evident in the photodepletion spectra (Figure 4.3), the photofragment production spectra of the X^-·A clusters were investigated. Each cluster was found to produce both [A-H]$^-$ and X^- as photofragment ions. For I^-·A, the [A-H]$^-$ photofragment was produced approximately

ten times more strongly than the I$^-$ photofragment, while for $H_2PO_3^-$·A, both

photofragments were produced with similar intensities.
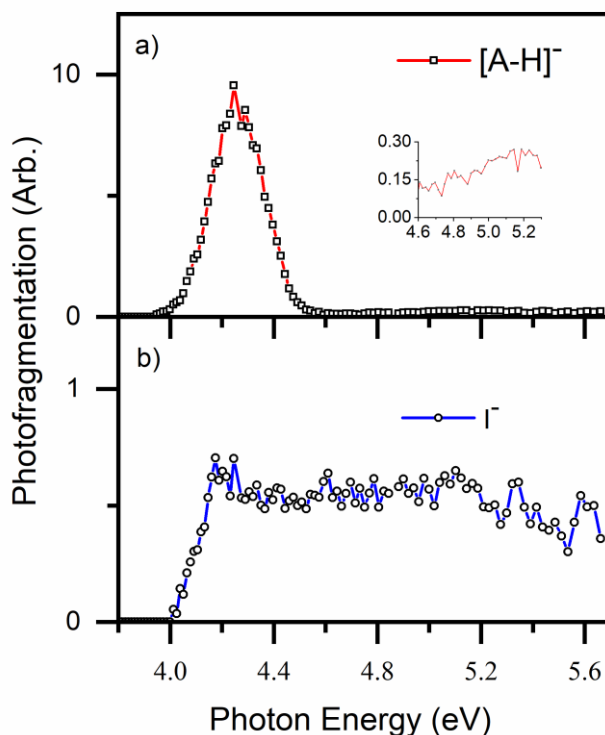
Figure 4.4 a) [A-H]$^-$ and b) I$^-$ photofragment action spectra produced from the I$^-$·A cluster. The insert in a) shows the expanded action spectrum of [A-H]$^-$ between 4.6 and 5.3 eV. The data were acquired by Edward Matthews.

The photofragment action spectra obtained from excitation of I$^-$·A are shown in Figure

4.4 and reveal that the [A-H]$^-$ and I$^-$ photofragments display dramatically different

production spectra. The more intense photofragment, [A-H]$^-$, is produced very strongly

over the lower-energy spectral region, peaking at ~ 4.2 eV within band **I** (Figure 4.3a).

We note that this energy is very close to the VDE calculated for I$^-$·A7 (4.34 eV). A

slight increase in [A-H]$^-$ production is also evident in the region leading up to 5.2 eV

(~2% the intensity of band **I**). For the I$^-$ photofragment, the product spectrum has an

onset at ~ 4.0 eV, with a small maximum at ~ 4.2 eV (close to the maximum of [A-H]$^-$

production) and a flat profile with a small enhancement in intensity at ~ 5.1 eV.

Figure 4.5 displays the photofragment action spectra of the primary $H_2PO_3^-$·A photofragments, $H_2PO_3^-$ and $[A-H]^-$ (this cluster also produces PO_3^- as a very minor photofragment, included in Figure 4.11). The production spectra of the $H_2PO_3^-$ and $[A-H]^-$ photofragments are again different from one another, with neither of these production spectra being similar to the photofragment spectra observed for I^-·A (Figure 4.4). The $[A-H]^-$ photofragment (Figure 4.5a) is produced across the whole region from 4.3 to 5.4 eV, with the photofragment intensity decreasing to the high-energy spectral edge. For the $H_2PO_3^-$ photofragment (Figure 4.5b), the production spectrum is also very broad, peaking between 4.8-5.2 eV. Above 5.2 eV, $H_2PO_3^-$ production decreases up to ~ 5.6 eV, but then starts increasing again.
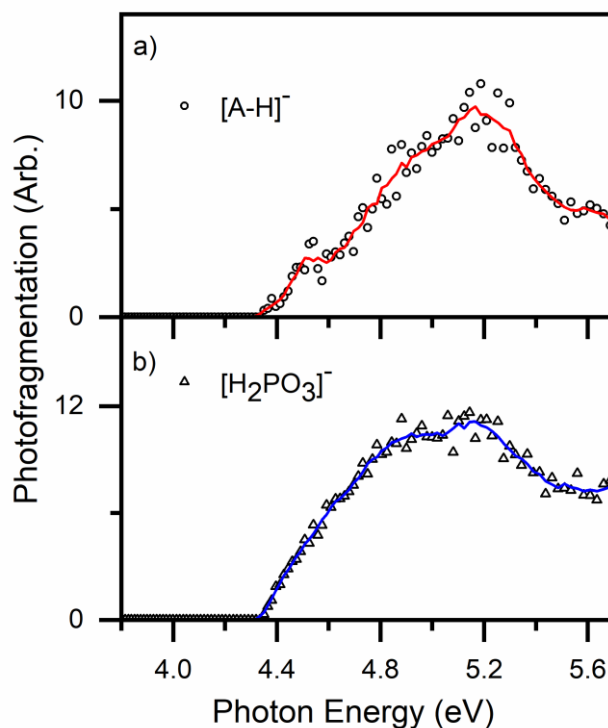
Figure 4.5 a) $[A-H]^-$ and b) $H_2PO_3^-$ photofragment action spectra produced from the $H_2PO_3^-$·A cluster. The lines are five-point adjacent average of the data points.

The distinctive photofragment profiles from I^-·A and $H_2PO_3^-$·A reveal that the decay pathways following photoexcitation are different for the two clusters. However, in both cases, it is notable that all of the photofragments are produced with very small

intensities, so that electron detachment represents the main photodepletion channel.

This is discussed further in Section 4.4.4.

4.4.4 Electron Detachment Yield Spectra of the $X^-·A$ Clusters

Figure 4.6 shows the electron detachment yields for the $X^-·A$ clusters overlaid with the

photodepletion yield (PD*) for comparison. It is notable that, for both $X^-·A$ clusters, the

electron detachment and the modified photodepletion spectra largely overlap, except

where ionic photofragmentation is maximised between 4.1-4.4 eV for $I^-·A$ (Figure 4.6a)

and 4.8-5.4 eV for $H_2PO_3^-·A$ (Figure 4.6b). Even in these regions, however, the

difference between electron detachment and photodepletion is small, indicating a high

yield of electron detachment.
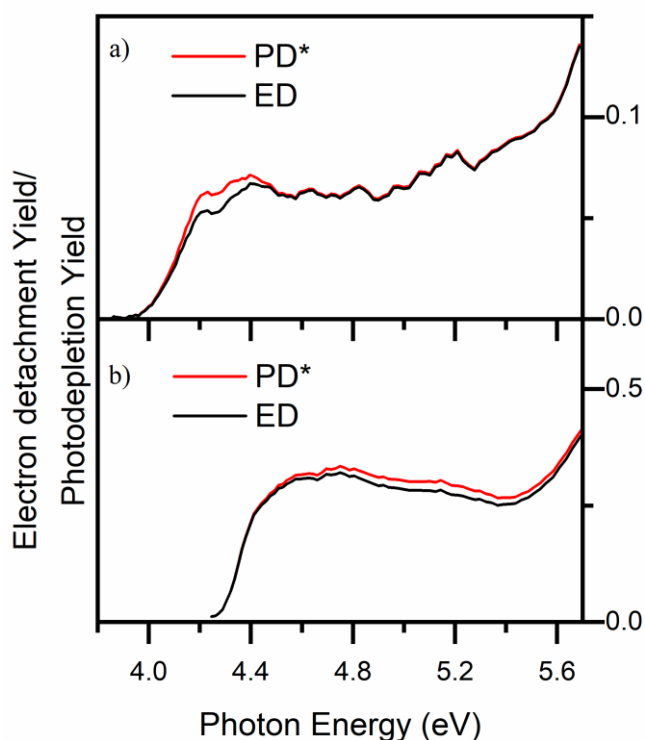
Figure 4.6 Photodepletion yield (PD*) and electron detachment yield (ED) of the $I^-·A$
a) and $H_2PO_3^-·A$ b) clusters. The curves are five-points adjacent averages of the data
points.

4.5 Discussion

4.5.1 Overview on Decay Channels

Before discussing the results in more detail, it is useful to consider the possible decay pathways for the $X^-\cdot A$ clusters. The first group of cluster decay channels result in fragmentation:

$$X^-\cdot A + h\nu \quad \rightarrow \quad X + A^- \tag{4.2a}$$

$$\rightarrow \quad X^- + A \tag{4.2b}$$

$$\rightarrow \quad HX + [A\text{-}H]^- \tag{4.2c}$$
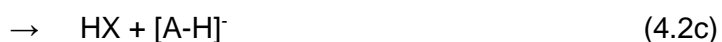
Alternatively, electron detachment can occur above the electron detachment threshold, either *via* direct detachment (4.3a) or indirectly from an excited state of the cluster (4.3b). Electron detachment can also occur from hot photofragments, *e.g.* (4.3c) and (4.3d):

$$X^-\cdot A \quad \rightarrow \quad X\cdot A + e^- \tag{4.3a}$$

$$\rightarrow \quad [X\cdot A]^{*-} \quad \rightarrow \quad [X\cdot A] + e^- \tag{4.3b}$$

$$\rightarrow \quad HX + [A\text{-}H]^{*-} \quad \rightarrow \quad HX + [A\text{-}H] + e^- \tag{4.3c}$$

$$\rightarrow \quad X + A^{*-} \quad \rightarrow \quad X + A + e^- \tag{4.3d}$$
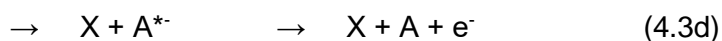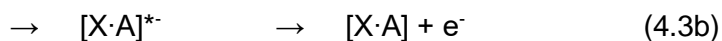
The ionic fragmentation products observed following photoexcitation of the $X^-\cdot A$ clusters are produced with very low intensities (Section 4.4.3), in line with pathways (4.3a)-(4.3d) dominating the cluster decay.

An additional possibility has been suggested by Wang and Kass, [249] where electron detachment leads to the transfer of hydrogen, either as a hydrogen atom or as a proton, on the neutral surface. For the $X^-\cdot A$ clusters studied here:

Hydrogen atom transfer:

$$X^- \cdot A + h\nu \quad \rightarrow \quad e^- + X \cdot A \quad \rightarrow \quad XH \cdot [A\text{-}H] \qquad (4.4a)$$

Proton transfer:

$$X^- \cdot A + h\nu \quad \rightarrow \quad e^- + [X^- \cdot A^+] \quad \rightarrow \quad XH \cdot [A\text{-}H] \qquad (4.4b)$$

4.5.2 Assignment of the Excited States of the X⁻·A Clusters

Band **I** in the photodepletion spectrum of I⁻·A (Figure 4.3a) peaks at 4.4 eV with a partially resolved shoulder evident at 4.17 eV. The VDE of the I⁻·A9 form of the cluster was measured as 3.96 eV by Neumark and co-workers, [72] and they also observed a dipole-bound (DB) state for this tautomer slightly below the VDE. The absence of any depletion of I⁻·A below 4 eV in this work indicates that the I⁻·A9 tautomer is not present in the electrospray-generated ion ensemble in our experiment, as predicted by our calculated relative energies (Table 4.1). Indeed, our calculations indicate that the dominant cluster tautomer that should be present in our experiment is I⁻·A7, which is predicted to have a VDE of 4.34 eV. This calculated value is close to the band **I** maximum, strongly indicating that a dipole-bound excited state of I⁻·A7 is being accessed in this region. We have previously shown that dipole-bound excited states can be observed in our instrument following near-threshold anion excitation. [250] [255] [256] The identity of the shoulder peak at 4.17 eV resembles similar structures present in the near-threshold photodepletion spectra of anionic alkali halide clusters (*e.g.* I⁻·NaI), [255] which were assigned to excitation of the vibrational envelope in the dipole-bound excited state of the cluster.

At higher energies, an enhancement on the flat photodepletion region is evident at ~5.2 eV, labelled **II** on Figure 4.4a. This photodepletion enhancement is also evident in the I⁻ action spectrum (Figure 4.4b). Indeed, if we focus on the I⁻ action spectrum,

band **I** appears clearly at ~4.2 eV with band **II** at ~5.2 eV, leading us to assign these features to the two spin-orbit states of the neutral cluster ($^2P_{1/2}$ and $^2P_{3/2}$, respectively), which are separated by 0.94 eV for iodine. [239] [247]Band **II** in the photofragmentation spectrum is therefore assigned as arising from direct detachment from the dipole-bound excited state built on the upper ($^2P_{1/2}$) spin-orbit state of I. [241] [257]

The TDDFT calculations for I$^-$·A7 predict a $\pi \rightarrow \pi^*$ transition at 4.9 eV, centred on the adenine moiety, with numerous charge-transfer transitions occurring across the spectral range. No distinct band around this energy is visible in either the photodepletion spectrum of I$^-$·A7 or its photofragmentation action spectra, presumably due to the relative strength of electron detachment, which represents the predominant contribute to the cluster's depletion. Some of the calculated $\pi \rightarrow \pi^*$ transitions are coupled to $n \rightarrow \sigma^*$ transitions (at 4.86 and 4.90 eV), reflecting similar results to the related I$^-$·C. [250]

For $H_2PO_3^-$·A, the photodepletion spectrum again displays an onset in the region close to the calculated VDE of the cluster. The strong absorption close to 4.8 eV corresponds to the well-known $\pi \rightarrow \pi^*$ transition on adenine moiety, [258] which appears prominently in the TDDFT calculated spectrum. Above 5.4 eV, photodepletion and production of $(H_2PO_3)^-$ begin to increase strongly, correlating with excitation of the $\pi \rightarrow \sigma^*$ transition (5.65 eV) predicted by the TDDFT calculation in this region (see Section 4.7.2).

4.5.3 Photofragment Production

The production of ionic photofragments from anions clustering with neutral nucleobase can usually be explained *via* two main mechanisms: an electron transfer from the anion (either through the formation of a dipole-bound excited state, followed

by the emission of a low-energy electron that interacts with the nucleobase, or a direct electron transfer to a valence orbital of the nucleobase) or from a transition localised on the nucleobase moiety. [212]

From the first type of process, we expect the production of the adenine, A^- (4.2a), or the deprotonated adenine anion $[A-H]^-$ (4.2c). In contrast, the adenine-centred transitions within the cluster are expected to produce the fragments that are associated with thermal fragmentation of the ground-electronic state, [259] following ultrafast decay of the initially populated nucleobase-localised electronic excited state. To identify the fragments that are produced upon thermal dissociation of the cluster ground electronic states, higher-energy collisional dissociation (HCD) of the $X^- \cdot A$ clusters was performed (see Section 4.7.1 for further details). [258] HCD over a wide collisional energy range revealed that $I^- \cdot A$ produces I^- as the only ionic fragment, whilst $H_2PO_3^- \cdot A$ produces both $H_2PO_3^-$ and $[A-H]^-$. The HCD profiles of these fragments are distinctive, with the $H_2PO_3^-$ being produced with a steeper onset from 0-12%, but with a decreasing intensity above 20%, while the $[A-H]^-$ fragment production profile increases only modestly across the collisional range from 4-45%. It is notable that the relative intensity of $[A-H]^-$ compared to $H_2PO_3^-$ is greater in the photodissociation experiment than in HCD.

The production of the $[A-H]^-$ photofragment from $I^- \cdot A$ in the region of the VDE is consistent with excitation to a dipole-bound excited state that facilitates capture of the excess electron into the valence orbitals of adenine, with subsequent ejection of a hydrogen atom and $[A-H]^-$. The production channel for $[A-H]^-$ drops very sharply at energies above the VDE due to autodetachment from the valence anion at higher internal energies. [240] [247] Production of I^- would be expected in the region of the adenine localised π-π^* transition, but instead it is observed weakly across the whole above-threshold region. This is a phenomenon that we have seen previously, since I^-

·U also produced an I$^-$ photofragment across a wide excitation range. [212] We attributed this behaviour to internal conversion to the ground electronic state followed by evaporation of I$^-$, possibly mediated by the weak charge transfer excitations that were predicted to occur across the spectral range. The behaviour of I$^-$·A seen here appears very similar, with the caveat that the [A-H]$^-$ fragment is produced relatively more strongly across the region close to the VDE. This indicates that the dissociative electron attachment cross section is significantly greater for adenine than for the other nucleobases within these clusters, i.e. within the neutral I$^-$A cluster, which is formed upon electron detachment. (We note that little attention has been paid in electron attachment experiments to the nature of the nucleobase tautomers present, [260] [261] and this may mean that results for the isolated nucleobases are not directly comparable to the clusters studied here).

For $H_2PO_3^-$·A (Figure 4.5a), all the thermal ground state fragments (see Sections 4.7.1 and 4.7.3) are produced as photofragments following cluster excitation across the entire spectral range. By comparison to I$^-$·A and also, I$^-$·U, this suggests that the excited states of the $H_2PO_3^-$·A cluster are able to ultimately decay across a wide spectral range *via* internal conversion to a hot ground state. It is notable that the shape of the photofragment production profiles (Figure 4.5) mirrors the production profiles of the corresponding HCD fragments (Figure 4.8a), with $H_2PO_3^-$ being produced relatively more strongly at the lower and higher collision energies than [A-H]$^-$. This similarity between the HCD fragment profiles and photofragment production profiles is indicative of cluster relaxation *via* ultrafast internal conversion and ground state thermal fragmentation. Ionic fragmentation of $H_2PO_3^-$·A is therefore largely associated with relaxation of electronic excitations localised on the adenine moiety.

Finally, it is useful to reflect on the relationship between photofragmentation and electron detachment that is revealed by the spectra presented in Figure 4.6. For I$^-$·A,

the biggest difference between photodepletion and electron detachment (*i.e.* the region where the most ionic fragments are produced) occurs close to the VDE, characteristic of the presence of a dipole-bound state, whereas for $H_2PO_3^-$·A, the region where the most ionic photofragments are produced occurs through a region centred at 5.2 eV, close to where the adenine-localised $\pi \rightarrow \pi^*$ transition is predicted to occur by the TDDFT calculations.

4.6 Further Discussion

Comparing the photophysics of the I^-·A cluster with our recent results on I^-·pyrimidine clusters, [250] two main differences are apparent. Firstly, the relative abundances of the two characteristic photofragments produced by these clusters (*i.e.* I^- and $[M-H]^-$) are inverted with respect to the I^-·pyrimidine clusters that were studied previously. [250] This phenomenon reflects the relative dissociative electron attachment properties of adenine versus uracil within the two clusters, i.e. in I·A versus I·U. Secondly, in I^-·A, no significant enhancement in $[A-H]^-$ production is observed in the region of the adenine $\pi \rightarrow \pi^*$ transition, in contrast to I^-·U and I^-·T. I^-·A mirrors the behaviour of I^-·C, where it was attributed to a relatively weaker $\pi \rightarrow \pi^*$ transition around 4.8 eV for cytosine compared to uracil and thymine. [250]

The photodepletion spectrum of $H_2PO_3^-$·A closely resembles those of gaseous deprotonated ATP, ADP, and AMP anions presented in Chapter 3. In the photodissociation study of this series of related bioanions, it was concluded that the adenine photochemistry was independent of the excess charge of the system or the length of the phosphate chain present. In a related series of experiments on the 3′-deoxy-adenosine-5′monophosphate nucleotide, and its di- and trinucleotides, Verlet and co-workers showed that the adenine dynamics are similarly insensitive to the surrounding environment, with excitation of the prominent $\pi \rightarrow \pi^*$ state and subsequent relaxation back to the ground state dominating the photodynamics. [206]

It is very notable that the photofragment production profile that we observe for [A-H]$^-$ in the region between 4.4 and 5.4 eV closely resembles the one observed following photoexcitation of [ADP-H]$^-$ (including the small sub-peak in [A-H]$^-$ production in the region between 4.4 and 4.6 eV close to the VDE). This strongly suggests that the chromophores and excited state morphology are similar in the two systems and dominated by the adenine moiety.

There are two possible explanations for the differences in the photophysics of the anion-adenine clusters observed here, linked to the fact that a near-threshold dipole-bound excited state dominates the photophysics of the I$^-$·A cluster, while such a state appears entirely absent for $H_2PO_3^-$·A. At the simplest level, the absence of a dipole-bound excited state for $H_2PO_3^-$·A could be traced to the nature of the anion-centred excess electron density of $H_2PO_3^-$·A compared to that in I$^-$·A. The more delocalised electron density on $H_2PO_3^-$·A will have a poorer Franck Condon overlap with a potential dipole-bound excited state, thus reducing the transition intensity. However, if this were the only effect, we might still expect to see a relatively weak dipole-bound state in the region of the electron detachment energy for $H_2PO_3^-$·A.

It is more convincing that the difference in photophysics displayed by I$^-$·A and $H_2PO_3^-$·A is linked to the reduced electron binding energy of $H_2PO_3^-$·A noted in Section 4.4.1. This lower electron binding energy is associated with hydrogen motion within the complex after electron detachment (Equations 4.4a and 4.4b). In this case, electron detachment leads to significant geometric rearrangement on the neutral surface, which ultimately produces the neutral (A-H) moiety, possibly within an intact H_3PO_4·(A-H) complex. Such a system clearly cannot be described as equivalent to I$^-$·A where the iodine is described as a spectator atom upon electron detachment. [71] Wang and Kass have explained the phenomena of hydrogen atom/proton transfer on the neutral surface as arising from a lowering of the ionization energy of the neutral

moiety in the initial cluster. [249] Evidence for this can be found by considering the spin densities of the detached complexes, as if the ionization energy of the neutral is reduced, it may be ionised rather than the anion.

Figure 4.7 presents spin density plots for $I^-{\cdot}A$ and $H_2PO_3^-{\cdot}A$ showing the unpaired electron density of the neutral clusters present upon electron detachment. The difference is striking, as the calculations reveal that the excess electron is removed from the iodine in $I^-{\cdot}A$ but from the adenine moiety in $H_2PO_3^-{\cdot}A$. These calculations support the idea that $H_2PO_3^-{\cdot}A$ is a system where significant geometric rearrangement occurs on the neutral surface. Indeed, these spin-density calculations indicate that the $I^-{\cdot}A$ and $H_2PO_3^-{\cdot}A$ clusters represent two extreme limits of behaviour with respect to electron ejection. Of key importance is the fact that the geometric rearrangement on the neutral surface for detached $H_2PO_3^-{\cdot}A$ will mean that there is significant difference between the adiabatic electron affinity and the vertical detachment energy for the system. This will lead to negligible Franck-Condon overlap between the anionic ground state complex and any dipole-bound excited state.
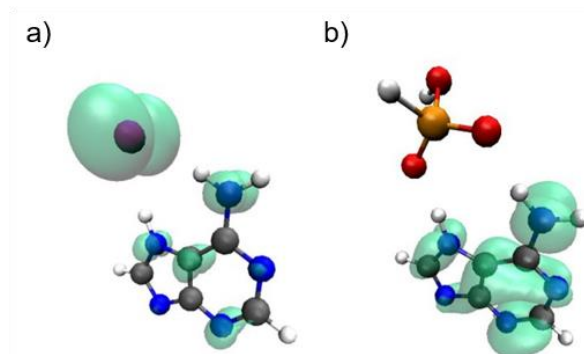
Figure 4.7 Spin density of a) $I^-{\cdot}A7$ and b) $H_2PO_3^-{\cdot}A$ with isovalues of 0.002 e^-/au^3.

Summarising, it is clear that $H_2PO_3^-{\cdot}A$ does not represent a system where the anion can be considered a spectator to allow the study of molecular electron capture within a cluster, and this study clearly demonstrates the importance of carefully selecting the anionic charge carrier for studies where a 'spectator' electron source is required.

$H_2PO_3^-$·A evidently provides a new example of a novel anionic cluster system where ionization occurs from the neutral component of the cluster, and where photoinduced hydrogen atom/proton electron transfer occurs. The system therefore represents a key example as a target for future time-resolved measurements.

4.7 Supplemental Material

4.7.1 Higher-Energy Collisional Dissociation of the X^-·A ($X^- = I^-$ and $H_2PO_3^-$) Anionic Clusters

HCD was performed to investigate the ground state fragmentation characteristics of the X^-·A ($X^-=I^-$ and $H_2PO_3^-$) anionic clusters. The Orbitrap was operated at a flow rate of 5 µL/min. The following settings were used for both clusters: MS1 detector ion trap, MS1 maximum injection time, 100 ms; MS1 automated gain control target, 100000; MS2 detector, ion trap; MS2 scan range, 50−600 MS2; AGC target, 100000; MS2 maximum injection time, 100; S-lens RF level, 50 V. HCD normalised collisional energy was varied between 0 and 46%

In order to obtain a good cluster production, some parameters were slightly changed when analysing the two clusters I^-·A (a) and $H_2PO_3^-$·A (b):

a) Spray voltage, 2100 V; sweep gas flow rate, 1; sheath gas flow rate, 45; aux gas flow rate, 17; ion transfer tube temperature, 150 °C; vaporizer temperature, 80 °C.

b) Spray voltage, 2000 V; sweep gas flow rate, 1; sheath gas flow rate, 40; aux gas flow rate, 5; ion transfer tube temperature, 230 °C; vaporizer temperature, 70 °C.

$H_2PO_3^-$, $[A-H]^-$ and PO_3^- are produced from $H_2PO_3^-$·A, whilst I^- is the only fragment produced by I^-·A.
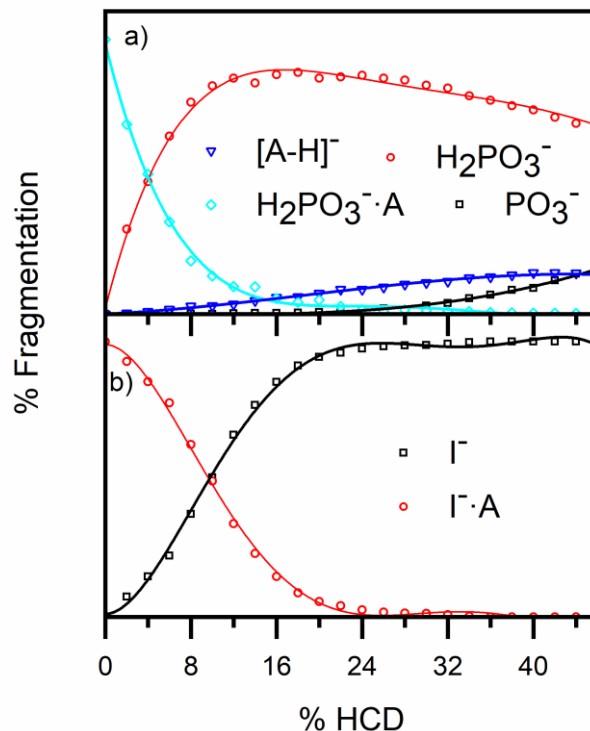
Figure 4.8 Fragment production curves for a) $I^-{\cdot}A$ and b) $H_2PO_3^-{\cdot}A$ upon HCD between 0 and 46% energy

4.7.2 TDDFT Transitions of $X^-{\cdot}A$ ($X^- = I^-$ and $H_2PO_3^-$)

Figure 4.2 shows the TDDFT spectra of the $X^-{\cdot}A$ ($X^- = I^-$ and $H_2PO_3^-$) clusters. The electronic transitions of the clusters, predicted by TDDFT, are summarised in Tables 4.2 and 4.3. They include transition assignments, transition energies and oscillator strengths.

The molecular orbitals involved in the electronic transitions predicted by TDDFT calculations (performed at the B3LYP/6-311++G(2d,2p)/SDD on I) of the $X^-{\cdot}A7$ ($X^-=I^-$ and $H_2PO_3^-$) clusters are presented in Figures 4.10 and 4.11. According to these calculations, the transitions at 4.86 and 4.90 eV of the $X^-{\cdot}A$ cluster are coupled, more details in Table 4.2.

Table 4.2 Calculated TDDFT transition energies and oscillator strengths of the $I^-\cdot A$ (N7H) cluster. Calculations were performed at the B3LYP/6-311++G(2d,2p)/SDD level. Only transitions below 5.5 eV with oscillator strength > 0.005 are listed.

Orbital transitions	Photon energy eV	f
$(1.00)39(n)\rightarrow40(\pi^*)$	3.8	0.0069
$(0.79)39(n)\rightarrow41(\sigma^*)$	4.2	0.024
$(0.77)38(n)\rightarrow41(\sigma^*)$	4.3	0.040
$(0.82)39(n)\rightarrow42(\sigma^*)$	4.4	0.0050
$(0.79)37(n)\rightarrow41(\sigma^*)$	4.5	0.048
$(0.79)38(n)\rightarrow42(\sigma^*)$	4.6	0.010
$(0.82)39(n)\rightarrow44(\sigma^*)$	4.6	0.0090
$(0.82)37(n)\rightarrow42(\sigma^*)$	4.7	0.0058
$(0.82)38(n)\rightarrow44(\sigma^*)$	4.8	0.016
$(0.65)36(\pi)\rightarrow40(\pi^*)$ $(0.18)37(n)\rightarrow44(\sigma^*)$	4.9	0.15
$(0.65)37(n)\rightarrow44(\sigma^*)$ $(0.19)36(\pi)\rightarrow40(\pi^*)$	4.9	0.027
$(0.70)35(\pi)\rightarrow40(\pi^*)$ $(0.26)36(\pi)\rightarrow41(\sigma^*)$	5.0	0.0064
$(0.56)39(n)\rightarrow45(\pi^*)$ $(0.36)39(n)\rightarrow46(\sigma^*)$	5.2	0.091
$(0.60)38(n)\rightarrow45(\pi^*)$ $(0.29)38(n)\rightarrow46(\sigma^*)$	5.3	0.064
$(0.87)39(n)\rightarrow47(\pi^*)$	5.4	0.011
$(0.60)37(n)\rightarrow45(\pi^*)$ $(0.27)37(n)\rightarrow46(\sigma^*)$	5.5	0.13
$(0.44)38(n)\rightarrow46(\sigma^*)$ $(0.18)38(n)\rightarrow45(\pi^*)$	5.5	0.011

Figure 4.9 Molecular orbitals of I⁻·A involved in the transitions predicted by TDDFT calculations between 3.78-5.50 eV described in Table 4.2. The isovalue for each orbital surface is 0.02 e/au^3. Separation between occupied and unoccupied orbitals is shown.

Table 4.3 Calculated TDDFT transition energies and oscillator strengths of the $H_2PO_3^-$ ·A (N7H) cluster. Calculations were performed at the B3LYP/6-311++G(2d,2p) level. Only transitions below 5.8 eV with oscillator strength > 0.005 are listed.

Orbital transitions	Photon energy eV	f
(0.54)56(π)→58(phosphate σ*) (0.35)56(π)→59(σ*)	4.7	0.0052
(0.84)56(π)→57(π*)	4.8	0.15
(0.73)56(π)→62(π*)	5.1	0.019
(0.29)55(π)→58(phosphate σ*) (0.67)55(π)→59(σ*)	5.6	0.057
(0.57)54(π)→58(phosphate σ*) (0.21)54(π)→59(σ*)	5.8	0.011
(0.46)54(π)→57(π*) (0.21)56(π)→65(π*)	5.8	0.17

Figure 4.10 Molecular orbitals of $H_2PO_3^-\cdot A$ involved in the transitions predicted by TDDFT calculations between 4.70-5.85 eV described in Table 4.3. The isovalue for each orbital surface is 0.02 e^-/au^3. Separation between occupied and unoccupied orbitals is shown.

4.7.3 Photofragment Action Spectrum of PO_3^- from $H_2PO_3^-{\cdot}A$

The ion PO_3^- (m/z 79) is produced with a very low cross-section in the photodepletion experiment in a similar way to the HCD spectrum shown in Figure 4.8b. Its photofragment action spectrum in shown in Figure 4.11.
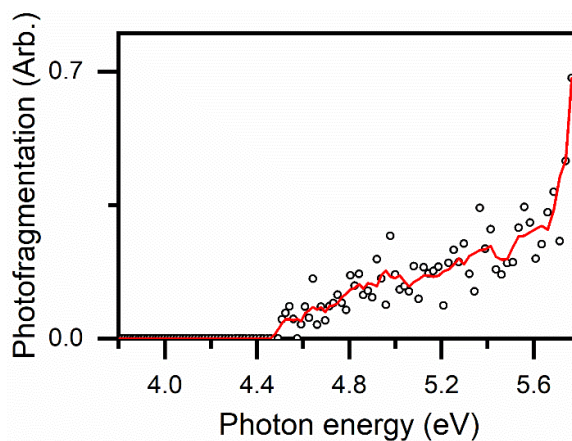
Figure 4.11 Photofragment action spectrum for PO_3^- that is produced from the $H_2PO_3^-$ ${\cdot}A$ cluster. The lines are five-point adjacent average of the data points.

4.7.4 Calculated Dipole Moments of $X^-{\cdot}A$ ($X^- = I^-$ and $H_2PO_3^-$)

Table 4.4 Calculated vertical and ground state dipole moments for the $X^-{\cdot}A$ clusters with A3, A7 and A9.

Cluster	MP2 Dipole Detached[a] Debye	MP2 Dipole Ground State Debye
$I^-{\cdot}A7$	8.80	1.40
$I^-{\cdot}A9$	3.71	9.02
$I^-{\cdot}A3$	5.41	7.95
$H_2PO_3^-{\cdot}A7$	5.88	1.73
$H_2PO_3^-{\cdot}A9$	14.8	6.09
$H_2PO_3^-{\cdot}A3$	14.5	4.79

[a] Vertical dipole moments

Chapter 5

Direct Measurement of the Visible to UV Photodissociation Processes for Tryptophan Manganese(I) Carbonyl (TryptoCORM)

5.1 Introduction

While the toxicity of carbon monoxide is well known, its biological significance and therapeutic properties have been increasingly recognised over recent years. [86] At low concentrations, CO is a powerful anti-inflammatory and organ transplantation agent that also has significant potential as chemotherapy and anti-microbial pharmaceutical. [126] [148] [262-265] However, controlled CO delivery remains a significant challenge for its medicinal use. The key to delivering localised CO is the development of carbon monoxide releasing molecules (CORMs) that exhibit CO release *only* when triggered. [86] [127] [149] [266] [267]

Pharmaceutical transition metal carbonyls that release CO upon light activation ("Photo-CORMs") have emerged among the most promising delivery agents over recent years. [150] [268] Long before the conception of Photo-CORMs, photoactive metal carbonyl complexes were the subject of extensive research due to their rich excited state properties which have led to applications across a wide range of photochemical and photophysical research fields. [269] [270] A review of the Photo-CORMs developed to date reveals that most incorporate group 7 and 8 transition metals, and require UV light to trigger CO release. [271] Low tissue penetration at UV wavelengths represents a significant problem for the wide-scale application of such Photo-CORMs, and further development of new visible-light activated Photo-CORMs, therefore, represents a major challenge in this field at the present time. [272]

The rational design of future Photo-CORMs could be considerably improved through obtaining a more complete understanding of their fundamental photomolecular properties. [273] A small number of groups are currently using this approach, combining known transition metal photochemistry with density functional theory calculations to predict and interpret trends for trial compounds. [144] [274] [275] However, progress is currently hampered by a sparsity of experimental measurements on Photo-CORMs that can be straightforwardly compared to results from the computational approaches. Gas-phase experiments offer considerable benefits in this context since results can be directly linked to computational results without deploying the very advanced calculations that are necessary to properly account for solvent effects on the photochemistry. [2]

In this Chapter, a new method is demonstrated that has the potential to contribute significantly to progress in this area by applying UV-VIS laser photodissociation spectroscopy to a known PhotoCORM, TryptoCORM, to better understand what makes this molecule a successful photo-pharmaceutical. [148] [151] This is the first time that the photochemical properties of a substituted PhotoCORM have been investigated in the gas-phase *via* a scan in the UV-Vis range, thus providing crucial experimental data against which to evaluate recent theoretical strategies.

Our experimental technique involves transferring the PhotoCORM from solution into the gas-phase *via* electrospray ionisation and then using novel laser-interfaced mass spectrometry (LIMS) to measure the gaseous absorption spectrum along with all of the ionic photoproducts produced at each scanned wavelength. Thus, we obtain a complete picture of the excited states, along with the accompanying photodissociation pathways. [276] We complement these measurements with cold ion vibrational spectroscopy (CIVS), an advanced experimental technique that allows us to structural

characterise the gaseous TryptoCORM species prior to interrogating their

photochemistry.
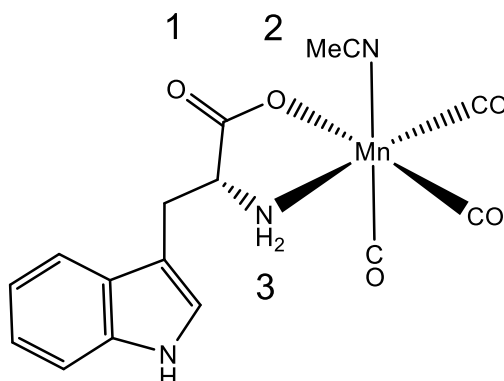
Scheme 5.1 The molecular structure of TryptoCORM (MnL(CO)$_3$(CH$_3$CN)) following
Ref. [148]. We underline that, while L-tryptophan was used in the previous work, D-
tryptophan is used in the current one. We note that the tryptophan ligand is the
deprotonated form of the molecule. Selected atom labels are included to indicate the
most likely protonation sites.

TryptoCORM, tryptophan manganese(I) tricarbonyl (Scheme 5.1) was the first visible-

light activated CORM to exhibit a potent effect against *Escherichia coli.* [148] One of

its key advantages as a potential therapeutic agent is that it shows low toxicity towards

mammalian cells and releases bio-benign tryptophan on photoexcitation in aqueous

solution. TryptoCORM is thought to release up to 2 CO molecules upon aqueous-

phase excitation at 400 nm (3.1 eV) dependent on conditions. [148] However, at the

lower excitation energies (465 nm, 2.66 eV) that are preferred for medical

applications, [142] [143] fewer CO molecules are released (1.4 equivalent). The

CH$_3$CN group of TryptoCORM is labile, [76] [146] [277] so that MnL(CO)$_3$,

TryptoCORM-CH$_3$CN, the complex is likely to exist in a dynamic equilibrium with

TryptoCORM in solution. In this work, we are able to directly compare the

photochemistry of the TryptoCORM and TryptoCORM-CH$_3$CN moieties since we are

able to independently isolate both molecular species prior to photoexcitation. In

addition, we directly measure the wavelength-dependent production of CO across a

wide UV-VIS spectral region, providing key information for selecting the excitation wavelength versus the amount of CO released.

5.2 Experimental and Computational Methods

TryptoCORM was synthesised, in the Lynam and Fairlamb groups, following a previously published protocol. [148] Solutions of TryptoCORM (1×10^{-5} mol dm^{-3}) in $H_2O:CH_3CN$ 1:1 and CH_3CN with 0.1% TFA (trifluoroacetic acid) were introduced to the mass spectrometer (for HCD and LIMS) through electrospray ionization at 140° C. The LIMS experiments were conducted across the range 2.1-5.3 eV (234-580 nm) at ~1 mJ photon energy. A 1 nm and 2 nm laser step sizes were employed in the UV and the visible spectral region, respectively, with photofragmentation experiments being run with an ion accumulation time of 100 ms.

For CIVS, solutions of TryptoCORM in CH_3CN (~ 10^{-3} M) with trace amounts of formic acid were electrosprayed to generate $[MnL(CO)_3]^{\cdot}H^+$ ions. An initial experiment was conducted in $H_2O:CH_3CN$ 1:1 resulting in the same IR spectrum with a lower signal to noise ratio, hence we conducted the following measurement in CH_3CN. The number of isomeric species contributing to the IR spectrum was determined by performing hole-burning spectroscopy.

Geometric optimisations were performed in Gaussian09 [188] at the PBE0/Def2-SV level. [193] [278] We calculated the vibrational frequencies to test whether the calculated structures corresponded to global minima. IR spectra were calculated at different levels of theory included CAM-B3LYP/Def2-SV level that resulted in best matching the experimental results.

5.3 Results

5.3.1 Characterisation of the Gas-Phase Structures of Electrosprayed TryptoCORM

Figure 5.1 displays the electrospray ionisation mass spectrum of TryptoCORM. The protonated pseudo-molecular ion, $[MnL(CO)_3(CH_3CN)]^{\cdot}H^+$ (L=deprotonated tryptophan), appears at m/z 384, with the most intense ion (m/z 343) being the protonated molecular species without the CH_3CN ligand, *i.e.* $[MnL(CO)_3]^{\cdot}H^+$.
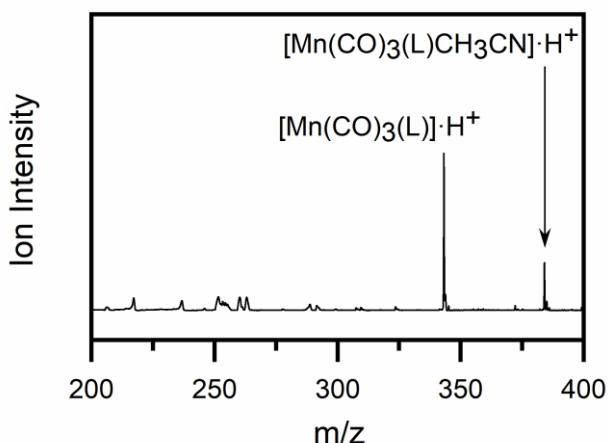
Figure 5.1 Positive ion mode electrospray ionisation mass spectrum of a 10^{-5} M solution of TryptoCORM in CH_3CN with 0.1% TFA.

TryptoCORM and TryptoCORM-CH_3CN have multiple possible protonation sites, with the most likely ones indicated on TryptoCORM on Scheme 5.1 (labels 1-3). Protonation on the Mn metal centre is also possible for the five-coordinate TryptoCORM-CH_3CN. [1] It is possible to predict which protonation isomer(s) will be formed upon electrospray by calculating the relative energies of the various protonation site isomers (or "protomers"). [220] [279] Such calculations are reported in Section 5.6.1. For $[MnL(CO)_3(CH_3CN)]^{\cdot}H^+$, the lowest-energy gas-phase protonation site corresponds to the O1 position, giving rise to the structures displayed in Figures 5.2a and 5.2b. This pair of isomers, where the tryptophan and acetonitrile ligands adopt *cis* (Figure 5.2a) and *trans* (Figure 5.2b) orientations, are expected to be present in a ratio of 86:14% under our experimental conditions. Protonation at

other sites leads to isomers with much higher relative energies that would not be populated in our electrosprayed ion ensemble (Section 5.6.1). Similarly, for $[MnL(CO)_3]\cdot H^+$, the lowest-energy gas-phase structure (Figure 5.2c) corresponds to protonation at the O1 position, with other protomers lying at significantly higher energies. Notably, the isomer with protonation on the Mn centre lies 221 kJmol^{-1} above the global minimum structure. The lowest-energy $[MnL(CO)_3]\cdot H^+$ structure involves the tryptophan ligand folding to coordinate to the vacant metal centre through the C=C bond of the indole (η^2, Figure 5.2c), at 2.5 Å from the metal. (Table 5.7 gives key geometric parameters for the calculated structures.) Coordination of the tryptophan ligand confers significant stability on $[MnL(CO)_3]\cdot H^+$, as the corresponding "open" structure where the tryptophan indole is uncoordinated to the Mn (Figure 5.2d) is calculated to lie 44.6 kJmol^{-1} above the folded structure.
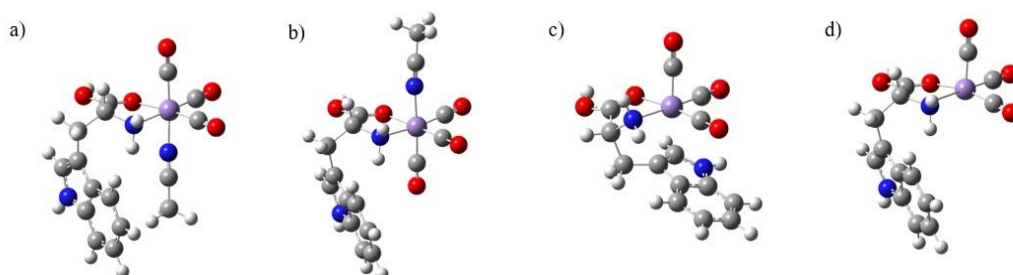
Figure 5.2 Optimised structures (PBE0/Def2-SV) of (a) and (b) the lowest-energy protomers of $[MnL(CO)_3(CH_3CN)]\cdot H^+$, with (c) the folded and (d) the open forms of $[MnL(CO)_3]\cdot H^+$.

A Boltzmann analysis of the gas-phase $[MnL(CO)_3]\cdot H^+$ protomers (Section 5.6.2) indicates that the folded O1 protomer (Figure 5.2c) would strongly dominate a gaseous sample of $[MnL(CO)_3]\cdot H^+$. To directly test the extent of the tryptophan-Mn coordination, cold ion vibrational spectroscopy was performed on the gaseous electrosprayed ions. In this method, described in Section 2.4, a single IR photon is used to detach a D_2 molecule that is tagged to the metal complex. We note that the tag may slightly shift the vibrational frequencies compared to the bare complex.

Furthermore, as the D_2 detaches with the IR photon, we do not suspect a direct coordination of the tag to the metal vacant site.

Figure 5.3c displays the acquired IR spectrum of $[MnL(CO)_3] \cdot H^+$ across the regions of the NH/OH stretches (3100 to 3600 cm^{-1}) and CO stretches (1600-2200 cm^{-1}) along with the calculated spectra of the open (Figure 5.3a) and folded (Figure 5.3b) structures. Table 5.1 lists the calculated and experimental IR frequencies.

Comparison of the experimental and computational spectra confirms that the computed spectrum for the folded structure (Figure 5.3a) most closely resembles the experimental spectrum (Figure 5.3c) since the strong 3254 cm^{-1} vibration associated with the NH$_2$ symmetric stretch of the open structure (Figure 5.3b) is shifted compared with the experimental spectrum.
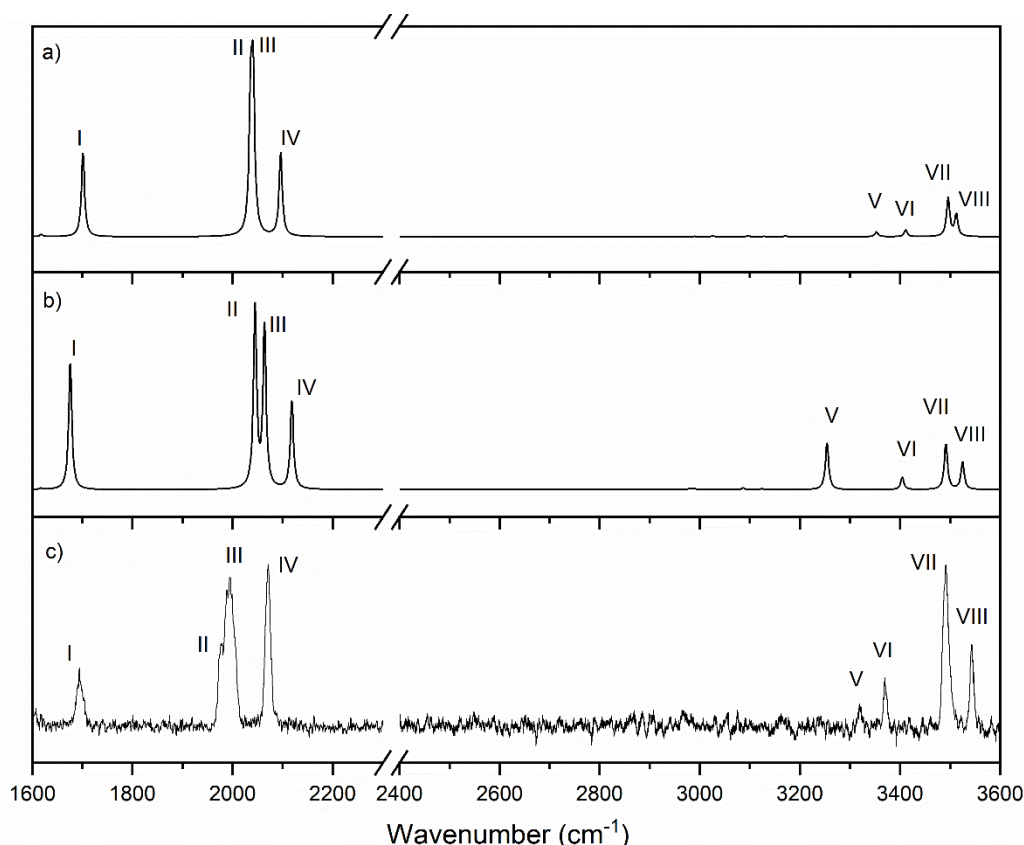
Figure 5.3 Calculated (CAM-B3LYP/Def2-SV) vibrational spectra of the a) folded and b) open structures of $[MnL(CO)_3] \cdot H^+$ compared to c) the experimental IR spectrum over the ranges and 3100-3600 cm^{-1}. The calculated spectra are scaled by 0.94 over the 1600-2200 cm^{-1} region, and by 0.97 over the 3100-3600 cm^{-1} region.

IR spectra of $[MnL(CO)_3]\cdot H^+$ across the CO stretching region displays one CO band in the carboxylic stretch region at 1694 cm^{-1}, along with three additional bands in the metal-bound CO stretching region. Two of these bands (1976 and 1994 cm^{-1}) are only partially resolved. The experimental spectrum is consistent with the predicted spectrum (Figure 5.3a) for the folded structure, and the experimental bands occur closer to the predicted vibrational frequencies for the folded structure than the open structure. For example, band I occurs at an experimental frequency of 1694 cm^{-1}, compared to predicted values of 1701 (folded) and 1676 cm^{-1} (open).

Table 5.1 Calculated (CAM-B3LYP/Def2-SV) and experimental vibrational frequencies for the folded and open conformational isomers of $[MnL(CO)_3]\cdot H^+$ displayed in Figure 5.2.

Spectral region	Vibrational mode	Band	Folded v cm^{-1}	Open v cm^{-1}	Experimental v cm^{-1}
CO stretch[a]	Carboxylic CO	I	1701	1676	1694
	CO asymm	II	2036	2045	1976
	CO asymm	III	2041	2064	1994
	CO symm.	IV	2096	2118	2071
XH stretch[b]	NH$_2$ symm	V	3353	3254	3323
	NH$_2$ asymm	VI	3412	3404	3372
	OH	VII	3496	3492	3491
	Indole NH	VIII	3512	3525	3544

[a] Scaled by 0.94
[b] Scaled by 0.97.

Hole-burning spectroscopy was performed to investigate whether multiple $[MnL(CO)_3]\cdot H^+$ isomers are present. These experiments are reported in Section

5.7.3. We conclude that a single $[MnL(CO)_3] \cdot H^+$ isomer is produced by electrospray, corresponding to a geometric structure compatible with the calculated Figure 5.2c structure where the tryptophan indole coordinates closely with the Mn centre.

5.3.2 Thermal Fragmentation Pathways of $[MnL(CO)_3(CH_3CN)] \cdot H^+$ and $[MnL(CO)_3] \cdot H^+$

To aid in our interpretation of the UV/VIS laser photodissociation results, we have investigated the thermal fragmentation pathways of $[MnL(CO)_3(CH_3CN)] \cdot H^+$ and $[MnL(CO)_3] \cdot H^+$ by subjecting the ions to higher-energy collisional dissociation (HCD). This experiment maps out the fragmentation pathways of a molecular system as a function of internal energy and is therefore also of interest in the context of the known propensity of TryptoCORM to release CO upon thermal exposure, *i.e.* to behave as a thermal-CORM. [151] [266] The HCD fragmentation curves are displayed in Figure 5.4.
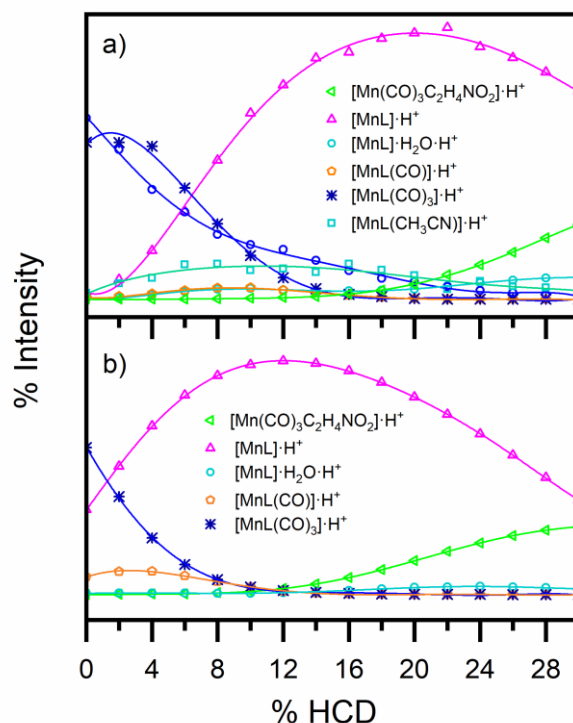
Figure 5.4 Precursor ion decay curves and fragment ion production curves for a) $[MnL(CO)_3(CH_3CN)] \cdot H^+$ and b) $[MnL(CO)_3] \cdot H^+$ upon HCD between 0-30%.

For $[MnL(CO)_3(CH_3CN)] \cdot H^+$ (Figure 5.4a), the major initial fragmentation pathway corresponds to loss of the CH_3CN ligand:

$$[MnL(CO)_3(CH_3CN)] \cdot H^+ \rightarrow [MnL(CO)_3] \cdot H^+ + CH_3CN \qquad (5.1)$$
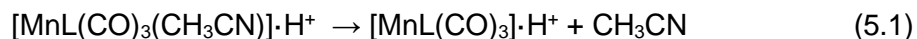
Indeed, the complex very readily loses the CH_3CN ligand as it dissociates into this channel even at 0% HCD, revealing that the ion is metastable in the gas-phase.[42] The resulting $[MnL(CO)_3] \cdot H^+$ ion subsequently decreases in intensity across the relatively low-energy region from 0-12%, with a concomitant rise in intensity of $[MnL] \cdot H^+$ corresponding to the loss of 3COs (*i.e.* loss of 3CO + CH_3CN from the precursor ion):

$$[MnL(CO)_3(CH_3CN)] \cdot H^+ \rightarrow [MnL] \cdot H^+ + 3CO + CH_3CN \qquad (5.2)$$
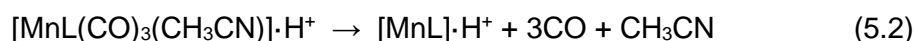
This behaviour is mirrored by the fragmentation behaviour of $[MnL(CO)_3] \cdot H^+$ (Figure 4b), where the major fragmentation channel corresponds to loss of all 3CO units:

$$[MnL(CO)_3] \cdot H^+ \rightarrow [MnL] \cdot H^+ + 3CO \qquad (5.3)$$

For both systems, fragmentation with loss of just two CO units is a much less intense channel, that occurs only in the lower-energy region < 10%), *i.e.*:

$$[MnL(CO)_3(CH_3CN)] \cdot H^+ \rightarrow [MnL(CO)(CH_3CN)] \cdot H^+ + 2CO \qquad (5.4a)$$

$$[MnL(CO)_3] \cdot H^+ \qquad \rightarrow [MnL(CO)] \cdot H^+ + 2CO \qquad (5.4b)$$
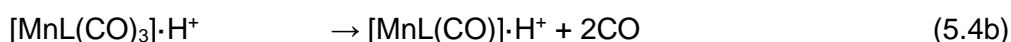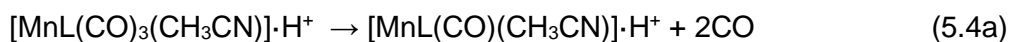
Notably, there is no channel associated with loss of a single CO molecule for either complex, revealing that if one CO is lost, the energetic barrier to loss of a second CO is very low. Similar energetics then appear to lead to the overall dominance of loss of 3CO units, compared to the loss of 2CO units. A number of other metal carbonyl

complexes have been studied previously by collision-induced dissociation. Butcher et al., for example, studied a series of anionic polynuclear transition metal complexes, including $Ru_3Co(CO)_{13}^-$, and found that the complexes sequentially lost CO units as collision-energy increased. [280] While such progressive loss of COs is common for anionic carbonyl clusters, exceptions have been observed, especially where there is the possibility of structural rearrangement of the core or ligands. [281] We suggest that the loss of the CO molecules may be compensated by further coordination of the indole ring, which can potentially bind with higher hapticity.

The $[Mn(CO)_3(C_2H_4NO_2)]\cdot H^+$ fragment (Figures 5.4a and 5.4b) increases in intensity through the high-energy collision range from 14-30% HCD, and arises from $C\alpha$-C_β homolytic dissociation bond rupture of tryptophan (Scheme 5.2), releasing the C_9H_8N neutral unit: [282]

$$[MnL(CO)_3(CH_3CN)]\cdot H^+ \rightarrow [Mn(CO)_3(C_2H_4NO_2)]\cdot H^+ + CH_3CN + C_9H_8N \quad (5.5)$$
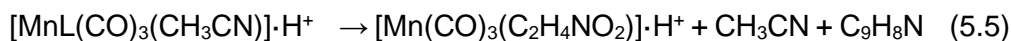
This pathway corresponds to a high-energy thermal fragmentation surface where the 3CO ligands remain bound to the Mn metal centre, while the tryptophan moiety breaks apart. Notably, we do not observe collisional-activated loss of the protonated tryptophan moiety from either complex.
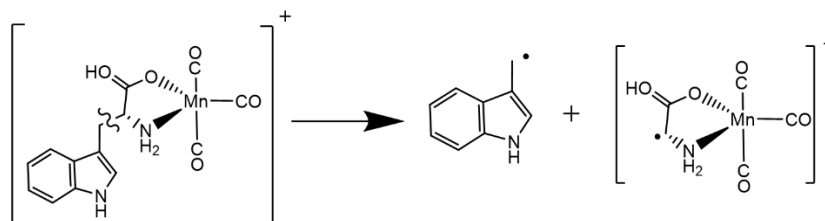
Scheme 5.2 Illustration of the $C\alpha$-$C\beta$ tryptophan bond rupture in $[MnL(CO)_3]\cdot H^+$

Finally, we note that $[MnL]\cdot H_2O\cdot H^+$ appears as a relatively low intensity fragmentation product at higher collision energies:

$$[MnL(CO)_3(CH_3CN)]\cdot H^+ \quad (+ H_2O)_{trap} \rightarrow [MnL]\cdot H_2O\cdot H^+ + CH_3CN + 3CO \qquad (5.6)$$
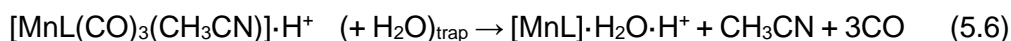
Addition of residual water vapour to reactive species in the ion trap is a common process, although the profile of the $[MnL]\cdot H_2O\cdot H^+$ fragment is intriguing as it increases at higher collision energy. One explanation of this observation would be that when $[MnL]\cdot H^+$ is formed from the precursor ions, it is produced in a different electronic state at the lower and higher collision energies.

5.3.3 Intrinsic (Gas-Phase) Electronic Spectroscopy of $[MnL(CO)_3(CH_3CN)]\cdot H^+$ and $[MnL(CO)_3]\cdot H^+$

The gas-phase absorption spectrum (recorded *via* photodepletion) of mass-selected $[MnL(CO)_3(CH_3CN)]\cdot H^+$ across the 2.1-5.3 eV range is shown in Figure 5.5a. Mass selection is a key feature of our experimental approach since it means that the gas-phase absorption spectra we record are unambiguously associated with the *m/z* selected ion. This situation is quite distinct from solution-phase UV spectroscopy, where overlapping spectra of distinctive chemical species may be present. We find that $[MnL(CO)_3(CH_3CN)]\cdot H^+$ displays strong photodepletion in the UV region above 4.4 eV, with a sharp onset around 4.2 eV, consistent with the known gaseous spectrum of protonated tryptophan. [283] Electronic excitations of the complex within this region can, therefore, be associated with predominantly tryptophan-localised transitions. [283] An additional, lower-intensity region of absorption is present between 2.5-3.9 eV, peaking at ~ 3.1 eV. Absorption in this region is expected to correspond to metal-to-ligand charge-transfer (MLCT) transitions. [144] [284] [285]
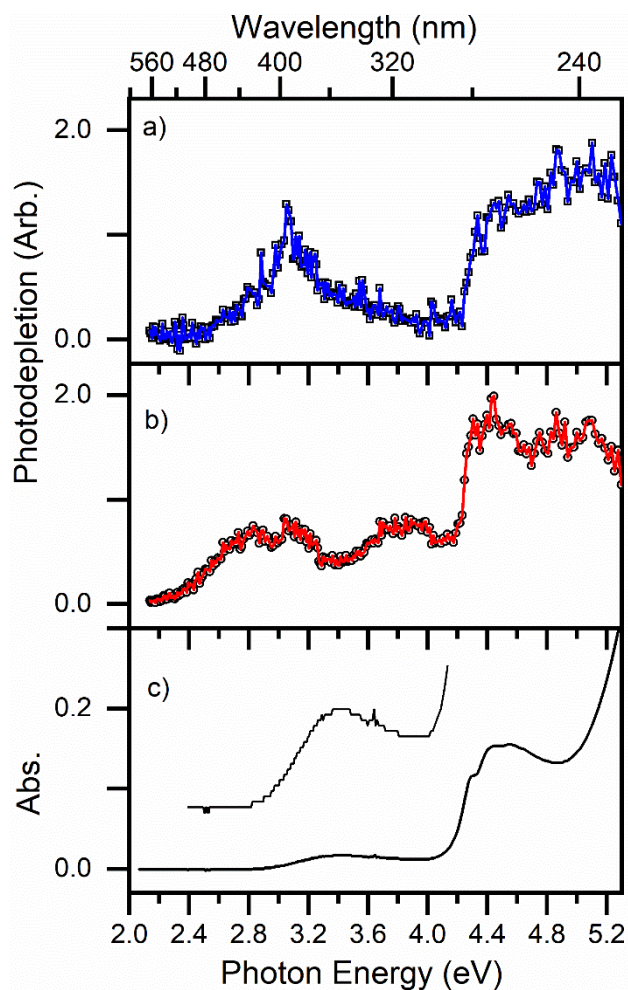
Figure 5.5 Gas-phase absorption (Photodepletion) spectra of a) $[MnL(CO)_3(CH_3CN)]\cdot H^+$ and b) $[MnL(CO)_3]\cdot H^+$ (solid lines connect data points), displayed with c) the solution-phase absorption spectrum of TryptoCORM (in $H_2O:CH_3CN$ 1:1), vertically expanded from 2.4-4.2 eV.

Figure 5.5b presents the gaseous absorption spectrum of $[MnL(CO)_3]\cdot H^+$, which again shows strong absorption in the UV region, with a sharp increase in photodepletion above 4.2 eV. While both complexes have absorption bands which peak around 3 eV, $[MnL(CO)_3]\cdot H^+$ displays additional absorption bands which peak at 2.8 and 3.8 eV. Figure 5.5c shows the solution-phase absorption spectrum of TryptoCORM for comparison with the gaseous spectra. We note that the difference between gas- and solution-phase absorption may be caused by TryptoCORM and TryptoCORM-CH_3CN not being protonated in solution.

5.3.4 Photodissociation Pathways of $[MnL(CO)_3(CH_3CN)]\cdot H^+$ and $[MnL(CO)_3]\cdot H^+$

To gain insight into the photo-induced fragmentation pathways of $[MnL(CO)_3(CH_3CN)]\cdot H^+$ and $[MnL(CO)_3]\cdot H^+$, we now turn to analyse the cationic photofragments produced following photoexcitation across 2.1−5.3 eV. Figure 5.6 presents the photofragment production spectra from $[MnL(CO)_3(CH_3CN)]\cdot H^+$ for the most intense photofragments, which correspond to the following processes:

$$[MnL(CO)_3(CH_3CN)]\cdot H^+ + h\nu \rightarrow [MnL(CO)_3]\cdot H^+ + CH_3CN \quad (5.7a)$$

$$\rightarrow [MnL]\cdot H^+ + CH_3CN + 3CO \quad (5.7b)$$

$$\rightarrow [MnL(CH_3CN)]\cdot H^+ + 3CO \quad (5.7c)$$

$$\rightarrow [MnL(CO)]\cdot H^+ + CH_3CN + 2CO \quad (5.7d)$$

$$\rightarrow [Mn(CO)_3(C_2H_4NO_2)]\cdot H^+ + CH_3CN + C_9H_8N \quad (5.7e)$$

$$\rightarrow (+ H_2O)_{trap} \rightarrow [MnL]\cdot H_2O \cdot H^+ + CH_3CN + 3CO \quad (5.7f)$$
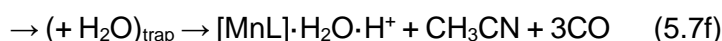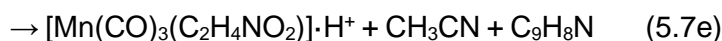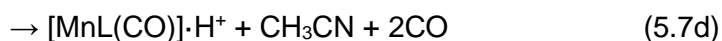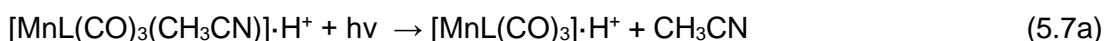
Process 5.7a corresponds to the loss of the labile CH_3CN ligand, which produces $[MnL(CO)_3]\cdot H^+$. This channel is seen only at the lowest excitation energies (between 2.4-3.2 eV), with the carbonyl loss channels dominating at higher energies. The $[MnL(CO)_3]\cdot H^+$ photofragment is unique compared to the other photofragments as it is the only fragment not produced at all in the UV region.

Process (5.7b) is one of the dominant channels, with $[MnL]\cdot H^+$ being produced across the same two regions as $[MnL(CH_3CN)]\cdot H^+$ (pathway (5.7c)) although $[MnL]\cdot H^+$ is formed much more strongly across the high-energy region, again with strongly rising production above 4.2 eV where the tryptophan localised transitions occur.[283] The next channel, (5.7c) is the second dominant fragmentation channel and results in production of the $[MnL(CH_3CN)]\cdot H^+$ photofragment. This product ion is striking, as it is unanticipated on purely energetic grounds since the HCD results presented above show that the CH_3CN ligand is more weakly bound than the CO ligands. Production

of $[MnL(CH_3CN)] \cdot H^+$ occurs across two regions, from 2.6-3.8 eV, and then with a rapid onset for higher-energy production above 4.2 eV.

Process (5.7d) corresponds to the loss of two CO molecules, along with the CH_3CN. This channel is the weakest (lowest ion intensity) channel we observe for gaseous photoexcitation of $[MnL(CO)_3(CH_3CN)] \cdot H^+$. The production spectrum for $[MnL(CO)] \cdot H^+$ (Figure 5.6d) is similar to that of the $[MnL(CH_3CN)] \cdot H^+$ photofragment (Figure 5.6c).

Process (5.7e), corresponds to fragmentation of the tryptophan moiety (Scheme 5.2) with the CH_3CN lost but the three CO ligands retained. This channel is more significant in the high energy region (> 4.2 eV) where tryptophan-localised transitions occur, but intriguingly, $[Mn(CO)_3(C_2H_4NO_2)] \cdot H^+$ is also seen across the low-energy region with a production spectrum matching that of $[MnL(CH_3CN)] \cdot H^+$. (This indicates that these two photochemical pathways are linked.) Pathway (5.7f) corresponds to the addition to the $[MnL] \cdot H^+$ of a water molecule in the ion trap, as in the HCD results. For the photoinduced product, the $[MnL] \cdot H_2O \cdot H^+$ production profile closely matches that of $[MnL] \cdot H^+$, suggesting that the $[MnL] \cdot H^+$ ions produced at all photon energies are able to react with water vapour. This result is different from the HCD results where the $[MnL] \cdot H^+$ fragment production profiles do not mirror those of $[MnL] \cdot H_2O \cdot H^+$.

For $[MnL(CO)_3(CH_3CN)] \cdot H^+$, the dominance of photofragmentation channels (5.7b) and (5.7c) is consistent with the profile of the gaseous absorption spectrum (Figure 5.5a), which matches the channel in 5.7c over the low-energy region and the channel in 5.7b spectrum above 4.2 eV. Both of these channels are characterised by relatively low intensity in the intermediate energy region between 3.6-4.2 eV.
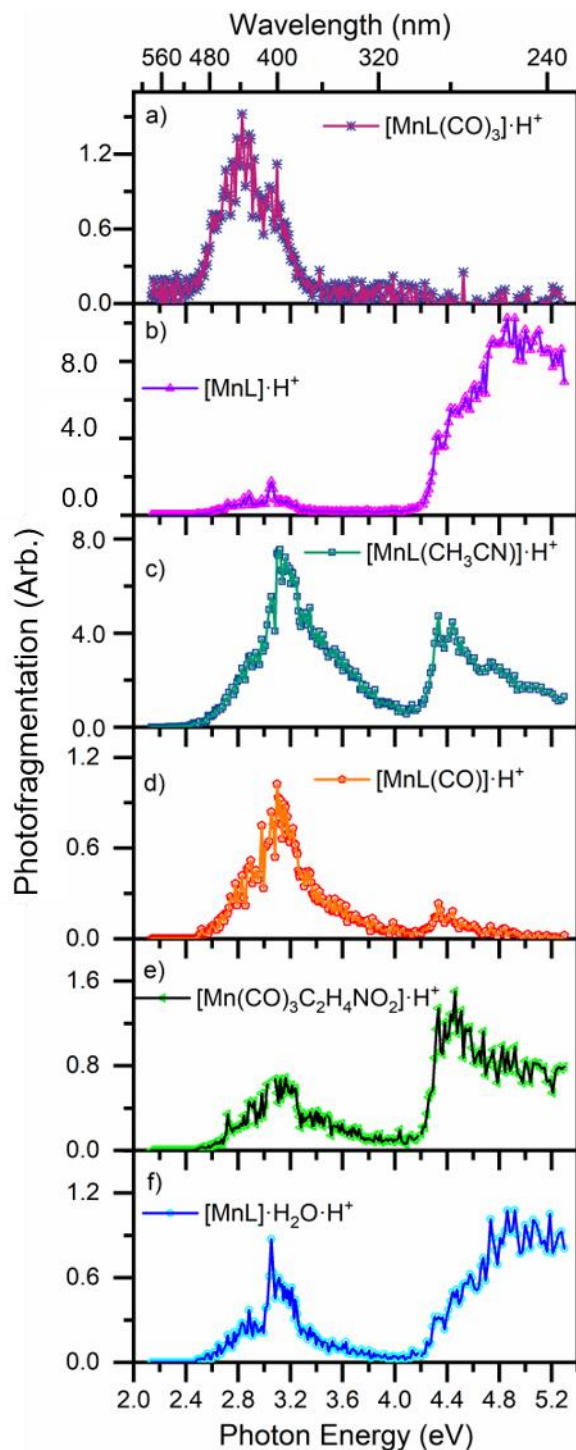
Figure 5.6 Photofragment production spectra from $[MnL(CO)_3(CH_3CN)]\cdot H^+$ across the range 2.1-5.3 eV, showing production of a) $[MnL(CO)_3]\cdot H^+$, b) $[MnL]\cdot H^+$, c) $[MnL(CH_3CN)]\cdot H^+$, d) $[MnL(CO)]\cdot H^+$, e) $[Mn(CO)_3(C_2H_4NO_2)]\cdot H^+$ and f) $[MnL]\cdot H_2O\cdot H^+$. The solid lines join the experimental data points.

We turn now to consider how the photofragmentation properties of $[MnL(CO)_3]\cdot H^+$ compare to those of $[MnL(CO)_3(CH_3CN)]\cdot H^+$. Figure 5.7 presents the photofragment

production spectra obtained from $[MnL(CO)_3]\cdot H^+$ for the major photofragments, produced *via*:

$$[MnL(CO)_3]\cdot H^+ + h\nu \quad \rightarrow [MnL]\cdot H^+ + 3CO \qquad (5.8a)$$

$$\rightarrow [MnL(CO)]\cdot H^+ + 2CO \qquad (5.8b)$$

$$\rightarrow [Mn(CO)_3(C_2H_4NO_2)]\cdot H^+ + C_9H_8N \qquad (5.8c)$$

$$\rightarrow (+ H_2O)_{trap} \rightarrow [MnL]\cdot H_2O\cdot H^+ + 3CO \qquad (5.8d)$$
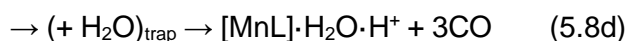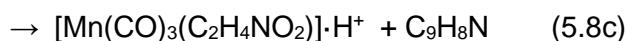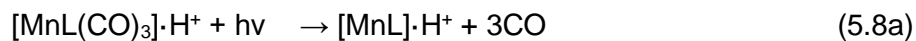
The fragmentation pathway corresponding to the loss of all three CO ligands is the most intense photofragmentation route for $[MnL(CO)_3]\cdot H^+$, as it was for $[MnL(CO)_3(CH_3CN)]\cdot H^+$. However, direct comparison of the two spectra corresponding to loss of 3 COs (Figures 5.6c and 5.7a) reveals a notable difference in the production profiles, with $[MnL(CO)_3]\cdot H^+$ displaying enhanced fragmentation into this channel between 3.4-4.0 eV. We note that, below 4.4 eV, the $[MnL]\cdot H^+$ production spectrum (Figure 5.7a) closely resembles the gaseous absorption spectrum of $[MnL(CO)_3]\cdot H^+$ (Figure 5.5b), and hence the difference in the intrinsic absorption spectra for the two complexes can be traced to the distinctive excitation channel that is open to $[MnL(CO)_3]\cdot H^+$ between 3.4-4.0 eV. Below 4.4 eV, processes (5.8b) and (5.8c) display similar spectral production profiles to processes (5.7d) and (5.7e). Pathway (5.8d) corresponds to a process where residual trap water adds to the $[MnL]\cdot H^+$ photofragment. Although the appearance of $[MnL]\cdot H_2O\cdot H^+$ as a photofragment can be readily accounted for, comparison of the spectra in Figures 5.7a and 5.7d reveal that $[MnL]\cdot H_2O\cdot H^+$ production does not match that of $[MnL]\cdot H^+$ as it did for the $[MnL(CO)_3(CH_3CN)]\cdot H^+$ photofragments. In particular, $[MnL]\cdot H_2O\cdot H^+$ is not produced to any significant extent from 3.2-4.0 eV. This is an important point as it indicates that the $[MnL]\cdot H^+$ photofragment is not the same electronic species across the entire excitation range. It is also interesting in this context to note that

$[MnL]·H_2O·H^+$ appears more prominently from $[MnL(CO)_3]·H^+$ than from $[MnL(CO)_3(CH_3CN)]·H^+$.
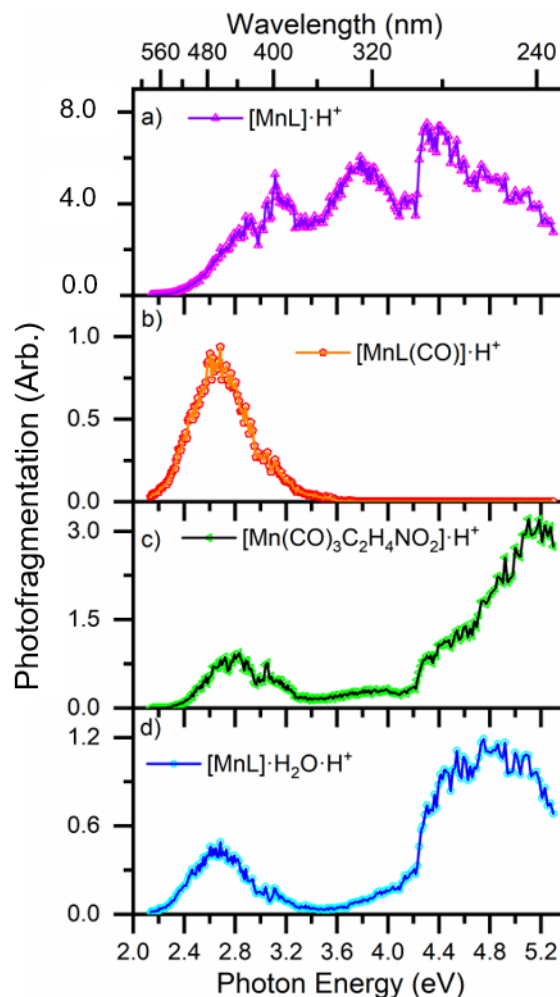
Figure 5.7 Photofragment production spectra from $[MnL(CO)_3]·H^+$ across the range 2.1-5.3 eV, showing production of a) $[MnL]·H^+$, b) $[MnL(CO)]·H^+$, c) $[Mn(CO)_3C_2H_4NO_2]·H^+$ and f) $[MnL]·H_2O·H^+$. The solid lines join the experimental data points.

The detailed photochemical information presented above reveals similarities but also notable differences in the wavelength-dependent photochemistry of $[MnL(CO)_3(CH_3CN)]·H^+$ and $[MnL(CO)_3H]^+$. We will return to discuss this point further in the next Section.

5.4 Discussion

5.4.1 Further Discussion of TryptoCORM's Photofragmentation Profiles.

An overview perspective on photofragment production is gained if we consider the ion yields (Eq. 2.14) for the dominant photofragmentation channels of $[MnL(CO)_3(CH_3CN)]\cdot H^+$ versus $[MnL(CH_3CN)]\cdot H^+$.

Figure 5.8 displays these quantum ion yields for the major photofragments as a function of the entire wavelength range scanned. These plots strikingly show how the photofragment production is controlled by the morphology of the excited states, and not simply by the internal energy of molecules following photoexcitation. For $[MnL(CO)_3(CH_3CN)]\cdot H^+$, the dominant channel which corresponds to the loss of 3COs follows a reasonably smooth bell curve shape that peaks at ~ 3.6 eV. Across the 2.9-4.8 eV region, the 3CO loss channel for $[MnL(CO)_3]\cdot H^+$ displays a very similar profile, again peaking at ~3.6 eV. This clearly demonstrates that both species access the same excited-state surface across the 2.9-4.8 eV region. At higher energies, $[MnL(CO)_3(CH_3CN)]\cdot H^+$ also loses its acetonitrile, while $[MnL(CO)_3]\cdot H^+$ displays an increased propensity to lose the C_9H_8N unit. Both of these channels reflect the increasing internal energy of the complexes as a function of photoexcitation.

The tryptophan $C\alpha$-$C\beta$ bond rupture fragment is characteristic of the dominant photofragment that would be expected from protonated tryptophan-localised excitations.[283] While these excitations should dominate in the region above 4.3 eV, the fact that the $-C_9H_8N$ loss photofragment is observed in the lower-energy bands is evidence that strong coupling occurs throughout the excitation range studied here. Indeed, this observation is in line with recent theoretical work from Fumanal *et al.,* which has shown that the central metal atom plays a controlling role in the early time photophysics of the complex. [284] In their studies of a manganese(I) complex, ultrafast decay of the absorbing MLCT S_2 state was found to be mediated by vibronic

coupling between the S_2/S_1 and the upper singlet metal-centred and MLCT states. Crucially, in the absence of strong spin-orbit coupling, $S_2 \to S_1$ internal conversion was found to be indirect and mediated by distinctive upper electronic states. This early time photophysics prepares the complex for subsequent carbonyl dissociation.
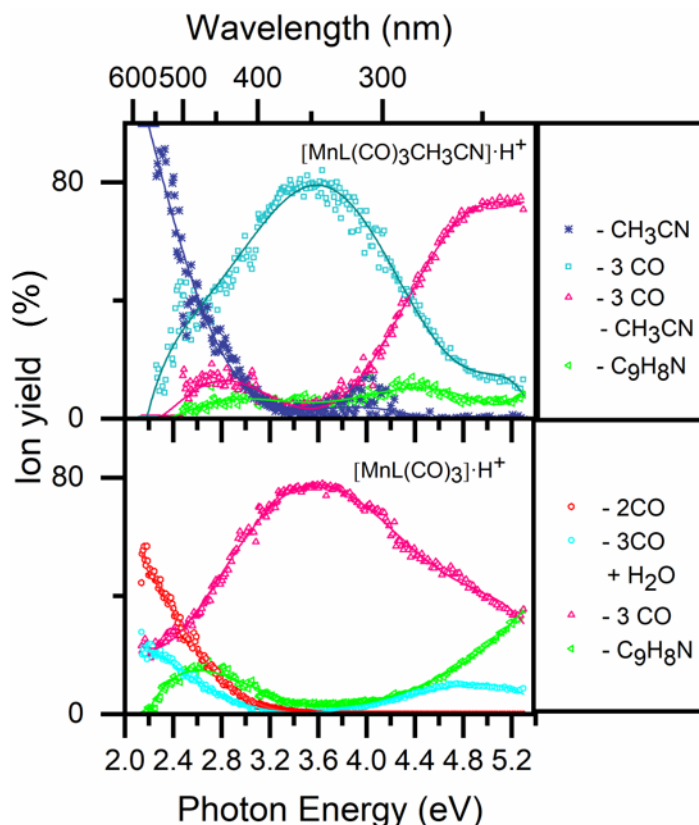
Figure 5.8 Quantum ion yield plots for photoexcitation of a) $[MnL(CO)_3(CH_3CN)]\cdot H^+$ and b) $[MnL(CO)_3]\cdot H^+$ across the range 2.1-5.3 eV. The solid lines are five-point adjacent averages of the data points.

The quantum yield plots provide clear evidence for the presence of three distinctive excitation regions for $[MnL(CO)_3(CH_3CN)]\cdot H^+$ and $[MnL(CO)_3]\cdot H^+$. The first occurs between 2.2-3.0 eV, the second from 3.0-4.4 eV, and the third from 4.4-5.3 eV. The locations of the regions are remarkably similar for the two complexes. High-level calculations of the dissociative excited-state surfaces are now highly desirable to test how accurately the computed excited-state surfaces map onto these quantum yield plots.

5.4.2 Implications for PhotoCORM Activity of TryptoCORM

Our measurements of the direct photodecay pathways of the isolated (*i.e.* gaseous) TryptoCORM complexes studied is interesting in the context of its solution-phase behaviour. Initial myoglobin-based spectroscopic assays of TryptoCORM indicated that the molecule does not release significant amounts of CO in the dark and that it releases two molar equivalents of CO upon irradiation at 400 nm. [151] However, subsequent work with Leg-haemoglobin revealed that TryptoCORM did in fact release CO in the dark. [272] This seeming contradiction can be attributed to differences in the binding constant of CO to TryptoCORM *versus* the myoglobin and at the difference in the binding affinity between Leg-Haemoglobin and myoglobin (which is 100 times bigger for Leg-haemoglobin). However, this is one example of the many known problems of using myoglobin assays to determine the amount of CO released. [145] The technique demonstrated here provides a new approach to determining the wavelength dependence of CO release from a potential PhotoCORM in a straightforward and unambiguous manner. While there will be known differences between the gaseous and solution-phase CO dissociation profile, [88] our results show that for TryptoCORM, lower molar equivalents of CO are produced (>410 nm in the gas-phase) in the visible region compared to the UV (<400 nm in the gas-phase). This result is entirely in line with solution-phase irradiation measurements. [148] Compared to the solution-phase photolysis measurements which were conducted with two fixed wavelength diode LEDs, however, our photolysis experiment incorporates a broad scanning laser source. We, therefore, obtain a full picture of the spectral regions where CO loss is maximised *via* loss of three CO units from the TryptoCORM, as shown in exquisite detail on the quantum ion-yield plots of Figure 5.8. Perhaps just as importantly, these plots allow us to trace the extent to which maximum CO loss is compromised at the redder wavelengths, and hence make an informed decision as to the optimum wavelength for clinical application.

5.5 Conclusions

In conclusion, we have measured the intrinsic absorption spectrum and photofragmentation pathways for TryptoCORM and TryptoCORM-CH$_3$CN as isolated molecular complexes in the gas-phase. In evaluating the differences between the two studied systems, we believe that the η^2-bonding indole may stabilise the TryptoCORM-CH$_3$CN and affect the overall energetics of the CO release. Furthermore, we note that, for both complexes, the indole binding has the potential to increase in hapticity as the metal is stripped of its CO ligands and therefore contribute to the lowered dissociation energy barrier. The photofragment production spectra reveal the optimum excitation wavelengths for maximising CO ejection from a PhotoCORM for the first time and therefore demonstrate a straightforward and widely applicable new methodology for assessing photoinduced CO release. The experiments reported here result from applying novel laser-interfaced mass spectrometry within an adapted commercial mass spectrometer, a technique that has considerable broader potential for applied photochemical and photophysical studies. Finally, we note that our results also represent the first direct measurement of the wavelength-dependent photochemical branching ratios (effectively quantum ion yields) for a transition metal carbonyl complex. The spectra presented here, therefore, provide a new benchmark against which high-level excited-state calculations of this challenging group of molecular systems can be compared. [286-288]

5.6 Supplementary material

5.6.1. Computational Study of MnL(CO)$_3$(CH$_3$CN) and [MnL(CO)$_3$(CH$_3$CN)]·H$^+$ Geometry

To explore the possible geometric structures adopted by [MnL(CO)$_3$(CH$_3$CN)]·H$^+$, we first optimised a range of geometric structures of MnL(CO)$_3$(CH$_3$CN). Geometric optimisations were performed in Gaussian 09 at the PBE0/Def2-SV level. We calculated the vibrational frequencies to test whether the calculated structures

corresponded to true minima. Geometric isomers of TryptoCORM with an L-Tryptophan identified previously by Ward et al. were used as starting points for these calculations. [148] (The calculations displayed below have been performed on TryptoCORM with a D-Tryptophan, as used in our experimental work). Table 5.2 displays the structures obtained along with their relative energies (non-zero-point energy corrected).

Protons were added to the most favourable protonation sites of $MnL(CO)_3(CH_3CN)$ (labelled 1-3 in Scheme 5.1) to obtain starting structures for $[MnL(CO)_3(CH_3CN)]^{\cdot}H^+$. The lowest-energy optimised resulting structures are displayed in Table 5.3, along with their relative energies (non-zero-point energy corrected). Boltzmann populations relative to the species in Table 5.3 are presented in Table 5.4.

Table 5.2 Optimised structures (PBE0/Def2-SV) of MnL(CO)$_3$(CH$_3$CN). Relative energies (kJ mol^{-1}) in the gas-phase and in CH$_3$CN solvent (in parentheses) are shown.[a]

[A2]	[B1]	[C2]
0	33.8	137
(0)	(54.7)	(173)

[A1]	[B2]	[C1]
8.36	46.6	160
(4.87)	(60.3)	(165)
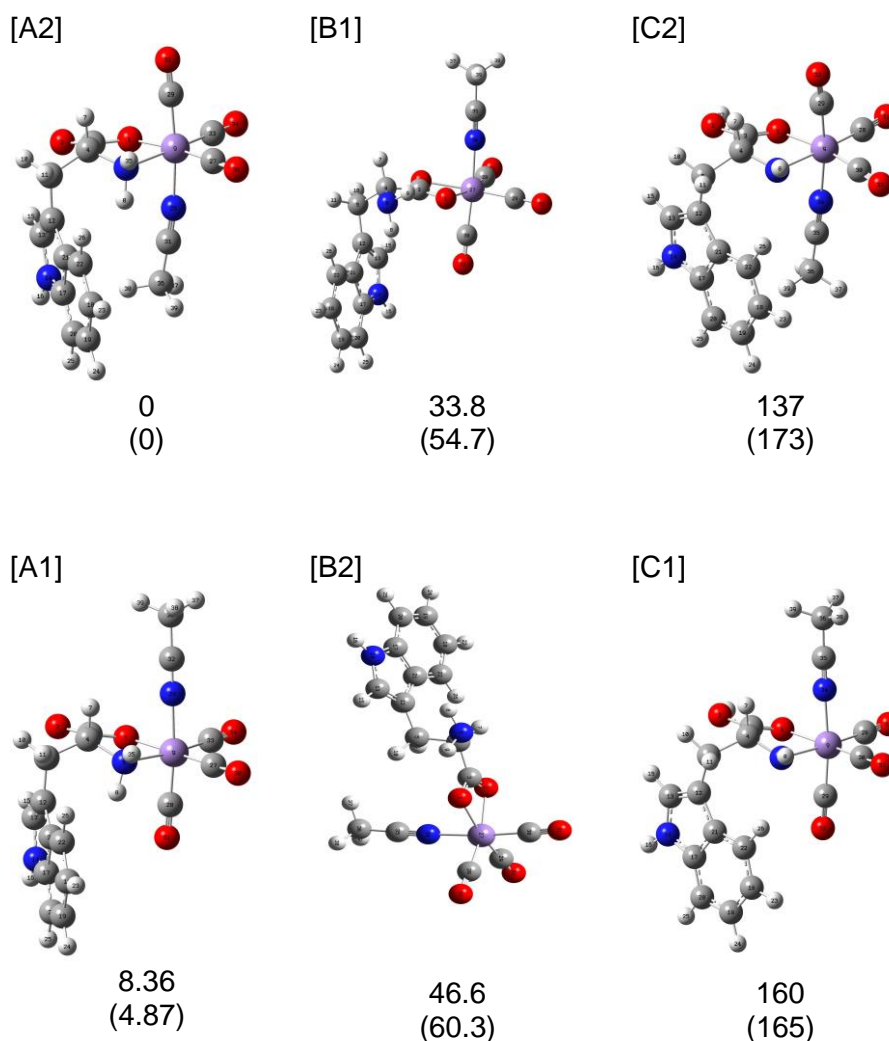
[a] Labels in square brackets follow assigned isomer names from Ref. [148].

DFT calculations performed by Ward et al. in Ref. [148] showed A1, A2, B1, and B2 similar in energy, however they excluded the presence of the B isomers on the account of the IR measured spectra and suggest the predominance of A1 and A2 structures, either individually or in an exchanging mixture.

Table 5.3 Optimised structures (PBE0/Def2-SV) of $[MnL(CO)_3(CH_3CN)]^{\cdot}H^+$. Relative

energies (kJ mol^{-1}) in the gas-phase and in CH$_3$CN solvent (in brackets) are shown.

[A2_O1]

[A2_O2]

[A1_O1]

0
(0)

34.0
(22.6)

42.0
(31.7)

[A1_O1]

[B1_N3]

[B2_N3]

6.92
(4.51)

35.7
(27.6)
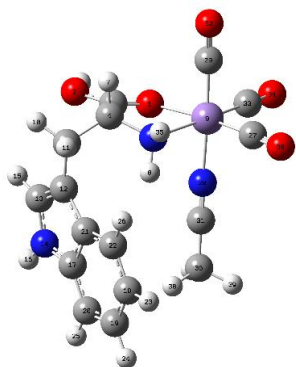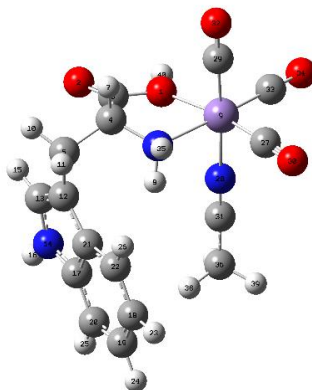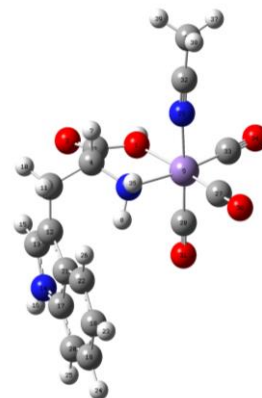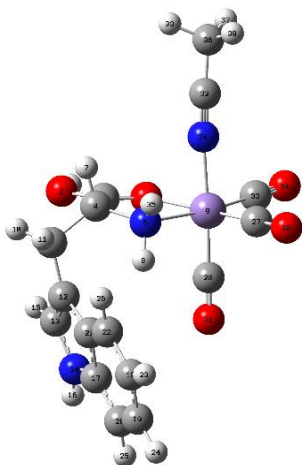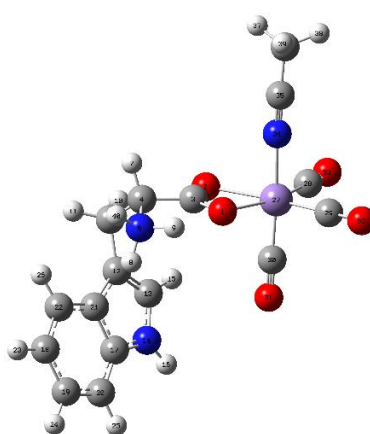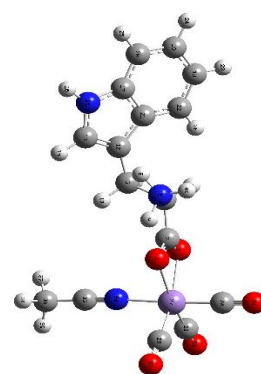
47.2
(23.8)

[a] The first part of the labels in square brackets follow assigned isomer names from
Ref. [148], with the second part referring to the protonation site (Scheme 5.1).

Table 5.4 Boltzmann Population of the isomers of [MnL(CO)3(CH3CN)]·H$^+$ presented in Table 5.3.

Structure	Gas-phase Boltzmann Population	Solution-phase Boltzmann Population
A2_O1	90.2	80.9
A1_O1	9.80	19.0
A2_O2	$1.66*10^{-3}$	$5.75*10^{-2}$
B1_N3	$9.60*10^{-4}$	$1.12*10^{-2}$
A1_O2	$1.27*10^{-4}$	$3.10*10^{-3}$
B2_N3	$2.45*10^{-5}$	$3.91*10^{-2}$

5.6.2. Computational Study of [MnL(CO)$_3$]·H$^+$ Geometry

To explore the possible geometric structures adopted by [MnL(CO)$_3$]$^.$H$^+$, we removed the CH$_3$CN group from the MnL(CO)$_3$(CH$_3$CN) structures displayed in Table 5.3, then introduced protons at the most favourable protonation sites (labelled 1-3 in Scheme 5.1 as well as directly on the Mn centre. Geometric optimisations were performed in Gaussian 09 at the PBE0/Def2-SV level, with frequency calculations being conducted to test that the structures obtained corresponded to true minima. Table 5.6 displays the resulting lowest-energy structures, along with their relative energies (non-zero point energy corrected). These structures include several where the indole ring (Scheme 5.3) coordinates directly to the vacant metal site (*i.e.* "folded" structures). Table 5.7 shows key distances between the Mn and the indole ring in the folded structures that suggest an η^2-bond. Finally, Table 5.8 presents the gas-phase and solution-phase Boltzmann populations for the structures presented in Table 5.6.
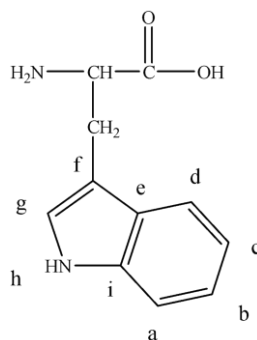
Scheme 5.3 2D structure of tryptophan with labels on the indole ring.

Table 5.6: Optimised structures (PBE0/Def2-SV) of $[MnL(CO)_3]^.H^+$.[a] Relative energies (kJ mol^{-1}) in the gas-phase and CH$_3$CN solvent (in brackets) are shown.
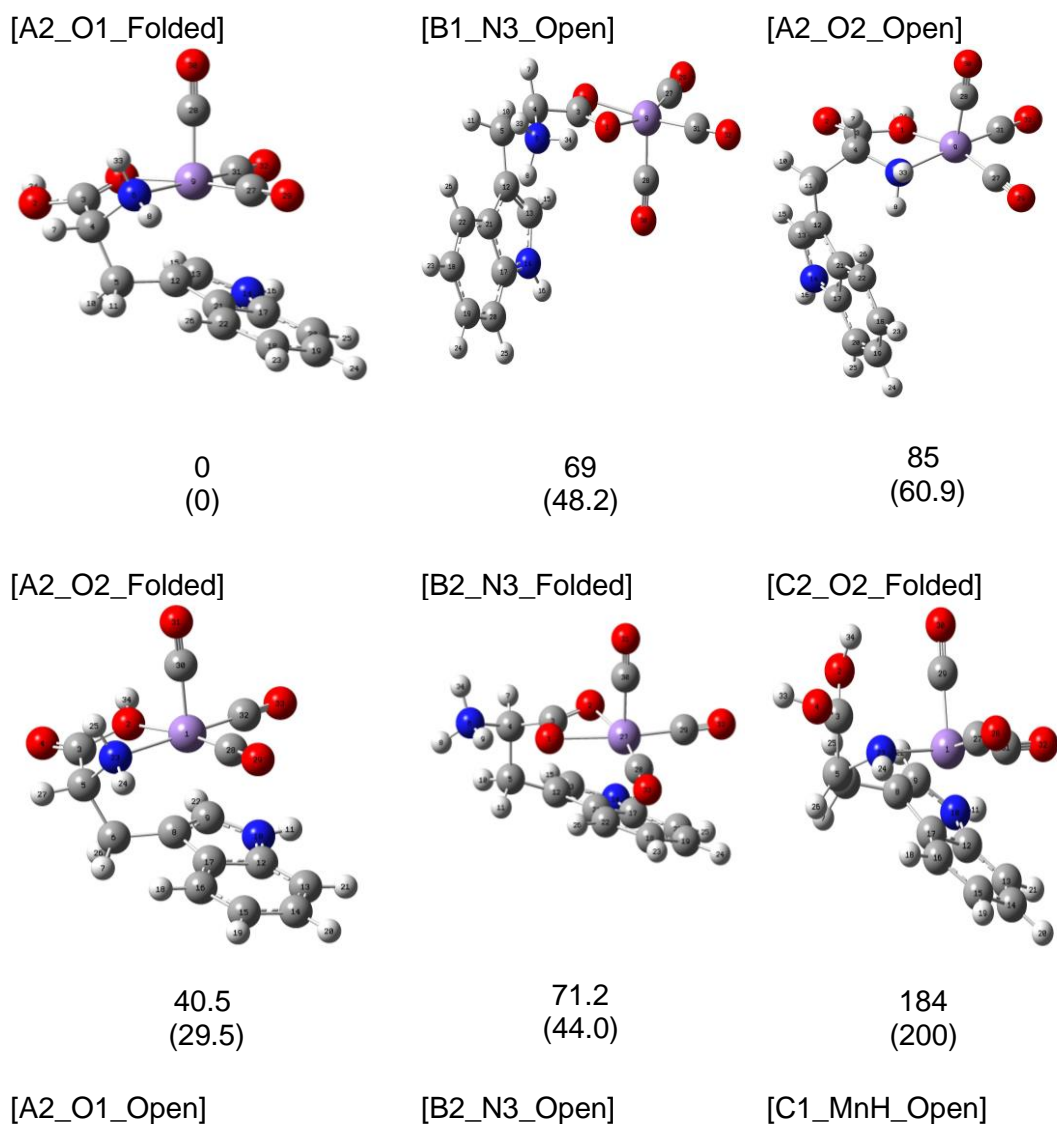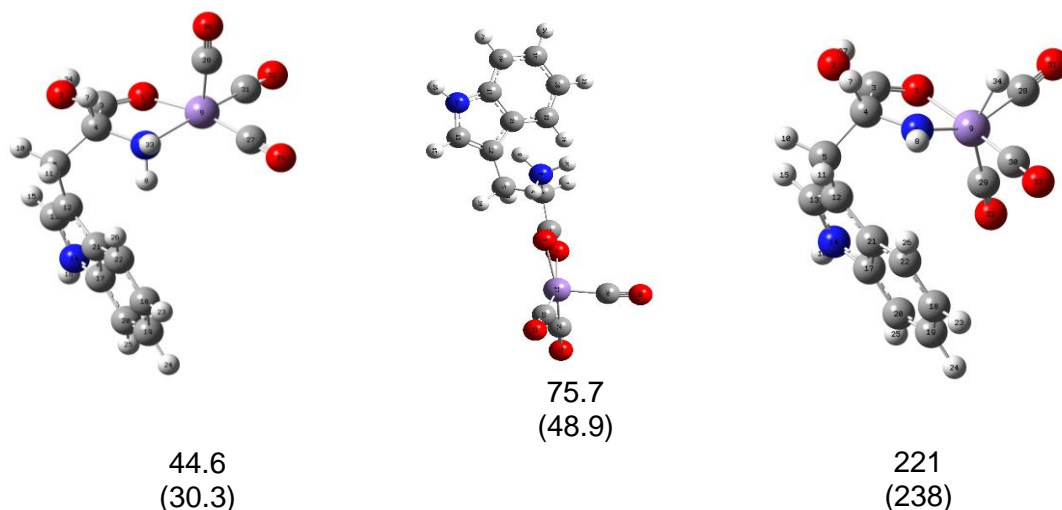
[A2_O1_Folded]

[B1_N3_Open]

[A2_O2_Open]

0
(0)

69
(48.2)

85
(60.9)

[A2_O2_Folded]

[B2_N3_Folded]

[C2_O2_Folded]

40.5
(29.5)

71.2
(44.0)

184
(200)

[A2_O1_Open]

[B2_N3_Open]

[C1_MnH_Open]

75.7
(48.9)

44.6
(30.3)

221
(238)

[a] The first part of the labels in square brackets follow assigned isomer names from Ref. [148], with the second part referring to the protonation site (Scheme 5.1). Folded refers to a structure where the metal centre closely coordinates with tryptophan (η^2), while open refers to a structure where the metal centre has a vacant coordination site.

Table 5.7: Distances between Mn and C and H atoms on the indole ring in the folded (η^2) structures. Only distances less than 3 Å are shown.

Structure	Bond	Bond Length (Å)
A2_O1_Folded	Mn-C_f	2.5
	Mn-C_g	2.6
	Mn-H_g	3.0
A2_O2_Folded	Mn-C_f	2.5
	Mn-C_g	2.5
	Mn-H_g	3.0
B2_N3_Folded	Mn-C_d	2.6
	Mn-H_d	2.7
	Mn-C_e	2.9
C2_O2_Folded	Mn-C_e	2.3
	Mn-C_f	2.4
	Mn-C_d	2.6
	Mn-H_d	2.9

Table 5.8: Boltzmann populations of the isomers of $[MnL(CO)_3] \cdot H^+$ at 373 K.

Structure	Gas-phase Boltzmann Population	Solution-phase Boltzmann Population
A2_O1_Folded	99.99	99.99
A2_O2_Folded	2.28×10^{-4}	7.77×10^{-3}
A2_O1_Open	6.13×10^{-5}	6.02×10^{-3}
B1_N3_Open	2.45×10^{-8}	1.93×10^{-5}
B2_N3_Folded	1.21×10^{-8}	7.43×10^{-5}
B2_N3_Open	2.85×10^{-9}	1.54×10^{-5}
A2_O2_Open	1.44×10^{-10}	3.29×10^{-7}
C2_O2_Folded	2.34×10^{-24}	1.38×10^{-26}
C1_MnH_Open	1.64×10^{-29}	7.03×10^{-32}

5.6.3 Hole-Burning Spectra of $[MnL(CO)_3]^{\cdot}H^+$

To verify that a single structural isomer of $[MnL(CO)_3] \cdot H+$ is present, hole-burning

spectra were obtained at 3347, 3494 and 3547 cm^{-1} (Figure 5.9) in the apparatus used

for CIVS. [183] [187] Hole-burning at these frequencies led to an overall decrease in

the general intensity of the entire spectrum, in line with the presence of just a single

structural isomer. Although multiple rotamers may be present, with very similar IR

absorption profiles, these are unlikely to display differing photochemical properties.

CIVS, therefore, demonstrates that a single conformational (and protonation) isomer

of $[MnL(CO)_3] \cdot H^+$ is present following electrospray ionisation, corresponding to the

A2_O1_Folded structure from Table 5.6.
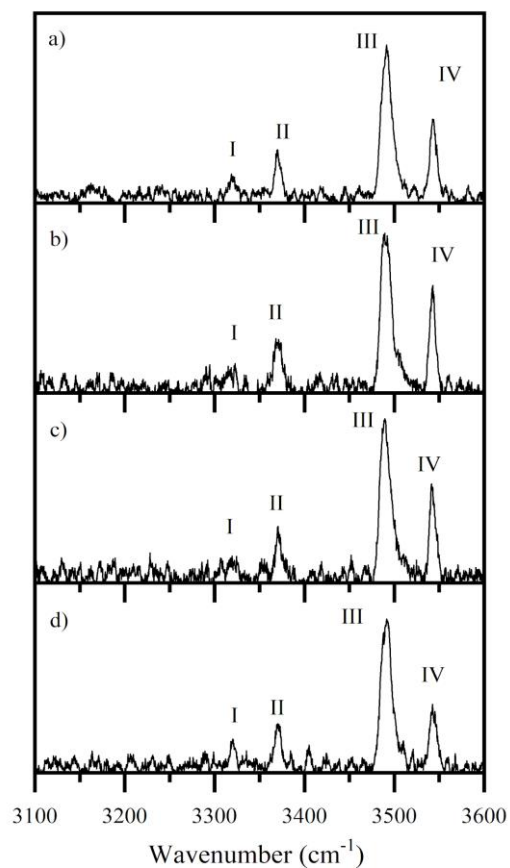
Figure 5.9: a) The gas-phase IR spectrum of $[Mn(CO)_3(L)] \cdot H^+$, with hole-burning spectra obtained at b) 3347, c) 3494 and d) 3547 cm^{-1}.

Chapter 6

Probing the Photochemical Properties of Metal-Carbonyls:

From Gas Phase to Solution

6.1 Introduction

Substituted metal carbonyls are widely studied for their photoreactivity. They are excellent photocatalysts (and precursors) for organic reactions, [289] [290] and intermediates for the synthesis of organometallics. [291] In current high-profile studies, they are also being investigated for the photocatalytic reduction of CO_2 to CO or formic acid. [292-294]

The use of metal carbonyls as CO-releasing molecules (CORMs) [127] is a promising area of research in medicinal chemistry. [86] [126] [262-265] CORMs are an efficient way to administer CO in a controlled manner, with CO release being activated once the drug reaches the disease site. Some CORMs release CO upon light activation (Photo-CORMs), with efficiencies that are frequently wavelength-dependent. [148] An ideal PhotoCORM releases CO in the visible or Near-IR spectral range to maximise skin penetration and minimise UV-induced side effects. [142] [143]

The CO-releasing properties of metal carbonyls can be tuned to achieve maximum CO photorelease at the medically suitable wavelengths by applying the principles of rational design. The metals that are chosen in this study are in a low-spin d^6 configuration, and can, therefore, access metal-to-ligand charge-transfer transitions (MLCT) leading to M-CO labilisation and CO release. The use of conjugate ancillary ligands, with low-lying π^* orbitals, can shift the absorption wavelength to the red, compared to homoleptic metal carbonyls. [144]

The interaction of substituted metal carbonyls with light can, therefore, be considered to be a fundamental property that can be employed for a range of photochemical

183

functions. It is therefore desirable to have robust theoretical methods that can predict their photochemistry. However, a lack of gas-phase studies on these systems means that there is currently a lack of data available that can be readily compared with computational results. [144] [284] [295] In this work, we investigate the intrinsic (*i.e.* gas-phase) CO releasing photochemistry of a series of metal carbonyls *via* laser-interfaced mass spectrometry (LIMS). [8] [173] LIMS is a way to transfer a molecule of interest from solution to the gas phase that allows the study of the complex's intrinsic photochemistry. However, gas-phase studies inevitably lead to questions about how these results link to solution-phase photochemistry. In this work, we try to address this issue directly by testing a new on-line photolysis system that allows us to compare the gas-phase results to solution-phase photochemistry.

Our gas-phase LIMS approach measures all the ionic photoproducts simultaneously with the gaseous absorption spectrum, thus providing a direct measurement of the number of CO units ejected per photon-interaction with the molecule and of the identity of the residual photofragments. We use higher-energy collisional dissociation (HCD) to identify the thermal fragments, and also to study the intrinsic stability of the species of interest.

For this study, we focus on two ruthenium metal carbonyl molecules, $[Ru(\eta^5\text{-}C_5H_5)(PPh_3)_2CO]^+$ and $[Ru(\eta^5\text{-}C_5H_5)(dppe)CO]^+$ (dppe = 1,2-Bis(diphenylphosphino)ethane) along with a Mn-centred complex, $[Mn(CO)_4Br_2]^-$ (EBOR-CORM-1) (Scheme 6.1). Ruthenium half-sandwich complexes are currently employed in a wide range of different applications, from catalysis – where they are used in transfer hydrogenation and alcohol oxidation reactions- [296-298] to anticancer drugs. [299] [300]

EBOR-CORM-1 was recently shown to be efficient against the bacterium *Pseudomonas aeruginosa.* [152] Although it releases CO spontaneously upon dissolution in water (*i.e.* a water-triggered CORM), it can be studied as a prototype of a PhotoCORM, since CO release can also be triggered by light. The three complexes selected for this study are ionic in their native forms, which allowed straightforward electrospray ionisation to transfer the molecules from solution to the gas-phase.
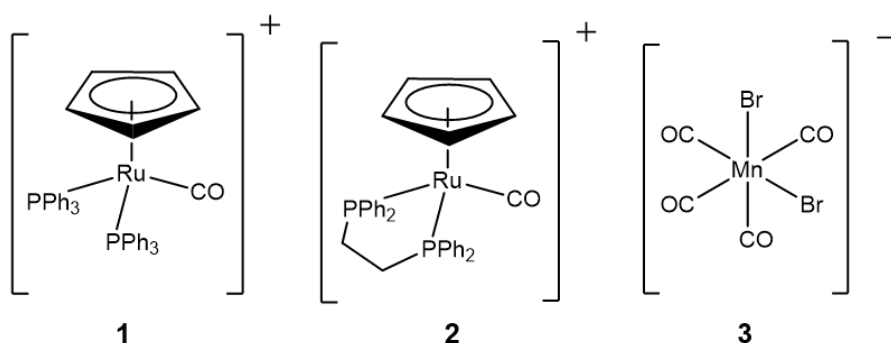
Scheme 6.1 Structures of **1**) $[Ru(\eta^5\text{-}C_5H_5)(PPh_3)_2CO]^+$, **2**) $[Ru(\eta^5\text{-}C_5H_5)(dppe)CO]^+$ and **3**) $[Mn(CO)_4Br_2]^-$.

6.2 Method

All chemicals were synthesised, in the Lynam and Fairlamb groups, according to previously published protocols. [152] [301] $[Ru(\eta^5\text{-}C_5H_5)(PPh_3)_2CO][PF_6]$ and $[Ru(\eta^5\text{-}C_5H_5)(dppe)CO][PF_6]$ were electrosprayed at 100° C from a 10^{-5} M solution of DCM:MeOH (3:1) and analysed in positive ion mode. PD spectra were acquired across the range 3.2-5.2 eV at ~1 mJ laser power. $[NEt_4][Mn(CO)_4Br_2]$ ($[NEt_4]$ = tetraethylammonium) was electrosprayed at 100° C from a 10^{-5} M solution of DCM and analysed in negative ion mode. For this species, the PD spectrum was acquired across the range 2.4-5.3 eV at ~1 mJ laser power.

Higher-energy collision-induced dissociation (HCD) was performed on both $[Ru(\eta^5\text{-}C_5H_5)(PPh_3)_2CO]^+$ and $[Ru(\eta^5\text{-}C_5H_5)(dppe)CO]^+$ electrosprayed from 10^{-6} M solution in DCM:MeOH 3:1. HCD was performed on the instrument described in Section 2.2,

using the quadrupole as the mass isolator and the Orbitrap as the mass analyser. For $[MnCO_4Br_2]^-$, HCD was performed on a 10^{-4} M solution in DCM, using the ion trap as the mass analyser.

Solution-phase photofragmentation spectra were obtained *via* irradiation of the CORM solutions with the on-line photolysis system described in Section 2.3. In this experiment, the mass spectrum of the solution was acquired for a minute, to provide a baseline MS, before turning on the respective LED. The syringe flow rate was 25 ml/h, and the mass spectra were acquired continuously. Once the LED was turned on, the solution was irradiated during the time needed to flow through the transparent capillary (approximately 70 μs).

Solution-phase UV-Vis absorption spectra (10^{-4} mol dm^{-3}) were recorded using a Shimadzu 1800 UV spectrophotometer with a 1 cm UV cuvette, using the relevant solvent as a baseline. DCM was used as the solvent for for $[Mn(CO)_4Br_2]^-$, and DCM:MeOH 3:1 for $[Ru(\eta^5-C_5H_5)(PPh_3)_2CO]^+$ and $[Ru(\eta^5-C_5H_5)(dppe)CO]^+$.

Density functional theory (DFT) was used to calculate the optimised, global minimum structures of the three complexes. Complexes **1** and **2** were studied at the PBE0/Def2TZVP level, with Stuttgart/Dresden ECP on Ru. Geometry optimisation for complex **3** was performed using PBE0 with the 6-31+G* basis set for the CO and the Mn; 6-31G* was used on Br; and Stuttgart/Dresden ECP was used for Mn, Br. The electron vertical detachment energy (VDE) was also calculated for complex **3** (Figure 6.13a). The calculations of the VDE were conducted at the PBE0/Def2-TZVPP level of theory. TDDFT calculations were used to predict the electronic excitation spectrum of complex **1** at a number of different levels of theory for comparison against the experimental results.

6.3 Results and discussion

6.3.1 Ruthenium Half-Sandwich Carbonyls

Complexes **1** ([Ru(η^5-C$_5$H$_5$)(PPh$_3$)$_2$CO]$^+$) and **2** ([Ru(η^5-C$_5$H$_5$)(dppe)CO]$^+$) have the same Ru(II)(η^5-C$_5$H$_5$)CO scaffold, with the two remaining coordination sites being occupied with either two triphenylphosphine ligands (**1**) or a chelating dppe ligand (**2**). Figure 6.1 shows the calculated structures of complexes **1** and **2**.
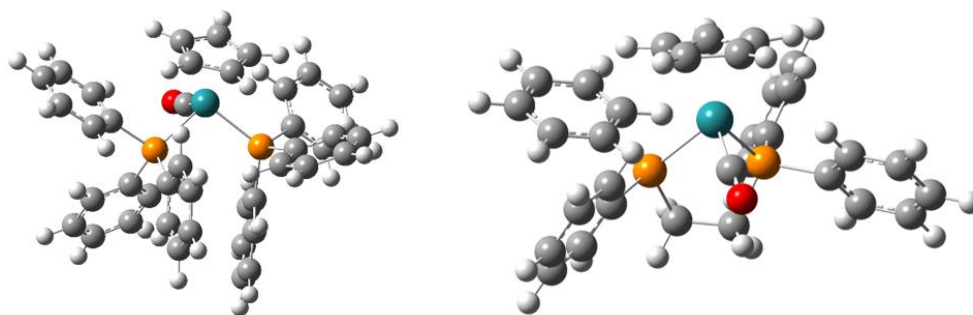
Figure 6.1 Global minimum structures of (left) **1** and (right) **2** at the PBE0/Def2-SV level with ECP on Ru.

Figures 6.2a and b show the mass spectra of the electrosprayed solutions of complexes **1** and **2**, respectively (the computational structures are compared to crystal structures in Table 6.1 and 6.2). We note that the low intensity of fragment ions in these spectra indicates that the parent compounds are stable solution- and gas-phase species, and do not readily fragment within the source or during the electrospray process.

Table 6.1 Comparison between main structural elements in the $[Ru(\eta^5\text{-}C_5H_5)(PPh_3)_2CO]^+$ calculated and crystal structures from Ref. [302]

	Experimental[a]	Computational
Ru-C(O) (Å)	1.89(2)	1.86
Ru-P (Å)	2.35(13), 2.36(7)	2.37
P-Ru-P (°)	97.8(4)	103
P-Ru-CO (°)	91.5(3)	89.9
CO-Ru-P (°)	97.8(3)	91.8

[a] As reported in Ref. [302] for the $[Co(CO)_4]^-$ salt

Table 6.2 Comparison between main structural elements in the calculated $[Ru(\eta^5\text{-}C_5H_5)(dppe)CO]^+$ and the crystal $[Ru(\eta^5\text{-}C_5H_5)(dppe)Cl]$ structure from Ref. [303]

	Experimental[a]	Computational
Ru-X[b] (Å)	2.45(2)	1.80[c]
Ru-P (Å)	2.28(2)	2.32
P-Ru-P (°)	83.5(1)	83.7
P-Ru-X (°)	83.0(1)	88.5
X-Ru-P (°)	93.3(1)	89.7
P-CH_2-CH_2-P (°)	-50.2	-41.2

[a] As reported in Ref. [303] for the $CDCl_3$ cluster.
[b] X = Cl in the experimental and C (carbonyl) in the computational structure.
[c] The difference in the bond length can be explained with the back-bonding between the metal and the carbonyl.
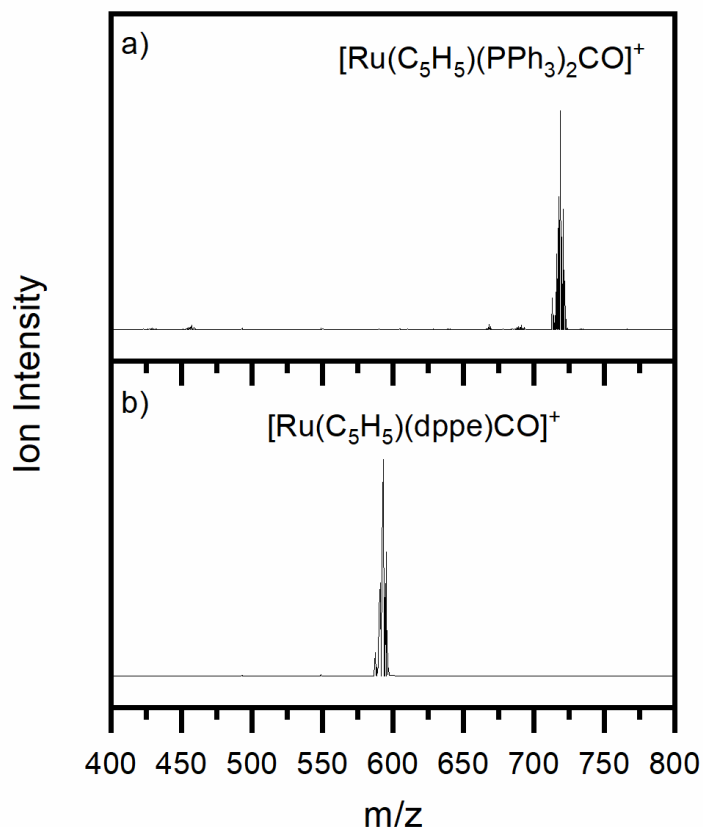
Figure 6.2 Positive ion mode electrospray mass spectrum of (a) [Ru(η^5-C$_5$H$_5$)(PPh$_3$)$_2$CO][PF$_6$] and (b) [Ru(η^5-C$_5$H$_5$)(dppe)CO][PF$_6$].

6.3.1.i Solution and Gas-Phase Absorption Spectra of [Ru(η^5-C$_5$H$_5$)(PPh$_3$)$_2$CO]$^+$ and [Ru(η^5-C$_5$H$_5$)(dppe)CO]$^+$

The gas-phase absorption spectra of [Ru(η^5-C$_5$H$_5$)(PPh$_3$)$_2$CO]$^+$ and [Ru(η^5-C$_5$H$_5$)(dppe)CO]$^+$ obtained *via* UVPD are presented in Figure 6.3. They are very similar to each other and display three distinct bands which are labelled **I**, **II** and **III** peaking at ~ 3.9, 4.6 and 5.1 eV for **1** and ~ 4.0, 4.5 and 5.2 eV for **2**. Band **II** for complex **1** (Figure 6.3a) is more evident in the photofragmentation action spectrum of this species, which is shown below, in Figure 6.6a. Figure 6.4 displays the solution-phase absorption spectra of [Ru(η^5-C$_5$H$_5$)(PPh$_3$)$_2$CO][PF$_6$] and [Ru(η^5-C$_5$H$_5$)(dppe)CO][PF$_6$] which agree with the gas-phase spectra. This similarity is consistent with single-photon absorption in the gas-phase spectra.
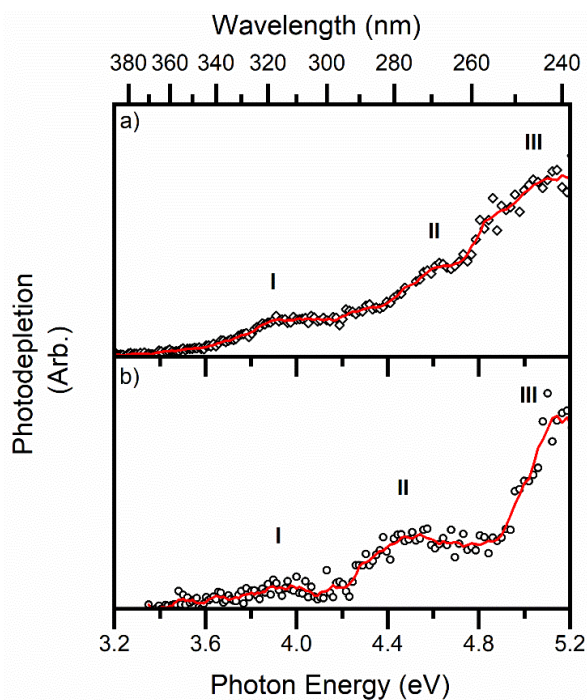
Figure 6.3 Photodepletion (gas-phase absorption) spectra of complexes a) **1** and b) **2**. Spectra are recorded across the range 3.2-5.2 eV. The solid lines are five-point adjacent averages of the data points.
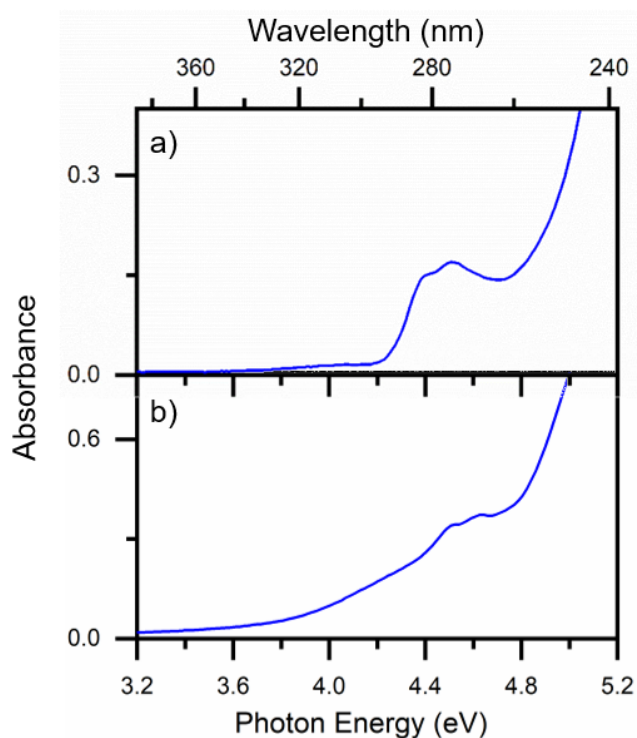
Figure 6.4 Solution-phase absorption spectra of [Ru(η^5-C$_5$H$_5$)(PPh$_3$)$_2$CO][PF$_6$] and (b) [Ru(η^5-C$_5$H$_5$)(dppe)CO][PF$_6$] in DCM:MeOH (3:1) between 3.2 and 5.2 eV.

6.3.1.ii Photodissociation pathways of $[Ru(\eta^5\text{-}C_5H_5)(PPh_3)_2CO]^+$ and $[Ru(\eta^5\text{-}C_5H_5)(dppe)CO]^+$

To obtain the gas-phase absorption and photofragmentation action spectra of **1** and **2**, the complexes were isolated in the ion trap and subjected to laser excitation. Figures 6.5a and 6.5b show the mass spectra of the ionic fragments produced following photoexcitation at 4.6 eV (270 nm) of **1** and **2**, respectively.
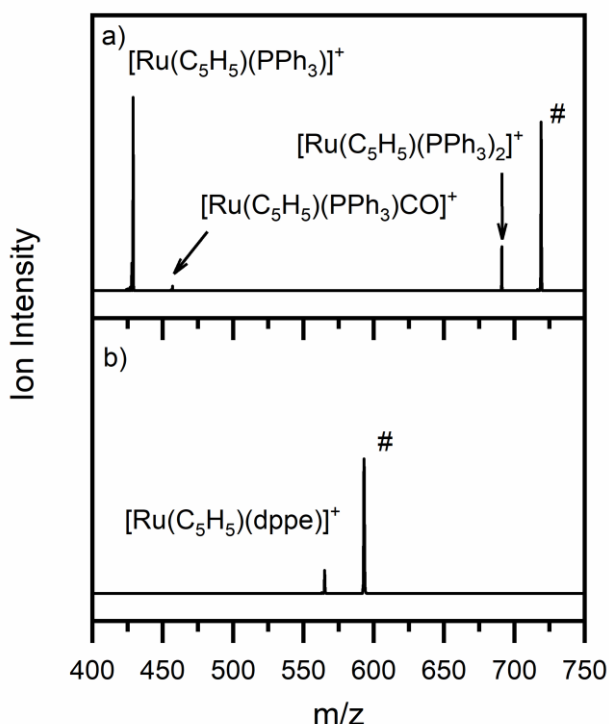
Figure 6.5 Photofragment mass spectra of (a) $[Ru(\eta^5\text{-}C_5H_5)(PPh_3)_2CO]^+$ and (b) $[Ru(\eta^5\text{-}C_5H_5)(dppe)CO]^+$ at 4.6 eV. # indicates the parent ion.

The main photofragment obtained upon laser-induced fragmentation of **1** (Figure 6.5a) corresponds to the loss of both a CO and a PPh_3 ligand from the precursor ion:

$$[Ru(\eta^5\text{-}C_5H_5)(PPh_3)_2CO]^+ + h\nu \quad \rightarrow \quad [Ru(\eta^5\text{-}C_5H_5)(PPh_3)]^+ + CO + PPh_3 \qquad (6.1a)$$
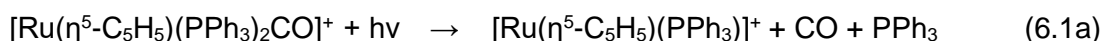
with additional fragments being produced corresponding to the photoinduced loss of either CO or PPh_3:

$$[Ru(\eta^5\text{-}C_5H_5)(PPh_3)_2CO]^+ + h\nu \quad \rightarrow \quad [Ru(\eta^5\text{-}C_5H_5)(PPh_3)_2]^+ + CO \qquad (6.1b)$$

$$[Ru(\eta^5\text{-}C_5H_5)(PPh_3)_2CO]^+ + h\nu \quad \rightarrow \quad [Ru(\eta^5\text{-}C_5H_5)(PPh_3)CO]^+ + PPh_3 \qquad (6.1c)$$
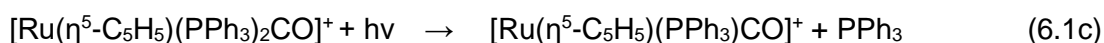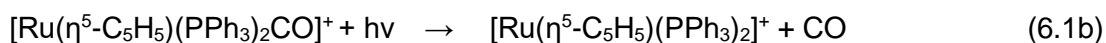
The formation of any by-products with the loss of PPh_3 upon photofragmentation would be considered undesirable both if complex **1** was under consideration as a PhotoCORM (PPh_3 is toxic for the humans), but also for other applications initiated by CO photorelease such as ligand substitution. [304]

To avoid this undesirable photoproduct, compound **2** offers a good alternative, considering that dppe is a chelating ligand and is, therefore, less likely to dissociate from the metallic centre. [76] Photoexcitation of **2** at 4.6 eV produces the photofragment mass spectrum shown in Figure 5b, with only a single photofragment corresponding to the loss of the carbon monoxide unit from the parent ion, with the dppe ligand remaining bound to the metal centre:

$$[Ru(\eta^5\text{-}C_5H_5)(dppe)CO]^+ + h\nu \quad \rightarrow \quad [Ru(\eta^5\text{-}C_5H_5)(dppe)]^+ + CO \qquad (6.2)$$
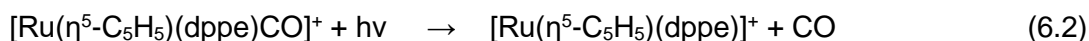
Indeed, $[Ru(\eta^5\text{-}C_5H_5)(dppe)]^+$ is the only significant photofragment observed across the entire spectral range.

A wavelength-dependent picture of the photochemistry of complexes **1** and **2** can be obtained by presenting the photofragment production spectra across the full spectral range. These plots are displayed in Figure 6.6. Photofragmentation of $[Ru(\eta^5\text{-}C_5H_5)(PPh_3)_2CO]^+$ (Figure 6.6a) follows the pathways illustrated by Eqs (6.1a-c). Above the onset at 3.2 eV, fragmentation according to Eq. 6.1b, where CO is ejected from the precursor ion, seems to be constant between 3.8 and 5.2 eV. The most intense photofragment is produced by the process shown in Eq. (6.1a) (*i.e.* from the loss of CO and PPh_3) across three main bands at 4.0, 4.6 and 5.1 eV. The loss of just

PPh$_3$ (Eq. 6.1c) is a minor channel, which shows a modest increase in intensity at the highest energies.
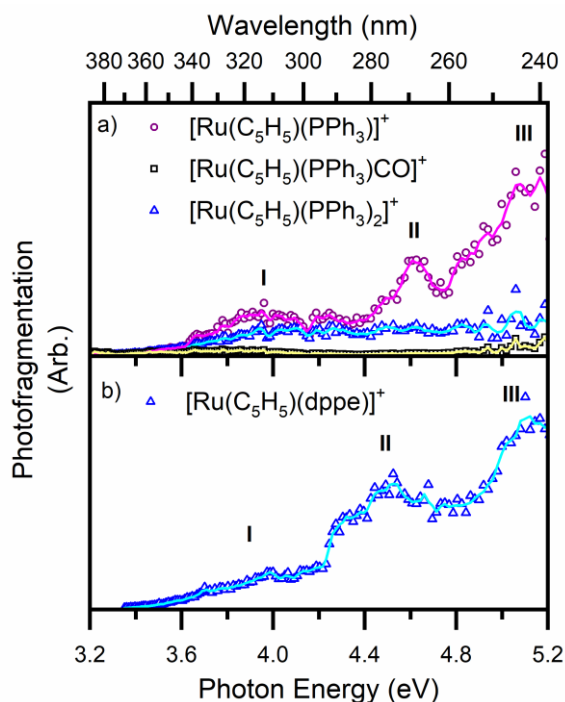
Figure 6.6 Photofragment production spectra from the complex ions a) **1** and b) **2**. Spectra are recorded across the range 3.2-5.2 eV. The solid lines are two-point adjacent averages of the data points.

Photofragmentation of **1** can also be represented as ion-yield spectra, which are shown in Figure 6.7. The loss of CO and PPh$_3$ (Eq. 6.1a) is the strongest channel at all energies above 3.4 eV, but the loss of solely CO (*i.e.* Eq. 6.1b) is enhanced at energies around 3.7 and 4.2 eV. At the lowest energies (3.2 to 3.4 eV), the loss of a single PPh$_3$ represents the strongest fragmentation pathway (Eq. 6.1c), although this channel falls away dramatically as internal energy increases.
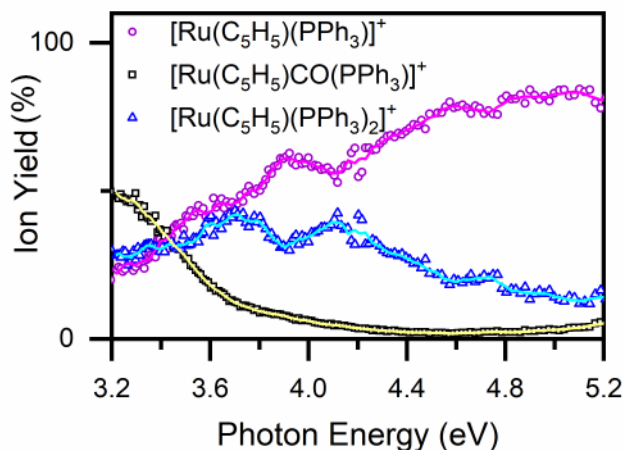
Figure 6.7 Ion yield spectra of the photofragments produced from complex **1** in the region between 3.2 and 5.2 eV. The solid lines are five-point adjacent averages of the data points.

Figure 6.6b shows the photofragment production spectrum of the $[Ru(\eta^5\text{-}C_5H_5)(dppe)]^+$ photofragment from complex **2**. This displays a profile that closely matches the gaseous absorption spectrum (Figure 6.3b), consistent with the loss of CO, leading to the only observed photofragment.

Comparison of the photodissociation results for $[Ru(\eta^5\text{-}C_5H_5)(PPh_3)_2CO]^+$ and $[Ru(\eta^5\text{-}C_5H_5)(dppe)CO]^+$ illustrates the potential of the technique as a tool to characterise the intrinsic photochemical properties of photoactivable metal carbonyls, as well as its potential for aiding the rational design of future photolabile complexes. Following our observation of the photofragments from complex **1**, we were motivated to develop complex **2** which prevents the loss of triphenylphosphine by using the chelating dppe ligand.

6.3.1.iii Computational Absorption Spectra of $[Ru(\eta^5\text{-}C_5H_5)(PPh_3)_2CO]^+$

To obtain further information on the photofragmentation channels that are shown in Figure 6.7, it is useful to understand the orbitals that are involved in the transitions where photofragment production is strongest. TDDFT calculated absorption spectra

of **1**, obtained at a number of different levels of theory are shown in Figure 6.8. B3LYP/6-31G* with SDD on Ru provides the calculated spectrum that is closest to our experimental results. Comparison between the TDDFT methods and our experimental results represent, therefore, a good example of how our experimental data provide an excellent benchmark for computational methods.

Table 6.1 reports a comparison between the experimental and computational absorption energy, and Table 6.2 shows the main transitions between 3 and 4.7 eV predicted at the B3LYP/6-31G* level with SDD basis set on Ru. [305-307] The orbitals that are involved in these transitions are shown in Figure 6.9. The orbital character in these calculations is always a combination of the metal d orbitals and the ligand π orbitals. At all the explored theory levels, numerous highly mixed transitions are predicted at energies higher than 4.7 eV.
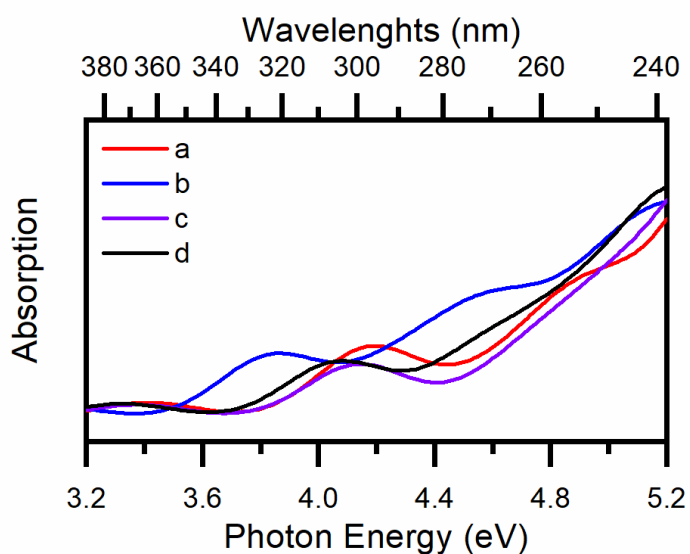
Figure 6.8 Calculated absorption spectra of complex **1** at a) PBE0/6-31G*, b) B3LYP/6-31G*, c) PBE0/Def2-SV and d) B3LYP/Def2-SV theory levels. ECP core potential of Ru is always included.

Table 6.3 Comparison between experimental absorption maxima and calculated absorption maxima at different levels of theory. The energies are given in eV.

Experimental	PBE0 6-31G*	B3LYP 6-31G*	PBE0 Def2-SV	B3LYP Def2-SV
-	3.4	3.1	3.4	3.3
3.9	4.2	3.8	4.1	4.1
4.6	4.8	4.6	4.8	4.8
5.1	5.4	5.2	5.4	5.2

Table 6.4 Calculated TDDFT transition energies and oscillator strengths of complex **3**. Calculations were performed at the B3LYP/6-31G*/SDD level. Only transitions below 4.7 eV with oscillator strength > 0.01 are listed.

Orbital transitions	Photon energy eV	f
(0.87)170→171	3.06	0.0151
(0.72)170→172	3.75	0.0147
(0.48)169→171 (0.10)170→172	3.85	0.0615
(0.54)169→172	4.17	0.0267
(0.52)168→172	4.31	0.0274
(0.25)167→171 (0.16)156→172	4.37	0.0199
(0.34)166→171 (0.17)168→171	4.51	0.0204
(0.23)166→171	4.57	0.0264
(0.65)170→173	4.60	0.0225
(0.58)162→171	4.67	0.0124
(0.29)170→174	4.67	0.142
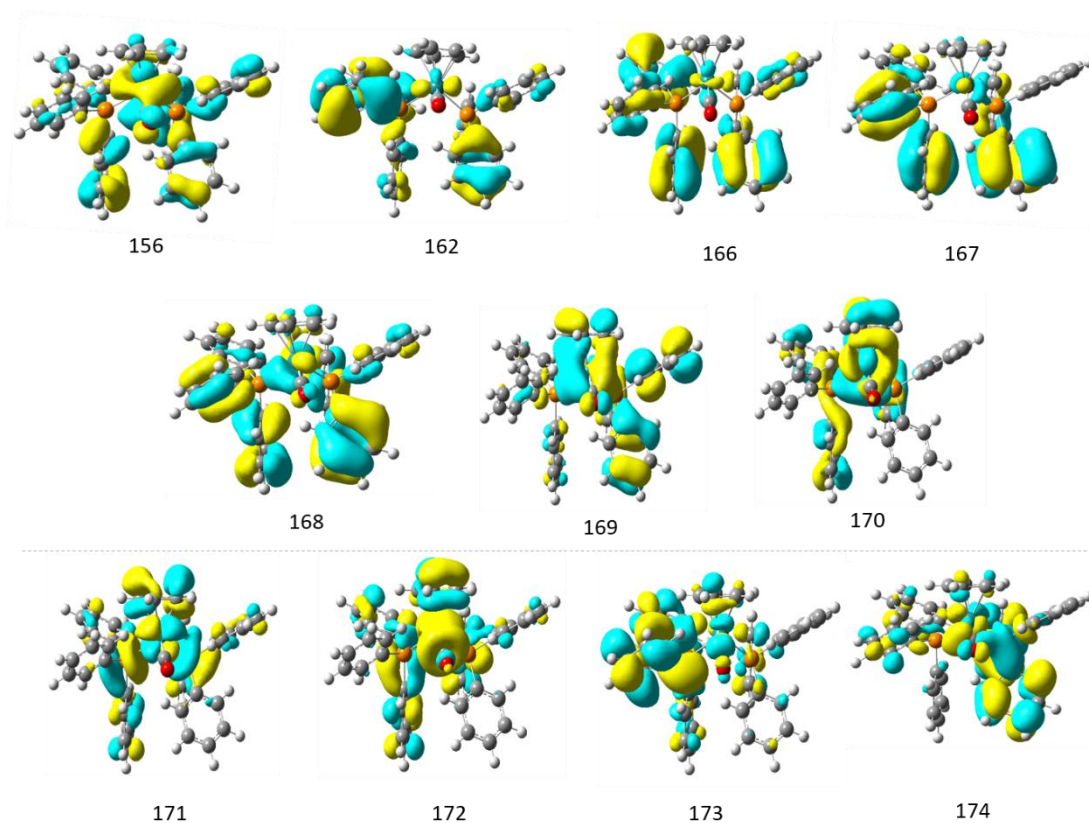
Figure 6.9 Molecular orbitals of **1** involved in the transitions predicted by TDDFT calculations between 3.06 – 4.67 eV described in Table 6.1. The iso-value for each orbital surface is 0.02 e/au^3. Separation between occupied and unoccupied orbitals is shown.

We can associate the TDDFT transitions in Table 6.2 with the ion yields displayed in Figure 6.7. The HOMO-LUMO (170-171) transition at 3.1 eV induces the loss of PPh$_3$ that is the main photofragment below 3.4 eV. At 3.7 and 4.2 eV, peaks in CO loss can be attributed to transfer of the electron density from the HOMO and the HOMO-1 to the LUMO+1 orbital (172). The peak at 3.9 eV, associated with increased loss of both CO and PPh$_3$, involves transfer to both the LUMO and LUMO+1. Comparing these results with the ion-yield spectra in Figure 6.7, it seems that an electron transfer to the LUMO (at 3.1 and 3.9 eV) leads to PPh$_3$ photodissociation, while a transfer to the LUMO+1 (at 3.7, 3.9 and 4.2 eV) causes the CO loss.

6.3.1.iv Thermal Fragmentation $[Ru(\eta^5\text{-}C_5H_5)(PPh_3)_2CO]^+$ and $[Ru(\eta^5\text{-}C_5H_5)(dppe)CO]^+$

Figure 6.10 shows the HCD spectra of **1** and **2**. The two compounds can be seen to be stable in the gas-phase, as neither fragments below 10% HCD energy. The thermal loss of CO from compound **1** (Eq. 6.1b) represents only a minor thermal fragmentation channel between 10 and 25% HCD Energy (Insert in Figure 6.10a). This indicates that loss of CO from compound **1** *via* heat activation is likely to be inefficient. In contrast, the loss of just PPh_3 (Eq. 6.1c) is to be the lowest-energy thermal gas-phase fragmentation pathway. These results mirror the observation by Crawford *et al.* where energy-dependent ESI was used to probe thermal fragmentation of $[Ru_6C(CO)_{16}(PPh_3)+OMe]^-$ by varying the source cone voltage. [116] They showed that, for this cluster, the phosphine ligand was lost first in the collision-induced fragmentation process. At higher HCD energies (> 20%) the $[Ru(\eta^5\text{-}C_5H_5)(PPh_3)]^+$ ion is produced as a secondary fragment from $[Ru(\eta^5\text{-}C_5H_5)(PPh_3)CO]^+$, as denoted by $[Ru(\eta^5\text{-}C_5H_5)(PPh_3)CO]^+$ simultaneous decay. We also note that this ion is the main photoproduct (Figure 6.6a) above 3.4 eV.
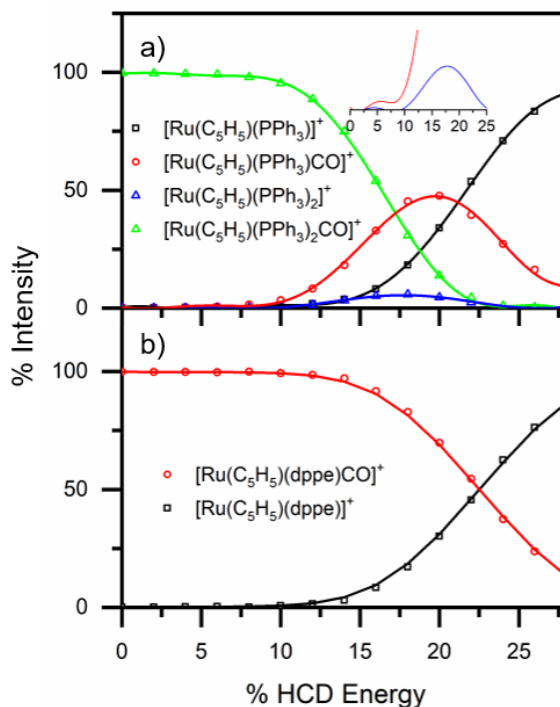
Figure 6.10 HCD spectra of complex ions (a) **1** and (b) **2** between 0 and 28% HCD energy. The insert in (a) shows the expanded section of the HCD spectrum between 0 and 25% and represents PPh$_3$ and CO loss as in Eqs (6.1b and 6.1c).

6.3.2 EBOR-CORM-1

Figure 6.11 shows the structure of the [Mn(CO)$_4$Br$_2$]$^-$ (EBOR-CORM-1) complex, [152] calculated by DFT at the PBE0/6-31+G* level with 6-31G* on Br and ECP on Mn and Br. This complex is a pseudo-octahedron with two *cis* bromides and four CO molecules binding to the Mn centre in a C$_{2v}$ symmetry. [152]
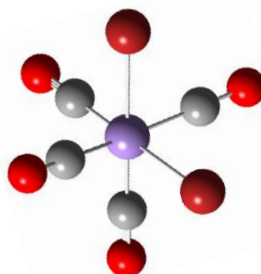
Figure 6.11 Calculated geometry of complex 3 at the PBE0/6-31+G* basis set for the CO and the Mn; 6-31G* on Br; and Stuttgart/Dresden ECP on Mn and Br.

6.3.2.i Thermal Fragmentation of [Mn(CO)$_4$Br$_2$]$^-$

Figure 6.12 shows the negative ion mode electrospray mass spectrum of a solution
of [NEt$_4$][Mn(CO)$_4$Br$_2$] in DCM. The anionic chromophore, [Mn(CO)$_4$Br$_2$]$^-$, is visible in
the mass spectrum, but the [Mn(CO)$_3$Br$_2$]$^-$ fragment ion formed *via* CO ejection:

$$[Mn(CO)_4Br_2]^- \quad \rightarrow \quad [Mn(CO)_3Br_2]^- + CO \qquad \qquad (6.3a)$$
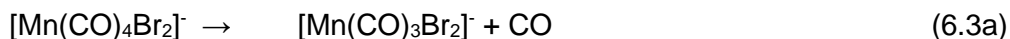
is the dominant species. This indicates that the precursor ion, [Mn(CO)$_4$Br$_2$]$^-$, is a
metastable complex, with a low barrier to CO loss. We note that the parent ion may
be fragmenting during the electrospray process, however, it may also be subject to
dissociation in DCM. This process is likely to occur as it was proven that [Mn(CO)$_4$Br$_2$]$^-$
releases CO in water. [152]

Several other lower m/z ions are evident in the mass spectrum, associated with
additional fragmentation channels:

$$[Mn(CO)_4Br_2]^- \quad \rightarrow \quad [Mn(CO)Br_2]^- + 3CO \qquad \qquad (6.3b)$$

$$[Mn(CO)_4Br_2]^- \quad \rightarrow \quad [MnBr_2]^- + 4CO \qquad \qquad (6.3c)$$
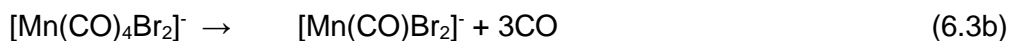
[MnBrO$_2$]$^-$ is also present in the electrospray mass spectrum. We believe that this
species is formed from the reaction of [MnBr$_2$]$^-$ (formed from Eq. 6.3c) with residual
O$_2$ that is present in the ion trap.
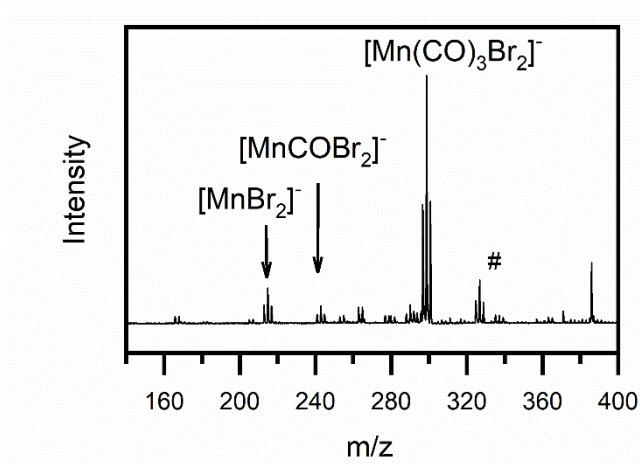
Figure 6.12 Negative ion mode mass spectrum of [NEt$_4$][Mn(CO)$_4$Br$_2$] in DCM. # indicates the parent ion

Figure 6.13 shows the HCD results for [Mn(CO)$_4$Br$_2$]$^-$. Even at 0 % HCD energy, the intact precursor ion, [Mn(CO)$_4$Br$_2$]$^-$, represents only ~ 5 % of the total ions, while ~ 75 corresponds to the [Mn(CO)$_3$Br$_2$]$^-$. The extent of [Mn(CO)$_4$Br$_2$]$^-$ fragmentation indicates that this species is significantly less intrinsically stable than the cationic complexes studied above.
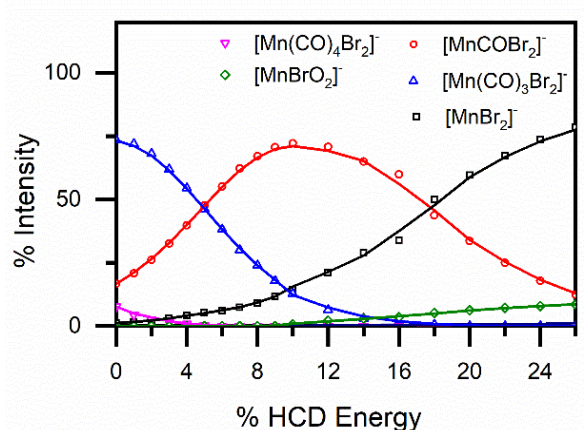
Figure 6.13 HCD spectrum of [Mn(CO)$_4$Br$_2$]$^-$ between 0 and 26% HCD energy.

6.3.2.ii Solution and Gas-Phase Absorption Spectra of [Mn(CO)$_4$Br$_2$]$^-$

Figure 6.14a displays the gas-phase absorption spectrum of [Mn(CO)$_4$Br$_2$]$^-$. this shows a weak absorption band in the key visible region of the spectrum between 2.6

and 3.4 eV arising from an MLCT transition. Therefore, the absorption onset of $[Mn(CO)_4Br_2]^-$ is substantially red-shifted compared to the absorption onsets for the two Ru complexes studied above (both onsets at ~3.6 eV). The weak MLCT absorption band between 2.6 and 3.4 eV of $[Mn(CO)_4Br_2]^-$ is followed by a rising absorption cross-section above 3.9 eV. This gas-phase spectrum is again in good qualitative agreement with the solution-phase spectrum shown in Figure 6.15. In interpreting the gas-phase absorption spectra of molecular anions, it is important to consider the value of the vertical electron detachment energy (VDE). The VDE is not known experimentally for $[Mn(CO)_4Br_2]^-$, thus, we have estimated it to be 3.9 eV for the gaseous anion using DFT calculation (see Section 6.2). The gradually rising absorption cross-section above 3.9 eV evident in Figure 6.14a is characteristic of electron detachment from the molecular anion above the threshold for electron detachment. [308]
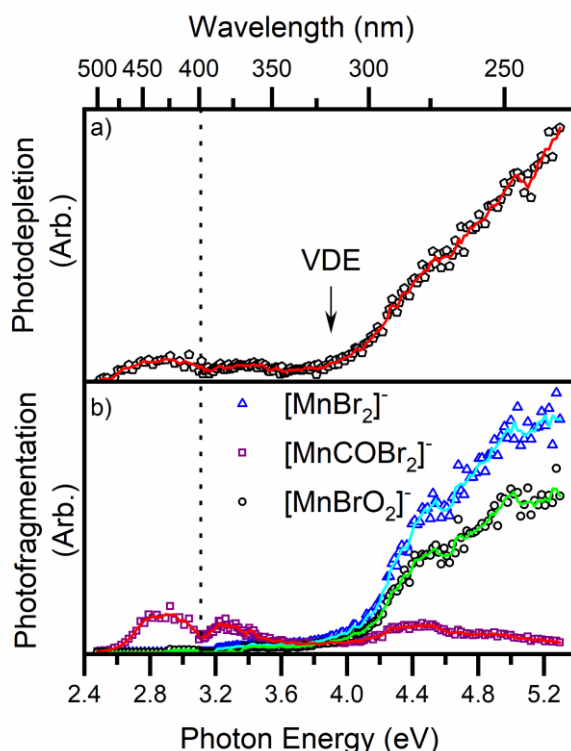
Figure 6.14 a) Gas-phase absorption spectrum of **3** and b) photofragment action spectra of the $[MnBr_2]^-$, $[Mn(CO)Br_2]^-$ and $[MnBrO_2]^-$ photofragments across the range 2.4-5.3 eV. The solid lines are five-point adjacent averages of the data points. The dotted line indicates where the OPO optics change on going from the visible to the UV, so the dip in the signal at this position may be an artefact.
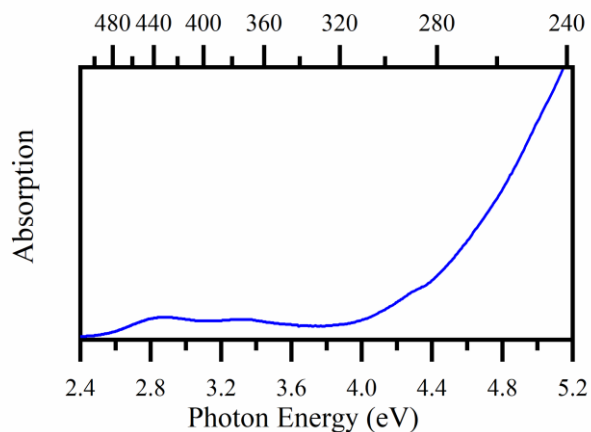
Figure 6.15 Absorption spectrum of [NEt$_4$][Mn(CO)$_4$Br$_2$] in DCM between 2.4 and 5.2 eV.

6.3.1.iii Photodissociation pathways of [Mn(CO)$_4$Br$_2$]⁻

To explore the photochemistry that accompanies photoexcitation, it is essential to inspect the photofragments that are produced. Figure 6.16 displays the photofragmentation mass spectrum of the [Mn(CO)$_4$Br$_2$]⁻ ion obtained at 4.9 eV. The major photofragment appears at m/z 215 and can be associated with the loss of all four CO units, following Eq. (6.3c). Photofragment peaks associated with [MnCOBr$_2$]⁻ (loss of 3 CO molecules following Eq. 6.3b) and [MnBrO$_2$]⁻, are also evident.
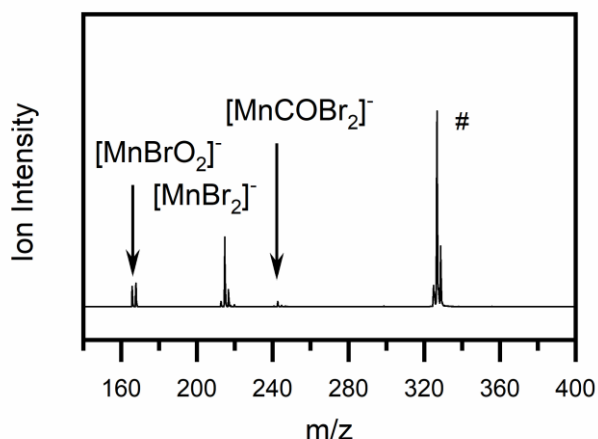
Figure 6.16 Photofragment mass spectrum of [Mn(CO)$_4$Br$_2$]⁻ excited at 4.9 eV.

Figure 6.14 displays the production spectra of the photofragments that are obtained upon photoexcitation. The most intense photofragment, $[MnBr_2]^-$, is associated with the maximum possible CO release (Eq. 6.3c). However, this fragmentation channel occurs extremely weakly in the visible region and becomes prominent only at energies above 4.1 eV. We note that the profile of the $[MnBrO_2]^-$ fragment closely mirrors that of the $[MnBr_2]^-$ photofragment, consistent with it being a secondary photoproduct of $[MnBr_2]^-$, resulting from reaction with O_2 in the ion trap. In contrast to $[MnBr_2]^-$ and $[MnBrO_2]^-$, the third significant photofragment, $[MnCOBr_2]^-$ which corresponds to the loss of 3CO molecules (Equation 6.3b) is produced relatively more strongly within the visible absorption range between 2.6 and 3.4 eV, indicating that this PhotoCORM does display a propensity to eject substantial quantities of CO in the key visible region of the spectrum, although with a lower cross-section than in the UV.

These results can be more conveniently visualised as ion yield spectra (Figure 6.17). Below 3.8 eV, $[MnCOBr_2]^-$ is produced as the main photofragment. The ion yield of $[MnBr_2]^-$ is very low below 3.2 eV, where it increases up to a plateau at 5.3 eV. $[MnBr_2]^-$ is the dominant photoproduct above 3.8 eV. The $[MnBrO_2]^-$ ion yield profile matches that of $[MnBr_2]^-$, confirming that $[MnBrO_2]^-$ is a secondary photoproduct.
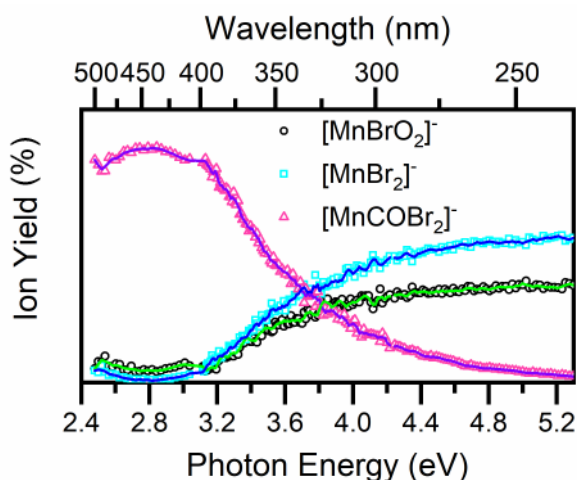
Figure 6.17 Ion yield spectra of the photofragments produced from $[Mn(CO)_4Br_2]^-$ in the region between 2.4 and 5.3 eV.

6.4 On-Line Photolysis

A key question that arises concerning the work presented here is the extent to which gas-phase measurements are a useful predictor of photochemistry that typically occurs in solution. It is well-known that organometallic photodissociation pathways and dynamics can be affected by the medium, and we can take the prototype $Cr(CO)_6$ system as an example. Upon UV photoexcitation of a solution of $Cr(CO)_6$ the dominating decay pathway is the loss of a single CO molecule, followed by solvent ligand substitution. [309] Gas-phase studies show that excitation of the lowest energy electronic transition leads to rapid ejection of one CO molecule, but the residual vibrational energy is then dissipated by the fragmentation of further CO units. [88] [101]

To explore how the gas-phase photochemistry of compounds **1** → **3** changes on going to the solution phase, we have performed single-wavelength solution-phase photochemistry measurements coupled with electrospray mass spectrometry to identify any solution-phase photoproducts. We are aware of possible complications with this approach, due to reactions of the excited precursor molecule or its photoproducts with the solvent such as ligand substitution, alongside reduction or oxidation in the aerated solution. However, this experiment provides a first basic insight, allowing some understanding of how the intrinsic gas-phase photochemistry can change within the solvent. A number of groups have adopted similar approaches to identifying photoproducts. [148] [305] [310-313]

Figure 6.18 shows the background-subtracted mass spectra obtained upon photoirradiation with the photolysis cell, for the Ru compounds **1** and **2**.
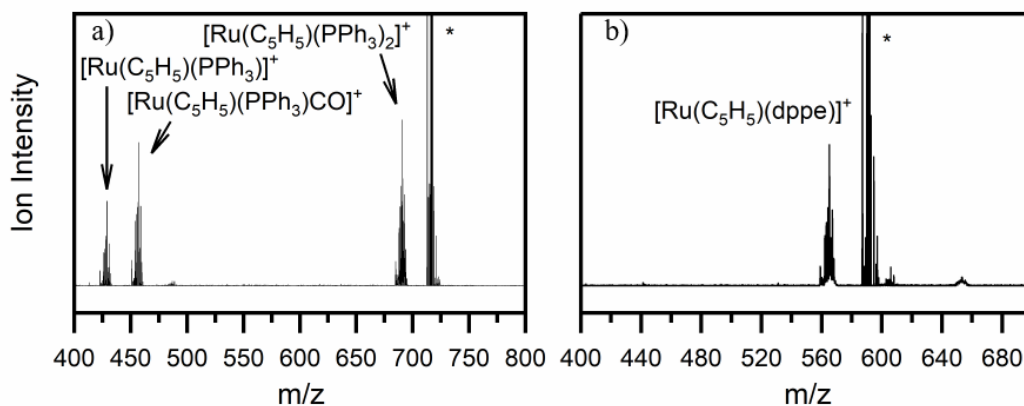
Figure 6.18 Photolysis mass spectra of a solution of a) $Ru(\eta^5\text{-}C_5H_5)(PPh_3)_2CO][PF_6]$ and (b) $[Ru(\eta^5\text{-}C_5H_5)(dppe)CO][PF_6]$ after irradiation at 3.4 eV for ~70 μs. The * indicates an unknown fragment, see text.

For compound **1** solution-phase irradiation at 365 nm resulted in the same three main photofragments as those observed upon gas-phase irradiation, i.e. pathways 6.1a, 6.1c and 6.1b, which correspond to the loss of CO, PPh_3 and $CO+PPh_3$ units, respectively. Similarly, compound **2**, which ejected CO upon photoexcitation in the gas-phase, also produced the corresponding photoproduct upon solution-phase irradiation. Finally, **1** and **2** produced photofragments with monoisotopic m/z values corresponding to the loss of two mass units. However, they could not be attributed to the loss of H_2 upon inspection of the isotopic pattern.

Compound **3** is challenging to study *via* solution-phase irradiation, due to the relative instability of the $[Mn(CO)_4Br_2]^-$ molecular ion, particularly concerning thermal dissociation into $[Mn(CO)_3Br_2]^-$. As discussed above, this fragmentation may occur either in solution or during the electrospray process, and to an extent, these processes can mask the photochemistry that is initiated by solution-phase irradiation. Figure 6.19 shows the mass spectrum obtained following solution-phase irradiation of $[NEt_4][Mn(CO)_4Br_2]$ at 460 nm. The fragments that were produced in the gas-phase are identifiable in the solution-phase photolysis mass spectrum. However, $[Mn(CO)_3Br_2]^-$, that was the main peak in the electrospray mass spectrum presented

in Figure 6.12, appears to be absent, suggesting that $[Mn(CO)_3Br_2]^-$ fragments upon

irradiation. New fragment peaks, marked with an asterisk, are identifiable and shown

in Figure 6.19, but they could not be assigned. A list of the observed mass spectrum

peaks is presented in Table 6.3, along with a list of the photofragments observed upon

gas-phase photoexcitation.
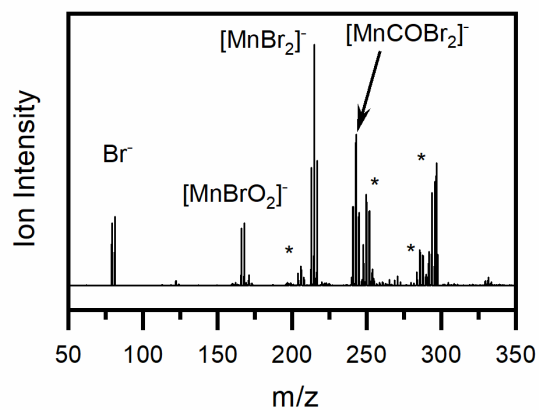
Figure 6.19 Photolysis mass spectrum of $[NEt_4][Mn(CO)_4Br_2]$ in DCM after irradiation at 2.7 eV.

Table 6.5 Comparison of main m/z peaks identified in the negative ion mass spectrum of $[Mn(CO)_4Br_2]^-$ following gas-phase and solution-phase photolysis at 2.7 eV.

Fragments	Monoisotopic m/z	Gas-phase	Solution-phase
Br^-	79	✓ (vw)	✓
$[MnBrO_2]^-$	166	✓ (vw)	✓
	206	✗	✓
$[MnBr_2]^-$	215	✓ (vw)	✓
$[MnCOBr_2]^-$	242	✓ (w)	✓
	250	✗	✓
	271	✗	✓
	286	✗	✓
	297	✗	✓
$[Mn(CO)_3Br_2]^-$	299	✓ (vw)	✗

✗= absent ✓ = present w = weak vw = very weak

More generally, we suggest that the gas-phase measurements on the Photo-CORMs may be just as valid for evaluating its effectiveness for application in a medical context. The biological mechanisms of PhotoCORM action are currently extremely poorly understood, [314] [315] and it is certainly not clear whether photoactivation of a PhotoCORM in a biological medium occurs on a typical "solution-phase" species, i.e. a fully solvated transition metal complex. It is possible that the PhotoCORM could be closely associated with, or even enclosed within, a sub-cellular component with a lower dielectric environment.

6.5 Conclusion

To summarise, LIMS was applied to a series of metal carbonyls, to obtain the absorption spectrum of the mass-selected parent compound, as well as the wavelength-dependent profiles of all photofragment channels. All three compounds display gas-phase absorption spectra that are in good qualitative agreement with the respective solution-phase spectra. In addition, photoexcitation of each compound leads to ejection of one or more units of CO, with the photofragment production spectra giving clear information on the wavelengths where the optimum amounts of CO are produced. For $[Ru(\eta^5\text{-}C_5H_5)(PPh_3)_2CO]^+$, photofragments associated with PPh_3 loss were prominent, motivating us to synthesise a modified Ru carbonyl, $[Ru(\eta^5\text{-}C_5H_5)(dppe)CO]^+$, which displayed dramatically improved photofragmentation properties, with CO loss being the sole photofragment channel. Finally, a Mn PhotoCORM, $[Mn(CO)_4Br_2]^-$, was studied for comparison. Our measurements allowed us to assess the extent to which CO release from $[Mn(CO)_4Br_2]^-$ varies in the visible and UV regions. The primary photofragmentation channel, corresponding to the loss of 4COs, is approximately five times greater in the UV region compared to the visible. Finally, we have integrated gas-phase photodissociation with solution-phase photolysis. For the metastable ion $[Mn(CO)_4Br_2]^-$, solution-phase photoexcitation resulted in a very complex mass spectrum, associated with the dissociation of $[Mn(CO)_4Br_2]^-$ prior to irradiation and consequent excitation of the fragments. The comparison between gas- and solution-phase photodissociation of $[Mn(CO)_4Br_2]^-$ has shown the benefit of isolating certain species of interest in the mass spectrometer prior to photoexcitation, in order to obtain straightforward information on their photochemistry.

Chapter 7

Summary and Outlook

This thesis has described gas-phase photodissociation spectroscopy of biological and pharmaceutical ions or anionic clusters within an adapted commercial mass spectrometer. The aim has been the study of fragmentation upon photoexcitation over a wide wavelength range to investigate relaxation pathways and mechanisms. The use of commercial mass spectrometry software has allowed the detection of every produced photofragment ion. The data collected have shown in detail how alternative photofragmentation pathways are accessed at different energies. In addition, comparison of the ground-state thermal fragments against the photofragment has allowed us to discriminate between statistical and non-statistical fragmentation mechanisms. Throughout this thesis, we have shown the versatility of gas-phase photodissociation spectroscopy in the investigation of the photophysics of a variety of molecular systems, ranging from nucleobases to organometallic complexes. In this Chapter, we summarise the results obtained in Chapters 3 to 6 and discuss possible avenues for future work.

7.1 Summary of the Experimental Results

7.1.1 Adenine anions and anionic clusters

Gas-phase photodissociation spectroscopy of anionic clusters and extended molecular systems containing adenine has been described in Chapters 3 and 4.

In Chapter 3, we have presented results on the adenosine mono-, di- and trinucleotides ($[AXP-nH]^{n-}$ X = M, D, T and n = 1, 2) anions, to explore whether the intrinsic DNA negative charge (on the phosphate chain) affects the photophysics of the nucleobase. We have also studied the effect of single versus multiple charges on the electronic position. Results led us to conclude that adenine is mostly unaffected

by the phosphate charge and that the photophysics at 4.9 eV is dominated by the adenine-centred π-π^* transition, as the subsequent ultrafast decay leads to statistical fragmentation on the hot ground state (see Table 3.3), with preferred cleavage of the glycosidic and the phosphoric anhydride bonds. Therefore, this type of excess charge, which is located at a distance from the chromophore and does not affect its photophysics, acts as a charge "tag" and can be used to study the photophysics of the neutral adenine. The length of the phosphate chain influences the stability of the ion more than the quantity of charge, an effect that can be traced to the number of hydrogen bonds that are formed between deprotonated oxygens and the sugar ring hydroxyl groups.

Additionally, photofragmentation of the $[AXP-nH]^{n-}$ anions mostly showed statistical fragmentation which is consistent with ultrafast decay onto the ground state, followed by hot ground-state fragmentation. The main difference observed between ground- and excited- state fragmentation occurred due to competing effects of electron detachment, which differed for the monoanionic plus dianionic species. Moreover, electron detachment was observed to occur at energies below the vertical detachment energy, suggesting a coupling between the π-π^* transition and the electron detachment continuum. A possible next step for these studies would be to increase the size of the molecule, *i.e.* to explore the photochemistry of nucleotide oligomers. This should provide insight into the extent to which the presence of other chromophores perturbs the π-π^* transition.

To explore the consequences of photoinduced electron attachment onto the adenine chromophore, Chapter 4 presented a study of the photodecay of the $I^-·A$ and $H_2PO_3^-$ $·A$ clusters. I^- and $H_2PO_3^-$ have lower vertical detachment energy than the adenosine nucleotide phosphate groups studied in Chapter 3. As discussed in the introduction, the interaction of nucleobases with low energy electrons can cause DNA damage

through electron capture by the nucleobase to form a transient negative ion. [68] [69] It is known that initially formed dipole-bound or valence-bound anions can evolve into dissociative fragmentation. [69] Several I$^-\cdot$N (N= nucleobase) complexes have been studied previously, and near-threshold photoexcitation has been found to lead to dipole- and valence-bound anion capture by the nucleobase. [71] [72] [73]We found that I$^-\cdot$A behaves similarly. In Chapter 4, we compared I$^-\cdot$A and H$_2$PO$_3^-\cdot$A and found that the anion strongly influences the electronic structure of the cluster.

For both I$^-\cdot$A and H$_2$PO$_3^-\cdot$A clusters, electron ejection above the vertical detachment energy was shown to be the main photofragmentation pathway. For I$^-\cdot$A, we observed enhanced photodepletion at near-threshold energies, accompanied by a sharp photofragmentation peak into the [A-H]$^-$ channel, characteristic of a dipole-bound state. The absence of these features for the H$_2$PO$_3^-\cdot$A cluster led us to exclude the formation of a dipole-bound state. Instead, it seems that the electron was detached from the adenine moiety and not from the anion itself. The photodepletion spectrum of the H$_2$PO$_3^-\cdot$A strongly resembles those of the [AXP-nH]$^{n-}$ anions studied in Chapter 3, with a strong π-π* transition in the UV region at ~ 4.8 eV. In light of these more recent results on H$_2$PO$_3^-\cdot$A, it is reasonable to assume that a similar mechanism occurs for the electron detachment from [AXP-nH]^n. Spin density calculation on these species would be useful to confirm this point.

7.1.2 Metal Carbonyls and CO-releasing Molecules.

Chapters 5 and 6 describe UVPD applied to substituted metal carbonyls over a wide wavelength range. These are the first such experiments performed for these systems in the gas-phase.

In Chapter 5, we explored the gas-phase photodissociation mechanism of protonated TryptoCORM ([MnL(CO)$_3$(CH$_3$CN)]$\cdot$H$^+$, L= deprotonated tryptophan) and the five-

coordinate $[MnL(CO)_3] \cdot H^+$ complex between 2.2 and 5.3 eV. TryptoCORM was previously shown to be efficient as a PhotoCORM against *E. Coli*. Photo-CORMs release CO upon photoexcitation and are of considerable current interest for pharmaceutical purposes. Their CO-releasing properties are generally tested *via* the myoglobin assay, where the results can often be complicated by solution-phase equilibria. In this work, we have tested the applicability of UVPD spectroscopy to characterise the photochemistry of these species and their characteristic CO-release in an isolated environment, away from the complications of the solution phase. Cold-ion vibrational spectroscopy was also performed to determine the geometry of $[MnL(CO)_3] \cdot H^+$, revealing a η^2 binding of the indole ring to the empty coordination site of the manganese.

Photofragmentation action spectra and ion yield spectra were obtained for both complexes, and we observed a remarkable agreement in the gas-phase photochemical properties of the two systems. Three distinctive excitation regions have been characterised at 2.2-3.0 eV, 3.0-4.2 eV, and 4.4-5.3 eV. In the visible part of the spectra (2.2-3.0 eV), that is the most interesting for photopharmaceutical action,[147,148] the loss of two CO units was observed, while the loss of three CO molecules was determined to be the main photofragmentation pathway above 3.0 eV. In Chapter 6, we applied LIMS to three charged organometallic complexes as further proof of its applicability to the investigation of metal carbonyl photochemistry. Photodissociation of $[Ru(\eta^5-C_5H_5)(PPh_3)_2CO]^+$ led to the loss of an undesirable PPh_3 ligand (which would be toxic in humans). This insight into the photofragmentation pathway was used to inform the rational design of an improved potential PhotoCORM, $[Ru(\eta^5-C_5H_5)(dppe)CO]^+$. Gas-phase photodissociation measurements on this molecule confirmed that it only releases CO.

Photodissociation Spectroscopy of the $[Mn(CO)_4Br_2]^-$ complex revealed the loss of 3 and 4 CO molecules in different ratios according to the excitation wavelength. HCD experiments demonstrated that $[Mn(CO)_4Br_2]^-$ is a very metastable species that is prone to CO releasing even before photoexcitation, either in solution or in the source. We have complemented the gas-phase photodissociation analysis of $[Ru(\eta^5\text{-}C_5H_5)(PPh_3)_2CO]^+$, $[Ru(\eta^5\text{-}C_5H_5)(dppe)CO]^+$ and $[Mn(CO)_4Br_2]^-$ with solution-phase photolysis *via* a newly developed "on-line" photolysis cell. This cell is positioned immediately before the electrospray needle, so to irradiate the solution while is flowing from the syringe to the mass spectrum. The two ruthenium species were shown to photodissociate in similar ways as upon the gas-phase photoexcitation. In-solution photolysis of $[Mn(CO)_4Br_2]^-$ resulted in a more complex distribution of photofragments that has been associated with a possible molecular dissociation in the dark. Indeed, $[Mn(CO)_4Br_2]^-$ is very challenging to study due to its delicate nature. In this context, the gas-phase photodissociation measurements are important as they provide an unambiguous picture of the photo-fragmentation profile.

7.2 Outlook and Future Work

Laser-interfaced mass spectrometry has been shown to be an excellent technique for the investigation of gas-phase photochemistry of organic and inorganic cations and anions, in combination with computational chemistry, solution-phase photolysis and thermal fragmentation experiments. While similar instruments have been used over the last decade to perform spectroscopy, the experiments presented in this thesis are some of the first to focus on using this instrument as a photochemical tool. The commercially adapted Bruker amaZon mass spectrometer has been confirmed to be a robust and reliable instrument for studying photodepletion and photofragmentation of diverse chemical systems.

As discussed in Section 7.1.1, since the gas-phase photofragmentation of simple adenosine nucleotides is now understood, the next step would be the investigation of the other nucleotides (*i.e.* guanosine, cytidine and thymidine) to build up to more complicated systems such as single and double strands DNA oligomers. However, issues related to the presence of multiple isomers could emerge. To overcome them it would be useful to integrate our LIMS experiment with ion mobility mass spectrometry (IMS) to separate the ions based on their mobility through a buffer gas (*i.e.* to their collisional cross-section). A similar instrument has been recently implemented by Dugourd and co-workers. [37] Very recently, they used IMS separation and photofragmentation to show how different protonation sites on modified peptides can influence their photophysics. [316]

Time-resolved experiments would be hugely beneficial to provide further insight into the dynamics of photofragmentation. This type of experiment has recently been implemented in a similar apparatus by Riehn and co-workers. [41-43] They have studied time-resolved gas-phase photodissociation of numerous organometallic complexes, such as the photocatalyst $[(^tbbpy)_2Ru(tpphz)Pt(Cl)_2]^{2+}$ (^tbbpy=4,4′-di-tert-butyl-2,2′-bipyridine and tpphz=tetrapyrido[3,2-a:2′3′-c:3″,2′-h:2‴,3‴-j]phenazine). Upon absorption by the conjugated bbpy ligands of the Ru centre, the Pt catalytic site is activated. By studying the MLCT(^tbbpy) transition at 440 nm, they observed a fast electron transfer to the bridging tpphz moiety prior to activation of the catalytic centre.[41]

The on-line photolysis cell that has been developed in this project represents an approach for conducting experiments that bridges the gap between gas- and solution-phase photochemistry. One of the great advantages of linking "on-line" solution photolysis to LIMS, is that LIMS can be used to analyse spectroscopically solution-phase photoproduct. In the future, the exploration of on-line photolysis methods

including time-dependent experiments (from ms to hours) should be implemented and automatised *via* the LabView software that controls the cell.

A further step towards the investigation of more complicated systems was implemented by Bieske and co-workers that have integrated on-line solution-phase photolysis to a custom IMS apparatus in order to investigate *Z-E* photoisomerisation in organic molecules. [313]

A further method to connect photodissociation spectroscopy to solution-phase properties would be the exploration of ions that are micro-solvated with an increasing number of water molecules. [317] For example, micro-solvation of adenine iodide clusters could be implemented to observe the suppression of the adenine dipole-bound state and the stabilisation of its valence-bound anion described in (Chapter 4), mirroring recent work Neumark's and co-workers on $I^-\cdot U\cdot H_2O$. [73]

In this thesis, UVPD spectroscopy of metal carbonyls over a wide wavelength range has been implemented for the first time as an approach to studying their intrinsic photochemical properties. In Chapter 5, gas-phase photochemistry of a PhotoCORM has been probed, and on-line photolysis investigation should be implemented in the future to explore to what extent our findings are reflected in solution. Preliminary comparisons between UVPD and TDDFT calculations were performed in Chapter 6. However, our work provides a new set of experimental results which can act as a benchmark for testing new high-level excited-state theory methods. [286-288]

The mechanism of medicinal action of some CORMs involves direct interaction of the CORM with subcellular components. [314] [315] It is interesting to consider to integrating the two parts of this thesis to explore the photochemistry of aggregates formed between nucleobases and nucleotides with CORMs, similarly to recent

experiments performed on the $PtCl_6^{2-} \cdot N$ (N=nucleobase) aggregates. [8] Such experiments could be highly useful in providing further benchmarks data for advanced theoretical methods.

References

[1] P. Atkins and J. de Paula, Atkins' Physical Chemistry (Ninth Edition), Oxford University Press, 2010.

[2] M. S. de Vries and P. Hobza, *Annu. Rev. Phys. Chem.,* vol. 58, pp. 585-612, 2007.

[3] M. Homocianu, A. Airinei and D. O. Dorohoi, *Journal of Advanced Research in Physics,* vol. 2, p. 011105, 2011.

[4] D. Chingakule, P. Gans, J. Gill and . P. Longdon, *Monatshefte für Chemie,* vol. 123, pp. 521- 535., 1992.

[5] T. Kawai, J. Umemura and T. Takenaka, *Colloid Polym. Sci.,* vol. 262, pp. 61-66, 1984.

[6] J. Brauman and . K. Smyth, *J. Am. Chem. Soc.,* vol. 91, pp. 7778-7780, 1969.

[7] O. Boyarkin, S. Mercier, A. Kamariotis and T. Rizzo, *J. Am. Chem. Soc.,,* vol. 128, pp. 2816-2817, 2006.

[8] E. Matthews, A. Sen, N. Yoshikawa, E. Bergström and C. Dessent, *Phys. Chem. Chem. Phys.,* vol. 18, pp. 15143-15152, 2016.

[9] D. Nolting, R. Weinkauf, I. Hertel and T. Schultz, *ChemPhysChem,* vol. 8, pp. 751-755, 2007.

[10] Z. Xu, J. Shaw and J. Brodbelt, *J. Am. Soc. Mass Spectrom.,* vol. 24, pp. 265-273, 2013.

[11] S. Raspopov, A. El-Faramawy, B. Thomson and K. Siu, *Anal. Chem.,* vol. 78, pp. 4572-4577, 2006.

[12] H. Telle, A. Ureña and . R. Donovan, Laser Chemistry: spectroscopy, dynamics and application, John Wiley & Sons, LTD, 2007.

[13] J. Brodbelt, *Chem Soc Rev.,* vol. 43, pp. 2757-2783, 2014.

[14] J. Stearns, S. Mercier, C. Seaiby, M. Guidi, O. Boyarkin and T. Rizzo, *J. Am. Chem. Soc.,* vol. 129, pp. 11814-11820, 2007.

[15] M. Guidi, U. Lorenz, G. Papadopoulos, O. Boyarkin and T. Rizzo, *J. Phys. Chem. A,* vol. 113, pp. 797-799, 2009.

[16] V. Gabelica, F. Rosu, T. Tabarin, C. Kinet, R. Antoine, M. Broyer, E. De Pauw and P. Dugourd, *J. Am. Chem. Soc.,* vol. 129, pp. 4706-4713, 2007.

[17] B. Bellina, I. Compagnon, L. Joly, F. Albrieux, A. Allouche, F. Bertorelle, J. Lemoine, R. Antoine and P. Dugourd, *Int. J. Mass. Spectrom.,* vol. 297, pp. 36-40, 2010.

[18] L. Sanche, *Eur. Phys. J. D,* vol. 35, pp. 367-390, 2005.

[19] H. Zeng , N. Yang and M. Johnson, *Faraday Discuss.,* vol. 217, pp. 8-33, 2019.

[20] M. Jarrold, . A. Illies and M. Bowers, *J. Chem. Phys.,* vol. 79, pp. 6086-6096, 1983.

[21] . C. Cassady and B. Freiser, *J. Am. Chem. Soc.,* vol. 106, pp. 6176-6179, 1984.

[22] C. Watson, G. Baykut, M. Battiste and J. Eyler, *Analytica Chimica Acta,* vol. 178, pp. 125-136, 1985.

[23] E. Williams and F. McLafferty, *J. Am. Soc. Mass Spectrom,* vol. 1, pp. 361-365, 1990.

[24] E. Williams , J. Furlong and F. McLafferty, *J. Am. Soc. Mass Spectrom,* vol. 1, pp. 288-294, 1990.

[25] J. Bakker, T. Besson, J. Lemaire, D. Scuderi and P. Maître, *J. Phys. Chem. A,,* vol. 111, pp. 13415-13424, 2007.

[26] L. MacAleese, A. Simon, T. McMahon, J. Ortega, D. Scuderi, J. Lemaire and P. Maitre, *Int. J. Mass Spectrom,* Vols. 249-250, pp. 14-20, 2006.

[27] J. Martens, G. Berden, C. Gebhardt and J. Oomens, *Rev. Sci. Instrum.,* vol. 87, p. 103108, 2016.

[28] D. Ortiz, M. Blug, X. Le Goff, P. Le Floch, N. Mezailles and P. Maître;, *Organometallics,* vol. 31, pp. 5975-5978, 2012.

[29] R. Dunbar, J. Martens, G. Berden and J. Oomens, *Phys. Chem. Chem. Phys.,* vol. 18, pp. 26923-26932, 2016.

[30] R. Dunbar, J. Martens, G. Berden and J. Oomens, *J. Phys. Chem. Lett.,* vol. 8, pp. 2634-2638, 2017.

[31] F. Schinle, C. Jacob, A. Wolk, J. Greisch, M. Vonderach, P. Weis, O. Hampe, M. Johnson and M. Kappes, *J. Phys. Chem. A,* vol. 118, p. 8453−8463, 2014.

[32] M. Ehsan, Y. Bozai, W. Pearson, N. Horenstein and J. Eyler, *Phys. Chem. Chem. Phys.,* vol. 17, pp. 25877-25881, 2015.

[33] D. Nolting, C. Marian and R. Weinkauf, *Phys. Chem. Chem. Phys.,* vol. 6, pp. 2633-2640, 2004.

[34] S. Koeniger, S. Merenbloom, S. Valentine, M. Jarrold, H. Udseth, R. Smith and D. Clemmer, *Anal. Chem.,* vol. 78, pp. 4161-4174, 2006.

[35] S. Warnke, C. Baldauf, M. Bowers, K. Pagel and G. von Helden, *J. Am. Chem. Soc.,* vol. 136, pp. 10308-10314, 2014.

[36] A. Masson, M. Kamrath, M. Perez, M. Glover, U. Rothlisberger, D. Clemmer and T. Rizzo, *J. Am. Soc. Mass Spectrom.,* vol. 26, pp. 1444-1454, 2015.

[37] A. Simon, F. Chirot, C. Choi, C. Clavier, M. Barbaire, J. Maurelli, X. Dagany, L. MacAleese and P. Dugourd , *Rev. Sci. Instrum.,* vol. 86, p. 094101, 2015.

[38] C. Choi, L. MacAleese, P. Dugourd, M. Choi and F. Chirot, *Phys. Chem. Chem. Phys.,* pp. 12223-12228, 2018.

[39] Q. Bian, M. Forbes, F. Talbot and R. Jockusch, *Phys. Chem. Chem. Phys.,* vol. 12, pp. 2590-2598, 2010.

[40] M. Czar, F. Zosel, I. König, ,. D. Nettels, B. Wunderlich, B. Schuler, A. Zarrine-Afsar and R. Jockush, *Anal. Chem.,* vol. 87, pp. 7559-7565, 2015.

[41] D. Imanbaew, J. Lang, . M. Gelin, S. Kaufhold, M. Pfeffer, S. Rau and C. Riehn, *Angew. Chem. Int. Ed.,* vol. 56, pp. 5471-5474, 2017.

[42] S. Kruppa, F. Bäppler, W. Klopper, S. Walg, W. Thiel, R. Diller and C. Riehn, *Phys. Chem. Chem. Phys.,* vol. 19, pp. 22785-22800, 2017.

[43] Y. Nosenko, C. Riehn and W. Klopper, *Chem. Phys. Lett.,* vol. 659, pp. 55-60, 2016.

[44] S. Boldissar and M. de Vries, *Phys. Chem. Chem. Phys.,* vol. 20, pp. 9701-9716, 2018.

[45] C. Crespo-Hernández, B. Cohen, . P. Hare and B. Kohler, *Chem. Rev.,* vol. 104, pp. 1977-2020, 2004.

[46] M. Merchán, R. González-Luque, T. Climent, L. Serrano-Andrés , E. Rodríguez, M. Reguero and D. Peláez, *J. Phys. Chem. B,* vol. 110, pp. 26471-26476, 2006.

[47] M. Barbatti, A. Aquino, J. Szymczak, D. Nachtigallová, . P. Hobza and H. Lischka, *Proc. Natl. Acad. Sci. U.S.A,* vol. 107, pp. 21453-21458, 2010.

[48] L. Marrot and J. Meunier, *J. Am. Acad. Dermatol.,* vol. 58, pp. S139-S148, 2008.

[49] W. Schreier, P. Gilch and W. Zinth, *Annu. Rev. Phys. Chem.,* vol. 66, pp. 497-519, 2015.

[50] E. Nir, . L. Grace, B. Brauer and M. de Vries, *J. Am. Chem. Soc.,* vol. 121, pp. 4896-4897, 1999.

[51] E. Nir, M. Muller, . L. Grace and M. de Vries, *Chem. Phys. Lett.,* vol. 355, pp. 59-64, 2002.

[52] E. Nir, P. Imhof, K. Kleinermanns and M. de Vries, *J. Am. Chem. Soc.,* vol. 122, pp. 8091-8092, 2000.

[53] W. Chin, M. Mons, I. Dimicoli, F. Piuzzi, B. Tardivel and M. Elhanine;, *Eur. Phys. J. D,* vol. 20, pp. 347-355, 2002.

[54] E. Nir, C. Janzen, P. Imhof, . K. Kleinermanns and M. de Vries, *J. Chem. Phys.,* vol. 115, pp. 4604-4611, 2001.

[55] D. Lührs, . J. Viallon and . I. Fischer, *Phys. Chem. Chem. Phys.,* vol. 3, pp. 1827-1831, 2001.

[56] S. Ullrich, . T. Schultz, M. Zgierski and A. Stolow, *J. Am. Chem. Soc.,* vol. 126, pp. 2262-2263, 2004.

[57] S. Ullrich, T. Schultz, M. Zgierski and A. Stolow, *Phys. Chem. Chem. Phys.,* vol. 6, pp. 2796-2801, 2004.

[58] H. Satzger, D. Townsend, M. Zgierski, S. Patchkovskii, . S. Ullrich and A. Stolow, *Proc. Natl. Acad. Sci. U.S.A.,* vol. 103, pp. 10196-10201, 2006.

[59] A. Broo, *J. Phys. Chem. A,* vol. 102, pp. 526-531, 1998.

[60] S. Perun, A. Sobolewski and W. Domcke, *J. Am. Chem. Soc.,* vol. 127, pp. 6257-6265, 2005.

[61] N. Evans and S. Ullrich, *J. Phys. Chem. A,* vol. 114, pp. 11225-11230, 2010.

[62] M. Nix, . A. Devine, B. Cronin and M. Ashfold, *J. Chem. Phys.,* vol. 126, p. 124312, 2007.

[63] W. Hassan, W. Chung, N. Shimakura, S. Koseki, H. Kono and Y. Fujimura, *Phys. Chem. Chem. Phys.,* vol. 12, pp. 5317-5328, 2010.

[64] U. Stange and F. Temps, *Chem. Phys,* vol. 515, pp. 441-451, 2018.

[65] M. Barbatti and H. Lischka, *J. Am. Chem. Soc.,* vol. 130, pp. 6831-6839, 2008.

[66] A. Chatterley, C. West, G. Roberts, V. Stavros and J. Verlet, *J. Phys. Chem. Lett.,* vol. 5, pp. 843-848, 2014.

[67] M. Stuhldreier and F. Temps, *Faraday Discuss.,* vol. 163, pp. 173-188, 2013.

[68] B. Boudaïffa, . P. Cloutier, D. Hunting, M. Huels and L. Sanche, *Science,* vol. 287, pp. 1658-1660, 2000.

[69] A. Kunin and D. Neumark, *Phys. Chem. Chem. Phys.,* vol. 21, pp. 7239-7255, 2019.

[70] F. Weik and L. Sanche, *J. Chem. Phys.,* vol. 112, pp. 9046-9051, 200.

[71] M. Yandell, S. King and D. Neumark, *J. Am. Chem. Soc.,* vol. 135, p. 2128–2131, 2013.

[72] A. Stephansen, S. King, Y. Yokoi, Y. Minoshima, W. Li, A. Kunin, T. Takayanagi and D. Neumark, *J. Chem. Phys.,* vol. 143, p. 104308, 2015.

[73] A. Kunin, W. Li and D. Neumark, *J. Chem. Phys.,* vol. 149, p. 084301, 2018.

[74] M. Gutowski, P. Skurski, K. Jordan and J. Simons, *Int. J. Quantum Chem.,* vol. 64, pp. 183-191, 1997.

[75] R. Compton, H. Carman, C. Desfrançois, H. Abdoul-Carime, J. Schermann, J. Hendricks, S. Lyapustina and K. Bowen, *J. Chem. Phys.,* vol. 105, pp. 3472-3478, 1996.

[76] P. Atkins, T. Overton, J. Rourke, M. Weller and F. Armstrong, Shriver & Atkins' Inorganic Chemistry (Fifth Edition), Oxford University Press, 2010.

[77] R. Crabtree, The Organometallic Chemistry of the Transition Metals (Fourth Edition), John Wiley & Sons, Inc., 2006.

[78] J. Calladine, S. Duckett, M. George, S. Matthews, R. Perutz, O. Torres and K. Vuong, *J. Am. Chem. Soc.,* vol. 133, pp. 2303-2310, 2011.

[79] A. Gabrielsson, F. Hartl, H. Zhang, J. Smith, M. Towrie, A. Vlček and R. Perutz, *J. Am. Chem. Soc.,* vol. 128, pp. 4253-4266, 2006.

[80] C. Windle, M. George, R. Perutz, P. Summers, X. Sun and A. Whitwood, *Chem. Sci.,* vol. 6, pp. 6847-6864, 2015.

[81] T. Morimoto, T. Nakajima, S. Sawa, R. Nakanishi, D. Imori and O. Ishitani, *J. Am. Chem. Soc.,* vol. 135, pp. 16825-16828, 2013.

[82] G. Wilke, *Pure Appl. Chem,* vol. 50, pp. 677-690, 1978.

[83] B. Kimmich, P. Fagan, E. Hauptman, W. Marshall and R. Bullock, *Organometallics,* vol. 24, pp. 6220-6229, 2005.

[84] P. Datta, A. Mukhopadhyay, P. Manna, E. Tiekink, P. Sil and C. Sinha, *J. Inorg. Biochem.,* vol. 105, pp. 577-588, 2011.

[85] D. Bandarra, M. Lopes, T. Lopes, J. Almeida, M. Saraiva, M. Vasconcellos-Dias, C. Nunes, V. Félix, P. Brandão, P. Vaza, M. Meireles and M. Calhorda, *J. Inorg. Biochem,* vol. 104, pp. 1171-1177, 2010.

[86] R. Motterlini and L. Otterbein, *Nat. Rev. Drug Discov.,* vol. 9, pp. 729-743, 2010.

[87] C. Tolman, *Chem. Soc. Rev.,* vol. 1, pp. 337-353, 1972.

[88] R. Perutz, O. Torres and A. Vlček, in *Comprehensive Inorganic Chemistry II (Second Edition)*, vol. 8, Elsevier, 2013.

[89] S. Sato, Y. Matubara, K. Koike, M. Falkenström, T. Katayama, ,. Y. Ishibashi, H. Miyasaka, S. Taniguchi, H. Chosrowjan, N. Mataga, N. Fukazawa, S. Koshihara, O. Ishitani and K. Onda, *Chem. Eur. J.,* vol. 18, pp. 15722-15734, 2012.

[90] R. Perutz and J. Turner, *J. Am. Chem. Soc.,* vol. 97, pp. 4800-4804, 1975.

[91] J. Burdett, *Coord. Chem. Rev.,* vol. 27, pp. 1-58, 1978.

[92] R. Perutz, *Annu. Rep. Prog. Chem., Sect. C: Phys. Chem.,* vol. 82, pp. 157-191, 1985.

[93] M. Graham, M. Poliakoff and J. Turner, *J. Chem. Soc. A,* pp. 2939-2948, 1971.

[94] R. Perutz and J. Turner, *Inorg. Chem.,* vol. 14, pp. 262-270, 1975.

[95] R. Perutz and J. Turner, *J. Am. Chem. Soc.,* vol. 97, pp. 4791-4800, 1975.

[96]   C. Pollak, A. Rosa and E. Baerends, *J. Am. Chem. Soc.,* vol. 119, pp. 7324-7329, 1997.

[97]   M. Paterson, P. Hunt, M. Robb and O. Takahashi, *J. Phys. Chem. A,* vol. 106, pp. 10494-10504, 2002.

[98]   G. Worth, G. Welch and M. Paterson, *J. Mol. Phys.,* vol. 104, pp. 1095-1105, 2006.

[99]   S. Trushin, W. Fuss and W. Schmid, *Chem. Phys.,* vol. 259, pp. 313-330, 2000.

[100] W. Fuss, S. Trushin and W. Schmid, *Res. Chem. Intermed.,* vol. 27, pp. 447-457, 2001.

[101] S. Trushin, K. Kosma, W. Fuss and W. Schmid, *Chem. Phys.,* pp. 309-323, 2008.

[102] T. Lian, S. Bromberg, M. Asplund, H. Yang and C. Harris, *J. Phys. Chem.,* vol. 100, pp. 11994-12001, 1996.

[103] K. Pierloot, E. Tsokos and L. Vanquickenborne, *J. Phys. Chem.,* vol. 100, pp. 16545-16550, 1996.

[104] A. Rosa, E. Baerends, S. van Gisbergen, E. van Lenthe, J. Groeneveld and . J. Snijders, *J. Am. Chem. Soc.,* vol. 121, pp. 10356-10365, 1999.

[105] I. Farrell, P. Matousek and A. Vlček Jr., *J. Am. Chem. Soc.,* vol. 121, pp. 5296-5301, 1999.

[106] I. Farrell, P. Matousek, M. Towrie, A. Parker, D. Grills, M. George and A. Vlček Jr., *Inorg. Chem.,* vol. 17, pp. 4318-4323, 2002.

[107] J. Vıchova, F. Hartl and A. Vlček Jr., *J. Am. Chem. Soc.,* vol. 114, pp. 10903-10910, 1992.

[108] L. Hammarback, A. Robinson, J. Lynam and I. Fairlamb, *J. Am. Chem. Soc.,* vol. 141, p. 2316−2328, 2019.

[109] B. Procacci, S. Duckett, M. George, M. Hanson-Heine, R. Horvath, R. Perutz, X. Sun, K. Vuong and J. Welch, *Organometallics,* vol. 37, p. 855−868, 2018.

[110] C. Daniel, J. Full, L. González, C. Kaposta, M. Krenz, C. Lupulescu, J. Manz, S. Minemoto, M. Oppel, P. Rosendo-Francisco, Š. Vajda and L. Wöste, *Chem. Phys.,* vol. 267, pp. 247-260, 2001.

[111] A. Freedman and R. Bersohn, *J. Am. Chem. Soc.,* vol. 100, pp. 4116-4118, 1978.

[112] D. Prinslow and V. Vaida, *J. Am. Chem. Soc.,* vol. 109, pp. 5097-5100, 1987.

[113] S. Kim, S. Pedersen and A. Zewail, *Chem. Phys. Lett.,* vol. 233, pp. 500-508, 1995.

[114] M. Bergt, T. Brixner, C. Dietl, B. Kiefer and G. Gerber , *J. Organomet. Chem.,* vol. 661, pp. 199-209, 2002.

[115] V. Nemykin and P. Basu, *Inorganica Chim. Acta,* vol. 358, p. 2876–2882, 2005.

[116] E. Crawford, P. Dyson, O. Forest, S. Kwok and J. McIndoe, *J. Clust. Sci.,* vol. 17, pp. 47-63, 2006.

[117] C. Butcher, P. Dyson, B. Johnson, T. Khimyak and J. McIndoe, *Chem. Eur. J.,* vol. 9, pp. 944-950, 2003.

[118] J. McIndoe and B. Nicholson, *J. Organomet. Chem.,* vol. 648, pp. 237-245, 2002.

[119] J. Haldane, *J. Physiol.,* vol. 18, pp. 430-462, 1895.

[120] T. Sjöstrand, *Nature,* vol. 164, pp. 404-405, 1949.

[121] I. Ghalayini, *Int. J. Impot. Res.,* vol. 16, pp. 459-469, 2004.

[122] T. Hambley, *Nature Med.,* vol. 6, pp. 422-428, 2000.

[123] P. Sawle, R. Foresti, B. Mann, T. Johnson, C. Green and R. Motterlini, *Br. J. Pharmacol.,* vol. 145, pp. 800-810, 2005.

[124] B. Zuckerbraun, B. Chin, B. Wegiel, T. Billiar, E. Czsimadia, J. Rao, L. Shimoda, E. Ifedigbo, S. Kanno and L. Otterbein, *J. Exp. Med.,* vol. 203, pp. 2109-2119, 2006.

[125] J. Clark, P. Naughton, S. Shurey, C. Green, T. Johnson, B. Mann, R. Foresti and R. Motterlini, *Circ. Res.,* vol. 93, pp. e2-e8, 2003.

[126] B. Chen, L. Guo, C. Fan, S. Bolisetty, R. Joseph, M. Wright, A. Agarwal and J.F. George, *Am. J. Pathol.,* vol. 175, pp. 422-429, 2009.

[127] R. Motterlini, J. Clark, R. Foresti, P. Sarathchandra, B. Mann and C. Green, *Circ. Res,* vol. 90, pp. e17-e24, 2002.

[128] S. Romanski, B. Kraus, U. Schatzschneider, J. Neudörfl, S. Amslinger and H. Schmalz, *Angew. Chem. Int. Ed.,* vol. 50, pp. 2392-2396, 2011.

[129] R. Rimmer, A. Pierri and P. Ford, *Coord. Chem. Rev.,* vol. 256, pp. 1509-1519, 2012.

[130] R. Foresti, J. Hammad, J. Clark, T. Johnson, B. Mann, A. Friebe, C. Green and R. Motterlini, *Br. J. Pharmacol.,* vol. 142, pp. 453-460, 2004.

[131] S. Lancel, S. Hassoun, R. Favory, B. Decoster, R. Motterlini and R. Neviere, *J. Pharmacol. Exp. Ther.,* vol. 329, pp. 641-648, 2009.

[132] M. Desmard, K. Davidge, O. Bouvet, D. Morin, D. Roux, R. Foresti, J. Ricard, E. Denamur, R. Poole, P. Montravers, R. Motterlini and J. Boczkowski, *Faseb J.,* vol. 23, pp. 1023-1031, 2009.

[133] T. Johnson, B. Mann, I. Teasdale, H. Adams, R. Foresti, C. Green and R. Motterlini, *Dalton Trans.,* vol. 15, pp. 1500-1508, 2007.

[134] T. Santos-Silva, A. Mukhopadhyay, J. Seixas, G. Bernardes, C. Romão and M. Romão, *J. Am. Chem. Soc.,* vol. 133, p. 1192–1195, 2011.

[135] T. Santos-Silva, A. Mukhopadhyay, J. Seixas, G. Bernardes, C. Romão and M. Romão, *Curr. Med. Chem.,* vol. 18, p. 3361–3366, 2011.

[136] A. Pena, N. Penacho, L. Mancio-Silva, R. Neres, J. Seixas, A. Fernandes, C. Romão, M. Mota, G. Bernardes and A. Pamplona , *Antimicrob. Agents Chemother.,* vol. 56, pp. 1281-1290, 2012.

[137] F. Zobi , O. Blacque, R. Jacobs, M. Schaub and A. Bogdanova, *Dalton Trans.,* vol. 41, pp. 370-378, 2012.

[138] J. Calderón-Montaño, E. Burgos-Morón, M. Orta, N. Pastor, C. Austin, S. Mateos and M. López-Lázaro, *Toxicol. Lett.,* vol. 222, pp. 64-71, 2013.

[139] R. Kim, M. Kim, C. Yoon, E. Lim, K. Yoo, G. Lee, Y. Kim, H. Kim, Y. Jin, Y. Lee, C. Cho, Y. Oh, M. Gye, Y. Suh and S. Lee, *Mol. Pharmacol.,* vol. 82, pp. 400-407, 2012.

[140] I. Fairlamb, A. Duhme-Klair, J. Lynam, B. Moulton, C. O'Brien, P. Sawle, J. Hammad and R. Motterlini, *Bioorganic Med. Chem. Lett.,* vol. 16, p. 995–998, 2006.

[141] I. Fairlamb, J. Lynam, B. Moulton, I. Taylor, A. Duhme-Klair, P. Sawle and R. Motterlini, *Dalton Trans.,* p. 3603–3605, 2007.

[142] A. Vogel and V. Venugopalan, *Chem. Rev.,* vol. 103, pp. 577-644, 2003.

[143] S. Waldchen, J. Lehmann, T. Klein, S. Van De Linde and M. Sauer, *Sci. Rep.,* vol. 5, p. 15348, 2015.

[144] I. Chakraborty, S. Carrington and P. Mascharak, *Acc Chem Res.,* vol. 47, pp. 2603-2611, 2014.

[145] A. Atkin, J. Lynam, B. Moulton, P. Sawle, R. Motterlini, N. Boyle, M. Pryce and I. Fairlamb, *Dalton Trans.,* vol. 40, pp. 5755-5761, 2011.

[146] B. Aucott, A. Duhme-Klair, B. MoultonIan, I. ClarkIgor, I. Sazanovich, M. Towrie, L. Hammarback, I. Fairlamb and J. Lynam, *Organometallics,* vol. 38, pp. 2391-2401, 2019.

[147] I. Chakraborty, S. Carrington, G. Roseman and P. Mascharak, *Inorg. Chem.,* vol. 56, pp. 1534-1545, 2017.

[148] J. Ward, J. Lynam, J. Moir and I. Fairlamb, *Chem. Eur. J.,* vol. 20, pp. 15061-15068, 2014.

[149] F. Zobi, *Future Med. Chem.,* vol. 5, pp. 175-188, 2013.

[150] U. Schatzschneider, *Inorganica Chim. Acta,* vol. 374, pp. 19-23, 2011.

[151] J. Ward, R. Morgan, J. Lynam, I. Fairlamb and J. Moir, *Med. Chem. Commun.,* vol. 8, pp. 346-352, 2017.

[152] L. Flanagan, R. Steen, K. Saxby, M. Klatter, B. Aucott, C. Winstanley, I. Fairlamb, J. Lynam, A. Parkin and V. Friman, *Front. Microbiol.,* vol. 9, p. 195, 2018.

[153] O. Svelto, Principle of Lasers (fifth Edition), Springer Science + Business Media, 2010.

[154] *Operation and Maintenance Manual for SureliteTM Lasers, Revision W,* Continuum Electro Optics, Inc, 2014.

[155] Continuum, 2014.

[156] E. Matthews, PhD Thesis, University of York, UK, 2018.

[157] F. McLafferty, P. Bente, R. Kornfeld, S. Tsai and I. Howe, *J. Am. Chem. Soc.,* vol. 95, pp. 2120-2129, 1973.

[158] M. Yamashita and J. Fenn, *J. Phys. Chem.,* vol. 88, pp. 4451-4459, 1984.

[159] Bruker Daltonik GmbH, 2009.

[160] M. Dole, L. Mack, R. Hines, M. Alice, L. Ferguson and R. Mobley, *J. Chem. Phys.,* vol. 49, pp. 2240-2249, 1968.

[161] J. Iribarne and B. Thomson, *J. Chem. Phys.,* vol. 64, pp. 2287-2294, 1975.

[162] F. Rayleigh, *Philos. Mag.,* vol. 14, pp. 184-186, 1882.

[163] S. Nguyen and J. Fenn, *Proc. Natl. Acad. Sci. U.S.A,* vol. 104, pp. 1111-1117, 2007.

[164] W. Paul, *Rev. Mod. Phys.,* pp. 531-540, 1990.

[165] W. Boxford, J. Pearce and C. Dessent, *Chem. Phys. Lett.,* vol. 399, pp. 465-470, 2004.

[166] M. Ince, B. Perera and M. Van Stipdonk, *Int. J. Mass Spectrom.,* vol. 207, pp. 41-55, 2001.

[167] R. Antoine and P. Dugourd, *Phys. Chem. Chem. Phys.,* vol. 13, pp. 16494-16509, 2011.

[168] M. Stockett and S. Nielsen, *Phys. Chem. Chem. Phys.,* vol. 18, pp. 6996-7000, 2016.

[169] S. Wellman and R. Jockusch, *J. Phys. Chem. A,* vol. 119, p. 6333–6338, 2015.

[170] W. Kaiser and C. Garrett, *Phys. Rev. Lett.,* vol. 7, pp. 229-232, 1961.

[171] B. Koplitz and J. McVeya, *J. Chem. Phys.,* vol. 80, pp. 2271-2281, 1984.

[172] D. Bomse, R. Woodin and J. Beauchamp, *J. Am. Chem. Soc.,* vol. 101, pp. 5503-5512, 1979.

[173] E. Matthews and C. Dessent, *J. Phys. Chem. A,* vol. 120, pp. 9209-9216, 2016.

[174] G. Grégoire, H. Kang, C. Dedonder-Lardeux, C. Jouvet, C. Desfrançois, D. Onidas, V. Lepere and J. Fayeton, *Phys. Chem. Chem. Phys.,* vol. 8, pp. 122-128, 2006.

[175] S. Kaufman, J. Weber and M. Pernpointner, *J. Chem. Phys.,* vol. 139, p. 194310, 2013.

[176] A. Sen, G. Hou, X. Wang and C. Dessent, *J. Phys. Chem. B,* vol. 119, pp. 11626-11631, 2015.

[177] I. Compagnon, A. Allouche, F. Bertorelle, R. Antoine and P. Dugourd, *Phys. Chem. Chem. Phys.,* vol. 12, pp. 3399-3403, 2010.

[178] J. Olsen, B. Macek, O. Lange, A. Makarov, S. Horning and M. Mann, *Nat. Methods,* vol. 9, pp. 709-712, 2007.

[179] Orbitrap Tribrid Series, Hardware Manual, Revision A, Thermo Fisher Scientific Inc, 2018.

[180] D. Douglas, *J. Am. Soc. Mass Spectrom.,* vol. 9, pp. 101-113, 1998.

[181] Y. Zhang, S. Ficarro, S. Li and J. Marto, *J. Am. Soc. Mass Spectrom.,* vol. 20, pp. 1425-1434, 2009.

[182] J. Diedrich, A. Pinto and J. Yates, *J. Am. Soc. Mass Spectrom.,* vol. 24, pp. 1690-1699, 2013.

[183] B. Marsh, J. Voss and E. Garand, *J. Chem. Phys.,* vol. 143, p. 204201, 2015.

[184] E. Garand, *J. Phys. Chem. A,* vol. 122, pp. 6479-6490, 2018.

[185] M. Kamrath, E. Garand, P. Jordan, C. Leavitt, A. Wolk, M. Van Stipdonk, S. Miller and M. Johnson,, *J. Am. Chem. Soc.,* vol. 133, pp. 6440-6448, 2011.

[186] A. Wolk, C. Leavitt, E. Garand and M. Johnson, *Acc. Chem. Res.,* vol. 47, pp. 202-210, 2014.

[187] J. Voss, S. Kregel, K. Fischer and E. Garand, *J. Am. Soc. Mass Spectrom.,* vol. 29, pp. 42-50, 2018.

[188] M. Frisch, G. Trucks, H. Schlegel, G. Scuseria, M. Robb, J. Cheeseman, G. Scalmani, V. Barone, B. Mennucci, G. Petersson, H. Nakatsuji, M. Caricato, X. Li, H. Hratchian, A. Izmaylov, J. Bloino, G. Zheng, J. Sonnenberg, M. Hada, M. Ehara, K. Toyota, R. Fukuda, J. Hasegawa, M. Ishida, T. Nakajima, Y. Honda, O. Kitao, H. Nakai, T. Vreven, J. Montgomery, J. Peralta, F. Ogliaro, M. Bearpark, J. Heyd, E. Brothers, K. Kudin, V. Staroverov, R. Kobayashi, J. Normand, K. Raghavachari, A. Rendell, J. Burant, S. Iyengar, J. Tomasi, M. Cossi, N. Rega, J. Millam, M. Klene, J. Knox, J. Cross, V. Bakken, C. Adamo, J. Jaramillo, R. Gomperts, R. Stratmann, O. Yazyev, A. Austin, R. Cammi, C.

Pomelli, J. Ochterski, R. Martin, K. Morokuma, V. Zakrzewski, G. Voth, P. Salvador, J. Dannenberg, S. Dapprich, A. Daniels, O. Farkas, J. Foresman, J. Ortiz, J. Cioslowski and D. and Fox, *Gaussian 09, Revision D.01,* Gaussian, Inc., Wallingford CT, 2009.

[189] A. Becke, *J. Chem. Phys.,* vol. 98, pp. 5648-5652, 1993.

[190] C. Lee, W. Yang and R. Parr, *Phys. Rev. B,* vol. 37, pp. 785-789, 1998.

[191] A. Becke, *Phys. Rev. A,* vol. 38, pp. 3098-3100, 1988.

[192] T. Yanai, D. Tew and N. Handy, *Chem. Phys. Lett.,* vol. 393, pp. 51-57, 2004.

[193] C. Adamo and V. Barone, *J. Chem. Phys.,* vol. 110, pp. 6158-6170, 1999.

[194] J. Perdew, K. Burke and M. Ernzerhof, *Phys. Rev. Lett.,* vol. 77, pp. 3865-3868, 1996.

[195] Y. Zhao and D. Truhlar, *Theor. Chem. Acc.,* vol. 120, pp. 215-241, 2008.

[196] Y. Zhao, N. Schultz and D. Truhlar, *J. Chem. Phys.,* vol. 123, p. 161103, 2005.

[197] J. Simons, *Acc. Chem. Res.,* vol. 39, pp. 772-779, 2006.

[198] A. Sobolewski and W. Domcke, *Europhysics News,* vol. 37, pp. 20-23, 2006.

[199] G. Roberts and V. Stavros, *Chem. Sci.,* vol. 5, pp. 1698-1722, 2014.

[200] S. De Camillis, J. Miles, G. Alexander, O. Ghafur, I. Williams, D. Townsend and J. Greenwood, *Phys. Chem. Chem. Phys.,* vol. 17, pp. 23643-23650, 2015.

[201] C. Bisgaard, H. Satzger, S. Ullrich and A. Stolow, *Chem. Phys. Chem.,* vol. 10, pp. 101-110, 2009.

[202] D. Tuna, A. Sobolewski and W. Domcke, *J. Phys. Chem. A,* vol. 118, pp. 122-127, 2014.

[203] M. Miyazaki, H. Kang, C. Choi, N. Han, J. Song, N. Kim and M. Fujii, *J. Chem. Phys.,* vol. 139, p. 124311, 2013.

[204] S. Nielsen, J. Andersen, J. Forster, P. Hvelplund, B. Liu, U. Pedersen and S. Tomita, *Phys. Rev. Lett.,* vol. 91, p. 048302, 2003.

[205] J. Marcum, A. Halevi and J. Weber, *Phys. Chem. Chem. Phys.,* vol. 11, pp. 1740-1751, 2009.

[206] A. Chatterley, C. West, V. Stavros and J. Verlet, *Chem. Sci.,* vol. 5, pp. 3963-3975, 2014.

[207] M. Berdakin, G. Férau, C. Dedonder-Lardeux, C. Jouvet and G. Pino, *Phys. Chem. Chem. Phys.,* vol. 16, pp. 10643-10650, 2014.

[208] S. Pedersen, K. Støchkel, C. Byskov, L. Baggesen and S. Nielsen, *Phys. Chem. Chem. Phys.,* vol. 15, pp. 19748-19752, 2013.

[209] A. Milosavljević, V. Cerovski, F. Canon, M. Ranković, N. Škoro, L. Nahon and A. Giuliani, *J. Phys. Chem. Lett.,* vol. 5, pp. 1994-1999, 2014.

[210] X. Yang, X. Wang, E. Vorpagel and L. Wang, *Proc. Natl. Acad. Sci. U. S. A.,* vol. 101, pp. 17588-17592, 2004.

[211] N. Rahman, J. Buck and L. Levin, *Front. Physiol.,* vol. 4, p. 343, 2013.

[212] W. Li, A. Kunin, E. Matthews, N. Yoshikawa, C. Dessent and D. Neumark, *J. Chem. Phys.,* vol. 145, p. 044319, 2016.

[213] A. Sen and C. Dessent, *J. Phys. Chem. Lett.,* vol. 5, pp. 3281-3285, 2014.

[214] R. Burke, J. Pearce, W. Boxford, A. Bruckmann and C. Dessent, *J. Phys. Chem. A,* vol. 109, pp. 9775-9785, 2005.

[215] R. Improta, F. Santoro and L. Blancafort, *Chem. Rev.,* vol. 116, pp. 3540-3593, 2016.

[216] L. Clark, G. Peschel and I. Tinoco, *J. Phys. Chem.,* vol. 69, pp. 3615-3618, 1965.

[217] R. Bock, N. Ling, S. Morell and S. Lipton, *Arch. Biochem. Biophys.,* vol. 62, pp. 253-264, 1956.

[218] F. Schinle, P. Crider, M. Vonderach, P. Weis, O. Hampe and M. Kappes, *Phys. Chem. Chem. Phys.,* vol. 15, pp. 6640-6650, 2013.

[219] X. Wang and L. Wang, *Annu. Rev. Phys. Chem.,* vol. 60, pp. 105-126, 2009.

[220] E. Matthews and C. Dessent, *Phys. Chem. Chem. Phys.,* vol. 19, pp. 17434-17440, 2017.

[221] T. Baer and P. Mayer, *J. Am. Soc. Mass Spectrom,* vol. 8, pp. 103-115, 1997.

[222] Y. Ho and P. Kebarle, *Int. J. Mass Spectrom.,* Vols. 165-166, pp. 433-455, 1997.

[223] C. Anstöter, J. Bull and J. Verlet, *Int. Rev. Phys. Chem.,* vol. 35, pp. 509-538, 2016.

[224] R. Ditchfield, W. Hehre and J. Pople , *J. Phys. Chem.,* vol. 54, pp. 724-728, 1971.

[225] G. Petersson, A. Bennett, T. Tensfeldt, M. Al-Laham, W. Shirley and J. Mantzaris, *J. Chem. Phys.,* vol. 89, pp. 2193-2218, 1988.

[226] A. McLean and G. Chandler, *J. Chem. Phys.,* vol. 72, pp. 5639-5648, 1980.

[227] B. Boudaiffa, P. Cloutier, D. Hunting, M. Huels and L. Sanche, *Science,* vol. 287, pp. 1658-1660, 2000.

[228] J. Wolken and F. Turecek, *J. Phys. Chem. A,* vol. 105, pp. 8352-8360, 2001.

[229] S. Ray, S. Daube and R. Naaman, *Proc. Natl. Acad. Sci. U.S.A.,* vol. 102, pp. 15-19, 2004.

[230] H. Abdoul-Carime, S. Gohlke and E. Illenberger, *Phys. Rev. Lett.,* vol. 92, p. 168103, 2004.

[231] I. Baccarelli, I. Bald, F. Gianturco, E. Illenberger and J. Kopyra, *Phys. Rep.,* vol. 508, pp. 1-44, 2011.

[232] H. Abdoul-Carime, S. Gohlke, E. Fischbach, J. Scheike and E. Illenberger, *Chem. Phys. Lett.,* vol. 387, pp. 267-270, 2004.

[233] J. Gu, J. Leszczynski and H. Schaefer, *Chem. Rev.,* vol. 112, pp. 5603-5640, 2012.

[234] S. Pimblott and J. LaVerne, *Radiat. Phys. Chem.,* vol. 76, pp. 1244-1247, 2007.

[235] L. Sanche, *Radiat. Phys. Chem.,* vol. 34, pp. 15-33, 1989.

[236] S. King, M. Yandell and D. Neumark, *Faraday Disscuss.,* vol. 163, pp. 59-72, 2013.

[237] S. King, M. Yandell, A. Stephansen and D. Neumark, *J. Chem. Phys.,* vol. 141, p. 224310, 2014.

[238] S. King, A. Stephansen, Y. Yokoi, M. Yandell, A. Kunin, T. Takayanagi and D. Neumark, *J. Chem. Phys.,* vol. 143, pp. J. Chem. Phys.,, 2015.

[239] C. H. Dessent, C. Bailey and M. Johnson, *J. Chem. Phys.,* vol. 105, p. 10416, 1996.

[240] C. Dessent, J. Kim and M. Johnson, *Faraday Discuss.,* vol. 115, pp. 395-406, 2000.

[241] F. Mbaiwa, M. Van Duzor, J. Wei and R. Mabbs, *J. Phys. Chem. A,* vol. 114, pp. 1539-1547, 2010.

[242] M. Schreiber and L. Gonzalez, *J. Comput. Chem.,* vol. 28, pp. 2299-2308, 2007.

[243] C. Desfrancois, H. Abdoul-Carime and J. Schermann, *J. Chem. Phys.,* vol. 104, p. 7792, 1996.

[244] M. Haranczyk, M. Gutowski, X. Li and K. Bowen, *Proc. Natl. Acad. Sci. U.S.A.,* vol. 104, pp. 4804-4807, 2007.

[245] E. Raczynska, M. Makowski, K. Zientara-Rytter, K. Kolczynska, T. Stepniewski and M. Hallmann, *J. Phys. Chem. A,* vol. 117, pp. 1548-1559, 2013.

[246] K. Asmis and D. Neumark, *Acc. Chem. Res.,* vol. 45, pp. 43-52, 2012.

[247] C. Dessent, C. Bailey and M. Johnson, *J. Chem. Phys.,* vol. 103, p. 2006, 1995.

[248] A. J. Castleman and K. Bowen Jr., *J. Phys. Chem.,* vol. 100, 1996.

[249] X. Wang and S. Kass, *J. Am. Chem. Soc.,* vol. 136, pp. 17332-17336, 2015.

[250] E. Matthews, R. Cercola, G. Mensa-Bonsu, D. Neumark and C. Dessent, *J. Chem. Phys.,* vol. 148, p. 084304, 2018.

[251] M. Gutowski and P. Skurski, *J. Phys. Chem. A,* vol. 102, pp. 2624-2633, 1998.

[252] P. Skurski, M. Gutowski and J. Simons, *Int. J. Quantum Chem.,* vol. 80, pp. 1024-1038, 2000.

[253] W. Morgan and R. Fortenberry, *Theor. Chem. Acc.,* vol. 134, p. 47, 2015.

[254] G. Mensa-Bonsu, D. Tozer and J. Verlet, *Phys. Chem. Chem. Phys.,* vol. 21, pp. 13977-13985, 2019.

[255] A. Harvey, N. Yoshikawa, J. Wang and C. Dessent, *J. Chem. Phys.,* vol. 143, p. 101103, 2015.

[256] E. Matthews and C. Dessent, *J. Phys. Chem. Lett.,* vol. 9, pp. 6124-6130, 2018.

[257] F. Mbaiwa, D. Dao, N. Holtgrewe, J. Lasinski and R. Mabbs, *J. Chem. Phys.,* vol. 136, p. 114303, 2012.

[258] R. Cercola, E. Matthews and C. Dessent, *J. Phys. Chem. B,* vol. 121, pp. 5553-5561, 2017.

[259] A. Sen, T. Luxford, N. Yoshikawa and C. Dessent, *Phys. Chem. Chem. Phys.,* vol. 16, pp. 15490-15500, 2004.

[260] K. Aflatooni, A. Scheer and P. Burrow, *J. Chem. Phys.,* vol. 125, p. 054301, 2006.

[261] S. Denifl, S. Ptasińska, G. Hanel, B. Gstir, M. Probst, P. Scheier and T. Märk, *J. Chem. Phys.,* vol. 120, p. 6557, 2004.

[262] A. Pamplona, A. Ferreira, J. Balla, V. Jeney, G. Balla, S. Epiphanio, A. Chora, C. Rodrigues, I. Gregoire, M. Cunha-Rodrigues, S. Portugal, M. Soares and M. Mota, *Nat. Med.,* vol. 6, pp. 703-710, 2007.

[263] N. Fujisaki, K. Kohama, T. Nishimura, H. Yamashita, M. Ishikawa, A. Kanematsu, T. Yamada, S. Lee, T. Yumoto, K. Tsukahara, J. Kotani and A. Nakao, *Med. Gas Res.,* p. 122–129, 2016.

[264] L. Nobre, H. Jeremias, C. Romão and L. Saraiva, *Dalton Trans.,* vol. 45, pp. 1455-1466, 2016.

[265] M. Klinger-Strobel, S. Gläser, O. Makarewicz, R. Wyrwa, J. Weisser, M. Pletz and A. Schiller, *Agents Chemother. Antimicrob.,* vol. 60, pp. 4037-4046, 2016.

[266] C. Romao, W. Blattler, J. Seixas and G. Bernardes, *Chem. Soc. Rev.,* vol. 41, pp. 3571-3583, 2012.

[267] U. Schatzschneider, *Br. J. Pharmacol.,* vol. 172, pp. 1638-1650, 2015.

[268] R. Rimmer, H. Richter and P. Ford, *Inorg. Chem.,,* vol. 49, pp. 1180-1185, 2010.

[269] C. Reichel and M. Wrighton, *J. Am. Chem. Soc.,* vol. 101, pp. 6769-6772, 1979.

[270] K. Fu, R. Whetten and E. Grant, *Ind. Eng. Chem. Prod. Res. Dev.,* vol. 23, pp. 33-40, 1984.

[271] E. Kottelat and F. Zobi, *Inorganics,* vol. 5, p. 24, 2017.

[272] M. Wright and J. Wright, *Dalton Trans.,* vol. 45, pp. 6801-6811, 2016.

[273] E. Kottelat, F. Lucarini, A. Crochet, A. Ruggi and F. Zobi, *Eur. J. Inorg. Chem.,* pp. 3758-3768, 2019.

[274] J. Jimenez, I. Chakraborty, A. Dominguez, J. Martinez-Gonzalez, W. Sameera and P. Mascharak, *Inorg. Chem.,* vol. 57, pp. 1766-1773, 2018.

[275] M. Fumanal, Y. Harabuchi, E. Gindensperger, S. Maeda and C. Daniel, *J. Comput. Chem.,* vol. 40, pp. 72-81, 2019.

[276] N. Wong, J. Berenbeim, M. Hawkridge, C. Dessent and E. Matthews, *Phys. Chem. Chem. Phys.,* vol. 21, pp. 14311-14321, 2019.

[277] L. Hammarback, I. Clark, I. Sazanovich, M. Towrie, A. Robinson, F. Clarke, S. Meyer, I. Fairlamb and J. Lynam, *Nature Catalysis,* vol. 1, pp. 830-840, 218.

[278] R. Joyce, PhD Thesis, North Carolina State University, 2018.

[279] E. Matthews, R. Cercola and C. Dessent, *Molecules,* vol. 23, p. 2036, 2018.

[280] C. Butcher, B. Johnson and J. McIndoe, *J. Chem. Phys.,* vol. 116, p. 6560, 2002.

[281] C. Butcher, P. Dyson, B. Johnson, P. Langridge-Smith, J. McIndoe and C. Whyte, *Rapid Commun. Mass Spectrom.,* vol. 16, pp. 1595-1598, 2002.

[282] L. B. V. Lepère, M. Barat, J. Fayeton, V. Picard, C. Jouvet, P. Çarçabal, I. Nielsen, C. Dedonder-Lardeux, G. Grégoire and A. Fujii, *J. Chem. Phys.,* vol. 127, p. 134313, 2007.

[283] F. Talbot, T. Tabarin, R. Antoine, M. Broyer and P. Dugourd, *J. Chem. Phys.,* vol. 122, p. 074310, 2005.

[284] M. Fumanal, E. Gindensperger and C. Daniel, *J. Phys. Chem. Lett.,* vol. 917, pp. 5189-5195, 2018.

[285] M. Gonzalez, S. Carrington, N. Fry, J. Martinez and P. Mascharak, *Inorg. Chem.,* vol. 512, pp. 111930-111940, 2012.

[286] T. Malcomson, M. R.G. and M. Paterson, *ChemPhotoChem,* vol. 3, pp. 825-832, 2019.

[287] F. Plasser, S. Mai, E. Gindensperger, C. Daniel and L. Gonzalez, *J. Chem. Theory Comput,* vol. 15, pp. 5031-5045, 2019.

[288] B. Pinter, A. Chankisjijev, P. Geerlings, J. Harvey and F. De Proft, *Chem. Eur. J.,* vol. 24, pp. 5281-5292, 2018.

[289] P. Gautam and B. Bhanage, *Catal. Sci. Technol.,* vol. 5, pp. 4663-4702, 2015.

[290] J. Peng, F. Wu and X. Wu, *Chem. Rev.,* vol. 119, pp. 2090-2127, 2019.

[291] C. Daniel, *Coord. Chem. Rev.,* Vols. 282-283, pp. 19-32, 2015.

[292] C. Yamazaki, H. Takeda and O. Ishitani, *J. Photochem. Photobiol. C,* vol. 25, pp. 106-137, 2015.

[293] A. Sinopoli, N. La Porte and J. Martinez, *Coord. Chem. Rev.,* vol. 365, pp. 60-74, 2018.

[294] P. Cheung, C. Machan, A. Malkhasian, J. Agarwal and C. Kubiak, *Inorg. Chem.,* vol. 55, pp. 3192-3198, 2016.

[295] C. Garino and L. Salassa, *Philos. Trans. Royal Soc. A,* vol. 371, 2013.

[296] T. Ikariya and A. Blacker, *Acc. Chem. Res.,* vol. 40, pp. 1300-1308, 2007.

[297] N. D. Reshi, D. Senthurpandi and A. Samuelson, *J. Organomet. Chem.,* vol. 866, pp. 189-199, 2018.

[298] X. Qiao, D. Qiu, N. Lin, J. Zhu, W. Deng and Z. Yao, *Appl. Organometal. Chem.,* vol. 33, p. e4875, 2019.

[299] F. Ballester, E. Ortega, V. Porto, H. Kostrhunov, N. Davila-Ferreira, D. Bautista, ,. V. Brabec, F. Domínguez, M. Santana and J. Ruiz, *Chem. Commun.,* vol. 55, pp. 1140-1143, 2019.

[300] P. Bruijnincx and P. Sadler, *Adv. Inorg. Chem.,* vol. 61, pp. Adv. Inorg. Chem.,, 2009.

[301] N. Mistry, PhD Thesis, University of York, 2013.

[302] G. Doyle and D. Van Engen, *J. Organomet. Chem.,* vol. 280, pp. 253-259, 1985.

[303] S. Suravajjala, and L. C. Porter, *Acta Crist.,* vol. C49, pp. 1456-1458, 1993.

[304] K. Koike, N. Okoshi, H. Hori, K. Takeuchi, O. Ishitani, H. Tsubaki, I. Clark, M. George, F. Johnson and J. Turner, *J. Am. Chem. Soc.,* vol. 124, pp. 11448-11455, 2002.

[305] Z. Li, A. Pierri, P. Huang, G. Wu, A. Iretskii and P. Ford, *Inorg. Chem.,* vol. 56, p. 6094−6104, 2017.

[306] A. R. a. F. Z. E. Kottelat, *Dalton Trans.,* vol. 45, pp. 6920-6927, 2016.

[307] S. Montanaro, I. Wrigh, A. Batsanov and M. Bryce, *J. Org. Chem.,* p. 12320−12326, 2018.

[308] C. Dessent, J. Kim and M. Johnson, *Acc. Chem. Res.,* vol. 31, pp. 527-534, 1998.

[309] M. Wrighton, *Chem. Rev.,* vol. 74, pp. 401-430, 1974.

[310] R. Baena-Nogueras, E. González-Mazo and P. Lara-Martín, *Environ. Sci. Technol.,* vol. 51, pp. 3148-3156, 2017.

[311] H. Zhang, X. Li, K. Yu, N. Li, J. He, H. You and J. Jiang, *Anal. Chim. Acta,* vol. 1013, pp. 36-42, 2018.

[312] A. Salma, S. Thoröe-Boveleth, T. Schmidt and J. Tuer, *J. Hazard. Mater.,* vol. 313, p. 49–59, 2016.

[313] J. Bull, E. Carrascosa, M. Scholz, N. Coughlan and E. Bieske, *Analyst,* vol. 142, pp. 2100-2103, 2017.

[314] A. Mansour, *Eur. J. Inorg. Chem,* pp. 4805-4811, 2018.

[315] T. Soboleva, H. Esquer, S. Anderson, L. Berreau and A. Benninghoff, *ACS Chem. Biol.,* vol. 13, pp. 2220-2228, 2018.

[316] C. Choi, A. Kulesza, S. Daly, L. MacAleese, R. Antoine, P. Dugourd and F. Chirot, *Rapid Commun Mass Spectrom.,* vol. 33, pp. 28-34, 2019.

[317] T.M. Chang, J. Prell, E. Warrick and E. Williams, *J. Am. Chem. Soc.,* vol. 134, pp. 15805-15813, 2012.